

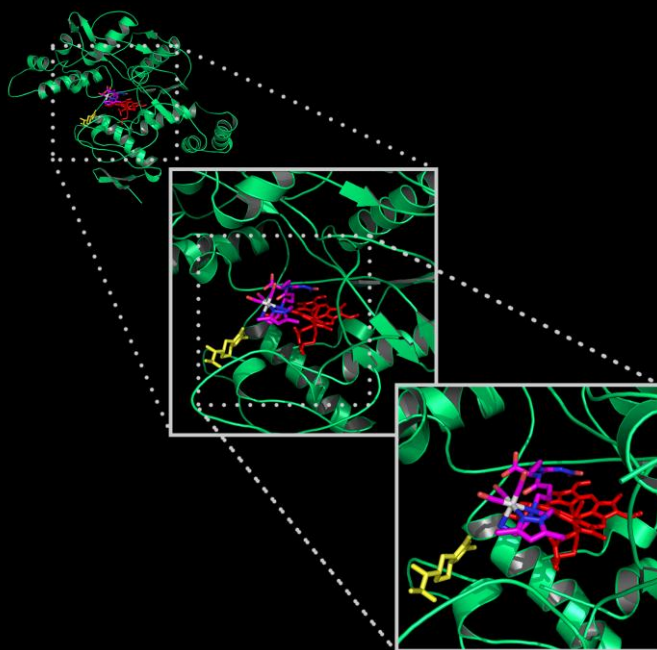
UNIVERSIDADE DE LISBOA

FACULDADE DE CIÊNCIAS

Departamento de Química e Bioquímica



Re and ^{99m}Tc Organometallic Complexes for Targeting Nitric Oxide Synthase



Bruno Luís Jesus Pinto de Oliveira

Doutoramento em Química

Especialidade Química Inorgânica

2012

UNIVERSIDADE DE LISBOA

FACULDADE DE CIÊNCIAS

Departamento de Química e Bioquímica



Re and ^{99m}Tc Organometallic Complexes for Targeting Nitric Oxide Synthase

Bruno Luís Jesus Pinto de Oliveira

Tese orientada por:

Doutor João Domingos Galamba Correia

Doutora Isabel Rego dos Santos (co-orientadora)

Doutoramento em Química

Especialidade Química Inorgânica

2012

The work described in this thesis was performed in the Radiopharmaceutical Sciences Group, Instituto Tecnológico e Nuclear, Sacavém, Portugal, under the supervision of Doctor João D. G. Correia.

The synthesis of the Dap bifunctional chelators have been performed in the group of Prof. Dr. Roger Alberto (Medicinal Inorganic Chemistry Group, Institute of Inorganic Chemistry, University of Zurich, Switzerland).

The computational studies were performed under the supervision of Prof. Dr. Maria João Ramos (Group of Computational BioChemistry, Departamento de Química e Bioquímica, Universidade do Porto, Portugal).

The work was financially supported by Fundação para a Ciência e a Tecnologia through the PhD grant SFRH/BD/38753/2007 and the projects POCI/SAU-FCF/58855/2004 and PTDC/QUI-QUI/121752/2010.

Acknowledgements

Ao meu orientador, Doutor João Galamba Correia, agradeço a forma rigorosa como orientou esta tese de Doutoramento, os conhecimentos transmitidos, a simplicidade, a amizade e principalmente a total disponibilidade demonstrada. Gostaria de manifestar o meu reconhecimento pela forma como contribuiu para a minha formação científica.

À Professora Doutora Isabel Rego dos Santos agradeço a oportunidade que me concedeu para realizar este trabalho no Grupo de Ciências Radiofarmacêuticas, bem como a forma interessada com que o seguiu. Gostaria ainda de demonstrar a minha admiração pelo rigor, entusiasmo e dedicação com que lidera este grupo de investigação.

I would like to thank Prof. Dr. Roger Alberto for the opportunity to work in his group. That was very important for me and for my scientific career.

À Professora Doutora Maria João Ramos agradeço a oportunidade que me concedeu para realizar parte deste trabalho no seu excelente grupo de investigação. Agradeço também o apoio, empenho e disponibilidade sempre presentes.

Ao Professor Doutor Pedro Alexandrino Fernandes agradeço as discussões e sugestões interessantes que decorreram ao longo da minha permanência no grupo de Bioquímica Computacional.

Ao Doutor Carlos Cordeiro e à Professora Ana Ponces Freire, agradeço por me terem recebido no Laboratório de Enzimologia, assim como a total disponibilidade no acompanhamento dos estudos efectuados.

À Doutora Filipa Mendes agradeço a orientação e ajuda na realização de parte dos estudos biológicos desta tese. A sua amizade e total disponibilidade foram muito importantes.

À Doutora Paula Raposinho e Elisabete Correia agradeço o empenho na realização dos estudos de biodistribuição e internalização.

À Doutora Célia Fernandes agradeço a forma amiga como sempre me ajudou.

Ao Amadeu Rodrigues agradeço o apoio técnico prestado em várias circunstâncias e a amizade.

Ao Doutor Joaquim Marçalo agradeço a sua disponibilidade na realização dos espectros de massa apresentados neste trabalho.

Ao Sr. António Soares agradeço a forma cuidadosa com que efectuou as análises elementares de C,H, N de todos os compostos apresentados nesta tese bem como a boa disposição.

À Doutora Isabel Cordeiro dos Santos agradeço a resolução das estruturas moleculares apresentadas nesta tese.

A todos os colegas do grupo de Bioquímica Computacional agradeço o óptimo ambiente de trabalho proporcionado, bem como a simpatia e amizade com que me acolheram. Não posso deixar de manifestar a minha gratidão àqueles que constantemente abdicaram do seu tempo para me ajudar, nomeadamente, Sílvia, Ângela, Marta, Natércia, Alexandra, Nuno, Sérgio, José, João, Daniel, Eduardo, Gaspar e Óscar. Gostava também de deixar um especial agradecimento à Irina por ter orientado e acompanhado o meu trabalho com maior proximidade.

To Dr. Paul Schmutz, Yu, Henrik, Lukas, Fabio, Tooyama, Michael, Daniel and Sebastian thanks for all the help in the lab and friendship.

Aos meus colegas de grupo, sem particularizar uma vez que são muitos, agradeço o óptimo ambiente de trabalho proporcionado, a amizade, a ajuda e o companheirismo.

A todos os meus amigos um especial agradecimento por compreenderem a minha ausência.

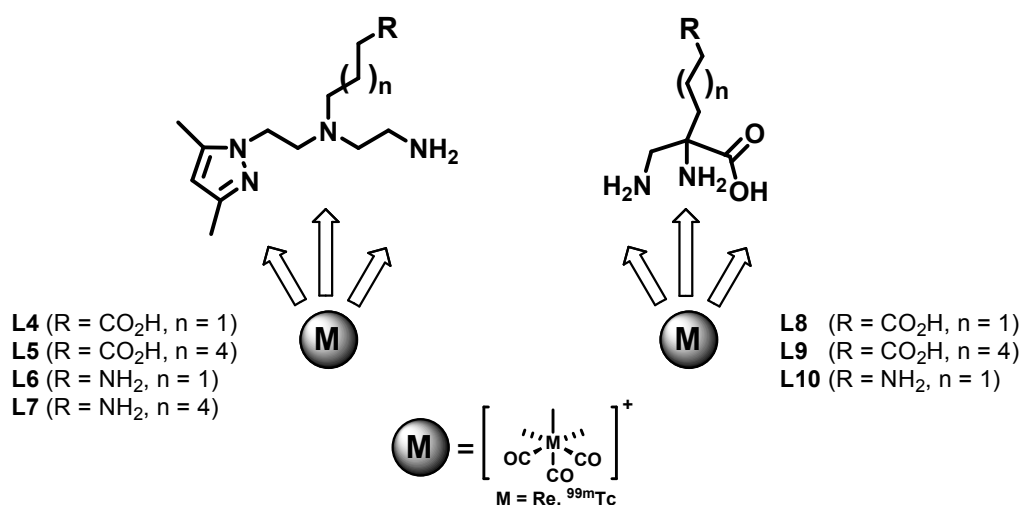
À Patrícia agradeço a paciência e o incentivo sempre presentes. A tua amizade, apoio e afecto foram indispensáveis para superar os momentos mais difíceis que surgiram neste trabalho. A ti concedo-te o título de Mestre em Química ;). Obrigado.

Por último agradeço à minha família, em especial aos meus pais, o apoio incondicional e o exemplo de vida.

Agradeço ao Instituto Tecnológico e Nuclear por me ter acolhido e à Fundação para a Ciência e a Tecnologia pela bolsa de doutoramento (SFRH/BD/38753/2007).

Resumo

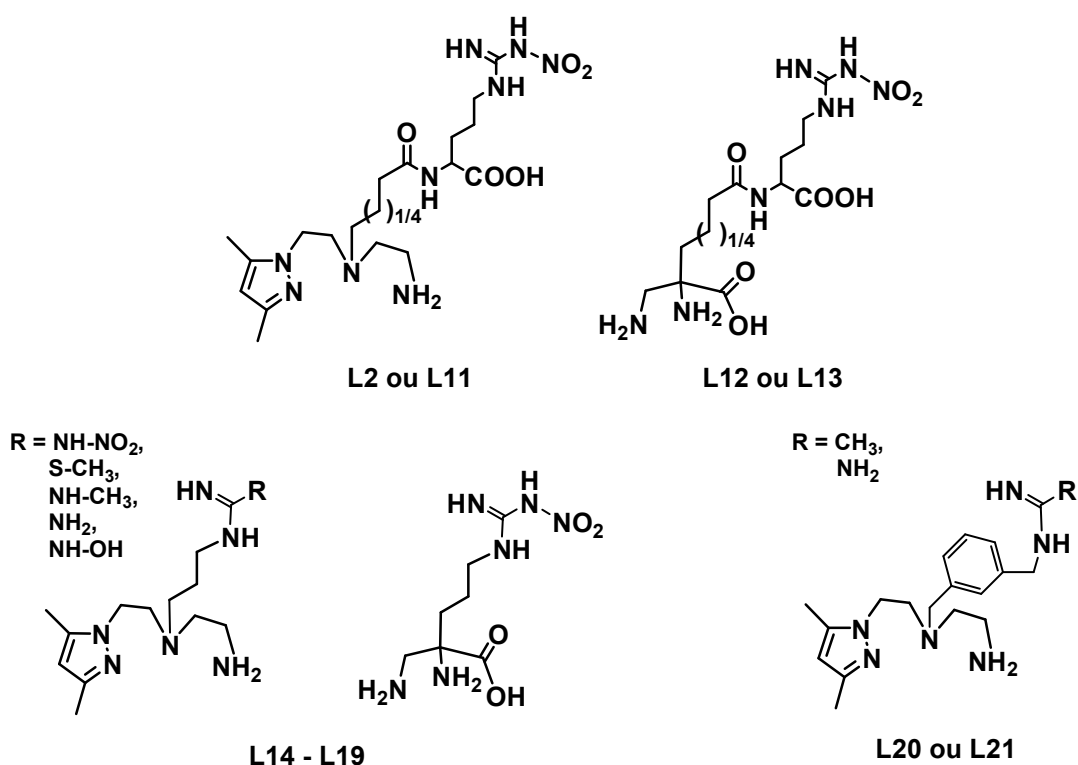
A **imagemologia molecular** permite a **visualização *in vivo*** de **biomoléculas ou processos bioquímicos associados a certas patologias**, mediante a **interacção da molécula alvo com uma sonda molecular**. Deste modo, é possível a **deteção e caracterização em tempo real das patologias**, assim como a **monitorização da terapia**. As **técnicas nucleares de imagem**, tomografia computadorizada por emissão de fóton único (**SPECT**) e tomografia por emissão de positrões (**PET**), são das **mais relevantes em imagemologia molecular**, não só devido ao seu carácter não invasivo como também à sua elevada **sensibilidade**. Estas características advêm essencialmente do facto de se utilizarem **radiofármacos** (compostos que têm na sua composição um elemento radioactivo) com elevada especificidade e actividade específica. O sucesso destas técnicas depende não só da sensibilidade e resolução do equipamento utilizado, mas também da possibilidade de se conceberem radiofármacos cada vez mais sensíveis e específicos para certos órgãos ou tecidos alvo. O trabalho apresentado nesta tese teve como objectivo principal a concepção de novos compostos de $^{99m}\text{Tc(I)}$ potencialmente úteis para a visualização *in vivo*, por SPECT, da sobre-expressão da isoforma induzida da óxido nítrico sintase (iNOS) associada a diferentes patologias. Para se alcançar este objectivo, conceberam-se novos complexos contendo a unidade $\text{fac-}[^{99m}\text{Tc}(\text{CO})_3]^+$ estabilizada por ligandos bifuncionais tridentados contendo grupos específicos para reconhecimento da iNOS. Assim, a primeira parte do trabalho envolveu a síntese e a caracterização dos novos ligandos modelo **L4 – L10** que contêm uma unidade quelante **pirazolo-diamina** ou **diamino propionato (Dap)** e grupos funcionais CO_2H ou NH_2 para posterior conjugação a derivados da L-Arg (inibidores da iNOS) ou transformação em unidades bioactivas (e.g. guanidina).



Ligandos bifuncionais contendo as unidades quelantes **pirazolo-diamina** e **Dap**.

Por reacção de **L4 – L10** com $(\text{NEt}_4)_2[\text{Re}(\text{CO})_3\text{Br}_3]$ e/ou $\text{fac-}[\text{M}(\text{CO})_3(\text{H}_2\text{O})_3]^+$ ($\text{M} = \text{Re}/^{99\text{m}}\text{Tc}$) obtiveram-se, com rendimentos elevados, complexos do tipo $\text{fac-}[\text{M}(\text{CO})_3(\kappa^3\text{-L})]^{+/0}$ ($\text{M} = \text{Re}/^{99\text{m}}\text{Tc}$; **Re4/Tc4**, **L = L4**; **Re5/Tc5**, **L = L5**; **Re6/Tc6**, **L = L6**; **Re7/Tc7**, **L = L7**; **Re8/Tc8**, **L = L8**; **Re9/Tc9**, **L = L9**; **Re10/Tc10**, **L = L10**). Os complexos hidrofílicos **Tc4 – Tc10**, obtidos com elevada actividade específica, são estáveis *in vitro* e *in vivo*. Estudos de biodistribuição em ratinhos demonstraram que os complexos **Tc4**, **Tc5**, **Tc8** e **Tc10** apresentam um perfil biológico mais adequado para imagiologia por SPECT, nomeadamente uma rápida eliminação por via renal. Os complexos radioactivos foram caracterizados por comparação dos seus tempos de retenção nos cromatogramas de HPLC de fase reversa com os tempos de retenção dos compostos análogos de rénio (**Re4 – Re10**) previamente caracterizados pelas técnicas analíticas usais em química, incluindo cristalografia de raios-X de cristal único no caso de **Re4**, **Re5** e **Re8**.

A segunda parte do trabalho contemplou a síntese e caracterização de novos conjugados contendo as unidades quelantes **pirazolo-diamina** ou **Dap** e grupos com reconhecida afinidade para a iNOS tais como a $\text{N}^0\text{-NO}_2\text{-L-Arg}$ (**L2**, **L11 – L13**), alquil-amidinas (**L14 – L19**) e benzil-amidinas (**L20** e **L21**).



*Conjugados contendo as unidades quelantes **pirazolo-diamina** ou **Dap** e grupos com reconhecida afinidade para a iNOS.*

Por reacção dos conjugados com os respectivos precursores organometálicos foi possível preparar com elevado rendimento complexos do tipo $\text{fac-}[\text{M}(\text{CO})_3(\kappa^3\text{-L})]^{+/0}$ ($\text{M} = \text{Re}/^{99\text{m}}\text{Tc}$; **Re2/Tc2**, **L**

= **L2**; **Re11/Tc11**, **L = L11**; **Re12/Tc12**, **L = L12**; **Re13/Tc13**, **L = L13**; **Re14/Tc14**, **L = L14**; **Re15/Tc15**, **L = L15**; **Re16/Tc16**, **L = L16**; **Re17/Tc17**, **L = L17**; **Re18/Tc18**, **L = L18**; **Re19/Tc19**, **L = L19**; **Re20/Tc20**, **L = L20**; **Re21/Tc21**, **L = L21**).

Os conjugados **L2** ($K_i = 178 \mu\text{M}$), **L11** ($K_i = 36 \mu\text{M}$), **L12** ($K_i = 6 \mu\text{M}$), **L13** ($K_i = 759 \mu\text{M}$), **L14** ($K_i = 1087 \mu\text{M}$), **L15** ($K_i = 1019 \mu\text{M}$), **L16** ($K_i = 29 \mu\text{M}$), **L17** ($K_i = 413 \mu\text{M}$), **L18** ($K_m = 553 \mu\text{M}$), **L19** ($K_m = 1675 \mu\text{M}$), **L20** ($K_i = 26 \mu\text{M}$), **L21** ($K_m > 10000 \mu\text{M}$) e os respectivos complexos **Re2** ($K_i = 84 \mu\text{M}$), **Re11** ($K_i = 6 \mu\text{M}$), **Re12** ($K_i = 57 \mu\text{M}$), **Re13** ($K_i = 258 \mu\text{M}$), **Re14** ($K_i = 257 \mu\text{M}$), **Re15** ($K_i = 183 \mu\text{M}$), **Re16** ($K_i = 240 \mu\text{M}$), **Re17** ($K_i = 454 \mu\text{M}$), **Re18** ($K_m = 1035 \mu\text{M}$), **Re19** ($K_m = 1465 \mu\text{M}$), **Re20** ($K_i = 188 \mu\text{M}$), **Re21** ($K_m > 10000 \mu\text{M}$) foram avaliados *in vitro* como inibidores ou substratos da iNOS, utilizando-se o método de captura do NO pela oxihemoglobina. Os resultados dos ensaios enzimáticos permitiram concluir que a afinidade dos conjugados contendo inibidores da iNOS é menos afectada após coordenação à unidade organometálica “Re(CO)₃” do que os conjugados contendo substratos. De facto, a capacidade de interacção de **Re18**, **Re19** e **Re21** com a enzima e a consequente biossíntese de NO é negligenciável ($K_m > 1000 \mu\text{M}$) se comparada com o substrato natural L-Arg ($K_m = 6 \mu\text{M}$). Os resultados enzimáticos permitiram também concluir que a afinidade dos conjugados contendo inibidores é melhorada após coordenação à unidade “Re(CO)₃” (e.g. **L2/Re2**, **L11/Re11**, **L13/Re13**, **L14/Re14**, **L15/Re15**), no entanto, esta tendência não foi observada para os pares **L12/Re12**, **L16/Re16** e **L20/Re20**. Os complexos de Re(I) contendo o inibidor N^ω-NO₂-L-Arg conjugado às unidades quelantes **pirazolo-diamina** e **Dap** através de um espaçador com 3 (**Re2** e **Re12**) ou 6 átomos de carbono (**Re11** e **Re13**) apresentam afinidade assinalável para a iNOS. O poder inibitório de **Re11** ($K_i = 6 \mu\text{M}$) é comparável ao do inibidor N^ω-NO₂-L-Arg livre não conjugado ($K_i = 3 \mu\text{M}$). A afinidade dos conjugados e dos complexos de rénio contendo uma unidade alquil-amidina para a iNOS (**L14** $K_i = 1087 \mu\text{M}$, **Re14** $K_i = 257 \mu\text{M}$; **L15** $K_i = 1675 \mu\text{M}$, **Re15** $K_i = 183 \mu\text{M}$; **L16** $K_i = 29 \mu\text{M}$, **Re16** $K_i = 240 \mu\text{M}$; **L17** $K_i = 413 \mu\text{M}$, **Re17** $K_i = 454 \mu\text{M}$) é em geral menor do que a observada para os compostos contendo a unidade N^ω-NO₂-L-Arg (**L2/Re2**, **L11/Re11**, **L12/Re12** e **L13/Re13**). Estes resultados indicam que a ausência da função aminoácido e o espaçador mais curto entre a unidade quelante e o grupo amidina perturba a interacção com a enzima. Os compostos **L20** ($K_i = 26 \mu\text{M}$) e **Re20** ($188 \mu\text{M}$), análogos do potente inibidor 1400W ($K_d = \sim 7 \text{ nM}$) da iNOS, apresentam baixa afinidade para a enzima comparativamente com a afinidade do inibidor original.

Os complexos **Re2** e **Re11** atravessam a membrana celular de macrófagos activados com lipopolisacárido (LPS) para sobre-expressão da iNOS e interactuam com a enzima alvo, como confirmado pela inibição da biossíntese de NO (ca. 30 - 50 % inibição).

Estudos de biodistribuição com os complexos radioactivos análogos **Tc2** e **Tc11** em ratinhos tratados com LPS revelaram uma maior acumulação da radioactividade nos órgãos que sobre-expressam a iNOS (e.g. pulmões; confirmado por western blot). No entanto, esta fixação não foi

bloqueada pela co-injecção dos compostos com um inibidor potente da iNOS, o que pode sugerir um mecanismo não específico de acumulação.

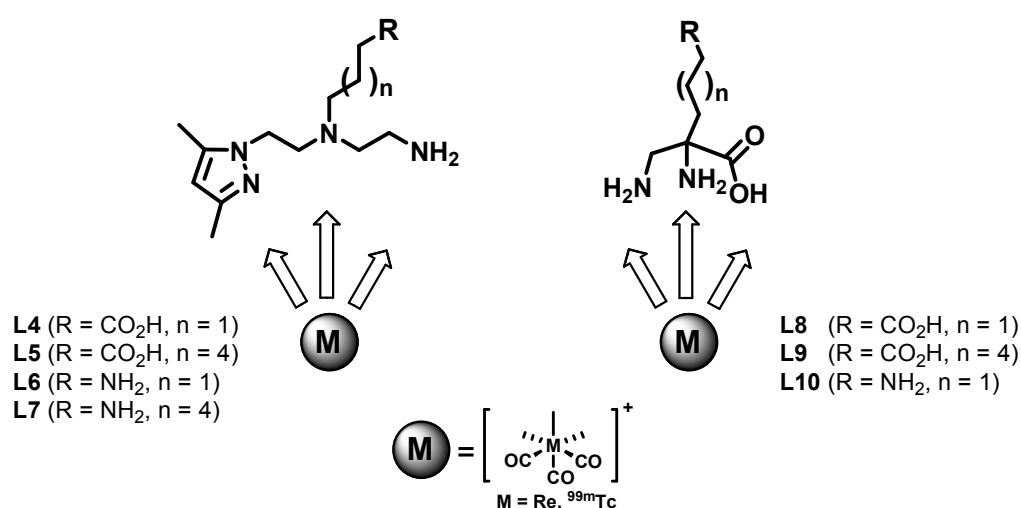
De modo a estabelecer-se uma relação estrutura-actividade, efectuou-se um estudo computacional (*docking* molecular, simulações de dinâmica molecular e cálculos da perturbação de energia livre) para compreender quais as interacções moleculares específicas responsáveis pela capacidade de reconhecimento da enzima pelos diferentes compostos sintetizados. Concluiu-se que a melhor afinidade de **Re11** para a iNOS, comparativamente com **Re2**, parece estar relacionada com interacções electrostáticas estabelecidas entre a unidade “Re(CO)₃” e os resíduos polares Arg260 e Arg382, que são apenas possíveis devido à maior flexibilidade do espaçador com 6 átomos de carbono.

A diferença observada na capacidade de inibição dos complexos **Re11** e **Re13**, que contêm a mesma unidade de reconhecimento da iNOS (espaçador de 6 carbonos + N^o-NO₂-L-Arg) mas possuem quelatos de natureza diferente (**Re11**: pirazolo-diamina e **Re13**: Dap), pode ser explicada com base no diferente posicionamento do fragmento organometálico “Re(CO)₃”. No caso de **Re13**, devido às interacções repulsivas observadas entre o grupo Dap-Re(CO)₃ e os carboxilatos do grupo heme, o fragmento organometálico não consegue acomodar-se no interior do centro activo da enzima, sendo deslocado para a entrada do mesmo. Deste modo, perdem-se contactos importantes entre o complexo e a enzima, que afectam negativamente a afinidade.

O efeito da transformação de **Re2** em **L2** e **Re11** em **L11** na afinidade para a iNOS foi estudado por cálculos de perturbação de energia livre. Os resultados obtidos mostraram que as diferenças de energia estão, de um modo geral, de acordo com o que foi observado experimentalmente ($\Delta\Delta G_{\text{ligação}}^{\text{calc}} \text{Re2} \rightarrow \text{L2} = 0.69 \pm 0.028 \text{ kcal/mol}$, $\Delta\Delta G_{\text{ligação}}^{\text{calc}} \text{Re11} \rightarrow \text{L11} = 6.80 \pm 1.10 \text{ kcal/mol}$; $\Delta\Delta G_{\text{ligação}}^{\text{exp}} \text{Re2} \rightarrow \text{L2} = 0.461 \pm 0.009 \text{ kcal/mol}$, $\Delta\Delta G_{\text{ligação}}^{\text{exp}} \text{Re11} \rightarrow \text{L11} = 1.129 \pm 0.210 \text{ kcal/mol}$): 1) existe uma penalização energética quando se transformam os complexos de rénio nos respectivos ligandos; 2) a maior penalização energética observada experimentalmente para o par **Re11/L11** foi confirmada por FEP. A correlação encontrada entre os valores calculados e determinados experimentalmente sugerem que as conclusões retiradas sobre o tipo de interacções moleculares propostas entre a enzima e os compostos estudados são possíveis de ocorrer. Os resultados obtidos nos estudos computacionais levaram-nos a propor alterações estruturais no complexo **Re11**, nomeadamente a introdução de grupos amina na posição 4- do anel de pirazolilo para promover a interacção com os braços propionato do grupo heme, com o objectivo de se conceberem complexos organometálicos com afinidade melhorada para a iNOS.

Abstract

Molecular imaging allows the visualization of biomolecules or biochemical processes associated to certain pathologies, through the interaction of a target molecule with a molecular probe. In this way it is possible to detect and characterize pathologies, and to follow therapeutical responses. The nuclear imaging techniques, single photon emission computed tomography (SPECT) and positron emission tomography (PET), are among the most relevant molecular imaging modalities due to their non-invasive character and high sensitivity. These characteristics arise from the use of radiopharmaceuticals (drugs that contain a radionuclide in its composition) with high specificity and high specific activity. The success of these techniques depends not only on the sensitivity and resolution of the equipment used to acquire the images, but also on the possibility of designing radiopharmaceuticals with higher sensitivity and specificity for the target organs and tissues. The work presented in this thesis aimed at developing new $^{99m}\text{Tc(I)}$ complexes potentially useful for *in vivo* SPECT-imaging of the overexpression of the inducible isoform of nitric oxide synthase enzyme (iNOS) associated to several pathologies. To achieve such goal we have designed new complexes containing the $fac\text{-}[^{99m}\text{Tc}(\text{CO})_3]^+$ core stabilized by bifunctional tridentate ligands containing specific groups for iNOS recognition. Therefore, the first part of the work involved the synthesis and characterization of the model ligands **L4** – **L10**, which contain a **pyrazolyl-diamine** or a diamino propionic acid (**Dap**) chelating unit, and CO_2H or NH_2 functional groups for conjugation to L-Arg derivatives (inhibitors of iNOS) or transformation into bioactive units (e.g. guanidine).

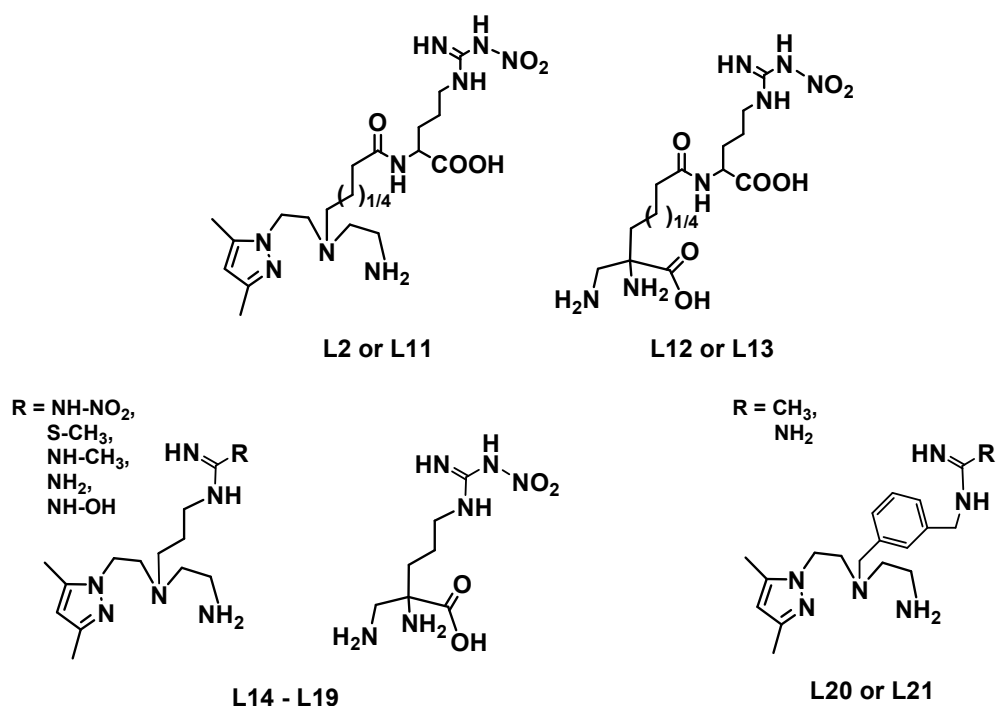


*Bifunctional ligands containing the **pyrazolyl-diamine** and **Dap** chelating units.*

The bifunctional model ligands **L4** – **L10** reacted with $(\text{NEt}_4)_2[\text{Re}(\text{CO})_3\text{Br}_3]$ and/or $fac\text{-}[\text{M}(\text{CO})_3(\text{H}_2\text{O})_3]^+$ ($\text{M} = \text{Re}/^{99m}\text{Tc}$) giving complexes of the type $fac\text{-}[\text{M}(\text{CO})_3(\kappa^3\text{-L})]^{+0}$ ($\text{M} = \text{Re}/^{99m}\text{Tc}$;

Re4/Tc4, L = L4; Re5/Tc5, L = L5; Re6/Tc6, L = L6; Re7/Tc7, L = L7; Re8/Tc8, L = L8; Re9/Tc9, L = L9; Re10/Tc10, L = L10) in high yield. The hydrophilic complexes **Tc4 – Tc10**, obtained with high specific activity, are stable *in vitro* and *in vivo*. Biodistribution studies in mice revealed that **Tc4, Tc5, Tc8** and **Tc10** present the most adequate overall biological profile for SPECT-imaging, namely a good clearance from all organs and tissues, being the major excretory route the renal-urinary pathway. The structural characterization of the ^{99m}Tc (I) complexes was performed by comparing their chromatographic behavior with that of the corresponding Re(I) complexes, which have been characterized by the usual analytical techniques in chemistry, including X-ray diffraction analysis in the case of **Re4, Re5** and **Re8**.

The second part of the work focused on the synthesis and characterization of new conjugates containing the **pyrazolyl-diamine** or **Dap** chelating units and iNOS recognizing moieties such as N^{O} - NO_2 -L-Arg (**L2, L11 – L13**), alkyl-amidines (**L14 – L19**) and benzyl-amidines (**L20** and **L21**).



Conjugates containing the **pyrazolyl-diamine** or **Dap** chelating units and groups with recognized affinity for iNOS.

Reaction of the conjugates with the respective organometallics precursors yielded (70 – 98 %) complexes of the type $fac\text{-}[M(\text{CO})_3(\kappa^3\text{-L})]^{+/0}$ ($M = \text{Re}/^{99m}\text{Tc}$; **Re2/Tc2, L = L2; Re11/Tc11, L = L11; Re12/Tc12, L = L12; Re13/Tc13, L = L13; Re14/Tc14, L = L14; Re15/Tc15, L = L15; Re16/Tc16, L = L16; Re17/Tc17, L = L17; Re18/Tc18, L = L18; Re19/Tc19, L = L19; Re20/Tc20, L = L20; Re21/Tc21, L = L21**).

The conjugates **L2** ($K_i = 178 \mu\text{M}$), **L11** ($K_i = 36 \mu\text{M}$), **L12** ($K_i = 6 \mu\text{M}$), **L13** ($K_i = 759 \mu\text{M}$), **L14** ($K_i = 1087 \mu\text{M}$), **L15** ($K_i = 1019 \mu\text{M}$), **L16** ($K_i = 29 \mu\text{M}$), **L17** ($K_i = 413 \mu\text{M}$), **L18** ($K_m = 553 \mu\text{M}$), **L19** ($K_m = 1675 \mu\text{M}$), **L20** ($K_i = 26 \mu\text{M}$), **L21** ($K_m > 10000 \mu\text{M}$) and the respective complexes **Re2** ($K_i = 84 \mu\text{M}$), **Re11** ($K_i = 6 \mu\text{M}$), **Re12** ($K_i = 57 \mu\text{M}$), **Re13** ($K_i = 258 \mu\text{M}$), **Re14** ($K_i = 257 \mu\text{M}$), **Re15** ($K_i = 183 \mu\text{M}$), **Re16** ($K_i = 240 \mu\text{M}$), **Re17** ($K_i = 454 \mu\text{M}$), **Re18** ($K_m = 1035 \mu\text{M}$), **Re19** ($K_m = 1465 \mu\text{M}$), **Re20** ($K_i = 188 \mu\text{M}$), **R21** ($K_m > 10000 \mu\text{M}$) have been tested *in vitro* as inhibitors or substrates of iNOS, using the oxyhemoglobin NO capture assay. The enzymatic studies demonstrated that the affinity for the enzyme of the conjugates with pendant enzyme inhibitors seemed to be less affected upon metallation with “Re(CO)₃” than the conjugates containing pendant substrates. In fact, the ability of **Re18**, **Re19**, and **Re21** to interact with the active site of iNOS and produce NO is negligible ($k_m > 1000 \mu\text{M}$) compared to the natural substrate L-Arg ($K_m = 6 \mu\text{M}$). Interestingly, metallation of the inhibitor-containing conjugates with the “Re(CO)₃” core led to complexes with improved affinity for iNOS (**L2/Re2**, **L11/Re11**, **L13/Re13**, **L14/Re14**, **L15/Re15**). Out of this trend are the matched pairs **L12/Re12**, **L16/Re16** and **L20/Re20**. The Re(I)-complexes with a N^o-NO₂-L-Arg moiety coupled to the **pyrazolyl-diamine** or **Dap** chelating unit through a spacer of 3- (**Re2** and **Re12**) or 6-carbon atoms (**Re11** and **Re13**) presented remarkable affinity for iNOS. The inhibitory potency of **Re11** ($K_i = 6 \mu\text{M}$) is comparable to that of the free inhibitor N^o-NO₂-L-Arg ($K_i = 3 \mu\text{M}$). The affinity of the conjugates and rhenium complexes containing an integrated alkyl-amidine moiety (**L14** $K_i = 1087 \mu\text{M}$, **Re14** $K_i = 257 \mu\text{M}$; **L15** $K_i = 1675 \mu\text{M}$, **Re15** $K_i = 183 \mu\text{M}$; **L16** $K_i = 29 \mu\text{M}$, **Re16** $K_i = 240 \mu\text{M}$; **L17** $K_i = 413 \mu\text{M}$, **Re17** $K_i = 454 \mu\text{M}$) for iNOS is in general smaller than that observed for the N^o-NO₂-L-Arg-containing compounds (**L2/Re2**, **L11/Re11**, **L12/Re12** and **L13/Re13**). These results indicated that the absence of an amino acid unit and the shortening of the spacer between the chelator and the iNOS recognizing moiety disturbs the interaction with the active site of iNOS. Compounds **L20** ($K_i = 26 \mu\text{M}$) and **Re20** ($K_i = 188 \mu\text{M}$), which have a conformationally-restricted benzyl-acetamide moiety, similar to the potent inhibitor 1400W (K_d value $\sim 7 \text{ nM}$), have a lower affinity for the enzyme than the parent compound.

The complexes **Re2** and **Re11** permeate through the cell membranes of macrophages activated with lipopolysaccharide (LPS) to overexpress the iNOS and interact with the cytosolic target enzyme, as confirmed by the inhibition of NO biosynthesis (ca. 30 – 50 % inhibition).

Biodistribution studies with the analog complexes **Tc2** and **Tc11** in LPS-treated mice revealed a higher accumulation of the radioactivity in the organs that overexpress iNOS (e.g. lungs; confirmed by western blot analysis). However, this accumulation was not blocked by the use of a potent inhibitor of iNOS, suggesting a non-specific mechanism of accumulation.

In order to establish structure-activity relationships, we performed computational studies (molecular docking, molecular dynamics simulations and free energy perturbations calculations) to

understand the specific molecular interactions responsible for the affinity of the compounds to the enzyme. The higher affinity of **Re11** for iNOS, when compared to **Re2**, seems to be related with electrostatic interactions between the “Re(CO)₃” core and the polar Arg260 and Arg382 residues at the active site, only possible due to the higher flexibility of the 6-carbon atoms linker.

The striking difference in inhibitory potency observed for complexes **Re11** and **Re13**, which share the common NOS recognizing unit (6-Carbon linker + N^ω-NO₂-L-Arg moiety) but have chelators of different nature (**Re11**: pyrazolyl-diamine based and **Re13**: Dap-based), can be rationalized in terms of the different position of the “Re(CO)₃” organometallic moiety. In the case of **Re13**, the bulky organometallic moiety is not well accommodated inside the active pocket of iNOS and is oriented towards its “open entrance”. Such orientation is due to the electrostatic destabilization found in the interaction between the C6-Dap-Re(CO)₃ organometallic tail and the heme carboxylate groups. This behavior explains the lower affinity of **Re13** for iNOS since there are a smaller number of contacts between the Re complex and the enzyme.

We have also studied the effect of the transformation of **Re2** into **L2** and **Re11** into **L11** on the binding affinity to iNOS using the FEP methodology. We have observed that the free energy differences match the trend observed in the experimental data ($\Delta\Delta G_{\text{bind}}^{\text{calc}} \text{Re2} \rightarrow \text{L2} = 0.690 \pm 0.028$ kcal/mol, $\Delta\Delta G_{\text{bind}}^{\text{calc}} \text{Re11} \rightarrow \text{L11} = 6.800 \pm 1.10$ kcal/mol; $\Delta\Delta G_{\text{bind}}^{\text{exp}} \text{Re2} \rightarrow \text{L2} = 0.461 \pm 0.009$ kcal/mol, $\Delta\Delta G_{\text{bind}}^{\text{exp}} \text{Re11} \rightarrow \text{L11} = 1.129 \pm 0.210$ kcal/mol): 1) there is an energetic penalty for the transformation of the Re complexes into the ligands; 2) the higher energetic penalty found experimentally for the pair **Re11/L11** was confirmed by FEP. This correlation between the calculated and experimental values validates our docking and MD approach and demonstrates that all drawn conclusions concerning the proposed interactions between complexes and the enzyme are likely to occur. The results from the computational studies prompted us to propose structural modifications to **Re11**, namely the introduction of amine groups at the 4-position of the pyrazolyl ring to promote the interaction with the propionate arms of the heme group, providing organometallic complexes with improved affinity for iNOS.

Palavras-Chave

Rênio

Tecnécio

Imagiologia

Óxido Nítrico Sintase (NOS)

Química computacional

Keywords

Rhenium

Technetium

Imagiology

Nitric Oxide Synthase (NOS)

Computational Chemistry

Table of Contents

| | |
|---|-----------|
| Acknowledgements | iii |
| Resumo | v |
| Abstract | ix |
| Palavras-Chave | xiii |
| Keywords | xiii |
| Table of Contents | xv |
| Figures | xxiii |
| Tables | xxix |
| Schemes..... | xxxii |
| Abbreviations | xxxiii |
| Scope and Aim | 1 |
| 1. Introduction..... | 7 |
| 1.1 – Imaging in Clinical Set | 7 |
| 1.2 – Nuclear Medicine and Radiopharmaceuticals..... | 8 |
| 1.2.1 – Diagnosis vs Therapy | 9 |
| 1.3 - Technetium and Rhenium Coordination Chemistry Relevant for Nuclear Medicine..... | 12 |
| 1.3.1 – The Radiochemistry of Technetium..... | 13 |
| 1.3.2 – ^{99m}Tc Radiopharmaceuticals | 15 |
| 1.3.3 – The <i>fac</i>-[M(CO)₃]⁺ Core (M = Tc, Re)..... | 19 |
| 1.4 – Nitric Oxide Synthase | 23 |
| 1.4.1 – Structure and Function..... | 23 |
| 1.4.2 - Catalytic Mechanism of Nitric Oxide Synthase | 26 |
| 1.4.3 – Chemical Biology of NO | 27 |
| 1.4.4 – NO/NOS and Disease | 29 |
| 1.4.5 – Radioactive Probes for Targeting NOS | 33 |
| 1.5 – Computational Chemistry: Importance in Drug Discovery..... | 35 |
| 1.5.1 - Molecular Docking..... | 36 |
| 1.5.1.1 - <i>Docking Algorithms</i> | 36 |
| 1.5.1.2 - <i>Scoring Functions</i> | 40 |
| 1.5.1.3 - <i>Docking Tools: AutoDock 4.2</i> | 40 |
| 1.5.1.3.1 - <i>Grid maps in AutoDock 4.2</i> | 40 |
| 1.5.1.3.2 – <i>Semi Empirical Free Energy Force Field of AutoDock 4.2</i> | 41 |

| | |
|---|----|
| 1.5.1.4 – Refinement of Docked Complexes | 44 |
| 1.5.2 – Molecular Mechanics, Molecular Dynamics and Force Fields | 45 |
| 1.5.2.1 – Classical Molecular Mechanics | 46 |
| 1.5.2.2 - CHARMM Force Fields | 48 |
| 1.5.2.3 - Classical Molecular Dynamics Simulations..... | 48 |
| 1.5.2.3.1 - Technical Aspects in Molecular Dynamics Simulations | 50 |
| 1.5.3 - Free Energy Calculations | 51 |
| 1.5.3.1 - Free Energy Perturbation..... | 52 |
| 2. Synthesis of Bifunctional Chelators (BFCs) and their Re(I) and ^{99m} Tc(I) Complexes..... | 57 |
| 2.1 – Pyrazolyl-Based BFCs and their Re(I)/ ^{99m} Tc(I) Complexes | 58 |
| 2.1.1 - Synthesis of the Pyrazolyl BFCs L4 – L7 | 58 |
| 2.1.2 - Reactions of L4 – L7 with <i>fac</i> -[M(CO) ₃] ⁺ Precursors (M = Re or ^{99m} Tc)..... | 60 |
| 2.1.2.1 - Synthesis and Characterization of the Re(I) Complexes Re4 – Re7 | 60 |
| 2.1.2.2 - Synthesis, Characterization and Biological Behavior of the ^{99m} Tc (I) Complexes Tc4 – Tc7 | 64 |
| 2.1.2.2.1 - <i>in vitro</i> studies of the ^{99m} Tc (I) Complexes Tc4 – Tc7 | 65 |
| 2.1.2.2.2 - <i>in vivo</i> Studies of the ^{99m} Tc (I) Complexes Tc4 – Tc7 | 65 |
| 2.2 – Dap-based BFCs and their Re(I)/ ^{99m} Tc(I) Complexes | 69 |
| 2.2.1 - Synthesis of the Dap BFCs L8 – L10 | 70 |
| 2.2.2 - Reactions of L8 – L10 with <i>fac</i> -[M(CO) ₃] ⁺ Precursors (M = Re or ^{99m} Tc)..... | 77 |
| 2.2.2.1 - Synthesis and Characterization of the Re (I) Complexes Re8 – Re10 | 77 |
| 2.2.2.2 - Synthesis, Characterization and Biological Behavior of the ^{99m} Tc (I) Complexes Tc8 – Tc10 | 81 |
| 2.2.2.2.1 - <i>In vitro</i> Studies of the ^{99m} Tc (I) Complexes Tc8 – Tc10..... | 82 |
| 2.2.2.2.2 - <i>In vivo</i> Studies of the ^{99m} Tc (I) Complexes Tc8 and Tc10..... | 83 |
| 2.3 – Conclusions..... | 84 |
| 3. Synthesis of Conjugates with iNOS Recognizing Moieties and their Re(I) and ^{99m} Tc(I) Complexes .. | 87 |
| 3.1 – Conjugates Containing N ^ω -NO ₂ -L-Arg and Amidine Moiety and their Re(I)/ ^{99m} Tc(I) Complexes | 87 |
| 3.1.1 - Conjugates Containing the N ^ω -NO ₂ -L-Arg Moiety | 87 |
| 3.1.2 - Conjugates Containing Alkyl-Amidine Moieties..... | 89 |
| 3.1.3 - Conjugates Containing Conformationally-Restricted Amidine Moieties | 92 |
| 3.1.4 - Reactions of L11 – L21 with <i>fac</i> -[M(CO) ₃] ⁺ Precursors (M = Re or ^{99m} Tc)..... | 95 |
| 3.1.4.1 - Synthesis and Characterization of the Re (I) Complexes | 95 |
| 3.1.4.2 - Synthesis, Characterization and Biological Behavior of the ^{99m} Tc (I) Complexes | 99 |

| | |
|---|-----|
| 3.1.4.2.1 - <i>In Vitro</i> Studies of the ^{99m} Tc Tricarbonyl Complexes Tc11 – Tc21..... | 100 |
| 3.2 – Conclusion | 100 |
| 4. <i>in vitro</i> and <i>in vivo</i> Biological Evaluation | 105 |
| 4.1 – Enzymatic Studies..... | 105 |
| 4.1.1 – Enzymatic Activity of iNOS in the Presence of L11 – L21 and Re11 – Re21. | 109 |
| 4.2 – <i>in vivo</i> Biological Evaluation: NO Inhibition in LPS-Induced RAW 264.7 Macrophages | 114 |
| 4.3 - <i>in vivo</i> Biodistribution Study in LPS-Tretreated Mice..... | 117 |
| 4.4 - Conclusion | 119 |
| 5. Theoretical Studies | 123 |
| 5.1 – Molecular Docking..... | 124 |
| 5.1.1 – Validation of the Docking Conditions | 124 |
| 5.1.2 - Docking of Conjugates and Re (I) Complexes Containing the Pyrazolyl-Diamine BFC.... | 127 |
| 5.1.3 - Docking of Conjugates and Re(I) Complexes Containing the Dap BFC..... | 129 |
| 5.2 – Molecular Dynamics (MD) Simulations | 131 |
| 5.2.1 – Evaluation of the Performance of CHARMM Force-Field Parameters for Modeling NOS Protein | 131 |
| 5.2.1.1 – MD Simulations of the iNOS Inhibitors 20 and 21 | 131 |
| 5.2.1.1.1 – Analysis of the Trajectories..... | 133 |
| 5.2.1.1.1.1 – Structural Stability During MD Simulations..... | 133 |
| 5.2.1.1.1.2 – Interactions Between Inhibitor 20 and NOS Isoforms | 134 |
| 5.2.1.1.1.3 – Interactions Between Inhibitor 21 and NOS Isoforms | 137 |
| 5.2.2 – MD Simulations of the Re(I) Complexes Containing the Pyrazolyl-diamine BFC | 138 |
| 5.2.2.1 – Analysis of the Trajectories..... | 139 |
| 5.2.2.1.1 – Structural Stability During MD Simulations..... | 139 |
| 5.2.2.1.2 – Interactions Between the Pyrazolyl-Diamine-Containing Compounds (L2, L11, Re2 and Re11) and iNOS..... | 142 |
| 5.2.3 – MD Simulations of the Re(I) Complexes Containing the Dap BFC..... | 147 |
| 5.2.3.1 – Analysis of the Trajectories..... | 147 |
| 5.2.3.1.1 – Structural Stability During MD Simulations..... | 147 |
| 5.2.3.1.2 – Interactions Between the Dap-Containing compounds (L12, L13, L16, Re12, Re13 and Re16) and iNOS..... | 148 |
| 5.2.4 - FEP Simulations | 154 |
| 5.3 - Conclusions..... | 157 |
| 6. Concluding Remarks and Perspectives..... | 161 |
| 7. Experimental Part..... | 171 |

| | |
|---|-----|
| 7.1 - Materials | 171 |
| 7.2 - Characterization and Purification Techniques | 171 |
| 7.3 - Synthesis and Characterization of Compounds | 174 |
| 7.3.1 - 4-((2-aminoethyl)(2-(3,5-dimethyl-1 <i>H</i> -pyrazol-1-yl)ethyl)amino)butanoic acid (L4) | 174 |
| 7.3.2 - Ethyl 7-((2-(<i>tert</i> -butoxycarbonylamino)ethyl)(2-(3,5-dimethyl-1 <i>H</i> -pyrazol-1-yl)ethyl)amino)heptanoate (29) | 175 |
| 7.3.3 - 7-((2-(<i>tert</i> -butoxycarbonylamino)ethyl)(2-(3,5-dimethyl-1 <i>H</i> -pyrazol-1-yl)ethyl)amino)heptanoic acid (L5-Boc) | 175 |
| 7.3.4 - 7-((2-aminoethyl)(2-(3,5-dimethyl-1 <i>H</i> -pyrazol-1-yl)ethyl)amino)heptanoic acid (L5.TFA) | 176 |
| 7.3.5 - <i>tert</i> -butyl 2-((2-(3,5-dimethyl-1 <i>H</i> -pyrazol-1-yl)ethyl)(3-(1,3-dioxo-2,3-dihydro-1 <i>H</i> -inden-2-yl)propyl)amino)ethylcarbamate (30) | 176 |
| 7.3.6 - <i>tert</i> -butyl 2-((3-aminopropyl)(2-(3,5-dimethyl-1 <i>H</i> -pyrazol-1-yl)ethyl)amino)ethylcarbamate (L6-Boc) | 177 |
| 7.3.7 - <i>N</i> -(2-aminoethyl)- <i>N</i> -(2-(3,5-dimethyl-1 <i>H</i> -pyrazol-1-yl)ethyl)propane-1,3-diamine (L6.2TFA) | 177 |
| 7.3.8 - <i>tert</i> -butyl 2-((2-(3,5-dimethyl-1 <i>H</i> -pyrazol-1-yl)ethyl)(6-(1,3-dioxoisindolin-2-yl)hexyl)amino)ethylcarbamate (31) | 178 |
| 7.3.9 - <i>tert</i> -butyl 2-((6-aminoethyl)(2-(3,5-dimethyl-1 <i>H</i> -pyrazol-1-yl)ethyl)amino)ethylcarbamate (L7-Boc) | 179 |
| 7.3.10 - <i>N</i> -(2-aminoethyl)- <i>N</i> -(2-(3,5-dimethyl-1 <i>H</i> -pyrazol-1-yl)ethyl)hexane-1,6-diamine (L7.2TFA) | 179 |
| 7.3.11 - <i>Tert</i> -butyl 2-acetamido-2-cyanoacetate (32) | 180 |
| 7.3.12 - 1- <i>tert</i> -butyl 6-ethyl 2-acetamido-2-cyanohexanedioate (33) | 180 |
| 7.3.13 - 1- <i>tert</i> -butyl 6-ethyl 2-acetamido-2-((<i>tert</i> -butoxycarbonylamino)methyl)hexanedioate (34) | 181 |
| 7.3.14 - 5-acetamido-6- <i>tert</i> -butoxy-5-((<i>tert</i> -butoxycarbonylamino)methyl)-6-oxohexanoic acid (35) | 182 |
| 7.3.15 - 2-amino-2-(aminomethyl)hexanedioic acid (L8.2Cl) | 182 |
| 7.3.16 - 1- <i>tert</i> -butyl 9-ethyl 2-acetamido-2-cyanononanedioate (37) | 183 |
| 7.3.17 - 1- <i>tert</i> -butyl 9-ethyl 2-acetamido-2-((<i>tert</i> -butoxycarbonylamino)methyl)nonanedioate (38) | 184 |
| 7.3.18 - 8-acetamido-9- <i>tert</i> -butoxy-8-((<i>tert</i> -butoxycarbonylamino)methyl)-9-oxononanoic acid (39) | 185 |
| 7.3.19 - 2-amino-2-(aminomethyl)nonanedioic acid (L9.2Cl) | 185 |
| 7.3.20 - Ethyl 2-acetamido-2-cyanoacetate (40) | 186 |
| 7.3.21 - Benzyl <i>N</i> -(3-bromopropyl)carbamate (41) | 186 |

| | |
|---|-----|
| 7.3.22 - Ethyl 2-acetamido-5-(benzyloxycarbonylamino)-2-cyanopentanoate (42) | 187 |
| 7.3.23 - Ethyl 8-acetamido-13,13-dimethyl-3,11-dioxo-1-phenyl-2,12-dioxo-4,10-diazatetradecane-8-carboxylate (43) | 187 |
| 7.3.24 - Ethyl 2-acetamido-5-amino-2-((<i>tert</i> -butoxycarbonylamino)methyl)pentanoate (44) . | 188 |
| 7.3.25 - 2,5-diamino-2-(aminomethyl)pentanoic acid (L10.3Cl) | 189 |
| 7.3.26 - Ethyl 2-acetamido-2-cyano-5-(1,3-dioxoisindolin-2-yl)pentanoate (46) | 190 |
| 7.3.27 - Ethyl 2-acetamido-2-((<i>tert</i> -butoxycarbonylamino)methyl)-5-(1-hydroxy-3-oxoisindolin-2-yl)pentanoate (47)..... | 190 |
| 7.3.28 - <i>tert</i> -butyl 2-acetamido-5-amino-2-(hydroxymethyl)pentylcarbamate (48) | 191 |
| 7.3.29 - 2,5-diamino-2-(aminomethyl)pentan-1-ol (L10-OH.3TFA) | 191 |
| 7.3.30 - Methyl 15-(2-(3,5-dimethyl-1 <i>H</i> -pyrazol-1-yl)ethyl)-1-imino-21,21-dimethyl-1-(nitroamino)-8,19-dioxo-20-oxa-2,7,15,18-tetraazadocosane-6-carboxylate (49)..... | 192 |
| 7.3.31 - 2-(7-((2-aminoethyl)(2-(3,5-dimethyl-1 <i>H</i> -pyrazol-1-yl)ethyl)amino)heptanamido)-5-(3-nitroguanidino)pentanoic acid (L11.TFA)..... | 193 |
| 7.3.32 - <i>tert</i> -butyl 2-acetamido-2-((<i>tert</i> -butoxycarbonylamino)methyl)-6-(1-methoxy-5-(3-nitroguanidino)-1-oxopentan-2-ylamino)-6-oxohexanoate (50) | 194 |
| 7.3.33 - 2-amino-2-(aminomethyl)-6-(1-carboxy-4-(2-nitroguanidino)butylamino)-6-oxohexanoic acid (L12.2TFA) | 195 |
| 7.3.34 - <i>Tert</i> -butyl 2-acetamido-2-((<i>tert</i> -butoxycarbonylamino)methyl)-9-(1-methoxy-5-(3-nitroguanidino)-1-oxopentan-2-ylamino)-9-oxononanoate (51)..... | 195 |
| 7.3.35 - 2-amino-2-(aminomethyl)-9-(1-methoxy-5-(3-nitroguanidino)-1-oxopentan-2-ylamino)-9-oxononanoic acid (L13) | 196 |
| 7.3.36 - 2-methyl-1-nitro-2-thiopseudourea (52) | 196 |
| 7.3.37 - 1-(3-((2-aminoethyl)(2-(3,5-dimethyl-1 <i>H</i> -pyrazol-1-yl)ethyl)amino)propyl)-3-nitroguanidine (L14.TFA) and methyl 3-((2-aminoethyl)(2-(3,5-dimethyl-1 <i>H</i> -pyrazol-1-yl)ethyl)amino)propylcarbamidithioate (L15.TFA)..... | 197 |
| 7.3.38 - 2-amino-2-(aminomethyl)-5-(3-nitroguanidino)pentanoic acid (L16.2Cl) | 198 |
| 7.3.39 - N-methyl-1 <i>H</i> -pyrazole-1-carboximidamide (53) | 199 |
| 7.3.40 - 1-(3-((2-aminoethyl)(2-(3,5-dimethyl-1 <i>H</i> -pyrazol-1-yl) ethyl)amino)propyl)-3-methylguanidine (L17.TFA)..... | 199 |
| 7.3.41 - 1-(3-((2-aminoethyl)(2-(3,5-dimethyl-1 <i>H</i> -pyrazol-1-yl)ethyl)amino)propyl)guanidine (L18.2TFA)..... | 200 |
| 7.3.42 - 1-(3-((2-aminoethyl)(2-(3,5-dimethyl-1 <i>H</i> -pyrazol-1-yl)ethyl)amino)propyl)-3-hydroxyguanidine (L19.TFA)..... | 201 |
| 7.3.43 - <i>Tert</i> -butyl 2-((3-cyanobenzyl)(2-(3,5-dimethyl-1 <i>H</i> -pyrazol-1-yl)ethyl)amino)ethylcarbamate (56)..... | 202 |
| 7.3.44 - <i>Tert</i> -butyl 2-((3-(aminomethyl)benzyl)(2-(3,5-dimethyl-1 <i>H</i> -pyrazol-1-yl)ethyl)amino)ethylcarbamate (57)..... | 202 |

| | | |
|--------|--|-----|
| 7.3.45 | – N-(3-(((2-aminoethyl)(2-(3,5-dimethyl-1H-pyrazol-1-yl)ethyl)amino)methyl)benzyl)acetimidamide (L20.TFA)..... | 203 |
| 7.3.46 | – 1-(3-(((2-aminoethyl)(2-(3,5-dimethyl-1H-pyrazol-1-yl)ethyl)amino)methyl)benzyl)guanidine (L21.2TFA)..... | 204 |
| 7.4 | – Synthesis and Characterization of Re Complexes of the Type <i>fac</i> -[Re(CO) ₃ (κ ³ -L)] | 205 |
| 7.4.1 | - <i>fac</i> -[Re(CO) ₃ (κ ³ -L4)] ⁺ (Re4.TFA) | 205 |
| 7.4.2 | - <i>fac</i> -[Re(CO) ₃ (κ ³ -L5)] ⁺ (Re5.TFA) | 206 |
| 7.4.3 | - <i>fac</i> -[Re(CO) ₃ (κ ³ -L6)] ⁺ (Re6.2TFA) | 206 |
| 7.4.4 | - <i>fac</i> -[Re(CO) ₃ (κ ³ -L7)] ⁺ (Re7.2TFA) | 207 |
| 7.4.5 | - <i>fac</i> -[Re(CO) ₃ (κ ³ -L8)] (Re8) | 208 |
| 7.4.6 | - <i>fac</i> -[Re(CO) ₃ (κ ³ -L9)] (Re9) | 209 |
| 7.4.7 | - <i>fac</i> -[Re(CO) ₃ (κ ³ -L10)] (Re10.TFA) | 210 |
| 7.4.8 | – Tentative synthesis of <i>fac</i> -[Re(CO) ₃ (κ ³ -L10-OH)] (Re10-OH.2TFA) | 210 |
| 7.4.9 | - <i>fac</i> -[Re(CO) ₃ (κ ³ -L11)] (Re11.TFA) | 211 |
| 7.4.10 | - <i>fac</i> -[Re(CO) ₃ (κ ³ -L12)] (Re12) | 212 |
| 7.4.11 | - <i>fac</i> -[Re(CO) ₃ (κ ³ -L13)] (Re13) | 213 |
| 7.4.12 | - <i>fac</i> -[Re(CO) ₃ (κ ³ -L14)] (Re14.TFA) | 213 |
| 7.4.13 | - <i>fac</i> -[Re(CO) ₃ (κ ³ -L15)] (Re15.TFA) | 214 |
| 7.4.14 | - <i>fac</i> -[Re(CO) ₃ (κ ³ -L16)] (Re16)..... | 215 |
| 7.4.15 | - <i>fac</i> -[Re(CO) ₃ (κ ³ -L17)] (Re17.TFA) | 215 |
| 7.4.16 | - <i>fac</i> -[Re(CO) ₃ (κ ³ -L18)] (Re18.TFA) | 216 |
| 7.4.17 | - <i>fac</i> -[Re(CO) ₃ (κ ³ -L19)] (Re19.TFA) | 217 |
| 7.4.18 | - <i>fac</i> -[Re(CO) ₃ (κ ³ -L20)] (Re20.TFA) | 217 |
| 7.4.19 | - <i>fac</i> -[Re(CO) ₃ (κ ³ -L21)] (Re21.2TFA) | 218 |
| 7.5 | - Synthesis of ^{99m} Tc Complexes of the Type <i>fac</i> -[^{99m} Tc(CO) ₃ (κ ³ -L)] | 218 |
| 7.5.1 | - Preparation of the <i>fac</i> -[^{99m} Tc(CO) ₃ (H ₂ O) ₃] ⁺ Precursor | 218 |
| 7.5.2 | - General Method for Preparing the ^{99m} Tc(I) Complexes | 219 |
| 7.6 | - <i>in vitro</i> Stability Studies: Stability in the Presence of Cysteine and Histidine..... | 219 |
| 7.7 | – Partition Coefficient | 219 |
| 7.8 | - <i>in vivo</i> Studies..... | 220 |
| 7.8.1 | - Biodistribution Studies in CD-1 Female Mice..... | 220 |
| 7.8.2 | - Biodistribution in C57BL/6 LPS-Treated Mice | 220 |
| 7.8.3 | - <i>in vivo</i> Stability/Metabolization | 221 |
| 7.8.4 | - Western Blot of Lungs of LPS-Treated Mice..... | 221 |

| | |
|---|-----|
| 7.9 - Enzymatic Assays..... | 222 |
| 7.9.1 - Preparation of Oxyhemoglobin..... | 222 |
| 7.9.2 - Determination of Kinetic Parameters | 222 |
| 7.9.2.1 - <i>Determination of K_m Values</i> | 222 |
| 7.9.2.2 - <i>Determination of K_i Values</i> | 222 |
| 7.10 - Cell studies: RAW 264.7 Macrophages | 223 |
| 7.10.1 - Cell Culture | 223 |
| 7.10.2 - Western Blot Analysis of LPS-Induced RAW 264.7 Macrophages..... | 223 |
| 7.10.3 - Evaluation of the Inhibitory Effect of Compounds L11 – L20 and Re11 - Re20 in NO Biosynthesis in LPS-Induced RAW 264.7 Macrophages | 223 |
| 7.10.3.1 - Nitrite Assay | 224 |
| 7.10.4 - Cell Viability Assay..... | 224 |
| 7.10.5 - Cellular Internalization of the ^{99m}Tc (I) Complexes | 224 |
| 7.11 – Computational Studies | 225 |
| 7.11.1 – Docking Calculations..... | 225 |
| 7.11.1.1 – Validation of Docking Conditions: Docking of L-Arg, N ^ω -OH-L-Arg, 13, 16, 18, 20, 58 – 62 Inside iNOS | 225 |
| 7.11.1.2 – Docking of L2, L11 – L13, L16, Re2, Re11 – Re13 and Re16 Inside iNOS..... | 226 |
| 7.11.1.3 – Docking of 20 – 21 inside iNOS, nNOS and eNOS Isoforms..... | 226 |
| 7.11.2 - Parameterization of the Compounds..... | 227 |
| 7.11.2.1 – Parameterization of 20 and 21..... | 227 |
| 7.11.2.2 – Parameterization of L2, L11 – L13, L16, Re2, Re11 – Re13 and Re16 | 227 |
| 7.11.3 – Molecular Dynamics Simulations | 228 |
| 7.11.3.1 – Analysis of the Trajectories | 229 |
| 7.11.4 – FEP Simulations | 230 |
| 8. Annexes | 235 |
| References..... | 285 |

Abbreviations

A

Ac = Acetyl

Ac₂O = Acetic anhydride

Arg = Arginine

Asp = Aspartate

ATC = Anatomical Therapeutic Chemical classification system

Avg = Average

B

BFC = Bifunctional chelator

BFCs = Bifunctional chelators

Boc = *tert*-butoxycarbonyl

Bq = Becquerel

br = Broad

BM = Biomolecule

BBB = Blood brain barrier

C

CXCR4 = Chemokine (C-X-C motif) receptor 4

Cbz = Benzyloxycarbonyl

Ci = Curie (1 Ci = 3.7 x 10⁷ Bq)

Cys = Cysteine

COSY = Correlation Spectroscopy

CaM = Calmodulin

cGMP = 3',5' cyclic monophosphate

CT = Computed Tomography

Cpm = counts per minutes

D

d = Day

d = Doublet

dd = Doublet of doublets

DCM = Dichloromethane

DIPEA = N,N-Diisopropylethylamine

DMF = N,N-Dimethylformamide

DMSA = Dimercaptosuccinic acid

DMSO = Dimethylsulfoxide

DTPA = Diethylenetriaminepentaacetic acid

Dap = 2,3 Diamino propionic acid

Dap-OH = 2,3 diaminopropan-1-ol

DMEM = Dulbecco's Modified Eagle's Medium

E

e.g. = exempli gratia

ESI = Electrospray ionization

EtOH = Ethanol

ECD = Ethylenecysteine diester

F

FDA = Food and Drug Administration

FDG = Fluorodeoxyglucose

FEP = Free Energy Perturbation

fac = Facial

G

Glu = Glutamic acid

Gly = Glycine

H

h = Hour

His = Histidine

HPLC = High-performance liquid chromatography

HYNIC = 6-Hydrazinopyridine-3-carboxylic acid

HMPAO = Hexamethyl-propylene-amine oxime

HBTU = O-Benzotriazole-N,N,N',N'-tetramethyl uroniumhexafluoro phosphate

I

IR = Infrared

ITN = Instituto Tecnológico e Nuclear

I.D. = Injected Dose

K

KeV = Kilo electron volt

L

Lys = Lysine

LET = Linear energy transfer

$\log P_{o/w}$ = Octanol water partition coefficient

LPS = Lipopolysaccharide

M

m (IR spectroscopy) = Medium

m (NMR spectroscopy) = Multiplet

MAG₃ = Mercaptoacetyl-triglycine

MDP = methylenediphosphonate

MeV = Mili electron volt

min = Minute

MS = Mass spectrometry

MRI = Magnetic Resonance Imaging

Me = Methyl

⁹⁹Mo = Molibdenium-99

MC1R = melanocortin type 1 receptor

MEP = Molecular Electrostatics Potential

MTT = 3-(4,5-Dimethylthiazol-2-yl)-2,5-diphenyltetrazolium bromide

N

NADPH = nicotinamide adenine dinucleotide phosphate-oxidase

NMR = Nuclear Magnetic Resonance

N.D. = Not Determined

NMDAR = N-methyl-D-aspartate receptor

NPT = Number of particles (N), Temperature (T) and Pressure (P) are constant

NVT = Number of particles (N), Volume (V), and Temperature (T) are constant

P

PBS = Phosphate buffered saline

PET = Positron emission tomography

p.i. = Post injection

ppm = Part per million

Pz = Pyrazole

P = Partition coefficient

Q

q = Quartet

R

RP = Reversed phase

rpm = Rotation per minute

RNOS = Reactive nitrogen oxide species

RMSD = root-mean-square-deviation

RRMS = Relative Root Mean Square

S

s = Singlet or strong

SPECT = Single Photon Emission Computed Tomography

S.D. = Standard deviation

T

t = Triplet

$t_{1/2}$ = Half-life

TFA = Trifluoroacetic acid

THF = Tetrahydrofuran

t_R = Retention time

TMS = Tetramethylsilane

U

US - Ultrasound

UV - Ultraviolet

UV-vis – Ultraviolet/Visible

V

vs = Very strong

Vs - versus

W

w = Weak

Y

y = Year

α -MSH = α -Melanocyte-stimulating hormone

α = Alpha

β = Beta

β^+ = Positron

γ = Gamma

κ = Denticity

δ = Chemical shift

ν = Frequency

1400W = N-(3-(aminomethyl)benzyl)acetamide

Scope and Aim

In 1896 Becquerel discovered the natural radioactivity in potassium uranyl sulphate. Since then, Pierre and Marie Curie, Ernest Rutherford and Frederick Soddy all made significant contributions to the discovery of radioactive elements. Artificial radioactivity was first reported in 1934 by Irene Curie and Frederic Joliot, when irradiating boron and aluminium with particles emitted by polonium they observed emission of positrons from the target even after removal of the particles source. Nowadays, more than 2700 radionuclides can be artificially produced in cyclotrons, nuclear reactors, neutron generators and linear accelerators.¹ Among several applications, medicine is one of the most significant fields which has benefit of such achievements, namely nuclear medicine.

Nuclear medicine is a branch of medicine that uses radiopharmaceuticals, drug products that contain a radioactive element in its composition, for diagnosis or treatment of diseases. The first great landmark for nuclear medicine occurred in 1946, when a patient with thyroid cancer was treated with radioactive iodine (^{131}I) and complete remission of the spread cancer was observed. This successful event has been considered as the true beginning of Nuclear Medicine.¹⁻²

With the expanding and development of molecular biology, molecular imaging with radioactive compounds has undergone an enormous advance. Molecular imaging is the *in vivo* visualization of biological or biochemical processes associated with certain pathologies (at the cellular or molecular level). The target molecule is visualized *in vivo* due to its interaction with a labeled biological vector. The decoding of the human genome and subsequent developments in proteomics enabled the identification of new targets (e.g. membrane receptors, enzymes, genes, etc.) associated to certain pathologies, with a significant impact in areas such as oncology and neurology. Despite these recent advances, development of specific probes for targeted imaging is a great challenge and a demanding task. To achieve such goal contribution from the radiopharmaceutical sciences, a multidisciplinary research area, which profits from the input of organic, inorganic and bioinorganic chemists, radiopharmacists and clinicians, is highly desired. One of the major current challenges facing nuclear molecular imaging is the detection and quantification of *in vivo* biochemical and metabolic changes at the molecular and cellular level that precede morphological and anatomical changes in case of disease, allowing early diagnosis. To achieve this goal the design of new radioactive probes with high specificity and molecular affinity that can recognize particular targets associated with certain disease states is mandatory.³

Within this frame, the long term goal of the work described in this thesis is to contribute for the design of new specific radiopharmaceuticals based on $^{99\text{m}}\text{Tc}(\text{I})$ for *in vivo* visualization of diseases associated to nitric oxide synthase (NOS).

Recently, we have introduced a family of complexes of the type $fac-[M(CO)_3(\kappa^3-L)]^+$ ($M = Re/^{99m}Tc$; **Re1/Tc1**, $L = L1$; **Re2/Tc2**, $L = L2$; **Re3/Tc3**, $L = L3$) stabilized by conjugates containing a pyrazolyl-diamine chelating unit and a pendant substrate (**Re1/Tc1**) or inhibitor (**Re2/Tc2** and **Re3/Tc3**) of NOS separated by a propyl spacer (**C3 linker**) (**Figure 1.1**).⁴

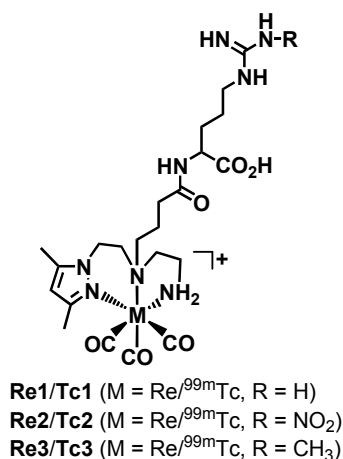


Figure 1.1: Complexes **Re1/Tc1** – **Re3/Tc3** stabilized by a pyrazolyl-diamine chelating unit coupled to L-Arg, N^ω -NO₂-L-Arg and N^ω -CH₃-L-Arg ($M = Re/^{99m}Tc$).

After *in vitro* enzymatic assays we have concluded that the substrate-containing conjugate **L1** ($K_m = 57 \mu M$) and its rhenium complex **Re1** have poor affinity towards the enzyme ($K_m = 245 \mu M$).⁴ On the contrary, the enzymatic activity of iNOS in the presence of **Re2** ($K_i = 84 \mu M$) and **Re3** ($K_i = 36 \mu M$) have shown that the complexes bearing N^ω -NO₂-L-Arg (**L2**) or N^ω -CH₃-L-Arg moieties (**L3**) still presented inhibitory action. Interestingly, **Re2** presented higher inhibitory potency than the corresponding metal free bioconjugate **L2** ($K_i = 178 \mu M$).⁴

Brought together, these encouraging results prompted us to design novel radioactive complexes based on the “ $M(CO)_3$ ” core with improved iNOS targeting properties with the aim of probing the expression of the enzyme *in vivo*. Therefore, in order to accomplish the main goal of this thesis, we considered the synthesis of novel complexes that are structurally analogs of the lead compounds **Re2/Tc2** (**Figure 1.2**). These analogs present on one hand, a longer alkyl chain (hexyl, **C6 linker**) between the N^ω -NO₂-L-Arg moiety and the chelating unit and, on the other hand, a chelating unit of different nature (**pyrazolyl-diamine**- or 2,3-Diamino propionic acid-based chelating unit, **Dap**), namely in terms of molecular weight, charge and type of the donor atom sets (**Figure 1.2 A**).

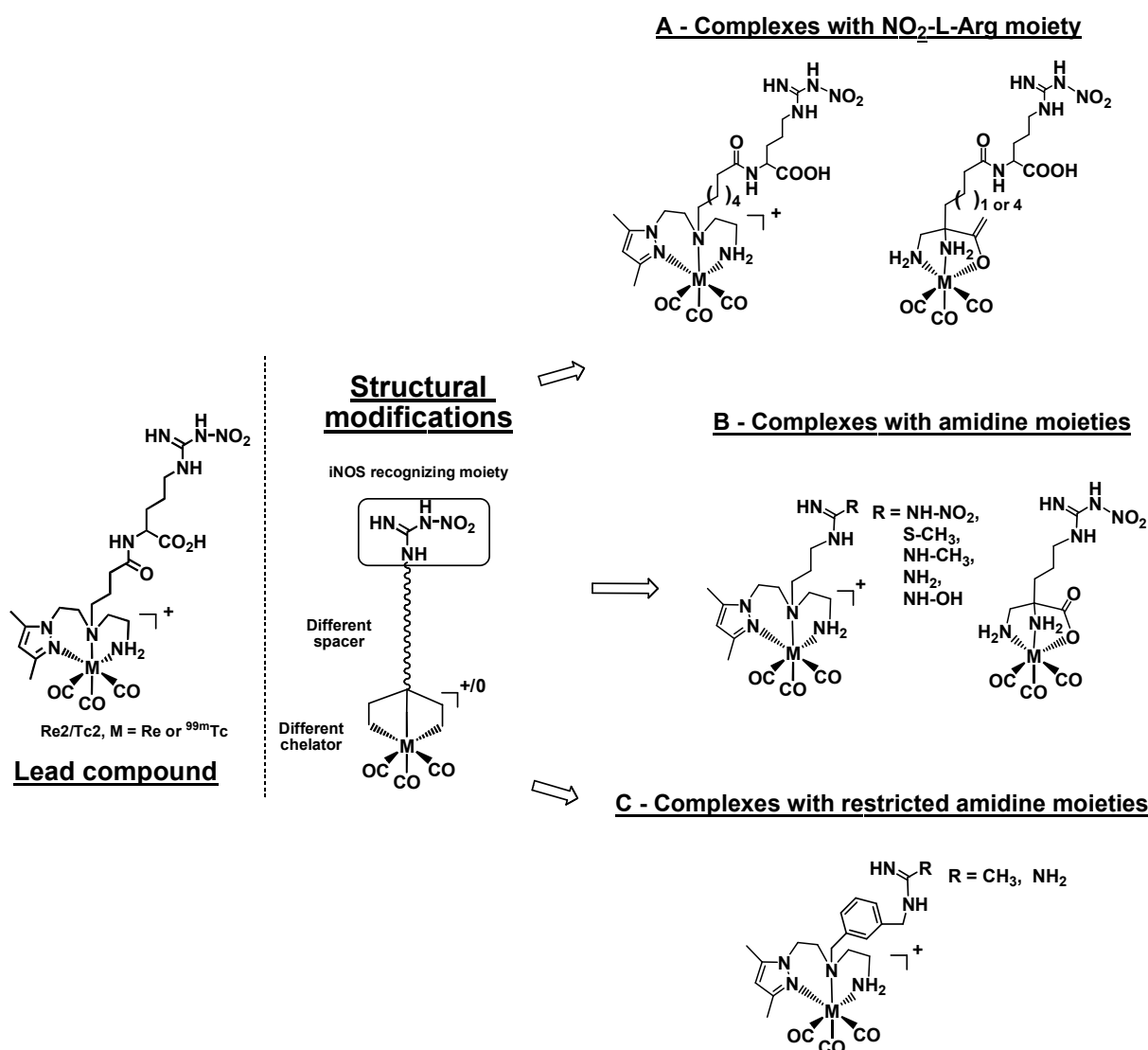


Figure 1.2: Structural modifications on the lead compounds **Re₂/Tc₂**.

We also decided to study “lighter” organometallic complexes, where the distance between the metallic fragment and the NOS-recognizing moiety is smaller than that found in the previously described complexes, and where the α -amino acid function is absent (**Figure 1.2 B**). From previous structure activity studies it is known that close analogs of L-Arg such as non α -amino acid compounds containing amidine moieties (e.g. guanidine, acetamidine, isothiurea, etc) are potent substrates or inhibitors of NOS.⁵ Indeed the α -amino acid moiety of such L-Arg derivatives can be removed without detrimental consequences, while the integrity of the guanidine function must be partially retained.^{5b} Besides the chelating unit (**pyrazolyl-diamine-** or **Dap-**based), this family of “lighter” complexes bear pendant amidine moieties (e.g. R₁C(=NR₂)NR₃) for iNOS recognition. Despite our previous results with substrate-containing complexes were less promising, we decided to include in this family of compounds pendant propyl guanidine or propyl hydroxy-guanidine moieties (**Figure 1.2 B**) since

recent studies have shown that substrates of the type N-alkyl-guanidines and N-alkyl-hydroxyguanidines exhibited interesting affinities for iNOS.^{5b,6}

We also hypothesized that complexes of the same type bearing pendant conformationally-restricted moieties, such as the highly potent and iNOS selective inhibitor N-(3-(aminomethyl)benzyl)acetamide (1400W), would be useful for probing the enzyme *in vivo*. Therefore, we also designed analogs complexes of 1400W as potential inhibitors or substrates of iNOS (**Figure 1.2 C**).

Concluding, in this thesis we describe the synthesis and characterization of model complexes of the type $fac-[M(CO)_3(\kappa^3-L)]^+$ (M = Re or ^{99m}Tc) stabilized by conjugates containing a **pyrazolyl-diamine**- or a **Dap**-based chelator and pendant moieties with affinity for iNOS, as well as their ability to recognize the enzyme *in vitro* (enzymatic assays with purified iNOS) and *in vivo*. Aiming to rationalize the results and establish a structure-activity relationship we will also present and discuss the computational studies (molecular docking, molecular dynamics and FEP calculations) performed to get an insight into the structural parameters underlying the iNOS-recognizing properties of the compounds.

The thesis is organized in 8 main chapters. The introductory chapter provides a state of the art of the concepts and background underlying the work performed in the remaining chapters. **Chapter 2** describes the synthesis and characterization of the **pyrazolyl-diamine**- and **Dap**-containing chelators, and their reactions with the adequate Re(I) and ^{99m}Tc(I) precursors. The *in vitro* stability and the *in vivo* biodistribution profiles of the ^{99m}Tc(I) complexes in an animal model will be presented too. The synthesis and characterization of the conjugates containing the **pyrazolyl-diamine** and **Dap** chelating units and the NOS recognizing moieties are presented in **Chapter 3**. The synthesis of the corresponding Re(I) and Tc(I) tricarbonyl complexes is also described in this chapter. The biological evaluation of the compounds prepared in **Chapter 3**, namely the *in vitro* (enzymatic assays with murine purified iNOS) and *in vivo* (cell and animal model) studies, will be reported in **Chapter 4**. The computational studies performed to rationalize the structural factors responsible for the different affinity of the compounds for the enzyme are described in **Chapter 5**. The main conclusions and perspectives of the work are outlined in **Chapter 6**. Finally, **Chapters 7** and **8** include the experimental details and the annexes, respectively.

1 INTRODUCTION

1. Introduction

1.1 Imaging in Clinical Set

Medical imaging is a key tool for improving the diagnosis of a large variety of diseases. Over the last century, technology has advanced from the discovery of X-rays to a variety of non-invasive imaging techniques such as the nuclear techniques Single Photon Emission Computed Tomography (SPECT) and Positron Emission Tomography (PET), Magnetic Resonance Imaging (MRI), Computed Tomography (CT) and Ultrasound (US).^{3,7} Nowadays, the **imaging techniques can be included into two large categories: structural and functional imaging**. Structural imaging is primarily aimed at anatomical localization of pathological processes, being X-rays, CT and MRI the most important techniques. **Functional imaging, rather than anatomical imaging, aims to visualize and characterize biochemical pathways, molecular interactions, drug pharmacokinetic and pharmacodynamics. SPECT and PET are currently accepted as the most important functional imaging techniques.** Examples of images obtained with all these techniques are shown in **Figure 1.3**.^{3,7}

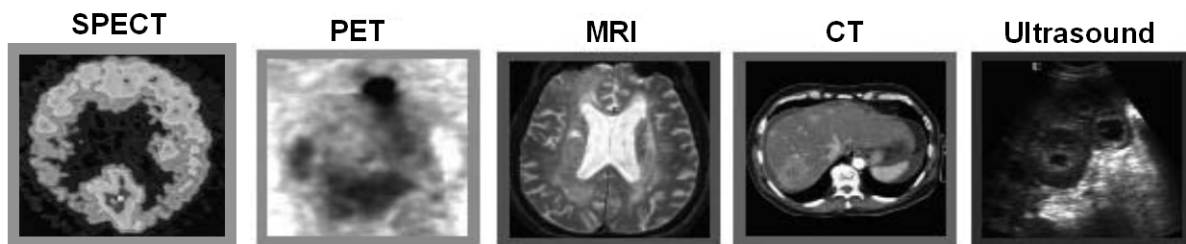


Figure 1.3: Examples of images obtained with SPECT, PET, MRI, CT and US techniques, adapted from ref 5.

Nuclear techniques present unlimited depth penetration and are the most sensitive techniques available to study *in vivo* processes at the molecular and cellular level. They **require the use of radioactive probes in very low concentrations ($\sim 10^{-6}$ - 10^{-10} M)**.⁸ **The relatively low spatial resolution, compared to other imaging techniques, was addressed by the introduction of dual modality imaging techniques, mainly nuclear/computed tomography (CT) fusion systems (PET-CT and SPECT-CT), that significantly increase the strength of nuclear techniques (high sensitivity) and CT (high spatial resolution).** **Table 1.1** summarizes the most relevant characteristics of the imaging modalities mentioned above.

Table 1.1: Most relevant characteristics of current imaging modalities used in the clinical set.⁸

| Technique | Spatial resolution | Amount of molecular probe used | Main use | Advantages | Disadvantages |
|-------------------|----------------------|--------------------------------|--------------------------|---|-----------------------------------|
| SPECT | 1–2 mm | nanograms | metabolic | highest sensitivity, quick, easy, low cost, relative high throughput | low spatial resolution |
| PET | 1–2 mm | | | high sensitivity, isotopes can substitute naturally occurring atoms, | PET cyclotron or generator needed |
| MRI | 25–100 μm | micrograms to milligrams | Morphological /metabolic | highest spatial resolution, combines morphological and functional imaging | Low sensitivity, amount of probe |
| CT | 50–200 μm | Not applicable | morphological | bone and tumor imaging, anatomical imaging | limited soft tissue resolution |
| Ultrasound | 50–500 μm | micrograms to milligrams | | real time, low cost | limited spatial resolution |

1.2 – Nuclear Medicine and Radiopharmaceuticals

Nuclear medicine is a medical specialty that uses radiopharmaceuticals to provide information about a specific organ or to treat diseases. In terms of imaging, this area takes advantage of the nuclear imaging techniques SPECT and PET to gain knowledge about the biochemical and physiological status of certain organs or tissues, being such information used to make an accurate diagnosis of the disease. For systemic radiotherapy, particle emitting radiopharmaceuticals to deliver a cytotoxic radiation dose to selected target tissues are used.⁹

Radiopharmaceuticals are drugs that contain a radionuclide in its composition, and are used routinely for the diagnostic (ATC code V09) or therapy (ATC code V10) of various diseases. These medicines, which comply with all the quality requirements applied to medicines in general, are used

in tracer quantities and have no “classical” pharmacological effect. Almost all radiopharmaceuticals are administered via intravenous injection but they can also be administered orally (e.g. Na¹³¹I capsules) or by inhalation (e.g. pulmonary ventilation).⁹ From a chemical point of view radiopharmaceuticals can be inorganic salts (e.g. Na¹³¹I), small organic molecules or inorganic or organometallic complexes, which may contain or not in its composition a biologically active molecule. The latter can be a macromolecule such as a monoclonal antibody, a small peptide, or inhibitors or substrates of enzymes, among others. Currently, the great majority of radiopharmaceuticals used in the clinical set are still based on radiometals, with ^{99m}Tc accounting for more than 90 % of all nuclear medicine procedures worldwide. These imaging agents are roughly divided in two main categories: perfusion and targeted specific agents. The pharmacokinetic profile of the perfusion radiopharmaceuticals, namely of those based on metals (**Figure 1.4 A**), is determined mainly by their chemical and physical properties (e.g. molecular weight, charge and lipophilicity). In the case of the targeted specific agents, the biodistribution is influenced not only by those properties, but also by the nature of the bioactive pendant molecule, which much interact specifically with the desired target. In general, metal-based target-specific radiopharmaceuticals comprise a radiometal stabilized by a bifunctional chelator (BFC), a spacer of different nature, and a targeting biomolecule (**Figure 1.4 B**).

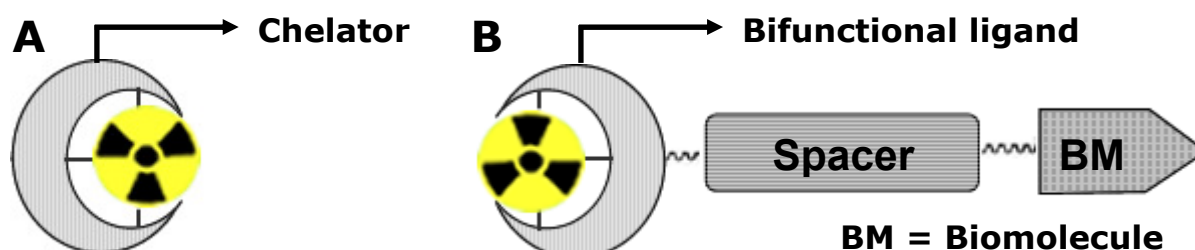


Figure 1.4: Schematic representation of a Perfusion (**A**) and targeted (**B**) Specific metal-based radiopharmaceutical.¹⁰

The radionuclide present in the radiopharmaceutical is an unstable nuclide, which undergoes a radioactive decay emitting gamma rays (γ) and/or subatomic particles (α , β^- , β^+ , Auger electrons).

1.2.1 – Diagnosis vs Therapy

A diagnostic radiopharmaceutical contains a positron- (β^+) or gamma- (γ) emitting radionuclide of sufficiently high energy (> 50 KeV), which after administration and distribution accumulates in the target organ or tissue. The external detection of the high penetrating γ photons

allows the construction of an image. The chemical and biological properties of the radiopharmaceutical determine its differential uptake and clearance between normal and diseased tissues.¹¹

As mentioned before, the two imaging techniques used in nuclear medicine are SPECT and PET. While SPECT scanners detect γ rays emitted by radiopharmaceuticals containing a γ -emitting radionuclide, PET scanners detect two high energy (511 KeV) anti parallel γ photons, which result from the annihilation of a β^+ emitted by the radiopharmaceutical with an electron (Figure 1.5 A).

As briefly discussed before, in order to overcome the low spatial resolution associated to the nuclear techniques, there has been an increase in the use of multimodal SPECT/CT or PET/CT systems, which allow the acquisition of fully registered SPECT or PET and, simultaneously, X-ray CT images. Registered functional and anatomical images are therefore acquired together.¹¹⁻¹² Figure 1.5 B displays an example of images obtained by PET/CT.

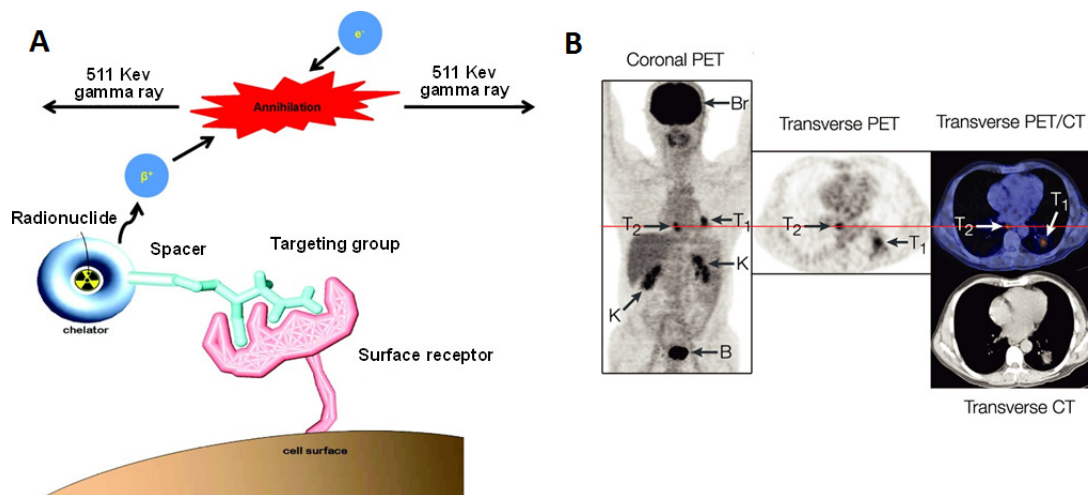


Figure 1.5: A - Fundamental principle of PET exemplified with a targeted specific radiopharmaceutical. As the targeting group interacts with a cell surface receptor, for instance, the positron-emitting radiometal decays by ejecting β^+ particles from its nucleus, which recombines with an electron in a process called annihilation. From this process two high energy (511 KeV) γ photons are produced.¹³ B – Example of images obtained from a PET/CT dual modality scanner.¹⁴

Although SPECT imaging has lower detector efficiency and less quantitative accuracy than PET, it is more practical and has broader clinical applications. Indeed, the radioisotopes used have longer half-lives, and therefore the radioisotopes can be produced away from the site of administration and transported whenever required. Owing to the longer half-life, the observation

time frame can be widened, allowing the observation of biological processes *in vivo* over several hours or days after the administration of the radioactive probe.¹⁵

The γ -emitting radionuclides with the most suited characteristics for SPECT imaging, currently used in nuclear medicine, are ^{99m}Tc ($t_{1/2} = 6.02$ h, $E_{\gamma(\text{max})} = 140$ KeV), ^{123}I ($t_{1/2} = 13.20$ h, $E_{\gamma(\text{max})} = 159$ KeV), ^{67}Ga ($t_{1/2} = 78.26$ h, $E_{\gamma(\text{max})} = 296$ KeV), ^{201}Tl ($t_{1/2} = 72$ h, $E_{\gamma(\text{max})} = 167$ KeV) and ^{111}In ($t_{1/2} = 67.9$ h, $E_{\gamma(\text{max})} = 245$ KeV). ^{99m}Tc is the most used radionuclide in SPECT imaging mainly due to its physical properties and availability (generator).^{10a}

Most of the β^+ -emitting radioisotopes used in PET imaging are short-lived non-metallic isotopes, such as ^{18}F ($t_{1/2} = 109.8$ min, $E_{\beta^+(\text{max})} = 202$ KeV), ^{11}C ($t_{1/2} = 20.4$ min, $E_{\beta^+(\text{max})} = 326$ KeV), ^{15}O ($t_{1/2} = 2.03$ min, $E_{\beta^+(\text{max})} = 650$ KeV), and ^{13}N ($t_{1/2} = 9.98$ min, $E_{\beta^+(\text{max})} = 432$ KeV). These radioactive elements can replace the natural elements in biologically active molecules, without disturbing significantly their activity and function. Because the atomic radius of fluorine is similar to that of hydrogen in most molecules, fluorine can be used as “pseudohydrogen”. Some β^+ -emitting radiometals such as ^{64}Cu ($t_{1/2} = 12.7$ h, $E_{\beta^+(\text{max})} = 660$ KeV) and ^{68}Ga ($t_{1/2} = 1.1$ h, $E_{\beta^+(\text{max})} = 1899$ KeV) are of great interest for developing new PET radiopharmaceuticals, due to their physical and chemical properties, and availability.^{2, 9, 10b, 11, 16} Most of the PET radionuclides have the disadvantage of requiring costly technology, and automated and sophisticated methods of synthesis, since they are produced in cyclotrons and have short half-lives. [^{18}F] 2-fluoro-2-deoxy-D-glucose ([^{18}F]-FDG) is the most widely used positron-emitting radiopharmaceutical for PET imaging, making ^{18}F the most used radionuclide in this nuclear imaging technique. ^{18}F -FDG has shown clinical usefulness in cardiology and neurology but is used mainly in oncology, in the diagnosis, staging and post-therapy evaluation of oncologic patients.¹⁷

Radiopharmaceuticals for therapy have in their composition a radionuclide that emits ionizing radiation with a high linear energy transfer (LET) to destroy selectively cells or tissues. The most used radionuclides are β^- -emitters, but intense research involving α - or Auger electron-emitting radionuclides is also underway. The selection of a radionuclide for therapy depends not only on the type, energy, half-life and range of emitted particles, but also on the size of the tumor or tissue to irradiate. Since the penetration depth range of β^- particles in biological tissues is relatively long (1 nm - 10 mm), radiopharmaceuticals containing β^- -emitting radionuclides can be used for the treatment large solid tumors. Among β^- -emitting radionuclides with potential application, ^{131}I ($t_{1/2} = 8.0$ d, $E_{\beta^-(\text{max})} = 0.81$ MeV, $E_{\gamma(\text{max})} = 0.364$ MeV), ^{153}Sm ($t_{1/2} = 1.9$ d, $E_{\beta^-(\text{max})} = 0.8$ MeV, $E_{\gamma(\text{max})} = 0.103$ MeV), ^{90}Y ($t_{1/2} = 2.7$ d, $E_{\beta^-(\text{max})} = 2.27$ MeV), ^{186}Re ($t_{1/2} = 3.8$ d, $E_{\beta^-(\text{max})} = 1.07$ MeV, $E_{\gamma(\text{max})} = 0.137$ MeV), and, more recently, ^{188}Re ($t_{1/2} = 0.7$ d, $E_{\beta^-(\text{max})} = 2.10$ MeV, $E_{\gamma(\text{max})} = 0.155$ MeV), are used in the clinical set for the treatment of different tumor types. Moreover, ^{177}Lu ($t_{1/2} = 6.7$ d, $E_{\beta^-(\text{max})} = 0.497$ MeV, $E_{\gamma(\text{max})} = 0.208$

MeV) and ^{166}Ho ($t_{1/2} = 1.1$ d, $E_{\beta^-(\text{max})} = 1.86$ MeV, $E_{\gamma(\text{max})} = 0.081$ MeV) have been fully explored both at the preclinical and clinical levels as bone palliative agents.¹⁸



The α particles are heavy and charged helium nuclei with high LET. These particles “travel” only short distances and cause the most ionizing damage over a small distance (40 μm - 100 μm). Owing to these features, α -emitting radionuclides are appropriate for the treatment of small tumors and/or metastasis. In general, most of these radioisotopes have half-lives that are too long to be compatible with *in vivo* applications. As a result, only a few α -emitters have received serious attention for radiotherapeutic applications, that is the case of ^{211}At ($t_{1/2} = 7.2$ h, $E_{\alpha(\text{Avg})} = 6.8$ MeV), ^{212}Bi ($t_{1/2} = 1$ h, $E_{\alpha(\text{Avg})} = 7.8$ MeV) and ^{223}Ra ($t_{1/2} = 11.4$ d, $E_{\alpha(\text{Avg})} = 5.65$ MeV).¹⁸⁻¹⁹ It is worth mentioning that $^{223}\text{RaCl}_2$ (Alpharadin®) was explored in the treatment of skeletal metastases, and, due to the promising preliminary results obtained, this compound is currently under clinical evaluation for the treatment of bone metastases resulting from prostate cancer.²⁰

The Auger electrons are less energetic particles with a very short range of penetration (< 1 μm), having a LET similar to that of α particles, which makes them potentially interesting for therapy. Unlike α and β^- particles, treatment based on Auger electron-emitters requires the targeting of individual cells, specifically the DNA in the nucleus. Among the available Auger electrons-emitting radionuclides, ^{125}I ($t_{1/2} = 60.5$ d, 25 electrons/decay), ^{111}In ($t_{1/2} = 2.8$ days 15 e^- /decay) and $^{99\text{m}}\text{Tc}$ ($t_{1/2} = 6.02$ h, 4 e^- /decay) are the most interesting for potential clinical applications.²¹

1.3 - Technetium and Rhenium Coordination Chemistry Relevant for Nuclear Medicine

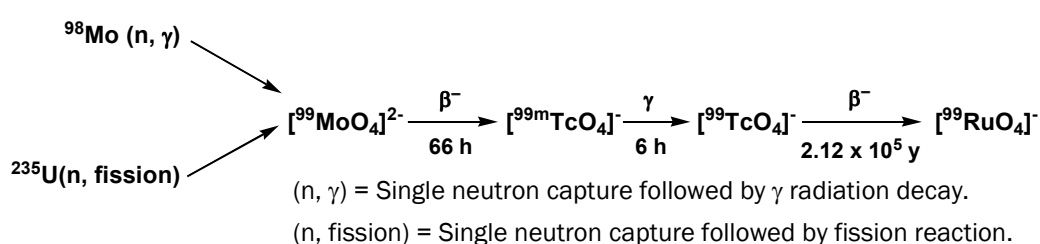
Technetium (Tc) and **rhenium** (Re) are transition metals of group 7 belonging respectively to the 2nd and 3rd transition series, with atomic numbers 43 and 75 and electronic configurations $[\text{Kr}]4d^55s^2$ and $[\text{Xe}]4f^{14}5d^56s^2$, respectively. Technetium complexes can have the metal in the oxidation states -I (d^8) to +VII (d^0), while for rhenium complexes the metal presents oxidation states -III (d^{10}) to +VII (d^0). Tc and Re present very similar atomic radii (Tc, 1.36 Å; Re, 1.37 Å), forming structurally analog complexes. Despite these similarities, there are differences between the two metals that must be taken into consideration in the preparation of analog Tc and Re complexes. The most striking differences relate with the higher kinetic inertness and easier oxidation associated to Re complexes.^{10b, 22}

1.3.1 – The Radiochemistry of Technetium

In the last three decades the inter relationship between chemistry and nuclear medicine has played a key role in the knowledge of technetium, first predicted by Mendeleev and isolated by Sergé and Perrier in 1938. Twenty one technetium isotopes with masses ranging from ^{90}Tc to ^{110}Tc were reported.^{2, 15} The most useful isotope of technetium in nuclear medicine is $^{99\text{m}}\text{Tc}$, as it displays almost ideal characteristics:

- has a half-life ($t_{1/2}$) of 6.02 hours, which is long enough to examine metabolic processes and yet short enough to minimize the radiation dose to the patient;
- decays by emitting γ photons (140 KeV), which have an energy sufficiently high to easily penetrate the human body and to be detected externally by a gamma camera, and sufficiently low to minimize the dose to the patient.
- available at reduced prices from a commercial $^{99}\text{Mo}/^{99\text{m}}\text{Tc}$ generator, being one of the greatest advantages of this radionuclide;
- diverse coordination chemistry, which enables the preparation of a wide variety of complexes with different physico-chemical and biological properties;

$^{99\text{m}}\text{Tc}$ can be obtained indirectly either by the neutron irradiation of ^{98}Mo or as a fission product of ^{235}U in a nuclear reactor. **Scheme 1.1** illustrates the decay scheme of ^{99}Mo in the form of $[\text{}^{99}\text{MoO}_4]^{2-}$ to $[\text{}^{99\text{m}}\text{TcO}_4]^-$.^{2, 10a}



Scheme 1.1: Production route of $^{99\text{m}}\text{Tc}$ and further decay thereof.²

As already mentioned, one of the main reasons for the widespread use of $^{99\text{m}}\text{Tc}$ worldwide relates with the availability of the $^{99}\text{Mo}/^{99\text{m}}\text{Tc}$ generator, which contains ^{99}Mo ($[\text{}^{99}\text{MoO}_4]^{2-}$ adsorbed onto an alumina column) that decays to $^{99\text{m}}\text{Tc}$ (**Scheme 1.1.** and **Figure 1.6**). The latter isotope is eluted from the generator in the form of sodium pertechnetate ($[\text{Na}^{99\text{m}}\text{TcO}_4]$) using saline (NaCl 0.9%).

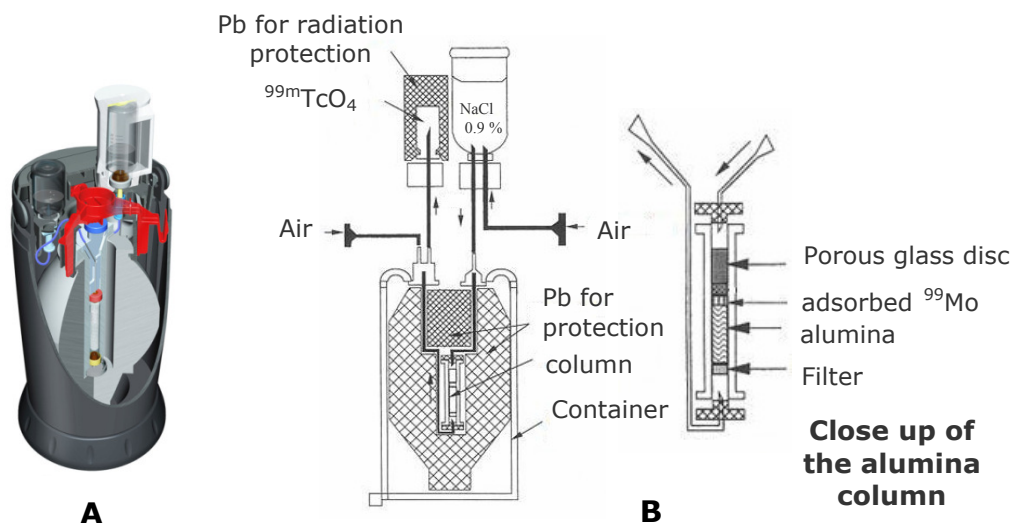


Figure 1.6: **A** – Schematic depiction of a $^{99}\text{Mo}/^{99\text{m}}\text{Tc}$ generator. **B** - A conceptual view of the generator. ^{99}Mo , in the form of $[\text{MoO}_4]^{2-}$ ion adsorbed on alumina, decays to $[\text{}^{99\text{m}}\text{TcO}_4]^-$. Because of its single charge, $[\text{}^{99\text{m}}\text{TcO}_4]^-$ is less tightly bound to the alumina and can be eluted from the generator with a saline solution.²³

The diluted nature of $[\text{}^{99\text{m}}\text{TcO}_4]^-$ solutions (10^{-8} - 10^{-10} M) makes the characterization of the $^{99\text{m}}\text{Tc}$ complexes by the spectroscopic and analytical methods used in chemistry impossible. Therefore, such complexes can be characterized by the synthesis of the analog complexes with the long-lived isotope ^{99}Tc ($t_{1/2} = 2.12 \times 10^5$ years, β^- emitter, $E_{\text{max}} = 0.3$ MeV), which is available in milligram amounts and can be characterized by the usual analytical techniques. Alternatively, structural characterization of the $^{99\text{m}}\text{Tc}$ complexes can be done by comparing their chromatographic behavior with that of the corresponding compounds prepared at macroscopic scale with natural rhenium (“cold metal”). Indeed, rhenium and technetium, share a similar coordination chemistry, and, consequently, rhenium complexes are often used as nonradioactive (“cold”) surrogates of $^{99\text{m}}\text{Tc}$ complexes.^{22b}

Besides its importance as surrogate of technetium, rhenium has two important radioisotopes with great importance in nuclear medicine, namely ^{186}Re and ^{188}Re . In a similar way to $^{99\text{m}}\text{Tc}$, the β^- emitter ^{188}Re is obtained from a $^{188}\text{W}/^{188}\text{Re}$ generator applying the beta decay of ^{188}W ($t_{1/2} = 69$ d). The availability of this generator makes ^{188}Re one of the most promising candidates for the development of novel radiopharmaceuticals for use in systemic radiotherapy.²⁴ ^{186}Re , produced in nuclear reactors, presents simultaneously β^- and γ emission, which allows imaging during radiotherapy.

1.3.2 – ^{99m}Tc Radiopharmaceuticals

The ^{99m}Tc -based radiopharmaceuticals are roughly divided into two general categories as mentioned before. The first include the perfusion agents, which are well established in routine nuclear medicine. These complexes follow a non-specific biological pathway after *in vivo* administration, accumulating in distinct tissues or organs according to size, charge and lipophilicity. Examples of such commercially available compounds are presented in **Figure 1.7**.^{10, 25}

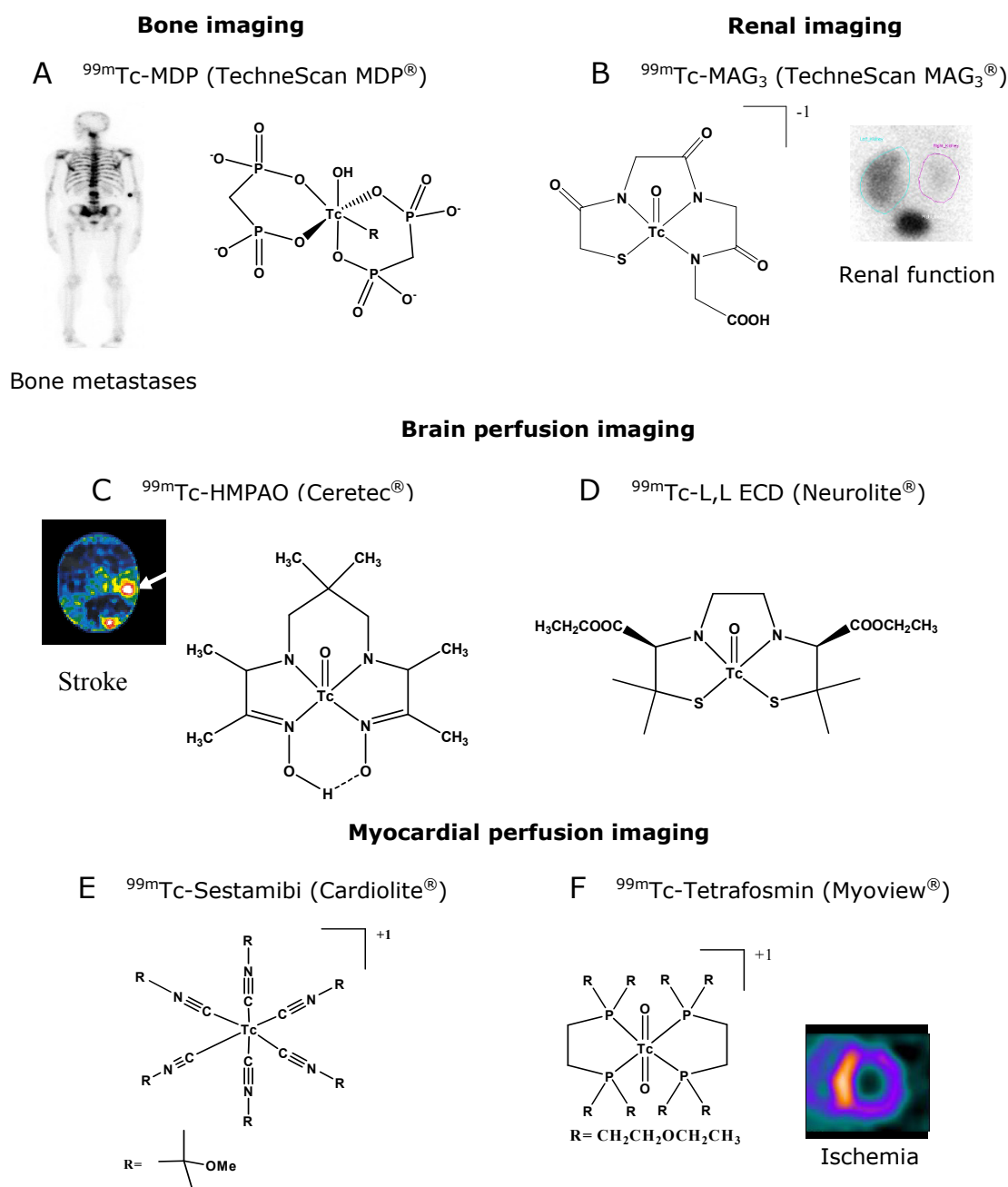


Figure 1.7: Perfusion ^{99m}Tc -based radiopharmaceuticals for diagnosis in clinical use.^{10b} (MDP = methylenediphosphonate, MAG₃ = mercaptoacetyl-triglycine, HMPAO = hexamethylpropyleneamine oxime, ECD = Ethyl cysteinate dimer).

Complexes of ^{99m}Tc with bisphosphonate (BP) ligands (e.g. $^{99m}\text{Tc-MDP}$, $^{99m}\text{Tc-HMDP}$) are widely used as diagnostic agents for the imaging of metastatic disease in bone (**Figure 1.7 A**). The mechanism of uptake in the bone is believed to be via coordination of the free phosphoryl oxygens to the calcium of the hydroxyapatite bone surface.²⁶ Despite their well-established use as diagnostic agents the exact composition and structure of the $^{99m}\text{Tc-BP}$'s is still unknown. In the case of Tc-MDP, a polymeric structure at macroscopic level was found by X-ray diffraction analysis, but the oxidation state of the metal could not be unambiguously assigned.²⁷

Complexes such as $^{99m}\text{Tc-DMSA}$ (DMSA = dimercaptosuccinic acid) and $^{99m}\text{Tc-DTPA}$ (DTPA = diethylenetriaminepentaacetic acid) have been used for functional kidney imaging. However, the most widely used is the anionic complex [$^{99m}\text{TcO}(\text{MAG}_3)$] (MAG_3 = Mercaptoacetyl-triglycine), which contains a free carboxylic group necessary for efficient excretion by the kidneys (**Figure 1.7 B**).²⁸

Radiopharmaceuticals for brain imaging must be able to penetrate the intact blood brain barrier (BBB). Using small, neutral, and lipophilic ^{99m}Tc complexes, such as $^{99m}\text{Tc-HMPAO}$ (**Figure 1.7 C**, HMPAO = hexamethylpropyleneamine oxime), such penetration has been possible by passive diffusion. This compound crosses the BBB and is retained in brain due to its enzymatic conversion into a more hydrophilic compound.²⁹ Another compound, which fulfills the basic requirements of an effective brain imaging agent is an oxotechnetium (V) complex stabilized with the Ethyl cysteinatate dimer (^{99m}Tc L,L-ECD, **Figure 1.7 D**). Brain retention is achieved by *in vivo* hydrolysis of the ester side chains, which results in the formation of charged complexes that are trapped in the brain.^{22b}

One of the most widely used SPECT imaging agents in routine nuclear medicine, the organometallic complex $^{99m}\text{Tc-Sestamibi}$ (**Figure 1.7 E**), originally developed as a myocardial perfusion agent, is nowadays successfully applied in tumor imaging and detection of multidrug resistance.³⁰ The myocardial uptake of the cationic complex $^{99m}\text{Tc-Sestamibi}$ does not occur via the Na^+/K^+ channels, but rather by a metabolic process, which involves its diffusion across the membranes. Retention of the agent in the myocytes is provided by partial enzymatic cleavage of the ether functionalities.^{22b} The cationic complex $^{99m}\text{Tc-Tetrafosmin}$ (**Figure 1.7 F**) also has favorable properties for heart imaging. This metal complex enters rapidly the myocardial cells due to its lipophilic properties, being the proposed uptake mechanism similar to that of $^{99m}\text{Tc-Sestamibi}$.^{22b, 25}

The most recent ^{99m}Tc -based radiopharmaceuticals approved by the regulatory authorities for SPECT imaging are target specific radiopeptides. A schematic representation of such type of compounds has been shown in **Figure 1.4 B**. The targeting ability of these complexes is dependent on

the pendant biologically active molecule. The capacity of the biomolecule to recognize its molecular target (receptor, antigen, enzyme, DNA, mRNA, etc.) together with the overall physico-chemical features of the resulting complex will determine the specific accumulation of the radiopharmaceutical in the target tissue.^{10b} Figure 1.8 depicts two ^{99m}Tc target specific radiopharmaceuticals based on peptides commercially available.

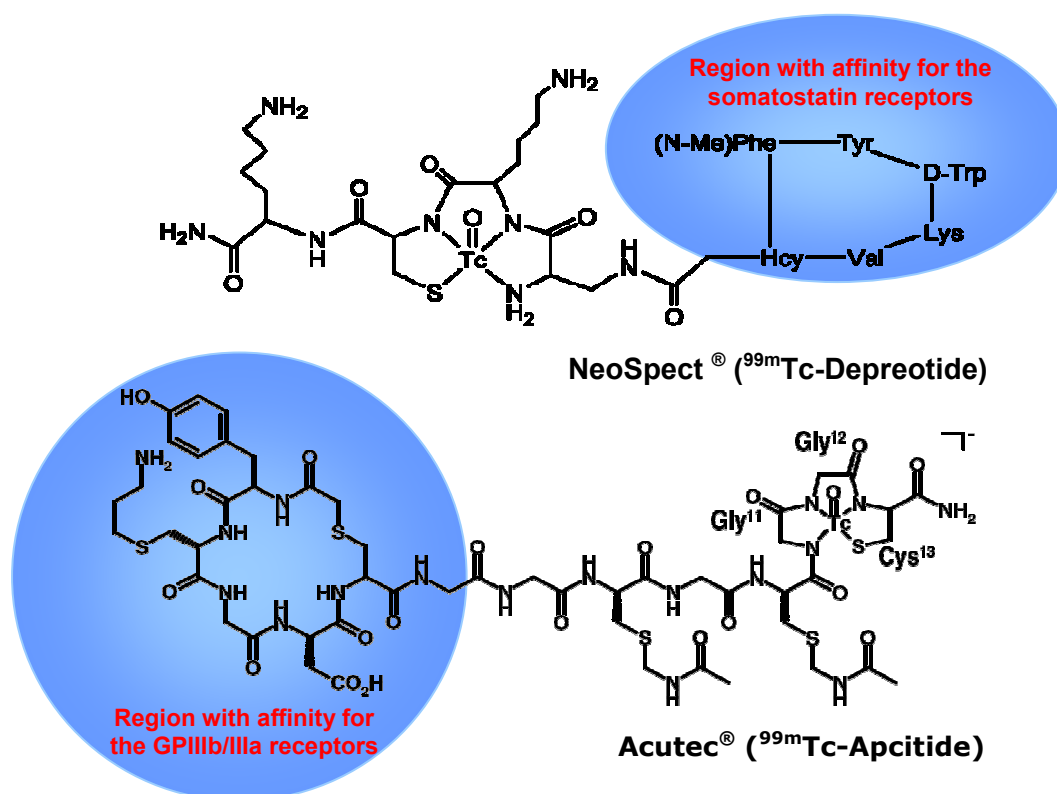


Figure 1.8: ^{99m}Tc-based target specific radiopharmaceuticals.

The complex ^{99m}Tc-depreotide (NeoSpect[®]) contains a synthetic somatostatin analog, which has higher affinity for somatostatin receptor subtypes 2 (SSTR2), 3 (SSTR3), and 5 (SSTR5). NeoSpect[®] was the first targeted radiopharmaceutical that entered clinical use as imaging agent for lung tumors.³¹ ^{99m}Tc-Apcitide (Acutec[®]) is a target specific radiopharmaceutical with affinity for the GPIIb/IIIa receptors overexpressed on the surface of activated platelets, and is indicated for scintigraphic imaging of acute venous thrombosis.³²

The ^{99m}Tc-TRODAT complex is another example of a target specific complex, which is in a Phase I clinical study (Figure 1.9). This tracer has high affinity for the Dopamine transporters allowing the diagnosis of Parkinson's disease.³³

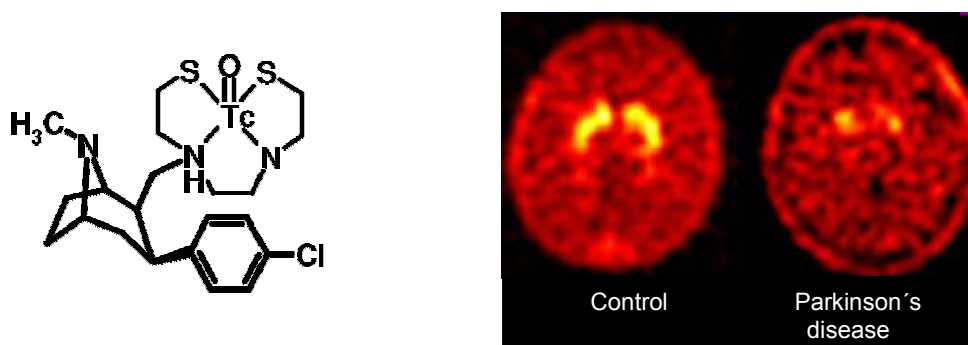


Figure 1.9: Structural formula of ^{99m}Tc -TRODAT-1 for SPECT imaging of dopamine transporters.

Besides the targeting moiety, also the coordination environment around the metal center has a decisive influence in the overall biological properties of the radiopharmaceutical. Therefore, modulation of the coordination environment of the metal with different chelators opens great opportunities towards the design of innovative target specific radiopharmaceuticals with improved biological properties. Indeed, the design and selection of the most appropriate BFC is a key issue for the development of clinically relevant imaging agents.

Figure 1.10 shows selected Tc cores, which have been used for the labeling of different type of biomolecules (BM) with ^{99m}Tc . In these compounds, nitrogen, oxygen, sulfur, and phosphorus containing chelating systems of various denticities were used as coordinating ligands. The spacer/linker between the metal and the biomolecule can also be of different nature, allowing also the modulation of the pharmacokinetics and biological profile of the complex.^{22b}

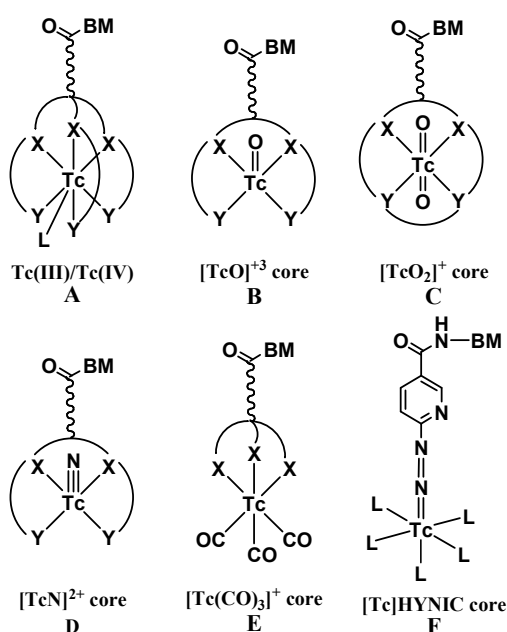


Figure 1.10: Technetium cores useful for labeling biomolecules.^{10b}

The oxidation state (+V), and more recently (+I), have been the most studied towards biomedical applications (**Figure 1.10**). The chemistry of Tc(V) is mainly dominated by the formation of oxo-complexes with the $[\text{Tc}=\text{O}]^{3+}$ or $\text{trans}-[\text{O}=\text{Tc}=\text{O}]^+$ moieties (**Figure 1.10 B and C**). Since the coordination chemistry of the $[\text{Tc}=\text{O}]^{3+}$ fragment has been optimized in the last three decades, further advances are more likely achieved in the development of bifunctional chelating systems for the lower oxidation states Tc(I) - Tc(III), still less explored. In particular, the *fac*- $[\text{Tc}(\text{CO})_3]^+$ core is being adopted more widely as a preferred moiety for labeling biomolecules. Investigation of various bifunctional chelators for linking this fragment to biomolecules is now underway.

1.3.3 – The *fac*- $[\text{M}(\text{CO})_3]^+$ Core (M = Tc, Re)

Owing to a set of recognized superior features, the *fac*- $[\text{M}(\text{CO})_3]^+$ core (M = Tc, Re) has been in recent years one of the most explored metallic fragments for the labeling of biomolecules. One favorable characteristic relates to the hypothesis that the smaller the technetium complex the higher the likelihood that the biological activity of the targeting agent will not be altered. Compared to Tc and Re complexes in the +V oxidation state, the tricarbonyl core exhibits a significantly reduced size (**Figure 1.11**).³⁴

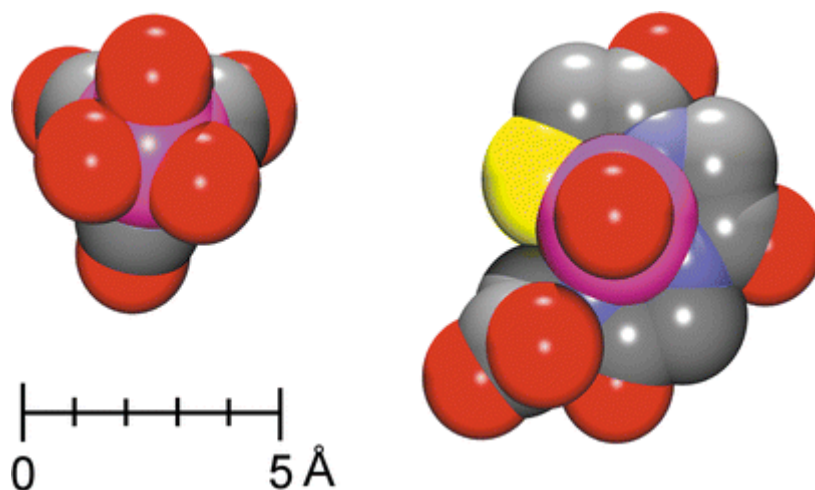
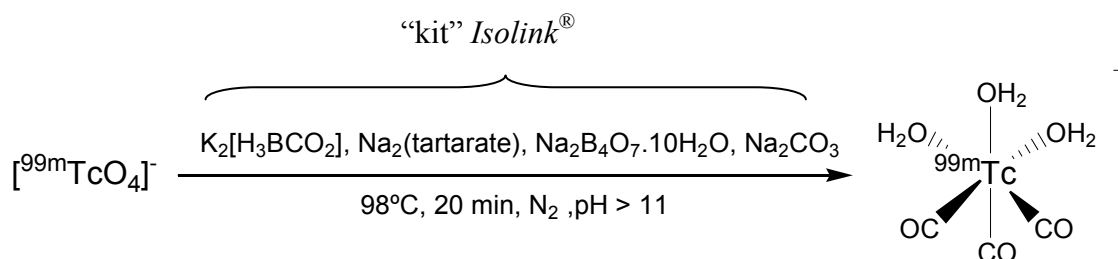


Figure 1.11: Qualitative size comparison of the organometallic precursor *fac*- $[\text{Tc}(\text{CO})_3(\text{H}_2\text{O})_3]^+$ (left) and Tc-MAG₃ (right) based on X-ray analyses. Purple = technetium, red = oxygen, grey = carbon, blue = nitrogen, yellow = sulphur. Hydrogen atoms are omitted.³⁴

A second favorable feature of this type of organometallic complexes is associated with the octahedral coordination sphere, which can be closed with an appropriate ligand system, becoming the metal center quite compact. Therefore, the metal center is protected against further ligand

attack or re-oxidation. On the contrary, the open square pyramidal structures of Tc(V) oxocomplexes anchored by tetradentate chelators can be characterized as unprotected metal centers, which are prone to further ligand attacks and protonation.³⁴ Finally, the metal center of the *fac*-[M(CO)₃]⁺ core contains a low spin d⁶ electronic configuration in an octahedral field. In general, such complexes are known to be kinetically inert.

The octahedral metal center in *fac*-[Tc(CO)₃]⁺ is facially arranged with three carbonyls and three vacant coordination sites. The +I oxidation state on the metal allows for coordination of a broad variety of donor and acceptor atoms. Alberto and coworkers were the first to report the one step synthesis of the precursor *fac*-[^{99m}Tc(CO)₃(H₂O)₃]⁺, by direct reduction of Na[^{99m}TcO₄] with sodium borohydride in aqueous solution in the presence of carbon monoxide. After this initial achievement, an even more attractive method was further developed, which involved the use of boranocarbonate (K₂[H₃BCO₂]) to produce CO *in situ* and, simultaneously, to reduce Tc(VII) to Tc(I).³⁵ Currently, the synthesis of *fac*-[^{99m}Tc(CO)₃(H₂O)₃]⁺ is done using a kit formulation (IsoLink[®], Covidien, former Mallinckrdot BV). As shown in **Scheme 1.2**, upon addition of [^{99m}TcO₄]⁻ to the IsoLink[®] kit, the complex *fac*-[^{99m}Tc(CO)₃(H₂O)₃]⁺ can be obtained in quantitative yield.



Scheme 1.2: IsoLink[®] kit and synthesis of *fac*-[^{99m}Tc(CO)₃(OH₂)₃]⁺.

The easy availability of this Tc(I) precursor represents a significant progress in radiopharmaceutical chemistry, being the major advantages summarized as follows:^{22a}

- applicability to a wide range of biologically relevant molecules;
- high thermodynamic and kinetic stability of the resultant ^{99m}Tc complexes;
- high specific activity, which can be achieved often without a purification step;
- relatively low molecular weight of the metal moiety.

All three water molecules in the precursor *fac*-[^{99m}Tc(CO)₃(H₂O)₃]⁺ are very labile with respect to substitution, and can interact with potential ligating sites in proteins in human serum (e.g.

histidine and cysteine residues). Therefore, the precursor itself is not suitable for diagnostic purposes displaying a very unfavorable biological profile as demonstrated by biodistribution studies in mice.³⁶ To develop useful radiopharmaceuticals, it is necessary to replace the water molecules by mono, bi, or tridentate chelating ligands to form stable complexes. A wide variety of organometallic complexes has already been described in literature, with those stabilized by tridentate chelating systems presenting the highest stability both *in vivo* and *in vitro*.³⁷ Histidine, pyridine, pyrazole, thioimidazole and cysteine derivatives, together with pure aliphatic or mixed aromatic aliphatic triamines, among others, are quite efficient tridentate bifunctional chelating ligands, useful for the labeling of relevant biomolecules. Selected complexes, stabilized by bifunctional chelators, bearing or not pendant targeting moieties (BM) are depicted in **Figure 1.12**.

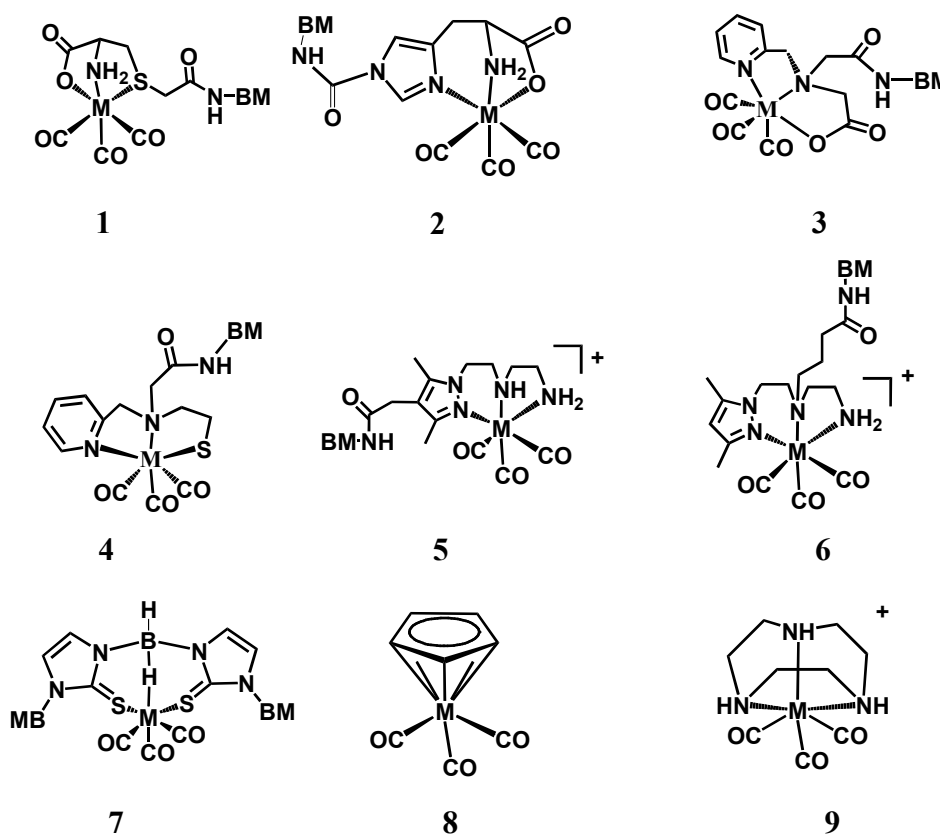
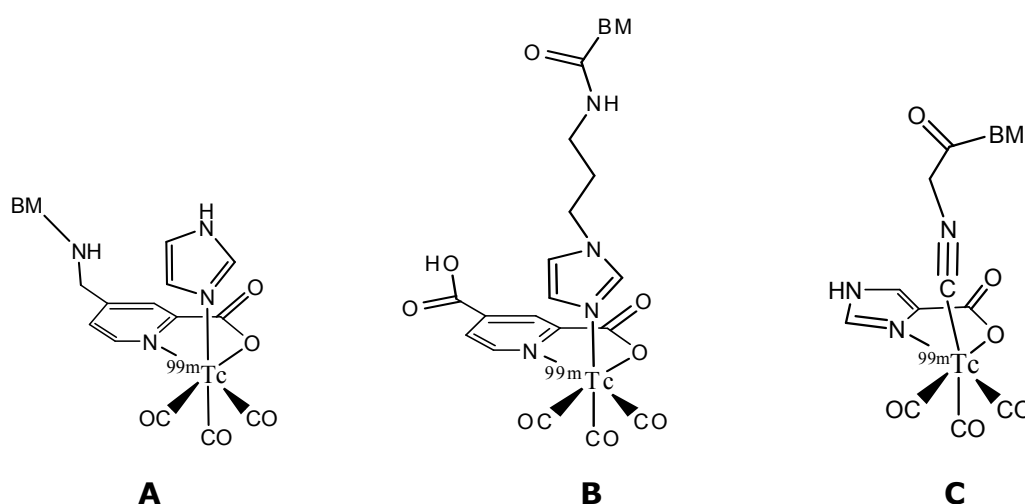


Figure 1.12: Examples of $M(\text{CO})_3$ -complexes stabilized by various types of chelating agents (BM = biomolecule; $M = \text{Re}/^{99\text{m}}\text{Tc}$). **1** - Functionalized cysteine;³⁸ **2** Functionalized histidine;^{37d, 39} **3** and **4** - Functionalized picolinic acid derivatives;⁴⁰ **5** and **6** Functionalized pyrazolyl-diamine containing ligands;⁴¹ **7** - Functionalized Bis(mercaptoimidazolyl)borates;⁴² **8** - Cyclopentadienyl;⁴³ **9** Triazacyclononane;⁴⁴.

In the past few years, the radiopharmaceutical sciences group of ITN has introduced a large family of tridentate bifunctional ligands that share a common pyrazolyl chelating unit. Those

chelators have a great ability to stabilize the organometallic unit $fac-[M(CO)_3]^+$ ($M = {}^{99m}\text{Tc}$, Re) (**Figure 1.12, 5 and 6**).⁴⁵ In this way it has been possible to label a wide range of biomolecules such as peptides, small molecules, and antibodies, just to mention a few examples, in high yield and high specific activity.^{41e}

The combination of both mono and bidentate ligands in the same molecule gave rise to a new mixed ligand concept, which aimed at overcoming some of the drawbacks associated sometimes to the functionalization of tridentate chelators. There are two ways for applying such concept, which are depicted in **Scheme 1.3**. The first way assumes that the bidentate chelator is attached to the targeting molecule ($[2_{\text{BM}} + 1]$, **Scheme 1.3 A**). Different characteristic complexes are prepared by attaching various monodentate chelators. The second way assumes that a monodentate chelator is attached to the biomolecule, and the variable portion is then represented by the bidentate chelator ($[2 + 1_{\text{BM}}]$, **Scheme 1.3 B**). As reported in several previous studies, isocyanides are very efficient for forming complexes of the second type (**Scheme 1.3 C**).^{37a, 46}



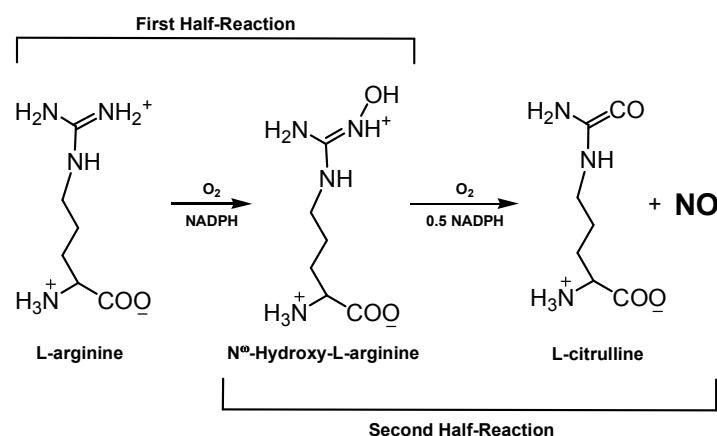
Scheme 1.3: The mixed ligand concept based on the $fac-[{}^{99m}\text{Tc}(\text{CO})_3]^+$ moiety.^{37a}

1.4 – Nitric Oxide Synthase

1.4.1 – Structure and Function

Nitric oxide (NO) is a simple gaseous molecule that had not drawn attention to most physiologists and pharmacologists until 1980's. In 1980 it was reported that a substance released from endothelial cells caused relaxation of smooth muscle tissue resulting in a blood pressure-lowering effect. Such substance was referred to as endothelium derived relaxing factor (EDRF), being its chemical identity unknown at the time.⁴⁷ After several thorough studies focused on the identification of EDRF, it was found that NO, an unstable and transient species, exhibited similar biochemical and pharmacological properties.⁴⁸ The discovery of NO as a key signaling molecule in blood pressure regulation prompted numerous studies that have elucidated a role for NO in a diverse array of physiological events. Nowadays, NO is known to be involved in different relevant physiological processes such as neuronal transmission, cytoprotection, and platelet aggregation.⁴⁷

NO is biosynthesized by a family of enzymes called Nitric Oxide Synthase (NOS, EC 1.14.13.39). NOS catalyzes the two step oxidation of L arginine (L-Arg) to L citrulline (L-Cit) and NO via N^o-hydroxy-L-Arginine (N^o-OH-L-Arg) (**Scheme 1.4**) in an NADPH (nicotinamide adenine dinucleotide) and O₂ dependent manner.⁴⁷



Scheme 1.4: Two step catalytic oxidation of L-Arg to L-Cit and NO by NOS in the presence of molecular oxygen and NADPH.

Three mammal isozymes of NOS have been identified so far, each associated with a distinct physiological function: neuronal NOS or nNOS (neuronal signal transmission), endothelial NOS or eNOS (smooth muscle relaxation), and inducible NOS or iNOS (immune response). The nNOS and eNOS are expressed constitutively, and intermittently produce small amounts of NO. On the

contrary, iNOS is inducible by cytokines and produces large amounts of NO for both a cytoprotective or cytotoxic effect.⁴⁷⁻⁴⁸

The three NOS isoforms share a similar structural architecture (**Figure 1.13, A**). The smallest among the three isoforms is iNOS (130 kDa, from mouse), while the largest isoform is nNOS (150 kDa, from rat). The higher molecular weight of nNOS is attributed to an additional 250 amino acids sequence at the N-terminal, which contains a postsynaptic density zipper (PDZ) motif that is responsible for the subcellular targeting of nNOS.^{48a} The eNOS (monomeric molecular weight of 135 kDa, from bovine) is acylated at the N-terminal. Post translational acylation such as myristoylation and palmitoylation are required for stabilizing the association of eNOS to cell membrane and to target the enzyme to caveolae.⁴⁹

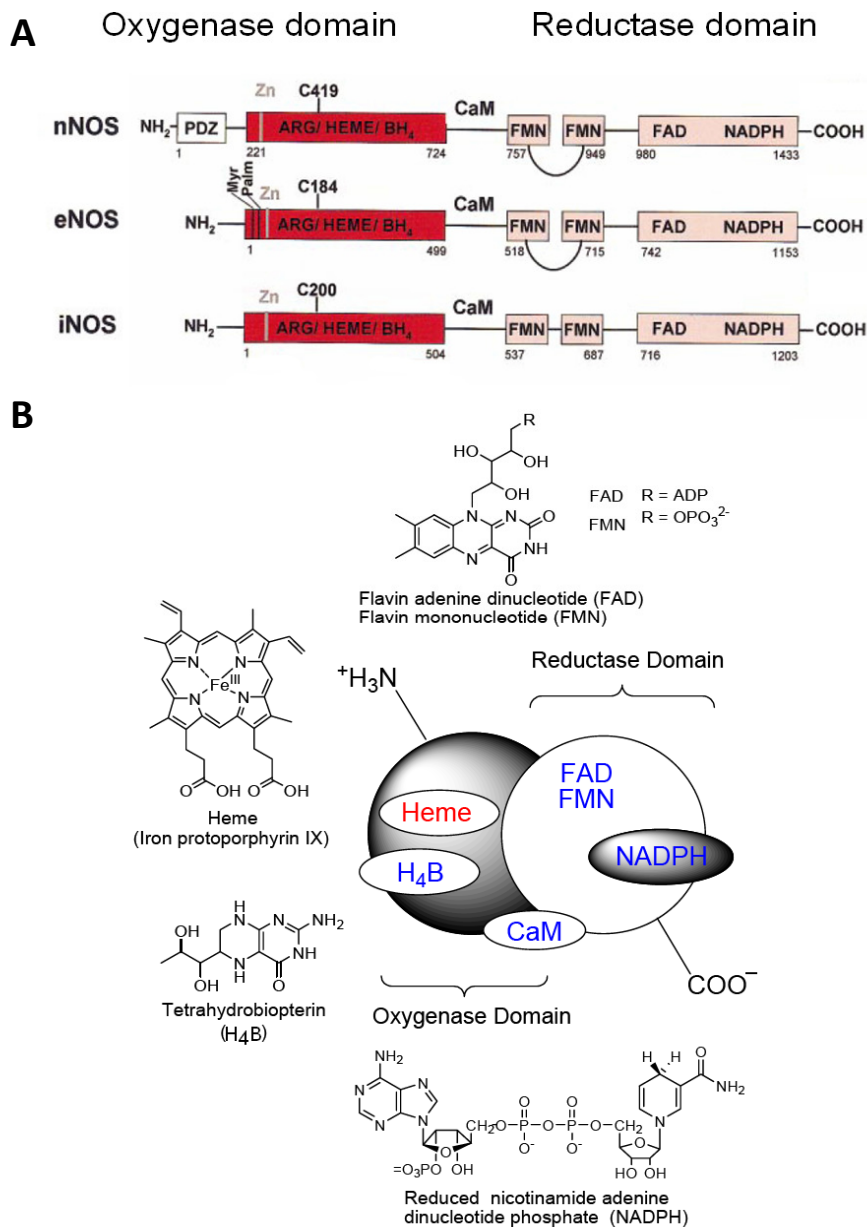


Figure 1.13: Domain structure of human nNOS, eNOS and iNOS (**A**), and respective cofactors (**B**).^{48a}

The activity of NOS isoforms is dependent on a number of cofactors: NADPH (nicotinamide adenine dinucleotide), FAD (flavin adenine dinucleotide), FMN (flavin mononucleotide), 5,6,7,8 tetrahydrobiopterin (H_4B), and iron protoporphyrin IX (Heme) (**Figure 1.13, B**).

The C-terminal of all isoforms is a reductase domain, homologous to cytochrome P450 reductase. NADPH, FAD, and FMN bound to this domain. The N-terminal is the oxygenase domain, which contains binding sites for the essential cofactors: H_4B , Heme, and the substrate (L-Arg).⁵⁰ The two domains are linked by a calmodulin binding motif (calmodulin = CaM) and form one monomer. The monomers dimerize to form a homodimer enzyme with the aid of a single intersubunit ZnS_4 cluster, which stabilizes dimerization.⁵¹ H_4B is located near the dimer interface and is also described to assist in dimerization and stabilization. H_4B is thought to have an effect on electron flow in the first oxidation of L-Arg and in modulation of the spin state of the heme iron. This unit is positioned adjacent to the heme group, and its N5 forms a hydrogen bond with a heme propionate arm. The heme group is covalently bound to NOS via a cysteine ligand, and the cavity above the porphyrin is considered the open binding pocket (**Figure 1.14**).^{51a, 52}

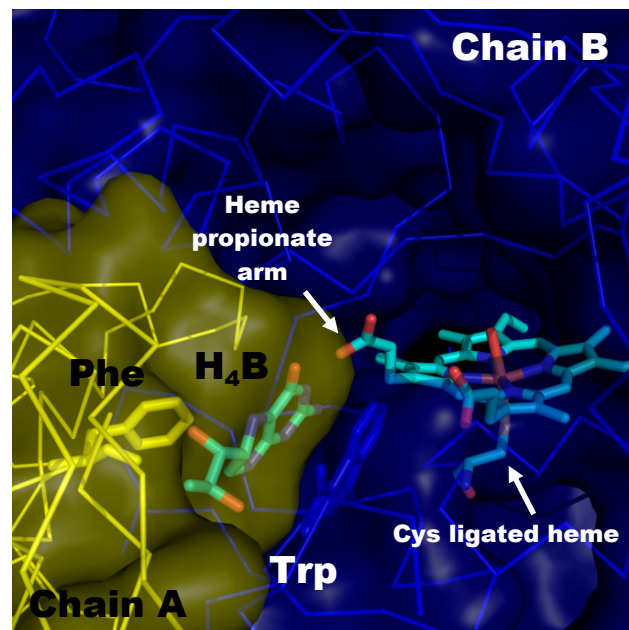


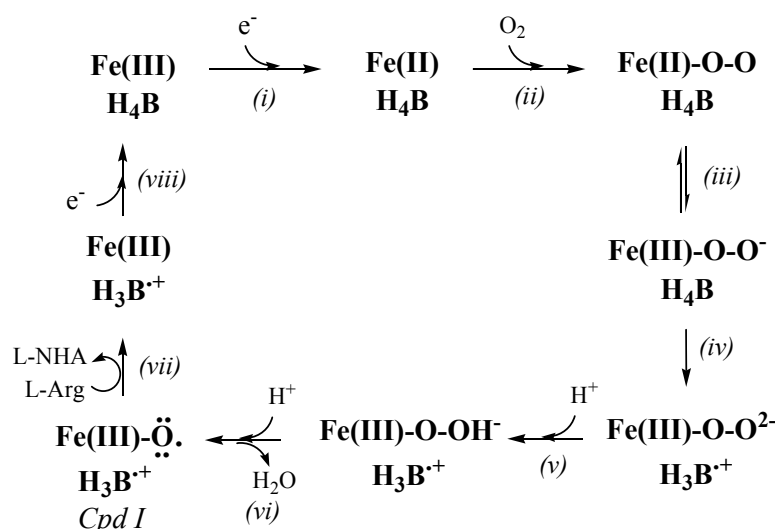
Figure 1.14: The NOS active site. The H_4B is situated at the dimer interface, stacked between the conserved Phe of Chain A and the Trp of chain B.

Critical to NOS catalysis is the transfer of electrons from NADPH to the heme group. With nNOS and eNOS, a Ca^{2+} CaM complex must bind to the enzyme for heme reduction to take place at a kinetically competent rate. Ca^{2+} CaM binding accelerates the rate of flavin reduction by NADPH and

facilitates electron transfer from the flavins to the heme.⁵³ Since iNOS binds CaM essentially irreversibly, electron transfer occurs readily in this isoform as isolated.⁵⁴

1.4.2 - Catalytic Mechanism of Nitric Oxide Synthase

During the catalytic reaction, L-Arg is located immediately above the heme group, with the guanidine moiety lying roughly coplanar to this unit. The nitrogen atoms of guanidine bond to the conserved Glu residue (iNOS Glu371, nNOS Glu592; eNOS Glu363) through two hydrogen bonds. This amino acid is the main residue with which the substrate forms extensive hydrogen bond network thereby orienting the guanidine nitrogen above the heme group for oxidation. The importance of the Glu residue has been revealed by site directed mutagenesis studies, where substitution of Glu by Gln, Leu, or Ala resulted in loss of activity.⁵⁵ There are two distinct steps in the NOS reaction, namely the oxidation of L-Arg to N^ω-OH-L-Arg (L-NHA) (**Scheme 1.5**), followed by its conversion to L-Cit and NO (**Scheme 1.6**). The heme cofactor of NOS directly regulates these two steps with molecular O₂, H⁺, and electrons from NADPH. Electron transfer from the reductase domain enables the reduction of Fe (III) to Fe (II) [**Scheme 1.5, (i)**] and subsequent binding of O₂ to form a Fe(II)-O₂ complex [**Scheme 1.5, (ii)**] that is best represented as a ferric iron superoxy state [Fe(III)-O₂⁻, **Scheme 1.5, (iii)**].

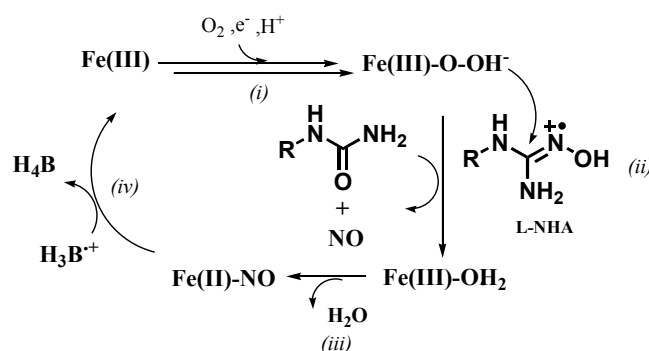


Scheme 1.5: The first step reaction of NOS showing the conversion of L-Arg to L-NHA.^{50b, 56}

The second electron for catalysis is delivered by H₄B to produce the ferric iron peroxo state [Fe(III)-O₂⁻², **Scheme 1.5, (iv)**] that was observed in low temperature cryoreduction experiments of eNOS.⁵⁷ This species accepts two protons [**Scheme 1.5, (v) and (vi)**] and turns into a Compound I (*Cpd I*) type reactant that will attack the substrate.^{50a, 58} However, some authors argue against the attack of *Cpd I* in the first step, and alternative mechanisms were proposed.⁵⁹ Recently, computational

studies supported *Cpd I* as the active intermediate in the oxidation of L-Arg.⁶⁰ The $\text{H}_3\text{B}^{\cdot+}$ radical can be recycled to H_4B by the NOS itself (using an electron supplied by the flavins). Alternatively, there is evidence that reducing agents such as ascorbic acid (which is present in cells in millimolar concentrations) can reduce the $\text{H}_3\text{B}^{\cdot+}$ radical back to H_4B .⁶¹

The second step (conversion of $\text{N}^{\text{O}}\text{-OH-L-Arg}$ to L-Cit and NO), involves the formation of the nucleophilic Fe(III)-O-OH^- species (i), which has been proposed to act as the active intermediate (**Scheme 1.6**). Oxygen activation proceeds as described for the first step depicted in **Scheme 1.5**, with electron donation from H_4B generating the Fe(III)-O-OH^- state. Instead of decomposing to *Cpd I*, it has been proposed that Fe(III)-O-OH^- reacted directly with $\text{N}^{\text{O}}\text{-OH-L-Arg}$ to produce L-Cit and NO (**Scheme 1.6**).



Scheme 1.6: Second step reaction of NOS. The cycle for turning L-NHA to NO and citrulline is similar except the reactive species might be Fe(III)-O-OH^- instead of Fe(III)-O . In addition, short lived $\text{H}_3\text{B}^{\cdot+}$ radical in the second reaction cycle acts as an electron acceptor getting reduced to H_4B .⁵⁶

1.4.3 – Chemical Biology of NO

NO is a highly reactive free radical in biological systems that has a variety of effects depending on its relative concentration and surrounding environment. There are two distinct effects in the chemical biology of NO: direct and indirect effects (**Figure 1.15**). Direct effects include the chemical reactions where NO reacts directly with its biological target. Conversely, the indirect effects are mediated by reactive nitrogen oxide species (RNOS) derived from NO metabolism. The direct effects are very rapid reactions that occur at low NO concentrations ($< 1 \mu\text{M}$) and generally involve heme proteins such as guanylate cyclase, cytochrome P450, and hemoglobin. The indirect effects require first the activation of NO by O_2^- or O_2 to form RNOS (e.g. N_2O_3 , ONOO , NO_3), which then undergo further reactions with the respective biological target.⁶²

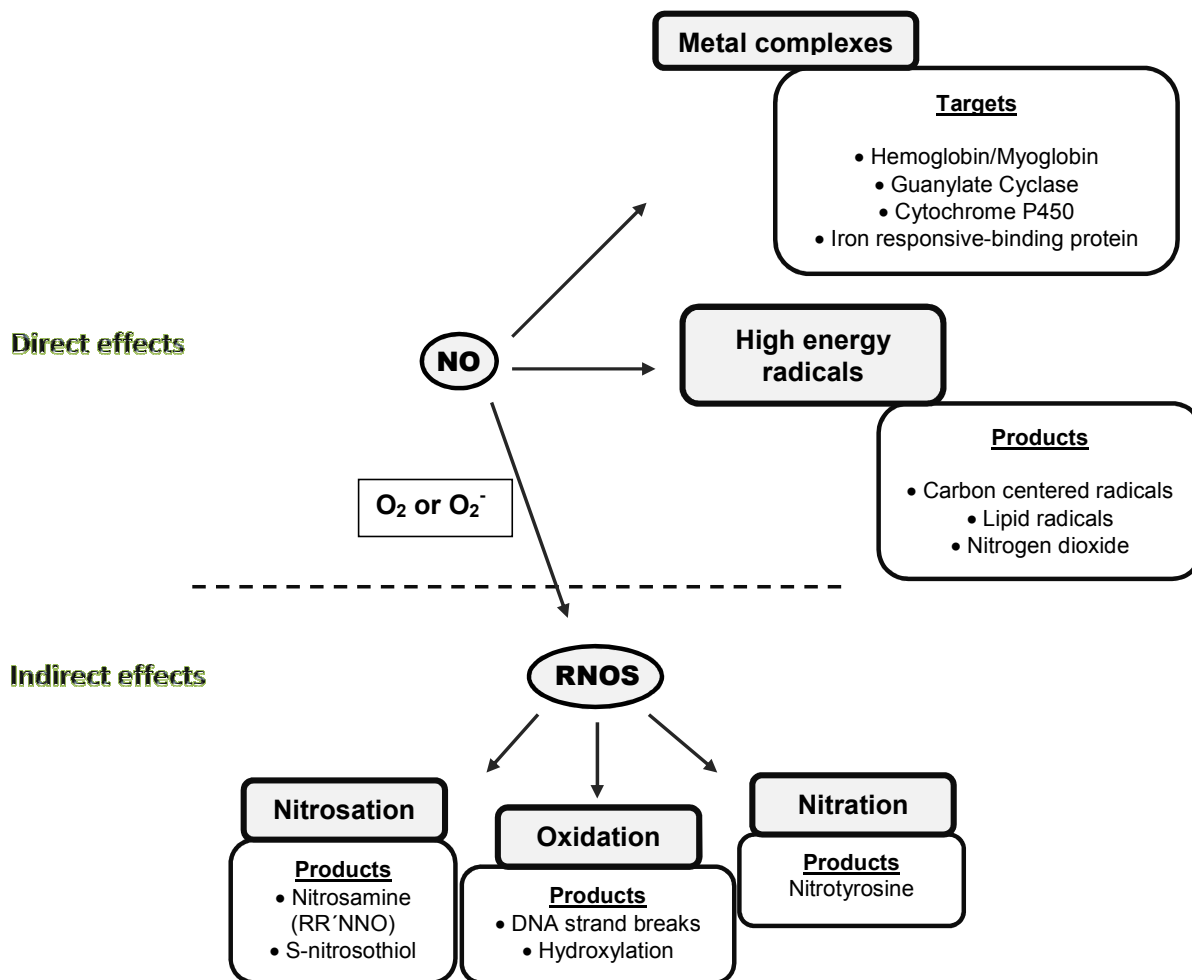


Figure 1.15: The chemical biology of NO.⁶²

The direct interaction of NO with soluble guanylate cyclase (sGC), originating the 3':5' cyclic monophosphate (cGMP), is described as the main mechanism by which nNOS and eNOS mediate most of their physiological effects. In neurons, the production of NO by nNOS is activated by binding of CaM in response to the accumulation of Ca²⁺ triggered by the N-methyl-D-aspartate receptor (NMDAR). The gas diffuses into neighboring cells such as the presynaptic terminal to activate sGC, which then results in the elevation of intracellular cGMP levels. The function of cGMP in the central nervous system (CNS) includes an effect on ion channels, activation of protein kinases, stimulation or inhibition of phosphodiesterase activity, among others.⁶³ In blood vessels, the production of NO by eNOS is activated through the acetylcholine that stimulates its receptor situated in the membrane of the endothelial cells, promoting intracellular Ca²⁺ accumulation. In a similar way to the one previously described, the Ca²⁺ ions induce a conformational change in CaM, which, in turn, binds to eNOS. eNOS mediated NO formation is released to the neighboring smooth muscle cells, inducing cyclin GMP mediated relaxation.⁶⁴

As opposed to the cGMP dependent mechanism of action of NO produced by nNOS and eNOS, the mechanism of action of iNOS isoform has been mainly associated to the indirect effects of NO (**Figure 1.15**). The high concentration of NO produced by immune system cells (dendritic cells, monocytes, macrophages, microglia, Kupffer cells, neutrophils, etc) penetrates easily in the target cells (pathogens or tumor cells) where is converted into RNOS, which act as cytotoxic agents by reaction, for example, with the cysteinyl residues or amine groups of proteins (Nitrosation; **Figure 1.15**).^{62, 64-65} Other effects include hydroxylation and nitrosation reactions, DNA damage, degradation of iron centers, among others (**Figure 1.15**).^{62, 64-66}

1.4.4 – NO/NOS and Disease

Excess generation of NO from nNOS has been linked to ischemia and neurodegeneration resulting from stroke, migraine headache and Parkinson's, Alzheimer's, and Huntington's diseases. Enhanced iNOS activity has been related to a wide variety of conditions, namely to arthritis, colitis, septic shock, inflammatory bowel disease, asthma and cancer.^{64, 66-67} On the contrary, NO produced by eNOS has mainly a physiological role.⁶⁸

The association of disordered NO generation with many pathological situations has considerably raised the interest in the modulation of NO levels with drugs. Therefore, directly altering the generation of NO is a pharmacologically attractive approach for treating several diseases. The development of isoform specific iNOS and nNOS inhibitors for treating NOS related diseases is an highly desirable goal.^{68b} Since NOS substrates have a less pharmacological interest, the development of such type of compounds has been less explored.⁶⁹

In most cases, a NO related disease state is linked to a particular isoform. Therefore, if one wants to design an inhibitor to have therapeutic potential, one would have to specifically target one isoform over the other two. Selectivity is especially mandatory over eNOS due to its importance in the fundamental physiology of blood pressure homeostasis as mentioned before. The high conservation of the heme active site residues of all three isoforms makes the task of achieving isoform selectivity quite difficult and challenging. The three NOS isoforms share about 50 – 60% sequence identity (**Figure 1.16**).^{48b, 70} Despite the structural homology of the active site in the three enzyme isoforms, the subtle differences found in both the active pocket and in the substrate access channel are being explored for the rational design of isoform specific NOS inhibitors.⁷¹

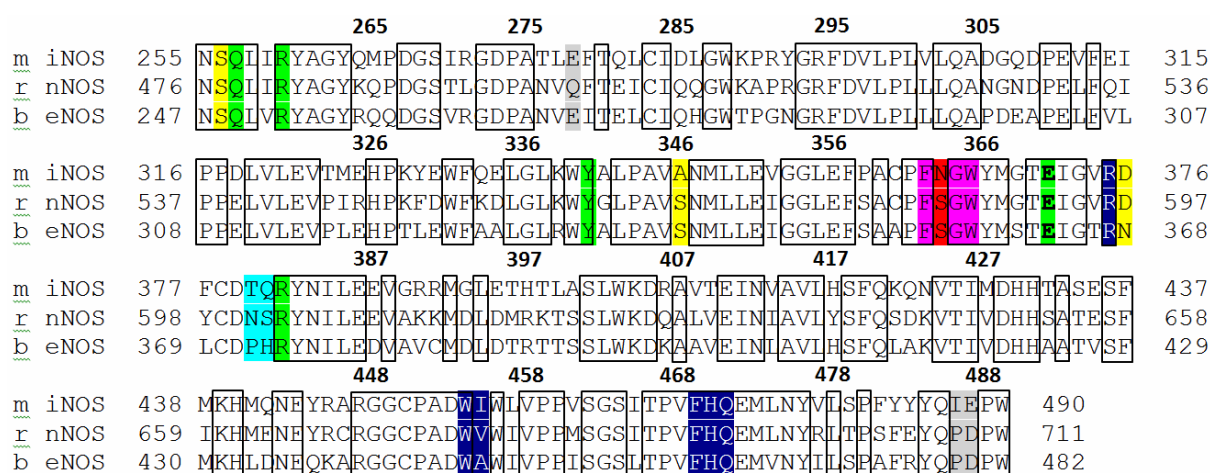
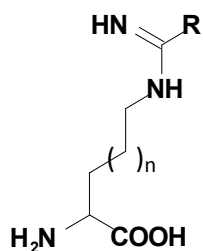


Figure 1.16: Swissprot (BLASTP) sequence alignment of NOS oxygenase domains (Altschul, Madden et al. 1997). The sequences shown are: murine iNOS (GenBank: 40889451), bovine eNOS (GenBank: 295789347), rat nNOS (GenBank: 295789339). Residues forming the backwall are colored in purple. Invariant residues of the active site include Gln, Arg, Tyr and Glu and are colored in green. Differences in the active site of the three NOS isoforms considered important are colored in red (S pocket), yellow (M pocket), light blue (C_1 pocket) and grey (C_2 pocket). Dark blue background denotes residues in contact with H_4B (cut off distance 3.6 Å). Conserved residues among the three isoforms are boxed. Numbering is based on the iNOS sequence.

The first generation of inhibitors include L-Arginine based analogs that were mono or di substituted at the guanidino site, such as N^ω - CH_3 -L-Arg (L-NMA, **10**), N^ω - NO_2 -L-Arg (L-NA, **11**), N^ω - NH_2 -L-Arg (L-NAA, **12**), and N^ω -propyl-L-Arg (L-NPA, **13**) (Table 1.2).^{5a} Aimed at the improvement of both isoselectivity and inhibitory potency, modifications on the guanidine moiety were explored. This effort led to the most notable compounds of this class, namely N^ω -Iminomethyl-L-Ornithine (L-NIO, **14**), N^ω -Iminomethyl-Lysine (L-NIL, **15**) and L-Thiocitrulline (L-Thio, **16**) depicted in Table 1.2.^{5a, 72}

Table 1.2: Inhibitors of NOS derived from L-Arg.

| Compound | R | n | Inhibitory constants (μM) | | |
|--|---|---|--|------------------|-------------------|
| | | | nNOS | iNOS | eNOS |
| $\text{N}^\omega\text{-CH}_3\text{-L-Arg}$ (L-NMA, 10) | NHCH ₃ | 1 | 5.9 ^a | 14 ^a | 10 ^a |
| $\text{N}^\omega\text{-NO}_2\text{-L-Arg}$ (L-NA, 11) | NHNO ₂ | 1 | 0.52 ^a | 7.6 ^a | 0.50 ^a |
| $\text{N}^\omega\text{-NH}_2\text{-L-Arg}$ (L-NAA, 12) | NHNH ₂ | 1 | 0.3 ^b | 3.0 ^b | 2.5 ^b |
| $\text{N}^\omega\text{-Propyl-L-Arg}$ (L-NPA, 13) | NHCH ₂ CH ₂ CH ₃ | 1 | 0.057 ^c | 180 ^c | 8.5 ^c |
| $\text{N}^\omega\text{-Iminomethyl-L-Ornithine}$ (L-NIO, 14) | CH ₃ | 1 | 3.9 ^d | 2.2 ^d | |
| $\text{N}^\omega\text{-Iminomethyl-Lysine}$ (L-NIL, 15) | CH ₃ | 2 | 92 ^d | 3.3 ^d | |
| L-Thiocitrulline (L-Thio, 16) | S | 1 | 0.36 ^e | 3.6 ^e | |

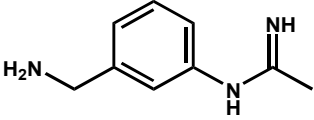
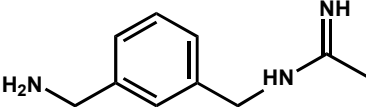
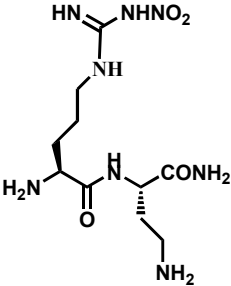
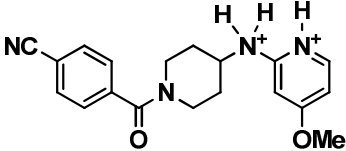
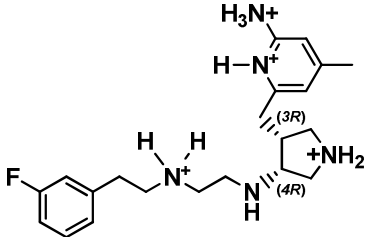


^a IC₅₀ from ref. ^{5a}; ^b K_i values from ref. ⁷³ and ⁷⁴; ^c K_i values from ref. ⁷⁵; ^d IC₅₀ values from ref. ⁷⁶; ^e K_i values from ref. ⁷⁷.

Elimination of the carboxyl group of L-NIO, followed by rigidification of the side chain, gave the inhibitor N-(3-(aminomethyl)phenyl)acetamide, also referred to as 5230W (**17**, **Table 1.3**).⁷⁸ Unlike the precursor compound L-NIO, which lacks isoform selectivity, 5230W is 155 fold more selective for nNOS over eNOS, and 50 fold more selective over iNOS. Addition of a methylene group between the amidine group and the phenyl ring of 5230W resulted in N-(3-(aminomethyl)benzyl)acetamide, known as 1400W (**18**, **Table 1.3**).⁷⁸⁻⁷⁹ Remarkably, this small change switched the selectivity to iNOS. 1400W is 535 fold more selective for iNOS over eNOS, and 14 fold more selective over nNOS.⁷⁸⁻⁷⁹

As mentioned before, the difficulty in achieving isoform selectivity arises mostly from the lack of distinctive residues among the different isozymes in the substrate binding pocket.⁸⁰ The only residues that differ in the pocket are Asn364 in iNOS, which is Ser585 and Ser356 in nNOS and eNOS, respectively (**Figure 1.16**). Therefore, to achieve high isoform selective inhibition, an inhibitor should possess functional groups that can reach the substrate access channel where the structural differences among the three isoforms are more evident (**Figure 1.16**). In this regard, Silverman *et al.* have designed an extensive family of dipeptide compounds derived from $\text{N}^\omega\text{-NO}_2\text{-L-Arg}$.⁸¹ The most potent analog, $\text{N}^\omega\text{-NO}_2\text{-L-Arg-L-Dbu-NH}_2$ (**19**, **Table 1.3**), display a K_i of 130 nM toward nNOS, with a selectivity over eNOS of 1538 and over iNOS of 192.

Table 1.3: Potent and isoselective inhibitors of NOS.

| Compound | Inhibitory constants (μM) | | |
|---|--|--------------------|--------------------|
| | nNOS | iNOS | eNOS |
| N-(3-(Aminomethyl)phenyl)acetamidine (17 , 5230W) | 0.04 ^a | 2.0 ^a | 6.2 ^a |
|  | | | |
| N-(3-(Aminomethyl)benzyl)acetamidine (18 , 1400W) | 2.0 ^b | 0.007 ^b | 50.0 ^b |
|  | 2.0 ^a | 0.14 ^a | 75.0 ^a |
| N ^ω -NO ₂ -L-Arg-L-Dbu-NH ₂ (19) | 0.13 ^c | 25.0 ^c | 200 ^c |
|  | | | |
| Aminopyridine benzonitrile derivative (20) | 0.074 ^e | 6.0 ^e | > 100 ^e |
|  | | | |
| (3R,4R) aminopyridine derivative (21) | 3.9 ^d | 0.005 ^d | 20.3 ^d |
|  | | | |

^a K_i values from ref. ⁷⁸; ^b K_i values from ref. ⁷⁹; ^c K_i values from ref. ^{81a}; ^d K_i values from ref. ^{71b}; ^e IC_{50} values from ref. ^{71a}

More recently, a family of large competitive inhibitors that contain an aminopyridine fragment have been introduced (compounds **20** and **21**, **Table 1.3**).⁷¹ These compounds have been designed using structure based-drug design methods, and are the most potent and selective inhibitors of nNOS and iNOS to date.

1.4.5 – Radioactive Probes for Targeting NOS

As stated before, several studies have shown that deregulation of NOS isoforms is implicated in a variety of diseases. In this context, the *in vivo* imaging of NO (e.g. by EPR) or NOS expression by PET or SPECT techniques, using radiolabeled NOS substrates/inhibitors, hold great potential for providing an insight into the wide variety of diseases linked to abnormal NO production.⁸² Until now only a limited number of labeled compounds have been proposed for the detection of NOS activity *in vivo*. Aiming to prepare nNOS selective imaging agents for the evaluation of regional brain uptake in rodents and primates, thiopheneamidine analogs were labeled with ¹¹C (**22**, **Figure 1.17**). In this case, most of the observed binding was nonspecific.⁸³ The inhibitor *N*^ω-NO₂-L-Arg-¹¹Cmethyl ester has been precluded as PET tracer for NOS distribution due to its *in vivo* instability (**23**, **Figure 1.17**).⁸⁴ Preliminary studies with S-¹¹Cmethylisothiurea (**24**) and S-(2-¹⁸Ffluoroethyl)isothiurea (**25**), β⁺-emitting iNOS selective inhibitors, showed potential for monitoring increased levels of iNOS *in vivo* (**Figure 1.17**).⁸⁵ In fact, using an LPS-pretreated rat model with widespread tissue expression of iNOS, enhanced uptake of both radioprobes was observed in lung and spleen, which are reported to possess increased levels of iNOS.

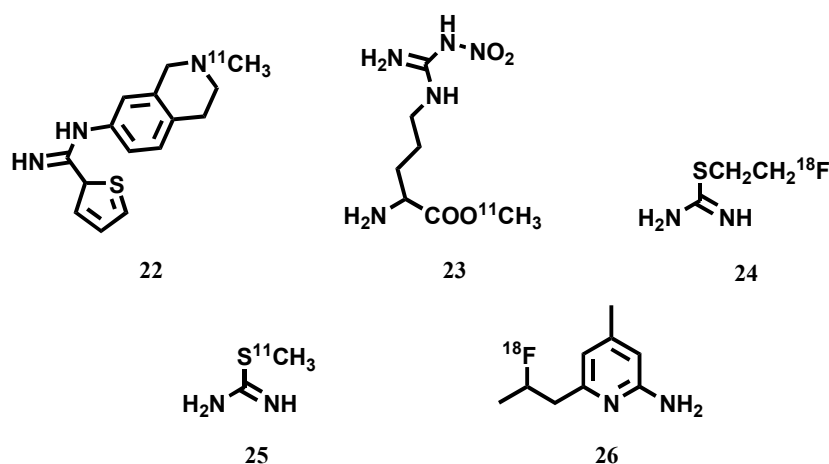


Figure 1.17: β⁺-emitting compounds potentially useful for *in vivo* imaging of NOS expression.

Most recently, the iNOS selective inhibitor 6-(2 fluoropropyl)-4-methylpyridin-2-amine (**26**, IC₅₀ = 220 ± 25 nM for iNOS, **Figure 1.17**) labeled with fluorine-18 presented a higher uptake in the lungs of LPS treated mice than the control (**Figure 1.18**). So far, the positron-emitting iNOS selective inhibitor **26** is the only compound with relevant properties for potential iNOS visualization *in vivo*.⁸⁶

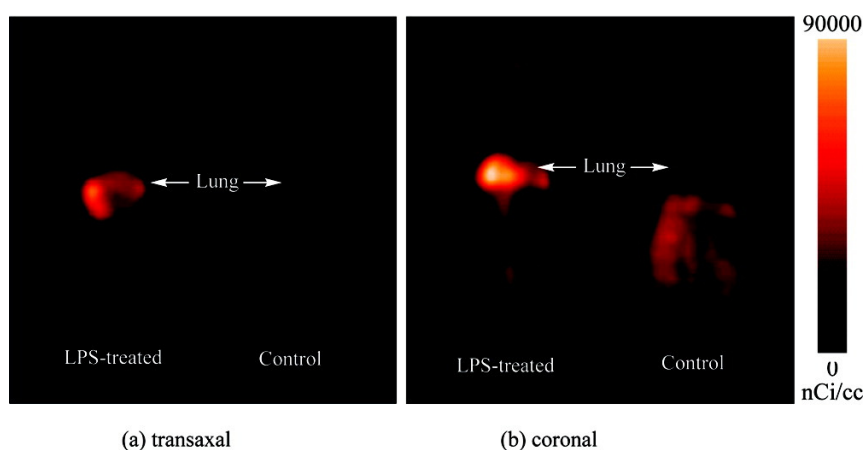


Figure 1.18: Whole body MicroPET images of **26** in the LPS-treated mice (left) and the control mice (right): (a) transaxal, (b) coronal. Accumulation of the activity was observed in the lungs of the LPS treated mouse, whereas there is no such accumulation in the normal control.⁸⁶

2 Synthesis of Bifunctional Chelators (BFCs) and their Re(I) and $^{99m}\text{Tc(I)}$ Complexes

2. Synthesis of Bifunctional Chelators (BFCs) and their Re(I) and ^{99m}Tc(I) Complexes

As mentioned before, the main goal of this work was to contribute for the design of radioactive probes potentially useful for imaging the iNOS expression *in vivo*. To achieve such goal we explored the labeling of iNOS-recognizing moieties with the *fac*-[^{99m}Tc(CO)₃]⁺ moiety. The bifunctional chelators selected were the **pyrazolyl**- and **Dap**-containing BFCs, which contain the *N,N,N* and *N,N,O* donor atom sets, respectively. Both chelator types contain pendant arms with different lengths (C3 or C6 carbon linker) and different groups (-CO₂H and -NH₂) for conjugation to biomolecules with affinity for iNOS or transformation into bioactive units (e.g. guanidine) (**Figure 2.1**).

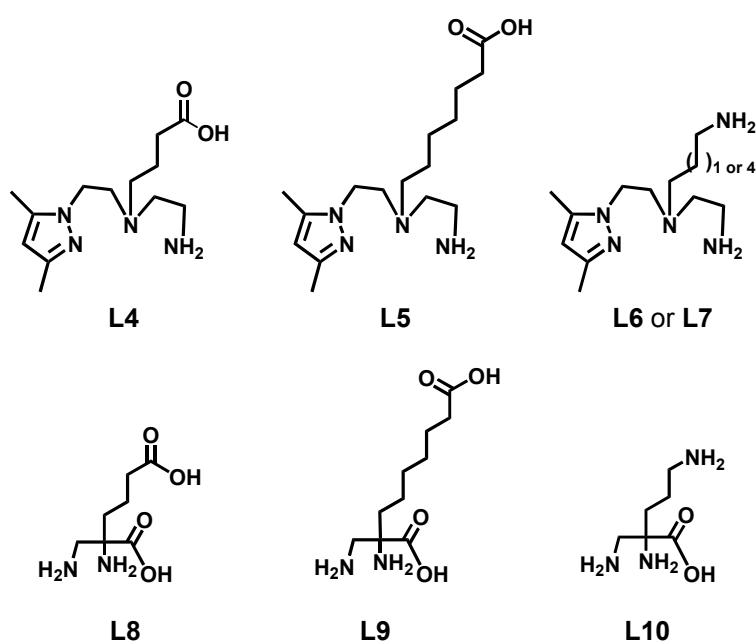


Figure 2.1: Pyrazolyl- and Dap-containing model BFCs.

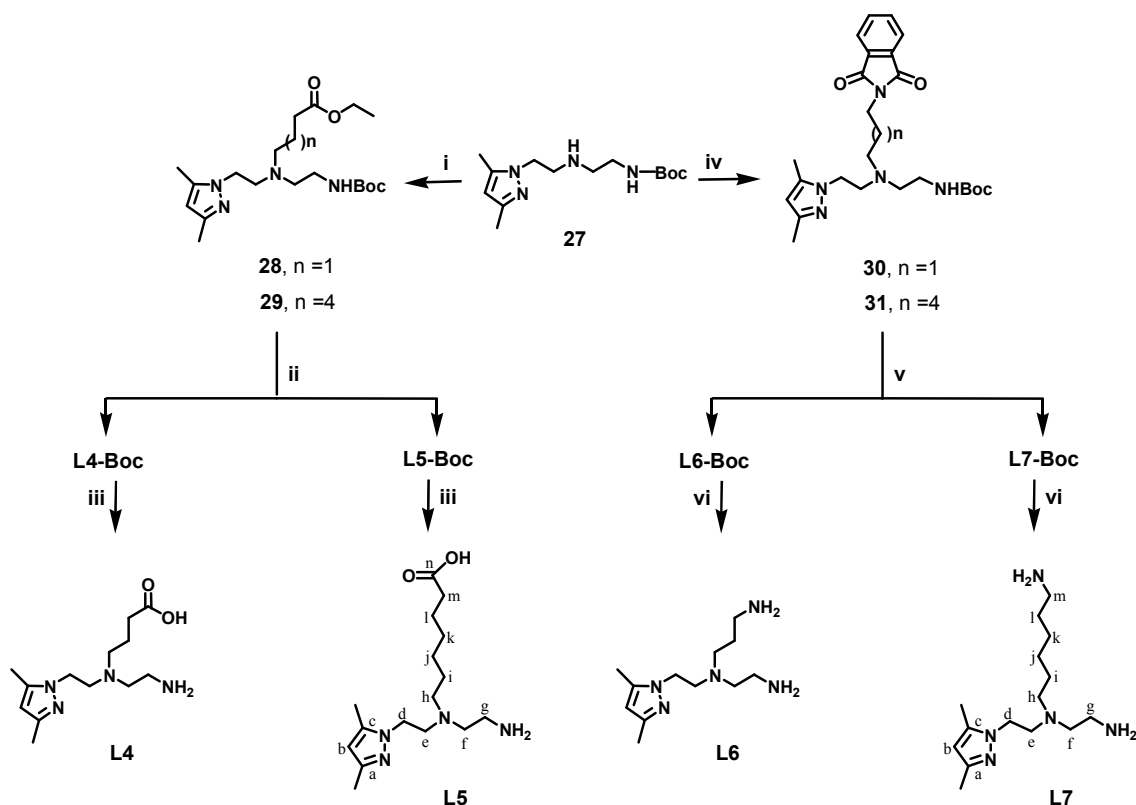
In this **Chapter** we describe the synthesis and characterization of the model **pyrazolyl**- and **Dap**-containing bifunctional chelators **L4 – L10** (**Section 2.1**), and their reactions with the organometallic precursors (NEt₃)₂[Re(CO)₃(Br)₃] and/or *fac*-[M(CO)₃(H₂O)₃]⁺ (M = Re, ^{99m}Tc) (**Sections 2.2** and **2.3**). The *in vitro* stability and biological behavior of the ^{99m}Tc(I) complexes will be also presented and discussed. The derivatization of the **pyrazolyl**- and **Dap**-containing chelators with the iNOS recognizing moieties will be described in **Chapter 3**.

2.1 – Pyrazolyl-Based BFCs and their Re(I)/^{99m}Tc(I) Complexes

In **Section 2.1.1** we describe the synthesis and characterization of **pyrazolyl-diamine** BFCs with a propyl or a hexyl linker between the chelating backbone and the carboxylic acid group or the free primary amine. Their ability to stabilize the *fac*-[M(CO)₃]⁺ (M = Re, ^{99m}Tc) core (**Section 2.1.2**) as well as the *in vitro/in vivo* behavior of the resulting ^{99m}Tc complexes (**Section 2.1.2.2**) are also described.

2.1.1 - Synthesis of the Pyrazolyl BFCs L4 – L7

The BFC **L4** was synthesized and characterized as previously reported by our group.^{41c} Following a similar procedure, the new chelators **L5 – L7** were synthesized by multistep synthetic procedures, as depicted in **Scheme 2.1**.¹³⁷



Scheme 2.1: Synthesis of the bifunctional chelators **L4 – L7**. i) ethyl-7-bromoheptanoate or ethyl-4-bromobutanoate, K₂CO₃, KI, CH₃CN, reflux, overnight, 79.0 % for **29**; ii) NaOH, H₂O, THF, reflux, overnight, 86 % for **L5-Boc**; iii) trifluoroacetic acid (TFA), CH₂Cl₂, r.t., 2 h, 92 % for **L5**; iv) N-(3-bromopropyl)phthalimide or N-(6-bromohexyl)phthalimide, K₂CO₃, dioxane, reflux, overnight, 78 % for **30** and 50 % for **31**; v) MeOH, NH₂NH₂·H₂O, reflux, 6 h, 86.0 % for **L6-Boc** and 90.0 % for **L7-Boc**; vi) TFA, CH₂Cl₂, r.t., 2 h, 50.0 % for **L6** and 49.0 % for **L7** (*identification system for NMR spectra assignment is displayed for L5 and L7 as an example*).

L5 was synthesized in high yield (92 %) by alkylation of the central secondary amine in the Boc-protected pyrazolyl precursor (**27**) with ethyl-7-bromoheptanoate, followed by ester hydrolysis and Boc-deprotection with TFA (**Scheme 2.1**).

The chelators **L6** and **L7** were synthesized by reaction of **27** with the alkylating reagents N-(3-bromopropyl)phthalimide or N-(6-bromohexyl)phthalimide, respectively, in refluxing dioxane in the presence of K₂CO₃, yielding intermediates **30** (78 %) and **31** (50 %). Phthalimide deprotection with hydrazine monohydrate in boiling MeOH, followed by treatment with TFA, gave the corresponding final molecules **L6** and **L7**.

All intermediates and final bifunctional chelators were fully characterized by the usual analytical techniques in chemistry, namely IR and NMR spectroscopy, electrospray ionization mass spectrometry (ESI-MS), and reversed-phase High-Performance Liquid Chromatography (RP-HPLC). The use of 2D-NMR experiments (¹H-¹H g-COSY and ¹H-¹³C g-HSQC) was crucial for peak assignment in the NMR spectra, and for the full characterization of the final compounds.

Briefly, the ¹H-NMR spectra (D₂O) of the bifunctional ligands presented the typical sharp singlet peaks for the H(4) proton (δ 6.11, **L4**; δ 5.94, **L5**; δ 5.83, **L6**; δ 6.03, **L7**) and the methyl groups of the azolyl ring (δ 2.16/2.10, **L4**; δ 2.20/2.12, **L5**; δ 2.11/2.01, **L6**; 2.20/2.12, **L7**). Resonances for all methylenic protons of the **pyrazolyl-diamine** backbone were also found and fully assigned. The ¹³C spectra presented signals corresponding to all the carbon nuclei of the molecules. As an example, the ¹H-NMR spectrum of **L4** is depicted in **Figure 2.2**.

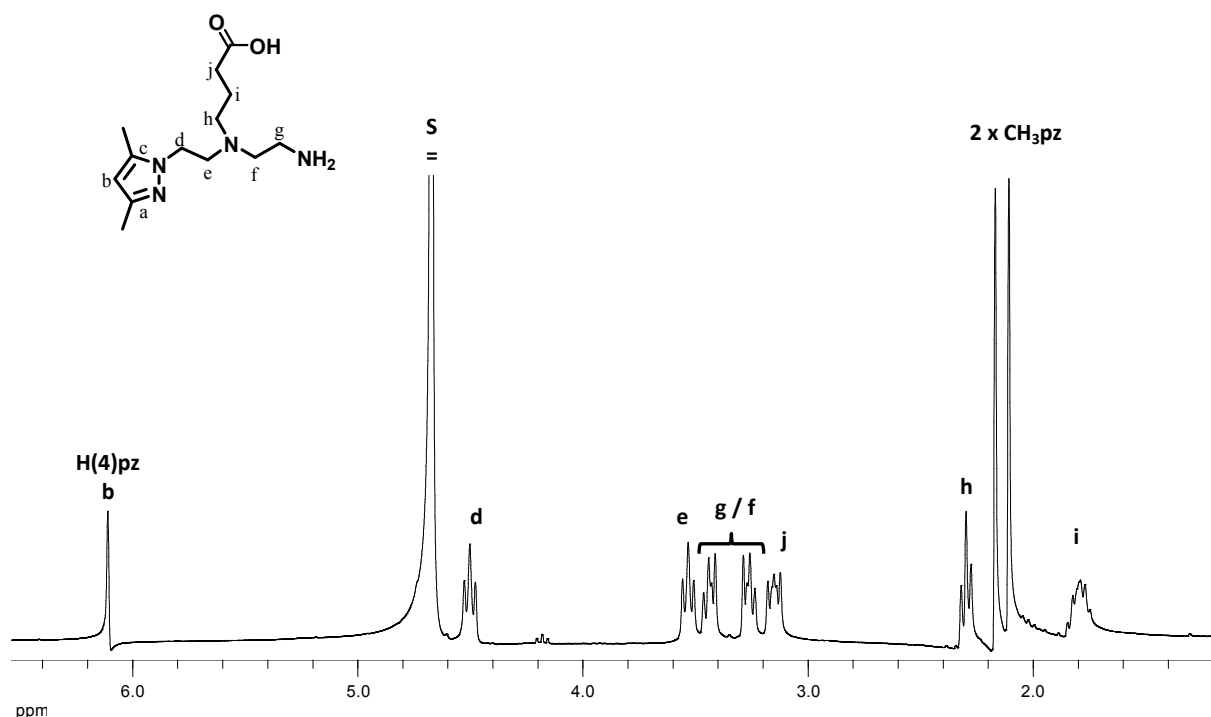
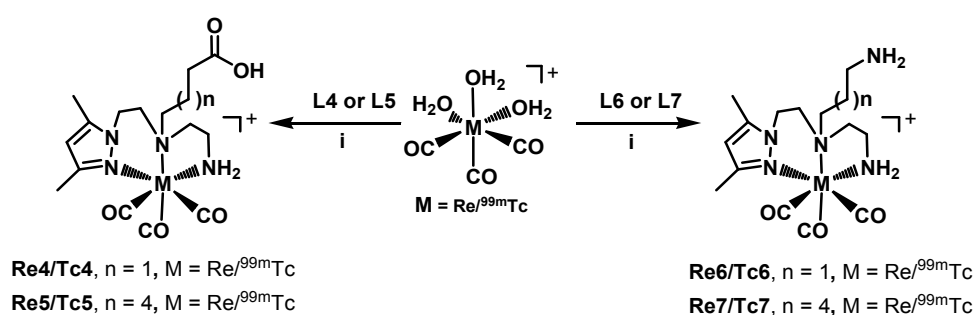


Figure 2.2: ¹H-NMR spectrum of compound **L4** in D₂O (S = residual water).

2.1.2 - Reactions of L4 – L7 with *fac*-[M(CO)₃]⁺ Precursors (M = Re or ^{99m}Tc)

2.1.2.1 - Synthesis and Characterization of the Re(I) Complexes Re4 – Re7

The BFCs **L4** - **L7** reacted with equimolar amounts of precursor *fac*-[Re(CO)₃(H₂O)₃]Br, in refluxing water for 18 h, yielding, after purification by preparative RP-HPLC (TFA 0.1% in H₂O/MeOH), complexes of the type *fac*-[Re(CO)₃(κ³-L)]⁺ (**Re4**, L = **L4**; **Re5**, L = **L5**; **Re6**, L = **L6**; **Re7**, L = **L7**) (**Scheme 2.2**). All compounds were obtained as white microcrystalline solids with high purity (> 95% by RP-HPLC).



Scheme 2.2: Synthesis of complexes **Re4/Tc4** – **Re7/Tc7**. i) H₂O, reflux, overnight (M = Re) or H₂O, 100 °C, 30 - 45 min (M = ^{99m}Tc).

The complexes **Re4** – **Re7** were prepared and fully characterized as non-radioactive surrogates of the corresponding ^{99m}Tc(I) complexes **Tc4** – **Tc7** (**Scheme 2.2**). They were fully characterized by the usual analytical techniques in chemistry, namely IR and NMR spectroscopy, ESI-MS, and RP-HPLC. Like in the case of the bifunctional chelators, the use of 2D-NMR experiments (¹H-¹H g-COSY and ¹H-¹³C g-HSQC) was crucial for peak assignment in the NMR spectra, and for full characterization of the compounds described in the experimental part. Additionally, complexes **Re4** and **Re5** were also characterized in the solid state by X-ray diffraction analysis. As expected, the chelators coordinate as neutral and tridentate through the nitrogen atoms of the pyrazolyl–diamine ligand backbone.

The *facial* arrangement of the carbonyl groups in the complexes was confirmed by the strong CO stretching bands in the IR spectra (2030s and 1920s cm⁻¹, **Re5**; 2038s and 1954s cm⁻¹, **Re6**; 2106s and 1974s cm⁻¹, **Re7**) being within the ranges normally found for other complexes with the “*fac*-Re(CO)₃” moiety.^{41a-d}

The ¹H-NMR spectra presented singlet peaks assigned to H(4) (δ 6.15, **Re4**, δ 6.20, **Re5**; δ 6.07, **Re6**; δ 6.07, **Re7**) and to the methyl groups of the pyrazolyl ring (δ 2.34/2.23, **Re4**; δ 2.43/2.35, **Re5**; δ 2.30/2.19, **Re6**; δ 2.30/2.19, **Re7**). The H(4) and the methyl protons of the pyrazolyl ring are shifted downfield (H(4), $\Delta = \sim 0.25 - 0.10$ ppm; Me, $\Delta = \sim 0.15 - 0.10$ ppm) relatively to the same resonances in the corresponding free chelators, indicating coordination to the metal center. The tridentate coordination mode of the chelator was also confirmed by the splitting of the NH₂ protons of the primary amine (δ 5.16 and δ 3.73, **Re4**; δ 5.49 and δ 3.55, **Re5**; δ 5.15 and δ 3.65, **Re6**; δ 5.09 and δ 3.64, **Re7**), as well as by the splitting of the methylenic protons of the coordinating backbone. For each of these protons, two resonances, integrating for one proton each, were found, due to the diastereotopic character of the methylenic protons after coordination to the metal center (e.g. δ 4.40 CH^d, δ 4.18 CH^{d'}, δ 3.43 CH^e, δ 2.63 CH^{e'} for **Re4**; δ 4.50 CH^d, δ 4.22 CH^{d'}, δ 3.41 CH^e, δ 2.68 CH^{e'} for **Re5**; δ 4.35 CH^d, δ 4.13 CH^{d'}, δ 3.32 CH^e, δ 2.63 CH^{e'} for **Re6**; δ 4.32 CH^d, δ 4.13 CH^{d'}, δ 3.32 CH^e, δ 2.58 CH^{e'} for **Re7**). This behavior, which is a strong evidence of ligand coordination, has been already observed in other tricarbonyl complexes previously described.^{41b,c} The ¹³C-NMR spectra present all the expected signals for the proposed structures. An important characteristic of the ¹³C spectra of compounds **Re4 - Re7** is the presence of three resonances for the C≡O ligands (δ 198.3, δ 194.5 and δ 194.3 for **Re4**; δ 198.5, δ 198.1 and δ 196.9 for **Re5**; δ 197.3, δ 196.7 and δ 195.5 ppm for **Re6**; δ 198.8, δ 198.3 and δ 197.2 ppm for **Re7**) coordinated facially to rhenium. The full assignment of the ¹³C resonances was based on ¹H-¹³C g-HSQC. The most important characteristic of the spectra was the correlation between the geminal diastereotopic protons and the respective carbons. The ¹H-NMR and ¹³C-NMR spectra of **Re6** with the corresponding peak assignment are presented in **Figure 2.3** as an illustrative example.

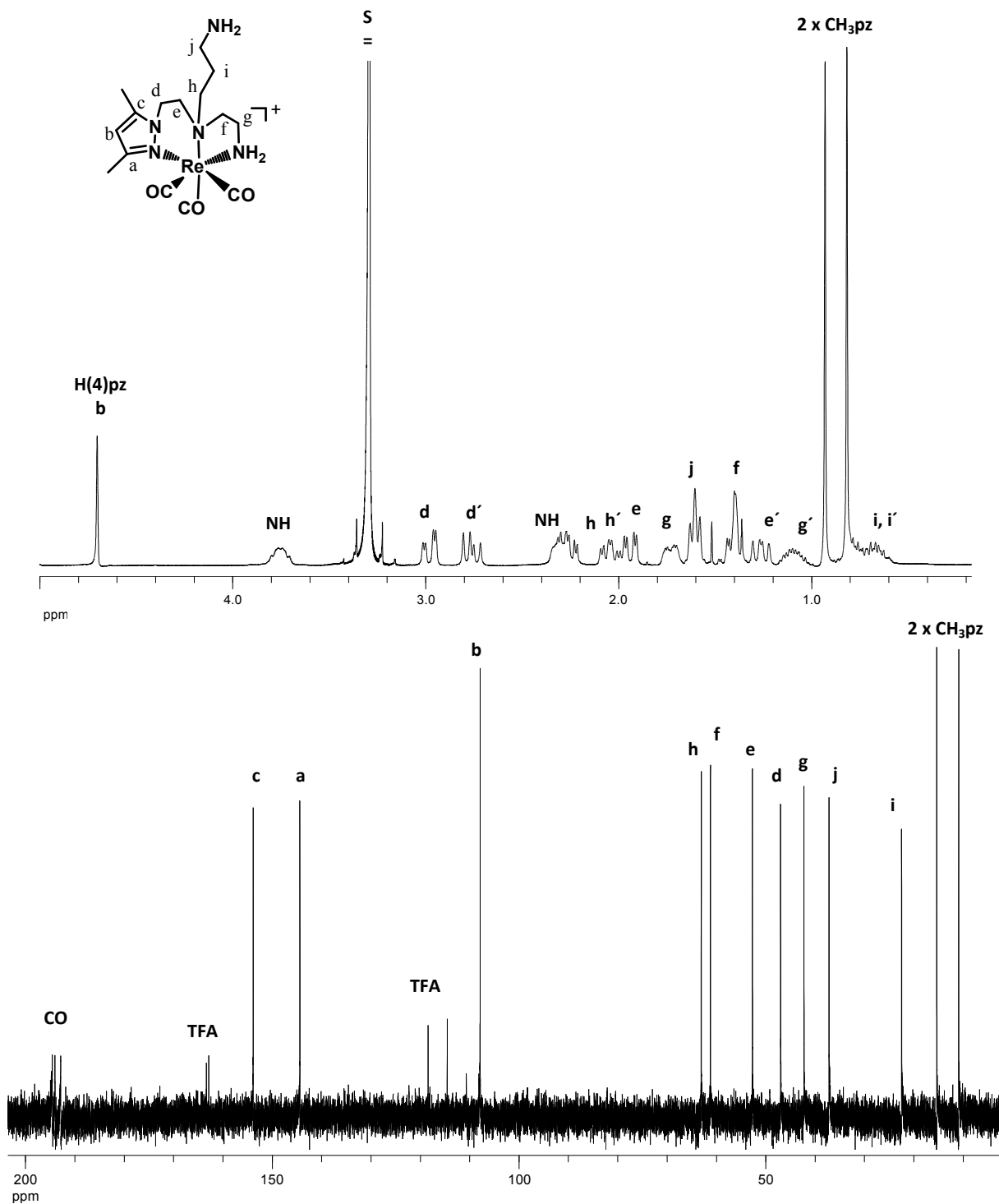


Figure 2.3: ^1H - (top) and ^{13}C -NMR (bottom) spectra of compound **Re6** in D_2O (S = residual water).

Solid state structures of **Re4** and **Re5**

Suitable crystals of *fac*- $[\text{Re}(\text{CO})_3(\kappa^3\text{-L4})]\text{TFA}\cdot\text{H}_2\text{O}$ (**Re4**·TFA· H_2O) and *fac*- $[\text{Re}(\text{CO})_3(\kappa^3\text{-L5})]\text{TFA}$ (**Re5**·TFA) were grown by slow diffusion of CHCl_3 into a solution of the compounds in MeOH. Complex **Re4**·TFA· H_2O crystallizes with three independent molecules per asymmetric unit, which can

be considered chemically equivalents. In the case of **Re5**-TFA the crystal contained one molecule per asymmetric unit. A summary of the crystal data, structure solution and refinement parameters are given in **Table 8.1** (Annexes). ORTEP diagrams of cation **Re4** and **Re5**, together with selected bond lengths and angles are given in **Figure 2.4**.

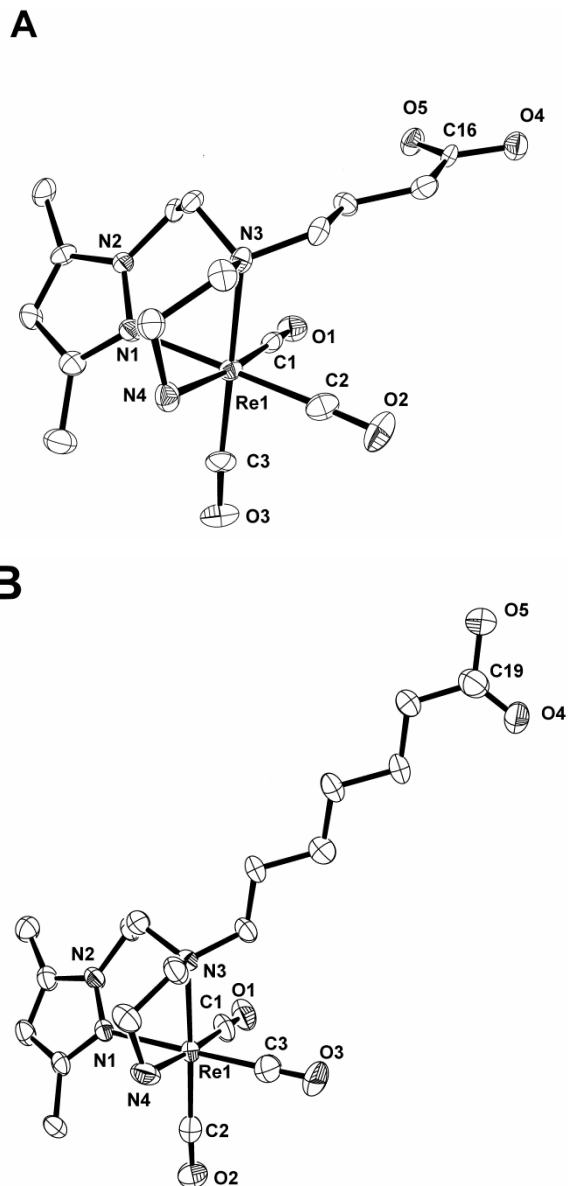


Figure 2.4: ORTEP views of cations **Re4** (**A**) and **Re5** (**B**). TFA counterion, H₂O solvate molecule and H atoms are omitted for clarity. Vibrational ellipsoids are drawn at the 50% probability level. Selected bond distances (Å) and angles (°) for **Re4** (**A**): Re1 - C1, 1.905(7) Å; Re1 - C2, 1.915(7) Å; Re1 - C3, 1.918(7) Å; Re1 - N1, 2.170(5) Å; Re1 - N3, 2.293(5) Å; Re1 - N4, 2.215(5) Å; C1 - Re1 - N1, 90.0(2)°; C2 - Re1 - N1, 95.1(2)°; C1 - Re1 - N3, 98.8(2)°; C3 - Re1 - N3, 92.8(2)°; C2 - Re1 - N4, 96.2(2)°; C3 - Re1 - N4, 94.4(2)°; C1 - Re1 - C2, 86.3(3)°; C1 - Re1 - C3, 91.3(3)°; N1 - Re1 - N3, 86.57(18)°; N1 - Re1 - N4, 84.22(19)°; for **Re5** (**B**): Re1 - C1, 1.891(3) Å; Re1 - C2, 1.927(2) Å; Re1 - C3, 1.920(5) Å; Re1 - N1, 2.202(2) Å; Re1 - N3, 2.288(3) Å; Re1 - N4, 2.199(4) Å; C1 - Re1 - N1, 90.9(4)°; C2 - Re1 - N1, 94.4(5)°;

C1 - Re1 - N3, 97.7(4)°; C3 - Re1 - N3, 92.9(4)°; C2 - Re1 - N4, 95.7(4)°; C3 - Re1 - N4, 93.2(2)°; C1 - Re1 - C2, 87.8(2)°; C1 - Re1 - C3, 89.01(15)°; N1 - Re1 - N3, 86.1(2)°; N1 - Re1 - N4, 86.8(2)°.

The Re is six coordinated in the cationic complexes, being one of the triangular faces of the octahedron defined by three carbonyl ligands and another one by the nitrogen atoms of the pyrazolyl ligand. The Re–C and Re–N bond distances and angles can be considered unexceptional and are in the range found for other tricarbonyl complexes stabilized by ligands containing the tridentate **pyrazolyl-diamine** chelating unit.^{41b, c}

2.1.2.2 - Synthesis, Characterization and Biological Behavior of the ^{99m}Tc (I) Complexes Tc4 – Tc7

The ^{99m}Tc(I) complexes **Tc4 – Tc7** were prepared in high yield (> 92 %) by reacting the chelators **L4 – L7** ([L] = 10⁻³ – 10⁻⁴ M) with the aquo precursor *fac*-[^{99m}Tc(CO)₃(H₂O)₃]⁺ in aqueous solution at 100 °C for 30 – 45 min (**Scheme 2.2**). The precursor *fac*-[^{99m}Tc(CO)₃(H₂O)₃]⁺ was obtained quantitatively by addition of a Na[^{99m}TcO₄] solution to an IsoLink® Kit, and heating at 100 °C for 30 minutes. After cooling, the pH was adjusted (~7.4) with 1N HCl to destroy the remaining boranocarbonate. The radiochemical purity of the precursor was controlled by RP-HPLC (**Section 7.5.1**).

As the concentration of the ^{99m}Tc(I) complexes is very low (10⁻⁸ - 10⁻¹⁰ M), their chemical identification/characterization was made by comparing their RP-HPLC profiles with those of the corresponding Re(I) tricarbonyl complexes, which were synthesized and characterized at the macroscopic level (**Section 2.1.2.1**). In this way, we confirmed that the ^{99m}Tc(I) complexes corresponded to the expected compounds, which means they had the same structure as the rhenium congeners, being formulated as *fac*-[^{99m}Tc(CO)₃(κ³-L)]⁺ (L = **Tc4, L4**; L = **Tc5, L5**; L = **Tc6, L6**; L = **Tc7, L7**) (**Scheme 2.2**). As an example, we present in **Figure 2.5** the RP-HPLC profiles of the matched pair **Re5/Tc5**.

The small differences found in the retention times of the Re and respective ^{99m}Tc(I) complexes are assigned to the different detection modes of the complexes. For Re complexes a UV/vis detector is used and for ^{99m}Tc complexes a γ detector. These two detectors are connected in line, which justifies the small differences found in the retention times.

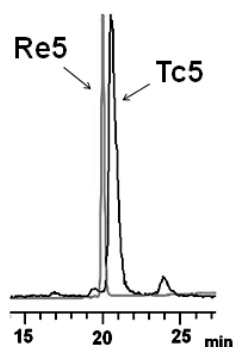


Figure 2.5: RP-HPLC traces of **Re5** (U.V. detection, 254 nm) and **Tc5** (γ detection).

2.1.2.2.1 - *in vitro* studies of the ^{99m}Tc (I) Complexes **Tc4 – Tc7**

The *in vitro* stability studies may help to partially predict the stability of the ^{99m}Tc(I) complexes *in vivo* towards reoxidation and/or transchelation of the metal by biological substrates. These biological substrates can be proteins, amino acids or other molecules present *in vivo*. Complexes **Tc4 – Tc7** were challenged in 1 mM solutions of strong coordinating amino acids such as cysteine or histidine. Briefly, 100 μ l of ^{99m}Tc(I) complexes solutions were incubated with 900 μ l of cysteine or histidine solutions at 37 °C. After 18 h incubation, aliquots of the solutions were collected and analyzed by RP-HPLC (**Section 7.6**). The results obtained have confirmed a high stability for the ^{99m}Tc complexes. In fact, no decomposition or reoxidation products were observed by RP-HPLC monitoring after incubation of the radioactive complexes.

The hydro(lipo)philic nature of the radiotracers can, to a certain extent, predict the biological profile of the ^{99m}Tc complexes (e.g. preferential pathway of elimination), although its real assessment can only be done *in vivo*. In this context, the lipophilicity ($\log P_{o/w}$) of **Tc4 – Tc7** was determined by the partition coefficient ($P_{o/w}$) in the biphasic system octanol/PBS (**Section 7.7**). The radiocomplexes **Tc4** and **Tc5** with pendant carboxylic acid groups presented a higher hydrophilic character (**Tc4**: -0.795 ± 0.017 , **Tc5**: -0.467 ± 0.071) than the free amine containing complexes **Tc6** and **Tc7** (**Tc6**, -0.366 ± 0.091 ; **Tc7**, 0.319 ± 0.009). As expected, the presence of longer alkyl chains enhanced the hydrophobic nature of the complexes, as can be concluded by comparing **Tc4** with **Tc5**, and **Tc6** with **Tc7**.

2.1.2.2.2 - *in vivo* Studies of the ^{99m}Tc (I) Complexes **Tc4 – Tc7**

The biological behavior of **Tc4 – Tc7** was studied in mice, to evaluate their pharmacokinetics and *in vivo* stability. In particular, we were interested in the evaluation of blood clearance, route of

elimination and preferential retention in some organs. In fact, the perfect radiopharmaceutical should be obtained in high yield and radiochemical purity and, after intravenous administration, should be rapidly excreted from the non-target organs, preferably by the kidneys, avoiding the hepatobiliary pathway. Moreover, the blood clearance must be fast enough to avoid long exposure to radiation, and slow enough to allow the radioactive compound to reach the target site.

Therefore, to access the potential of **L4 – L7** to be used as bifunctional chelators for the labeling of biomolecules, the biodistribution of **Tc4 – Tc7** was evaluated in CD-1 mice at 1 h, and 4 h after administration (**Section 7.8.1**). Tissue distribution data of these complexes were expressed as the percentage of injected dose (I.D.) per gram of organ, and the uptake and clearance from the organs can be overviewed in **Table 2.1** and **2.2**. For a better comparison of the excretion profiles of **Tc4 - Tc7**, the activity present in the liver, intestine and kidney (% I.D./g organ), as well as the total excretion (% I.D.) at 1 h and 4 h post-injection, are shown in **Figure 2.6**.

Table 2.1: Biodistribution (% I.D./g) and total excretion (% I.D.) for complexes **Tc4** and **Tc5** in CD-1 Charles River, 1 h and 4 h after intravenous administration.

| Organ | Tc4 | | Tc5 | |
|---------------------------------|---------------------|---------------------|---------------------|---------------------|
| | 1h | 4h | 1h | 4h |
| Blood | 1.10 ± 0.10 | 0.60 ± 0.10 | 0.50 ± 0.10 | 0.19 ± 0.09 |
| Liver | 5.00 ± 0.50 | 2.50 ± 0.20 | 9.80 ± 1.20 | 2.40 ± 0.40 |
| Intestine | 10.40 ± 1.90 | 9.90 ± 2.70 | 12.50 ± 2.50 | 15.70 ± 2.40 |
| Pancreas | 0,53 ± 0.04 | 0.50 ± 0.10 | 0.40 ± 0.20 | 0.34 ± 0.08 |
| Heart | 0.30 ± 0.20 | 0.28 ± 0.04 | 0.13 ± 0.03 | 0.06 ± 0.01 |
| Lung | 0.60 ± 0.10 | 0.33 ± 0.08 | 0.32 ± 0.04 | 0.15 ± 0.03 |
| Kidney | 5.00 ± 0.50 | 1.40 ± 0.20 | 8.50 ± 3.20 | 1.80 ± 0.40 |
| Muscle | 0.17 ± 0.02 | 0.10 ± 0.02 | 0.09 ± 0.02 | 0.03 ± 0.01 |
| Bone | 0.22 ± 0.03 | 0.12 ± 0.01 | 0.09 ± 0.02 | 0.04 ± 0.02 |
| Stomach | 1.60 ± 0.30 | 0.26 ± 0.01 | 0.70 ± 0.40 | 0.20 ± 0.10 |
| Total Excretion (% I.D.) | 50.10 ± 4.80 | 60.20 ± 4.80 | 31.30 ± 3.80 | 37.60 ± 5.50 |

Table 2.2: Biodistribution (% I.D./g) and total excretion (% I.D.) for complexes **Tc6** and **Tc7** in CD-1 Charles River, 1 h and 4 h after intravenous administration.

| Organ | Tc6 | | Tc7 | |
|---------------------------------|---------------------|---------------------|---------------------|---------------------|
| | 1h | 4h | 1h | 4h |
| Blood | 0.34 ± 0.05 | 0.13 ± 0.02 | 0.19 ± 0.01 | 0.12 ± 0.01 |
| Liver | 10.7 ± 1.80 | 10.80 ± 2.30 | 18.20 ± 2.80 | 16.50 ± 1.80 |
| Intestine | 9.60 ± 0.60 | 9.80 ± 1.60 | 7.00 ± 0.90 | 8.00 ± 1.00 |
| Pancreas | 0.30 ± 0.10 | 0.19 ± 0.06 | 2.30 ± 1.20 | 2.60 ± 0.80 |
| Heart | 0.18 ± 0.03 | 0.12 ± 0.01 | 1.14 ± 0.08 | 0.80 ± 0.30 |
| Lung | 0.30 ± 0.10 | 0.18 ± 0.06 | 0.30 ± 0.10 | 0.25 ± 0.02 |
| Kidney | 24.50 ± 1.70 | 19.80 ± 1.80 | 50.40 ± 6.70 | 46.20 ± 4.60 |
| Muscle | 0.08 ± 0.02 | 0.05 ± 0.01 | 0.14 ± 0.02 | 0.11 ± 0.02 |
| Bone | 0.08 ± 0.01 | 0.06 ± 0.03 | 0.17 ± 0.02 | 0.13 ± 0.01 |
| Stomach | 1.40 ± 0.40 | 1.10 ± 0.20 | 1.05 ± 0.06 | 0.40 ± 0.10 |
| Total Excretion (% I.D.) | 26.50 ± 9.50 | 33.90 ± 3.60 | 16.20 ± 0.80 | 25.50 ± 2.90 |

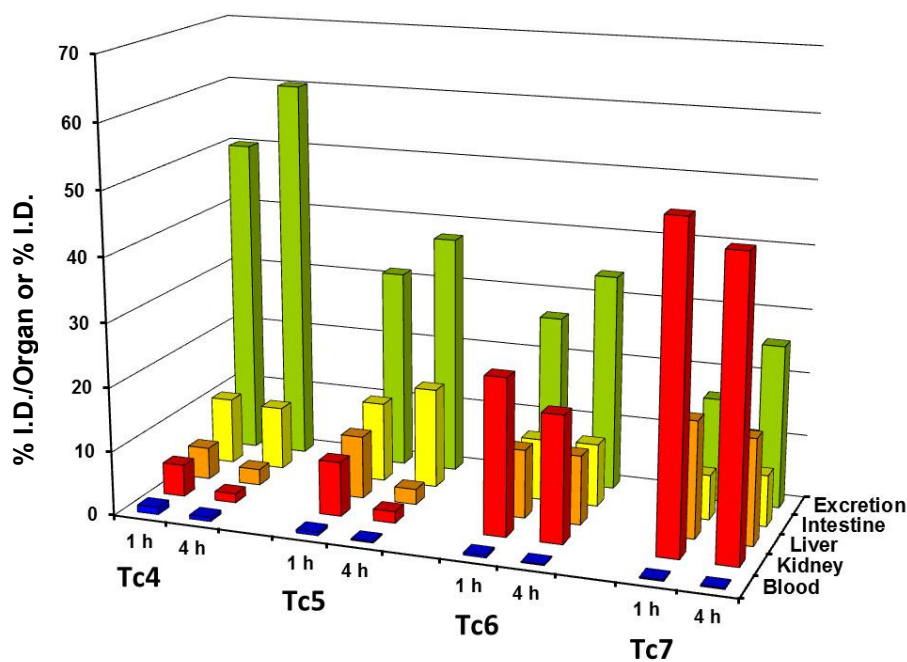


Figure 2.6: Biodistribution in the blood and excretory organs (% I.D./ g organ), and total excretion (% I.D.) for complexes **Tc4 – Tc7** in CD-1 Charles River mice, 1 h and 4 h after intravenous administration.

The main differences in the biodistribution profile of **Tc4** – **Tc7** complexes are related to the clearance from tissues as well as to the rate of overall excretion. No preferential uptake in the main organs or tissues was observed, except those involved in the excretory routes (liver, intestines and kidney). **Tc4** shows a faster clearance from the main organs, an enhanced overall excretion (**Tc4**: 60.20 ± 4.80 I.D.; **Tc5**, 37.60 ± 5.50 I.D.; **Tc6**, 33.90 ± 3.60 I.D.; **Tc7**, 25.50 ± 2.90 I.D.; 4 h p.i.), and a higher hepatobiliary clearance (**Tc4**, liver: 2.50 ± 0.20 I.D./ g organ, intestine: 9.80 ± 2.70 I.D./ g organ Vs **Tc5**, liver: 2.40 ± 0.40 I.D./ g organ, intestine: 16.50 ± 1.80 I.D./ g organ; **Tc6**, liver: 10.80 ± 2.30 I.D./ g organ, intestine: 9.80 ± 1.60 I.D./ g organ; **Tc7**, liver: 16.50 ± 1.80 I.D./ g organ, intestine: 8.00 ± 1.00 I.D./ g organ; 4 h p.i.). The presence of spacers with different alkyl chain lengths affects the *in vivo* behavior of the corresponding complexes independently of the terminal functional group. Indeed, a longer spacer led to a significant increase in the hepatobiliary uptake and a pronounced reduction of the total radioactivity excretion as concluded by comparing **Tc5** with **Tc4**, and **Tc7** with **Tc6**. This effect is most likely due to the increase of the lipophilic character of the $^{99m}\text{Tc}(\text{CO})_3$ complexes stabilized by ligands bearing hexyl chains.

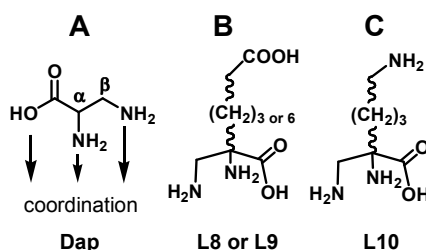
There was no significant uptake in the stomach, indicating a high stability of the complexes to reoxidation. In the case of **Tc6** and **Tc7** it was observed a higher retention of radioactivity in the kidneys over time, which should be related with the electrostatic interaction between the positive charge of the $-\text{NH}_3^+$ group and the negatively charged surface of the proximal tubule cells.¹³⁸

To verify the *in vivo* stability of **Tc4** – **Tc7**, serum and urine samples were analyzed by radiometric HPLC (Section 7.8.2). The murine serum, isolated from blood collected 1h after administration of the complexes, was treated with ethanol to precipitate the proteins. Analysis of the supernatant by RP-HPLC showed no pertechnetate or other decomposition products, being complexes **Tc4** – **Tc7** the only species present. The urine collected at 1 h post injection also did not show any metabolites, demonstrating the *in vivo* stability of the complexes.

In summary, the results have shown that complexes **Tc4** and **Tc5** presented the most favorable *in vivo* biological behavior, with rapid blood clearance, no radioactivity accumulation in any major organ except those involved in the excretory route (liver and intestines), and high/moderate total excretion. These features suggest that **Tc4** and **Tc5** are more appropriate to be used as BFC for labeling biomolecules.

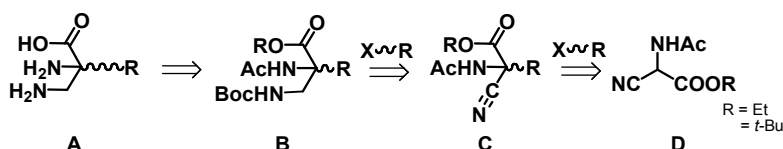
2.2 – Dap-based BFCs and their Re(I)/^{99m}Tc(I) Complexes

We have also studied a family of BFCs with a diamino propionic (Dap) chelating unit (**Scheme 2.3, A**). These chelators are supposed to be tripod ligands with very low molecular weight, hydrophilic character and superior coordinating properties towards the *fac*-[M(CO)₃]⁺ moiety (M = Re, ^{99m}Tc).¹³⁹ In a close collaboration with Prof. Alberto's group, we synthesized novel **Dap**-based bifunctional chelators containing a propyl or a hexyl linker, and a carboxylic acid group (**L8** and **L9**) or a free primary amine (**L10**) (**Scheme 2.3, B and C**).



Scheme 2.3: Dap-based bifunctional chelators.

With the scope of subjecting **L8** – **L10** to derivatization of biomolecules, the conjugating functions need be unprotected but the **Dap** unit should be protected. A retro-synthetic analysis revealed that derivatization at the α carbon of the **Dap** ligand is best achieved by starting from the commercially available precursor **D** (**Scheme 2.4**).¹³⁹



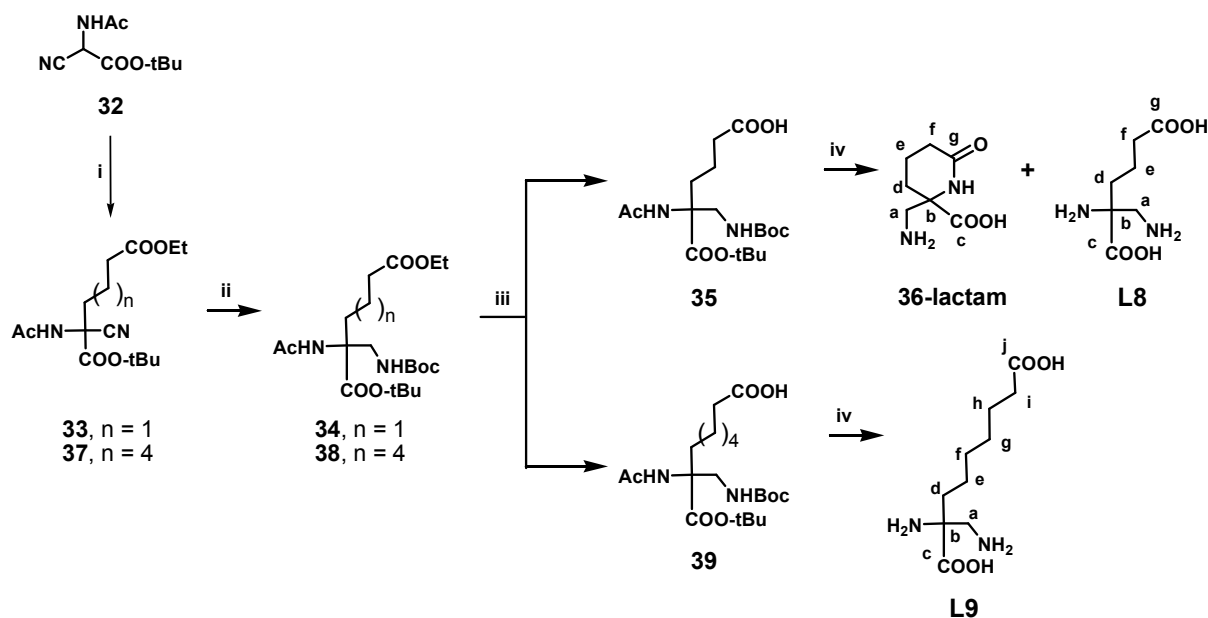
Scheme 2.4: Retro-synthetic analysis of the target **Dap**-containing chelators.

The key step in the retro-synthetic analysis is the functional group interconversion step, involving the reduction of the nitrile group (-CN) to the amine group (-CH₂NH₂). Although there are many catalysts for this conversion, it was important to find a selective one which did not interfere with the other functional groups of the molecule (ethyl ester and acetamide; **Scheme 2.4 C**).¹³⁹ The mild reducing agent NaBH₄ does not reduce CN groups at room temperature.¹⁴⁰ However, Alberto and coworkers have demonstrated that the use of NaBH₄ and NiCl₂, combined with Boc₂O for *in situ* protection of the reduced amine, allowed the preparation of the fully protected **Dap** chelators (**Scheme 2.4 B**).¹³⁹⁻¹⁴⁰

In the following section the synthetic strategy applied to the synthesis of **L8** – **L10** will be described in detail. Full characterization of the **Dap** bifunctional chelators, including X-ray structures of intermediates, their reactions with “ $\text{Re}(\text{CO})_3$ ”, as well as labeling studies with “ $^{99\text{m}}\text{Tc}(\text{CO})_3$ ”, will be also presented in **Sections 2.2.1**, **2.2.2.1** and **2.2.2.2**. In **Sections 2.2.2.2.1** and **2.2.2.2.2** is presented the *in vitro* and *in vivo* behavior of the **Dap**^{99m}Tc complexes.

2.2.1 - Synthesis of the Dap BFCs **L8** – **L10**

The synthetic strategy applied for the preparation of the **Dap**-based chelators **L8** – **L10** is described in **Schemes 2.5** and **2.6**. The synthesis of **L8** and **L9**, which have a propyl or a hexyl spacer between the **Dap** chelating backbone and the CO_2H group, respectively, is shown in **Scheme 2.5**. The precursor **32** has been synthesized following a multistep procedure already described in the literature and presented in the experimental part (**Section 7.3.11**).¹⁴¹ The preparation of the intermediate **33** by alkylation of **32** with ethyl-4-bromobutyrate in the presence of NaOEt/EtOH was unsuccessful due to a transesterification reaction (*-tert* butyl by a *-ethyl* group). The compound could only be obtained in moderate yields using NaH in DMF (**Scheme 2.5**). Subsequent reduction of **33** with $\text{NaBH}_4/\text{NiCl}_2$ in the presence of Boc_2O gave **34** in almost quantitative yield.



Scheme 2.5: Synthesis of **L8** and **L9**. *Reagents and conditions:* i) NaH , ethyl-4-bromobutyrate or ethyl-7-bromoheptanoate, DMF, reflux, 54.1 % for **33** and 24 % for **37**; ii) 1) NaBH_4 , NiCl_2 , Boc_2O , MeOH, r.t. 2) diethylenetriamine, r.t., 97.0 % for **34** and 55.0 % for **38**; iii) MeOH/ NaOH 2M, r.t., 67.9 % for **35** and 58.1 % for **39**; iv) HCl 4M, reflux, 30.0 % for **L8** and 84.7 % for **L9** (*identification system for NMR assignments is displayed for 36-lactam, L8 and L9 as an example*).

Sequential hydrolysis of the ethyl ester and deprotection of the **Dap** unit in **34** gave **35**, and finally the desired product **L8**. Compound **L8** was not obtained in a pure form. Indeed, it was always contaminated with a second species formulated as a lactam (**36-lactam**). Based on ¹H-NMR spectroscopy, compounds **L8** and **36-lactam** were obtained in 60 % and 40 % yield, respectively. All attempts to minimize the formation of the undesired **36-lactam** were unsuccessful. At higher pH, compound **L8** was quantitatively converted to **36-lactam**. The identification of **36-lactam** and **L8** in the reaction mixture was based on NMR spectroscopy. In fact, 1D and 2D ¹H- and ¹³C-NMR experiments at different pH values allowed a complete assignment of the resonances due to both species. For illustration, **Figure 2.7** shows the ¹H-NMR spectra of a mixture of **36-lactam** and **L8** immediately after BOC deprotection, at pH 1.4 (**Figure 2.7, A**). The same mixture at pH 4.3 (**Figure 2.7, B**) shows an almost complete lactamisation of **L8** → **36-lactam**. The main differences in the ¹H-NMR spectra of **36-lactam** and **L8** are related to the splitting and/or chemical shifts of H^a and H^d protons. In **L8**, the H₂^a protons appear as a sharp singlet at δ 3.17, while in **36-lactam** these protons appear as a quartet centered at δ 3.03. The H₂^d protons in **36-lactam** become diastereotopic due to the rigidity imposed by cyclization. Accordingly, two resonances at δ 2.00 and δ 1.60 appeared, each integrating for one proton. In the ¹³C-NMR spectra of **36-lactam** and **L8** no relevant differences were observed. The assumed structure of **36-lactam** was confirmed by X-ray diffraction analysis since adequate single crystals could be obtained after recrystallization of the lactam from a CH₂Cl₂–EtOH solution. **Figure 2.8** shows an ORTEP diagram of **36-lactam**, confirming its lactam authenticity. The ESI-MS of the mixture **36-lactam** + **L8** presented two main peaks at m/z values which agree with the expected values for **36-lactam** ([M + H]⁺, 172.9) and **L8** ([M + H]⁺, 191.0).

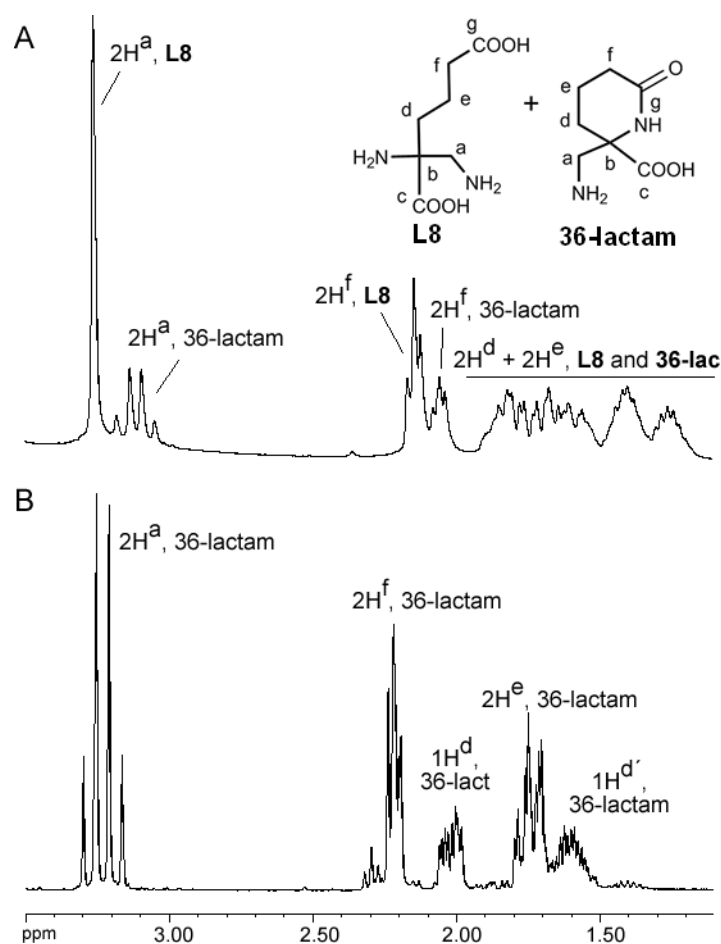


Figure 2.7: ^1H -NMR spectra (D_2O) of the mixture **36-lactam** + **L8** at pH 1.4 (A) and 4.3 (B).

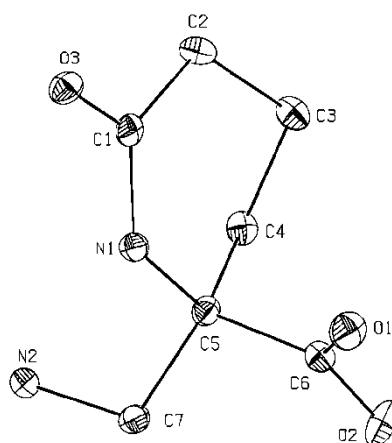
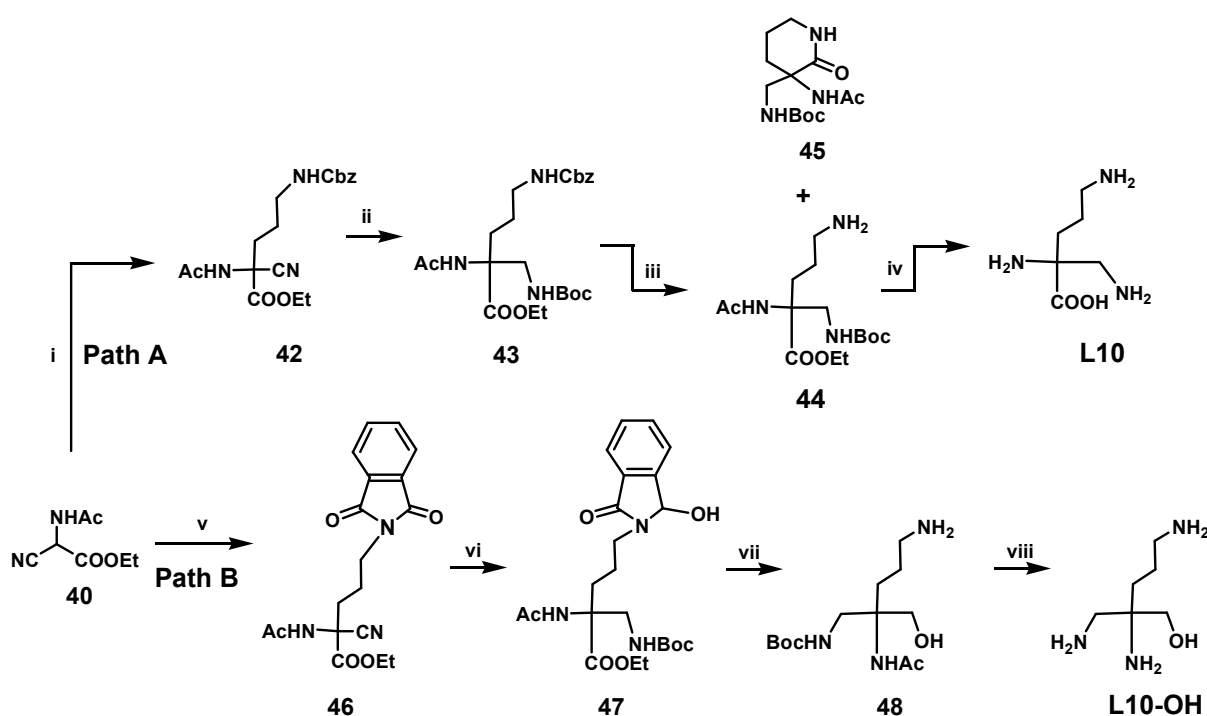


Figure 2.8: ORTEP drawing of **36-lactam** in 50 % probability (H atoms were omitted for clarity). Selected bond lengths (\AA) and angles (deg): C5 - N1, 1.465(2) \AA ; C5 - C4, 1.536(2) \AA ; C5 - C7, 1.544(2) \AA ; C5 - C6, 1.553(2) \AA ; N1 - C5 - C4, 110.10(12) $^\circ$; C7 - C5 - C6, 107.83(12) $^\circ$.

The bifunctional ligand with the 6 carbon linker **L9** was prepared in a straightforward way using a procedure similar to the one described for the synthesis of **L8** (Scheme 2.5). It is worth to

mention that in this particular case the lactam species was not observed, suggesting that the formation of the six membered β -lactam ring (**36-lactam**), is more favored than the formation of a nine membered β -lactam. The ¹H-NMR spectrum of **L9** can be found in **Figure 8.1** (Annexes).

In the case of **L10**, which contains a primary amine group, the synthesis starts from precursor **40** (**Scheme 2.6, Path A**), which was synthesized following a procedure similar to the one described for **32** (**Scheme 2.5**). Deprotonation of the α C–H in **40** with NaOEt and subsequent reaction with benzyl-*N*-(3-bromopropyl)carbamate (**41**), prepared by bromination of benzyl-*N*-(3-hydroxypropyl)carbamate with CBr₄ and PPh₃, gave **42** in moderate yield.



Scheme 2.6: Synthesis of **L10**. *Reagents and conditions:* **Path A:** i) NaOEt, benzyl-*N*-(3-bromopropyl)carbamate (**41**), EtOH, reflux, overnight, 39.4 %; ii) 1) NaBH₄, NiCl₂, Boc₂O, MeOH, r.t., overnight 2) diethylenetriamine, r.t., 1 h, 40.3 %; iii) H₂, Pd/C, EtOH, r.t., 22 h, 89.9 %; iv) HCl 4M, reflux, overnight, 92.4 %. **Path B:** v) NaOEt, 3-bromo-propylphthalimide, EtOH, reflux, overnight, 38.5 %; vi) 1) NaBH₄, NiCl₂, Boc₂O, MeOH, r.t., overnight 2) diethylenetriamine, r.t., 1 h, 97.0 %; vii) 1) NaBH₄/isopropanol/H₂O, r.t., 24 h 2) AcOH, 80 °C, 24 h, 39.9 %; viii) HCl 4M, reflux, overnight, 70.0 %.

Reduction of the –CN group in **42** to –CH₂NH₂, and *in situ* protection with Boc₂O, allowed the preparation of compound **43**. Deprotection of the *N*-benzyloxycarbonyl (Cbz) group in **43** to give **44** was accomplished almost quantitatively by catalytic hydrogenation using an optimized amount of catalyst (Pd/C, Pd content 10%). When a large excess of Pd/C catalyst was used, compound **44** was

always obtained in a lower yield (51.4 %) due to the formation of a side product, formulated as **45** (18.7 % yield). The compounds were isolated and characterized independently by multinuclear NMR spectroscopy, ESI-MS and X-ray diffraction analysis in the case of **45** (Figure 2.9). The formation of **45** was due to *in situ* cyclization, which resulted from the reaction of the terminal amine with the ethyl ester. Compound **L10** was obtained in good yield after full deprotection of **44** under acidic conditions (Scheme 2.6).

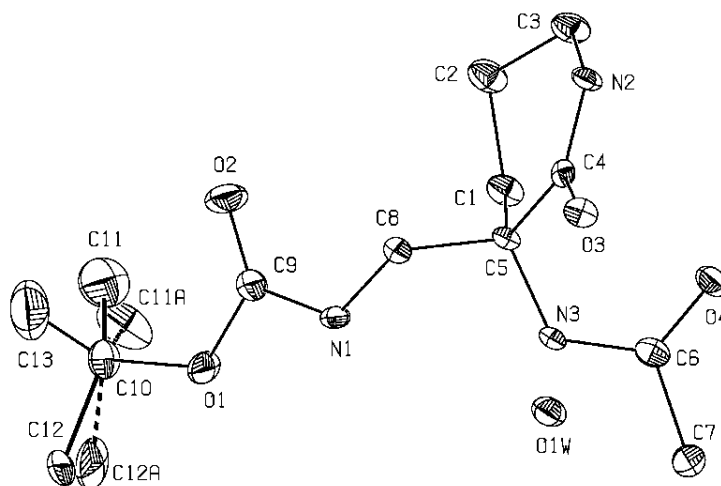


Figure 2.9: ORTEP drawing of compounds **45** in 50% probability (H atoms were omitted for clarity). Selected bond lengths (Å) and angles (deg): C5 - C1, 1.528(4) Å; C5 - C4, 1.545(4) Å; C5 - C8, 1.550(5) Å; C5 - N3, 1.453(4) Å; C1 - C5 - C4, 112.91(10)°; N3 - C5 - C8, 107.50(11)°.

Compound **L10** was characterized by IR and multinuclear NMR spectroscopy (^1H , ^{13}C), ESI-MS and elemental analysis. To assign the ^1H - and ^{13}C -NMR resonances, 2D experiments, ^1H - ^1H g-COSY and ^1H - ^{13}C g-HSQC, were performed. As an illustrative example, in **Figure 2.10** are presented the fully assigned ^1H - and ^{13}C -NMR spectra of **L10** in D_2O .

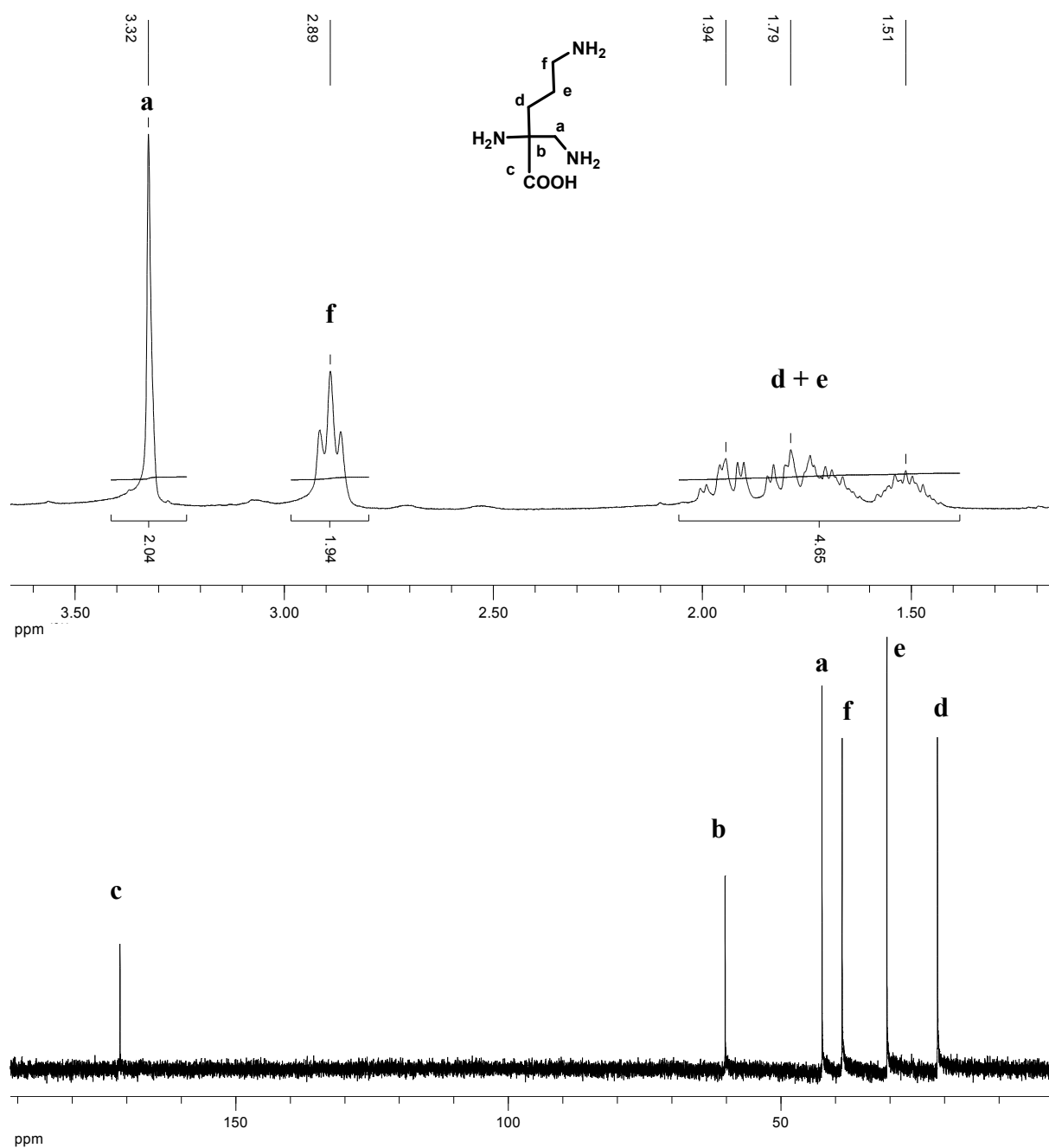


Figure 2.10: 1H -NMR (top) and ^{13}C -NMR spectra (bottom) of **L10** in D_2O .

Alternatively, we have also tried to prepare **L10** following the synthetic strategy shown in **Scheme 2.6, Path B**, where the amine was protected with a phthalimide group instead of Cbz. Upon reaction of precursor **40** with 3-bromo-propylphthalimide and subsequent reduction with $NaBH_4/NiCl_2$ in the presence of Boc_2O , the intermediate **47** was obtained. The phthalimide deprotection step in **47** was a critical step. Indeed, attempts to remove this protecting group with hydrazine hydrate were unsuccessful (different solvents and temperatures were tried). This failure was likely due to the partial opening of the phthalimide in the presence of $NaBH_4/NiCl_2$ (confirmed by ESI-MS). The use of another protocol proved to be useful for deprotection of the phthalimide.

Treatment of **47** with NaBH_4 /isopropanol/ H_2O , and then acetic acid at 80°C , yielded the deprotected amine.¹⁴² However, under those conditions the $-\text{COOEt}$ group of **47** was also reduced to $-\text{CH}_2\text{OH}$, giving compound **48**. When the acetamide and Boc protecting groups were removed with HCl the product obtained was **L10-OH**. NMR and IR spectroscopy and ESI-MS spectrometry confirmed the hypothesized reduction of the carboxylic group. The fully assigned ^1H -NMR spectrum of **L10-OH** is shown in **Figure 2.11**.

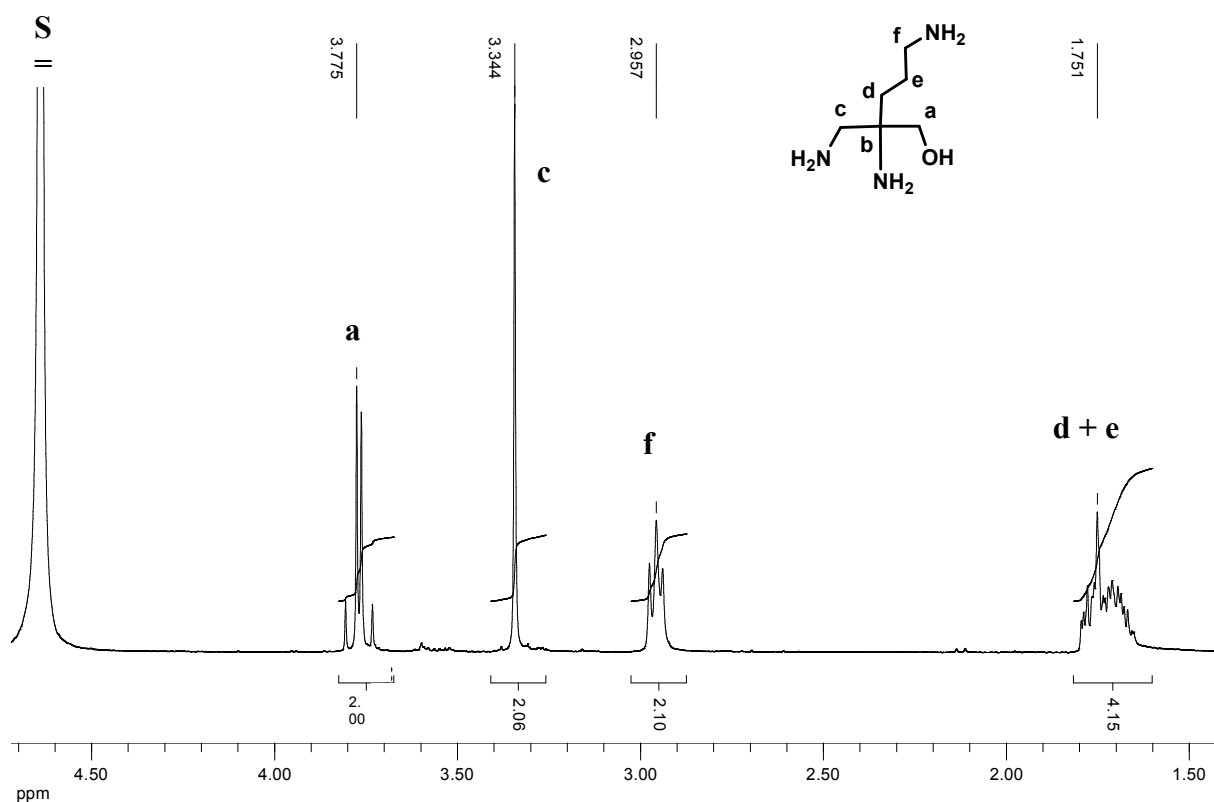


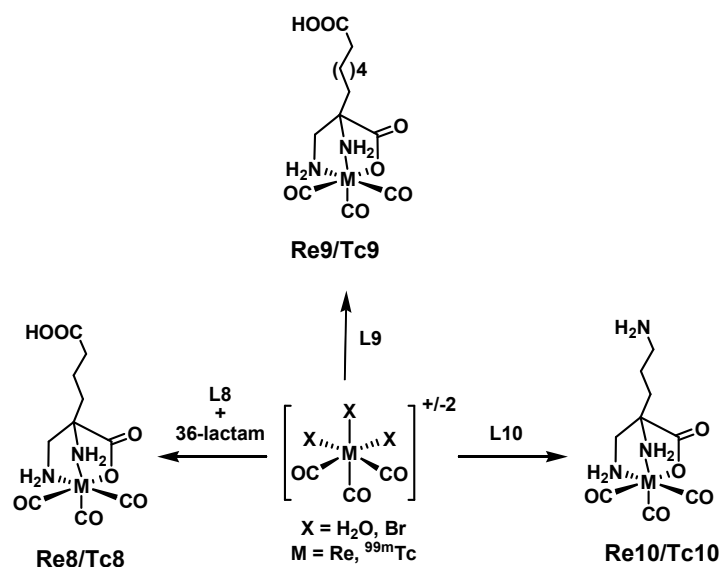
Figure 2.11: ^1H -NMR spectrum of **L10-OH** in D_2O (S = residual water).

The main differences observed in the ^1H -NMR spectra of **L10** and **L10-OH** are related to the additional resonance observed for **L10-OH**, a doublet of doublets at $\delta \sim 3.7$ ppm, which is assigned to the methylenic protons close to the OH group. The identity of **L10-OH** was also confirmed by ^{13}C -NMR (disappearance of the peak assigned to the CO_2H group, δ 171.2) and by IR spectroscopy (loss of the strong absorptions in the range 1619 to 1606 cm^{-1} due to the carbonyl stretching vibrations).

2.2.2 - Reactions of L8 – L10 with *fac*-[M(CO)₃]⁺ Precursors (M = Re or ^{99m}Tc)

2.2.2.1 - Synthesis and Characterization of the Re (I) Complexes Re8 – Re10

The BFCs **L8** - **L10** reacted with equimolar amounts of the precursors *fac*-[Re(CO)₃(H₂O)₃]⁺ or *fac*-[Re(CO)₃(Br)₃]⁻², in refluxing water for 18 h, yielding complexes of the type *fac*-[Re(CO)₃(κ³-L)]⁺ (**Re8**, L = **L8**; **Re9**, L = **L9**; **Re10**, L = **L10**) in moderate yields (**Scheme 2.2**).



Scheme 2.7: Reaction pathways to Re(I) complexes with the tripod ligands **L8** – **L10**.

The reaction of *fac*-[Re(CO)₃Br₃]⁻² with a mixture of **L8** + **36-lactam** overnight at pH ~ 4 gave a white precipitate. After washing with water and CH₂Cl₂, the solid obtained was dried under vacuum. Based on multinuclear NMR and IR spectroscopy, X-ray diffraction analysis and ESI-MS the compound obtained was formulated as *fac*-[Re(CO)₃(κ³-**L8**)] (**Re8**). After precipitation of **Re8** from the reaction mixture, HPLC analysis of the supernatant still revealed small amounts of dissolved **Re8** (R_t = 9.9 min), unreacted *fac*-[Re(CO)₃Br₃]⁻² precursor (R_t = 6.5 min) and the **36-lactam** (R_t = 5.5 min). To force the reaction to completion, the pH of the solution was increased to 8 and the mixture refluxed overnight. After this time, HPLC analysis of the solution indicated that all Re(I) precursor *fac*-[Re(CO)₃Br₃]⁻² had been consumed and a new species (R_t = 13.2 min) was formed, which could be isolated by RP-HPLC. Based on multinuclear NMR and IR spectroscopy, and ESI-MS this complex was tentatively formulated as "*fac*-[Re(CO)₃(**36-lactam**)]". The spectroscopic data of this second species can be found in **Figure 8.2** (Annexes).

Reaction of **L9** and **L10** with $fac\text{-}[\text{Re}(\text{CO})_3(\text{H}_2\text{O})_3]^+$ in refluxing water afforded in a straightforward way the rhenium complexes $fac\text{-}[\text{Re}(\text{CO})_3(\kappa^3\text{-L9})]$ (**Re9**) and $fac\text{-}[\text{Re}(\text{CO})_3(\kappa^3\text{-L10})]$ (**Re9**), which were purified by semi-preparative RP-HPLC (**Scheme 2.7**).

Complexes **Re8** - **Re10** are soluble in water and in most common polar organic solvents. These complexes are also stable towards air oxidation, and their characterization involved the usual spectroscopic techniques (IR and NMR spectroscopy), ESI-MS, elemental analysis and X-ray diffraction analysis in the case of **Re8**.

The IR spectrum confirmed the *facial* arrangement of the carbonyl groups in the complexes ($2028 - 1906 \text{ cm}^{-1}$). The ESI-MS spectra showed dominant single peaks with the expected isotopic pattern and correct m/z values (**Re8**, $[\text{M}+\text{Na}]^+ = 482.9 \text{ m/z}$; **Re10**, $[\text{M}+\text{H}]^+ = 431.8 \text{ m/z}$).

The NMR (^1H and ^{13}C) and IR data obtained for **Re9** and **Re10** are compatible with the tridentate coordination mode of **L9** and **L10** and compare well with the results found for **Re8**, which was characterized both in the solid state and in solution. **Figure 2.12** displays the molecular structure of **Re8**, as well as selected bond lengths and angles. In this neutral compound, the Re is six coordinated, being one of the triangular faces of the octahedron defined by three carbonyl ligands and the other one by the *N,N,O* donor atom set of the **Dap** unit.

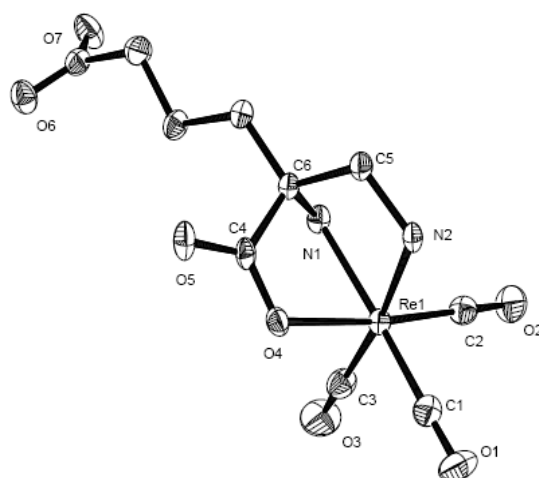


Figure 2.12: ORTEP view of complex **Re8**; thermal ellipsoids are drawn at the 40 % probability level. Selected bond lengths (Å) and angles (deg): Re1-C1, 1.915(3) Å; Re1-C2, 1.906(3) Å; Re1-C3, 1.914(3) Å; Re1-N1, 2.218(2) Å; Re1-N2, 2.206(2) Å; Re1-O4: 2.154(2) Å; C1-Re1-N1, 168.48(10)°; C3-Re1-N2, 172.90(11)°; C2-Re1-N1, 100.11(12)°; C1-Re1-O4, 96.25(11)°; C3-Re1-C1, 89.67(14)°; C3-Re1-C2, 87.28(14)°; O4-Re1-N1, 74.32(8)°; N2-Re1-N1, 76.49(9)°; O4-Re1-N2, 77.96(8)°.

The ^1H -NMR spectra of **Re8**, **Re9** and **Re10** (D_2O or CD_3OD) were very similar. The most interesting features are four broad multiplets in the range δ 5.32 – 4.31, integrating for 1 H each

(assigned to the diastereotopic protons of the coordinated NH₂ groups), and two other resonances, integrating for 1 H each due to the CH₂^a protons, which became diastereotopic upon coordination of the **Dap** derivatives to the metal (**Re8**, δ 2.76 and 2.59, **Re9**; δ 2.66 and 2.47; **Re10**, δ 2.79 and 2.51). Together with the ¹³C-NMR spectra, these data are consistent with a tridentate coordination of the chelators in **Re8** – **Re10**. This has been confirmed by X-ray diffraction analysis of crystals of **Re8** as previously described. As an example, in **Figure 2.13** is presented the fully assigned ¹H-NMR spectrum of **Re8**.

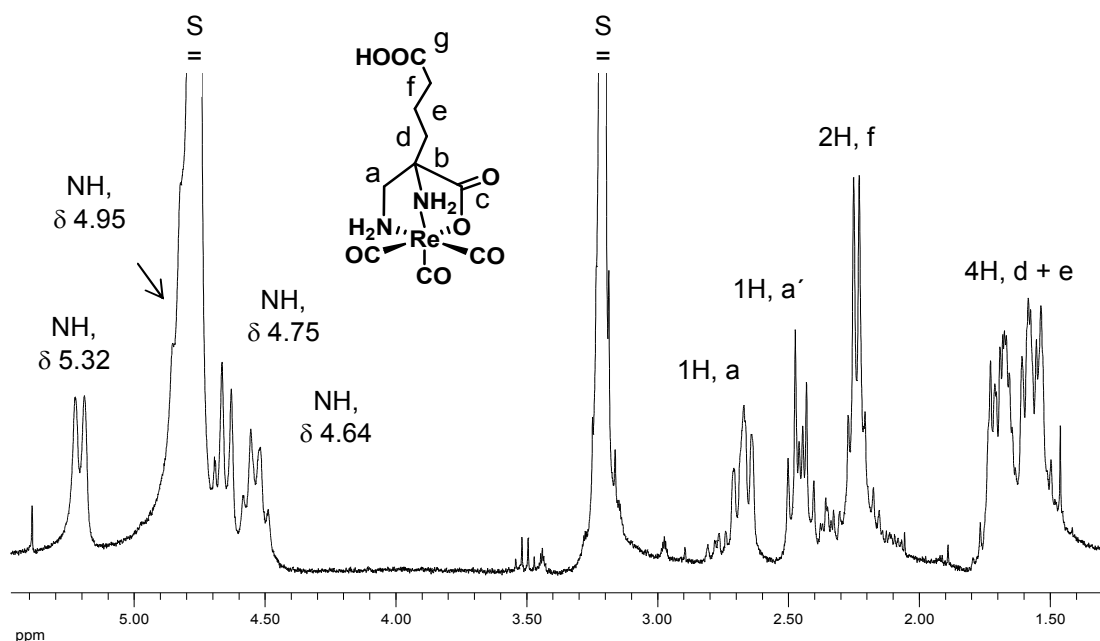


Figure 2.13: ¹H-NMR spectrum of the crystals of **Re8** in CD₃OD (S = residual solvent).

The lack of known Re(I) complexes stabilized by tridentate ligands with a *N,N,OH* donor atom set encouraged us to attempt the preparation of the rhenium complex *fac*-[Re(CO)₃(**L10-OH**)] (**Re10-OH**) by reaction of **L10-OH** with *fac*-[Re(CO)₃(H₂O)₃]⁺, at neutral pH, in refluxing water for 18 h.¹⁴³ After appropriate work-up (**Section 7.4.8**) **Re10-OH** was obtained as a colorless oil that is air and water stable and soluble in methanol and water. The characterization of **Re10-OH** involved the usual analytical techniques (IR, ESI-MS, ¹H-NMR, ¹³C-NMR and 2D-NMR experiences). Based on these data we tentatively assigned a structure to **Re10-OH** similar to **Re8** – **Re10**. In **Figure 2.14** we present the ¹H-NMR, ¹³C-NMR and ESI-MS spectra of **Re10-OH**. The ESI-MS spectrum shows a peak at *m/z* = 418.0 with the expected isotopic pattern for the Re metal.

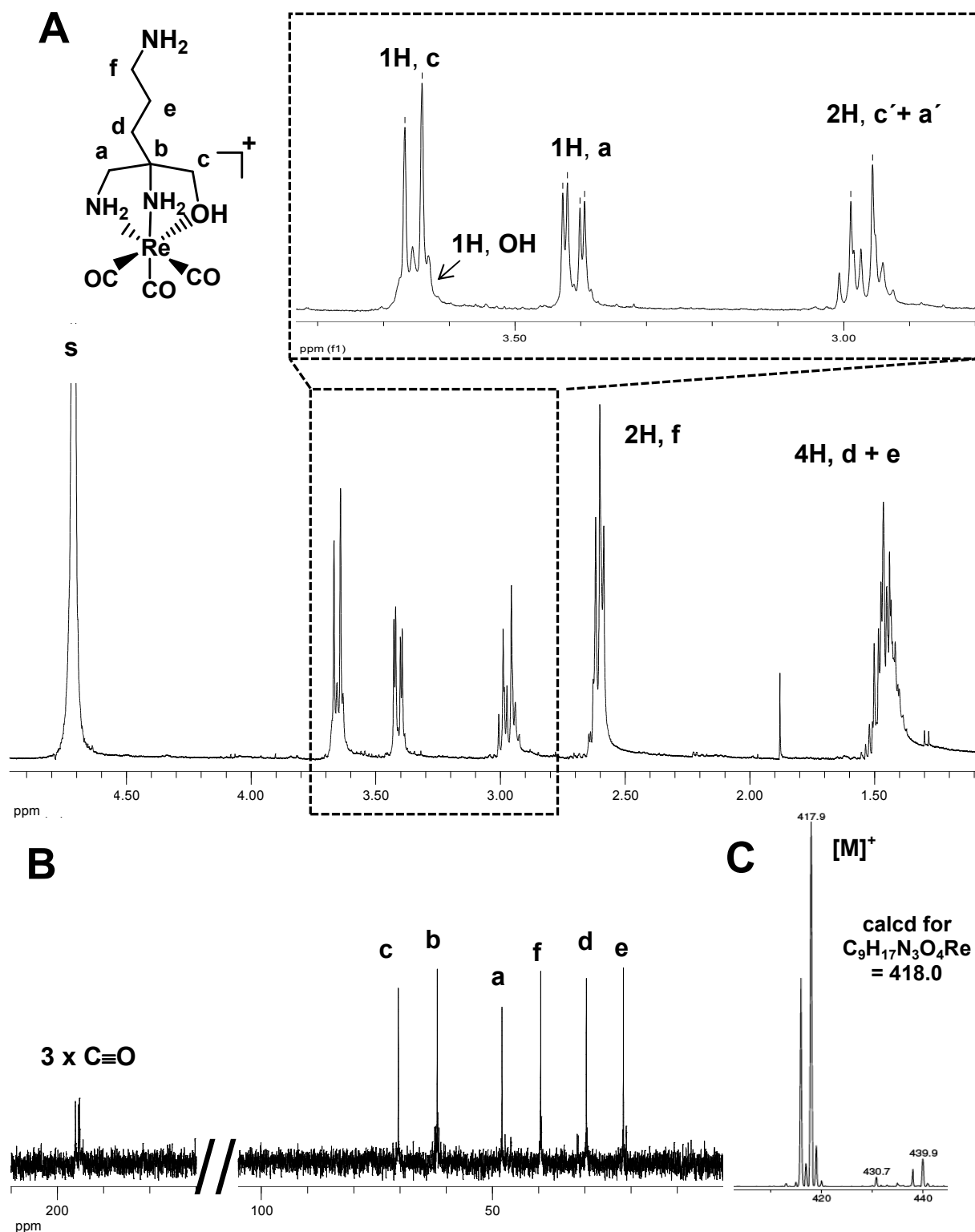


Figure 2.14: A) ^1H -NMR (D_2O), B) ^{13}C -NMR (D_2O) and C) ESI-MS (+) spectra of $[\text{Re}(\text{CO})_3(\text{L10-OH})]^+$ (Re10-OH).

The IR spectrum supports the presence of the CO groups due to the presence of two intense bands at 2028 cm^{-1} and 1906 cm^{-1} assigned to the carbonyls stretching vibration.

As no X-ray structure was obtained for this complex, the ¹H-, ¹³C- and 2D-NMR studies were essential for its tentative structural characterization (**Figure 2.14 A**). We have considered that **L10-OH** coordinates to the metal through the primary amines and the alcohol groups. As shown previously in the ¹H-NMR spectrum of the free ligand **L10-OH** (**Figure 2.11**), the methylenic protons of the **Dap-OH** unit appeared as a doublet of doublets and a singlet centered at δ 3.77 and δ 3.34, respectively. Each of these resonances, upon coordination to “Re(CO)₃”, splits into two multiplets centered at δ 3.67, δ 3.42, δ 2.97 and δ 2.95, integrating for 1 H each (**Figure 2.14, A**). Besides the splitting observed for the methylenic protons of the **Dap-OH** unit, we also observed the presence of a multiplet centered at δ 3.67, integrating for 1 H, attributed to the *coordinated* OH group. Although the resonances of the protons of the Re(I)-coordinated amines are not observed in the ¹H-NMR spectrum, analysis of the ¹H–¹H COSY spectrum revealed the presence of, at least, two resonances attributed to the NH₂ protons of the NH₂CH₂- arm, under the strong signal of the water solvent. ¹H-NMR analysis of **Re10-OH** performed in DMSO-d⁶ confirmed the presence of four resonances attributed to the diastereotopic protons of the NH₂ groups, suggesting the coordination to the “Re(CO)₃” core. The ¹³C-NMR spectrum of **Re10-OH** presents the expected resonances including three resonances at δ 196.0, δ 195.4 and δ 195.2 assigned to the carbon atoms of the CO ligands (**Figure 2.14, B**).

Brought together, the collected data suggest the formation of a complex where the metal is stabilized by the tridentate **DapOH** unit through the *N,N,OH* donor atom set. Nevertheless, we do not exclude the possibility of ambiguous coordination, with the OH-containing arm changing from coordinated to uncoordinated, through a fast dynamic process. Since a complete elucidation of the structure of **Re10-OH** is still missing, further efforts to obtain single crystals of **Re10-OH** for X-ray structural analysis, as well as variable temperature NMR studies are envisaged.

2.2.2.2 - Synthesis, Characterization and Biological Behavior of the ^{99m}Tc (I) Complexes Tc8 – Tc10

The compounds **L8**, **L9** and **L10** ([L] = 1 x 10⁻⁴ - 8 x 10⁻⁵ M) reacted with the aquo complex *fac*-[^{99m}Tc(CO)₃(H₂O)₃]⁺ (75 – 100 °C; 30 - 45 min) giving the complexes **Tc8** – **Tc10** in almost quantitative yield (**Table 8.3**, Annexes). It is worth mentioning that the reaction of a mixture of **36-lactam** + **L8** with *fac*-[^{99m}Tc(CO)₃(H₂O)₃]⁺ gave only *fac*-[^{99m}Tc(CO)₃(κ^3 -**L8**)], most probably due to kinetic reasons. Incubation of *fac*-[^{99m}Tc(CO)₃(κ^3 -**L8**)] with a large excess of pure **36-lactam** (100 X, 2 h at 100 °C) revealed the high stability of **Tc8** since no transchelation could be observed. Interestingly, when the pure complex “*fac*-[^{99m}Tc(CO)₃(**36-lactam**)]” was incubated with a large excess of pure **Dap**

amino acid (100 X, 2 h at 100 °C), transchelation occurred with formation of “ $fac-[^{99m}\text{Tc}(\text{CO})_3(\text{Dap})]$ ” in ca. 70% radiochemical yield.

Tc10 is very hydrophilic and is eluted, using the standard gradient 0.1 % TFA/MeOH, with the same retention time as the precursor $fac-[^{99m}\text{Tc}(\text{CO})_3(\text{H}_2\text{O})_3]^+$. Owing to this behavior a different gradient was required in order to differentiate between the two complexes. This was achieved by using $\text{Et}_3\text{N}/\text{CH}_3\text{COOH}$ [2.1 : 2.8 (v/v)]/MeOH as eluent (**Figure 2.15**). The chemical identity of **Tc8** – **Tc10** was ascertained by comparing their HPLC γ traces with the corresponding Uv/Vis HPLC traces of the Re congeners.

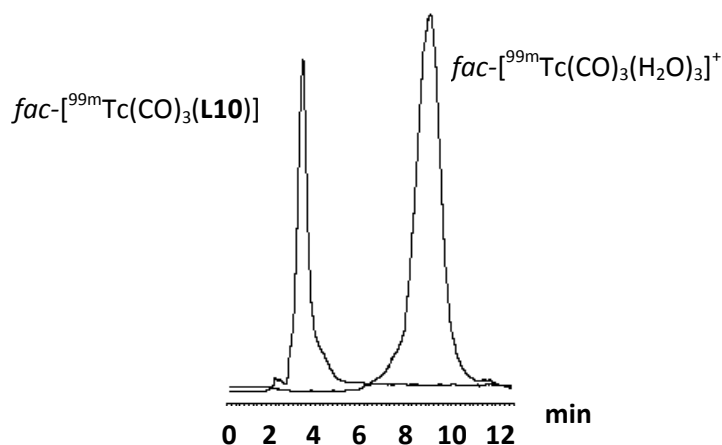


Figure 2.15: RP-HPLC radioactive traces of $fac-[^{99m}\text{Tc}(\text{CO})_3(\kappa^3\text{-L10})]$ and $fac-[^{99m}\text{Tc}(\text{CO})_3(\text{H}_2\text{O})_3]^+$ obtained using a gradient with $\text{Et}_3\text{N}/\text{CH}_3\text{COOH}$ [2.1:2.8 (v/v)] and MeOH.

2.2.2.2.1 - *In vitro* Studies of the ^{99m}Tc (I) Complexes **Tc8** – **Tc10**

To ascertain the *in vitro* stability of the organometallic $^{99m}\text{Tc}(\text{I})$ complexes stabilized by the **Dap** unit, **Tc8** – **Tc10** were incubated with a large excess of cysteine or histidine (37 °C for 18 h) as described in **Section 7.6**. These complexes presented high stability, since no decomposition or reoxidation to $[^{99m}\text{TcO}_4]^-$ was observed by RP-HPLC analysis.

As mentioned before, although there are many factors that can affect the *in vivo* biological behavior of a ^{99m}Tc complex, the lipophilicity is a physico-chemical characteristic that can affect the biodistribution profile, mainly the route of elimination. The lipophilicity of **Tc8** and **Tc10** was evaluated by determination of the partition coefficient in a n-octanol/PBS solution, as described in the experimental part (**Section 7.7**). The $\log P_{o/w}$ were determined to be -2.006 ± 0.030 and -1.025 ± 0.022 for **Tc8** and **Tc10**, respectively, indicating that these complexes have a more hydrophilic character than the similar complexes **Tc4** (-0.795 ± 0.017) and **Tc6** (-0.366 ± 0.091) stabilized with the pyrazolyl-diamine chelating unit.

2.2.2.2.2 - *In vivo* Studies of the ^{99m}Tc (I) Complexes **Tc8** and **Tc10**

The biodistribution of **Tc8** and **Tc10** was examined in CD-1 mice, 1 h and 4 h post-injection (Section 7.8.1), and the data are summarized in Table 2.3 and Figure 2.16.

Table 2.3: Biodistribution (%I.D./g organ) and total excretion (% I.D.) for complexes **Tc8** and **Tc10** in CD-1 Charles River, 1 h and 4 h after intravenous administration.

| Organ | Tc8 | | Tc10 | |
|---------------------------|-------------------|-------------------|-------------------|-------------------|
| | 1h | 4h | 1h | 4h |
| Blood | 3.1 ± 0.3 | 0.98 ± 0.24 | 0.4 ± 0.1 | 0.2 ± 0.1 |
| Liver | 1.2 ± 0.2 | 0.4 ± 0.1 | 6.7 ± 0.8 | 2.9 ± 0.2 |
| Intestine | 0.36 ± 0.07 | 0.6 ± 0.1 | 1.5 ± 0.3 | 2.3 ± 1.0 |
| Spleen | 1.6 ± 0.4 | 0.9 ± 0.4 | 0.6 ± 0.2 | 0.6 ± 0.1 |
| Heart | 1.1 ± 0.1 | 0.44 ± 0.05 | 0.17 ± 0.03 | 0.14 ± 0.02 |
| Lung | 2.0 ± 1.1 | 1.0 ± 0.3 | 0.35 ± 0.06 | 0.27 ± 0.03 |
| Kidney | 7.6 ± 1.0 | 3.5 ± 0.7 | 7.1 ± 1.4 | 2.1 ± 0.4 |
| Músculo | 2.3 ± 0.4 | 0.8 ± 0.2 | 0.36 ± 0.02 | 0.28 ± 0.03 |
| Bone | 0.6 ± 0.4 | 0.19 ± 0.14 | 0.09 ± 0.07 | 0.08 ± 0.05 |
| Stomach | 1.3 ± 0.5 | 0.5 ± 0.1 | 0.3 ± 0.1 | 0.21 ± 0.04 |
| Excretion (% I.D.) | 86.6 ± 3.8 | 95.3 ± 0.3 | 73.2 ± 1.6 | 85.2 ± 1.6 |

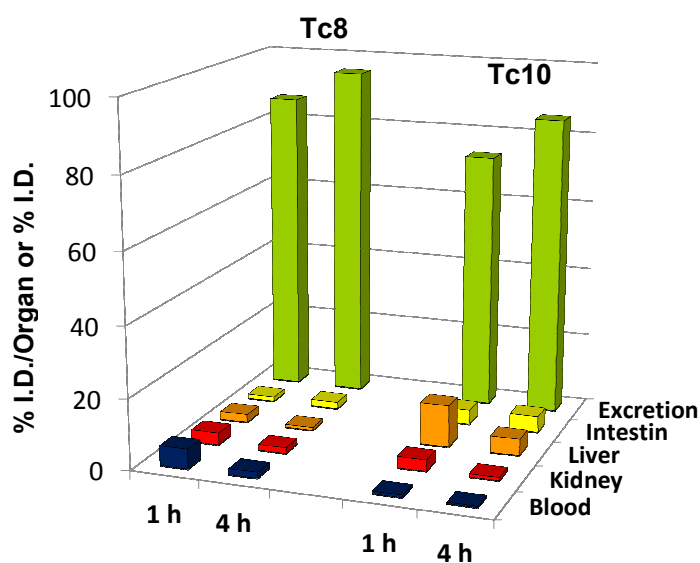


Figure 2.16: Biodistribution in the blood and excretory organs (% I.D./ g organ), and total excretion (% I.D.) for complexes **Tc8** and **Tc10** in CD-1 Charles River mice, 1 h and 4 h after intravenous administration.

The results showed a rapid clearance from blood and other main organs, and the excretion was mainly renal. At 4 h p.i. 95 % of **Tc8** and 85 % of **Tc10** had been excreted (**Table 2.3** and **Figure 2.17**). The lowest kidney retention found for **Tc10** when compared with **Tc6** (**Table 2.3** Vs **Table 2.2**), which also has a terminal $-\text{NH}_3^+$ group, can be likely assigned to the total charge of the complexes (+2 for **Tc6** and +1 for **Tc10**). A less positively charged complex is expected to interact less with the negatively charged surface of the proximal tubule cells in the kidneys.¹³⁸ Comparative analysis of the biodistribution profiles of **Tc4** and **Tc6** with those of **Tc8** and **Tc10** demonstrated that the latter have an enhanced total excretion. To verify the *in vivo* stability of **Tc8** and **Tc10**, serum and urine samples were analyzed by radiometric HPLC as described in the experimental part (**Section 7.8.2**). RP-HPLC analysis of blood and urine confirmed also the high stability of these ^{99m}Tc complexes *in vivo*.

2.3 – Conclusions

Aiming to explore BFCs with different properties (molecular weight, charge, hydrophilicity, and donor atom sets) we synthesized and characterized **pyrazolyl-** (**L4 – L7**) and **Dap-**containing chelators (**L8 – L10**), with different linkers (propyl or hexyl) and different terminal pendant arms (CO_2H and NH_2) for posterior conjugation to iNOS recognizing moieties or transformation into bioactive units. Compounds **L4 – L10** react with $\text{fac-}[\text{M}(\text{CO})_3(\text{H}_2\text{O})_3]^+$ yielding complexes of the type $\text{fac-}[\text{M}(\text{CO})_3(\kappa^3\text{-L})]$ ($\text{M} = \text{Re}/^{99\text{m}}\text{Tc}$; **Re4/Tc4**, **L = L4**; **Re5/Tc5**, **L = L5**; **Re6/Tc6**, **L = L6**; **Re7/Tc7**, **L = L7**; **Re8/Tc8**, **L = L8**; **Re9/Tc9**, **L = L9**; **Re10/Tc10**, **L = L10**). 1D- and 2D-NMR studies performed for **Re4 – Re10** allowed a complete assignment of the resonances and elucidation of the structure of the compounds in solution. In the case of **L4 – L7** the chemical shifts and splitting pattern of the diastereotopic protons of the pyrazolyl coordinating unit are comparable to those found for other complexes of the same type previously described by our group.^{41a-d} The tridentate coordination mode of the pyrazolyl chelators through the *N,N,N* donor atom set was confirmed by X-ray structural analysis performed for **Re4** and **Re5**. For **Re8 – Re10** the tridentate coordination mode of the BFCs through the *N,N,O* donor atom set of the **Dap** unit was also confirmed by NMR studies (diastereotopic pattern of the amine protons) and X-Ray analysis in the case of **Re8**. The ^{99m}Tc tricarbonyl complexes **Tc4 – Tc10** were prepared in high yield and high radiochemical purity. The complexes are stable against cysteine and histidine exchange. Biodistribution studies of **Tc4 – Tc8** and **Tc10** indicate that **Tc4**, **Tc5**, **Tc8** and **Tc10** present the most promising biological profile for the labeling of biologically relevant molecules. In fact, these ^{99m}Tc(I) complexes showed high stability *in vivo* and good clearance characteristics from all organs and tissues, being the major excretory route the renal-urinary pathway. These results encouraged the use of the **pyrazolyl-** and **Dap-**containing chelators for labeling iNOS recognizing molecules with $\text{fac-}[^{99\text{m}}\text{Tc}(\text{CO})_3]^+$.

3 **Synthesis of Conjugates with iNOS- Recognizing Moieties and their Re(I) and ^{99m}Tc(I) Complexes**

3. Synthesis of Conjugates with iNOS Recognizing Moieties and their Re(I) and ^{99m}Tc(I) Complexes

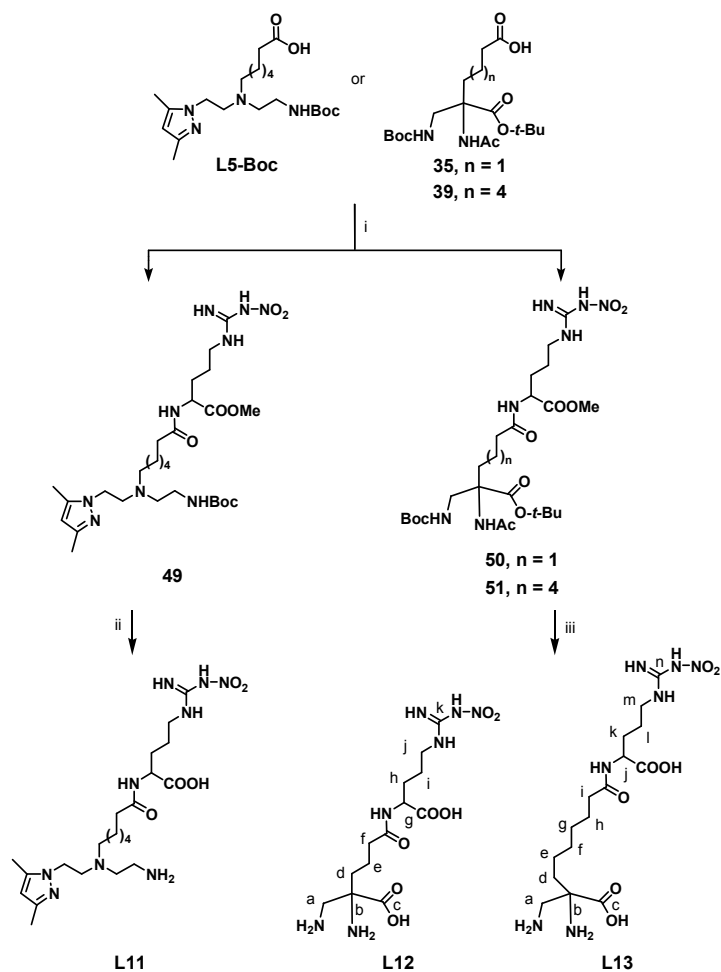
In **Sections 3.1.1 - 3.1.3** we describe the synthesis of compounds containing N^ω-NO₂-L-Arg, alkyl-amidine and conformationally-restricted benzyl-amidine moieties, respectively. The ability of these conjugates to stabilize the *fac*-[M(CO)₃]⁺ (M = Re, ^{99m}Tc) core will be described in **Section 3.1.4**.

3.1 – Conjugates Containing N^ω-NO₂-L-Arg and Amidine Moiety and their Re(I)/^{99m}Tc(I) Complexes

3.1.1 - Conjugates Containing the N^ω-NO₂-L-Arg Moiety

The conjugates containing a **pyrazolyl** or a **Dap** chelating unit, an alkyl spacer with different lengths (C3 or C6 linker), and a pendant N^ω-NO₂-L-Arg moiety were prepared as depicted in **Scheme 3.1**.

The new conjugates **L11 - L13** were synthesized in a two step procedure by direct conjugation of the protected precursors **L5-Boc**, **35**, and **39** to the N^ω-NO₂-L-Arginine methyl ester derivative using standard coupling reagents. After hydrolysis of the protecting groups under acidic conditions (**Scheme 3.1**), **L11 - L13** were obtained as air stable colorless oils with purity higher than 95 % (monitored by analytical RP-HPLC), after purification by semi-preparative RP-HPLC. The compounds were thoroughly characterized, and their structure unambiguously assigned by IR and multinuclear NMR spectroscopy, ESI-MS, and elemental analysis.



Scheme 3.1: Synthesis of conjugates **L11** – **L13**: i) $\text{N}^{\omega}\text{-NO}_2\text{-L-Arginine}$ methyl ester, HBTU, Et_3N , DMF, r.t., 2 h, 66.6 % for 23, 81.4 % for 24 and 71.5 % for 25; ii) HCl 3 N, r.t., 70 h, 33.3 %. iii) HCl 3 N, reflux, 22 h, 23.6 % (*identification system for NMR assignments is displayed for L12 and L13 as an example*).

The $^1\text{H-NMR}$ spectrum (D_2O) of the bioconjugate containing the **pyrazolyl** chelator (**L11**) presented the typical sharp singlet peaks for the H(4) proton (δ 5.76, 1H) and the methyl groups of the azolyl ring (δ 2.16 /2.06, 6H) and the resonances for the methylenic protons of the **pyrazolyl-diamine** backbone (δ 3.98, 2H; δ 2.65, 2H; δ 2.31, 2H; δ 2.14, 2H; δ 1.70 – 1.40, 6H; δ 1.39 – 1.00, 6H). Resonances for the $\text{N}^{\omega}\text{-NO}_2\text{-L-Arg}$ pendant unit, namely the characteristic resonance of the α -proton of the amino acid (δ 4.34, 1H) and the resonances of the methylenic protons (δ 3.87, 2H; δ 2.65, 2H; δ ~1.79, 2H) were also observed in the spectrum. Analysis of the $^1\text{H-NMR}$ spectra of **L12** and **L13**, which contain the **Dap** BFC, confirmed also the identity of the compounds. The spectra present one singlet at δ 3.34 (**L12**) and δ 3.27 (**L13**) attributed to the H^a proton of the **Dap** BFC and three or six multiplets attributed to the methylenic protons of the pendant arm (**L12** - δ 3.13, 2H; δ 2.29, 2H; δ 1.93 - 1.40, 2H; **L13** - δ 2.11, 2H; δ 1.83 - 1.12, 10H). Four multiplets due to the α and aliphatic protons of the N^{ω} -

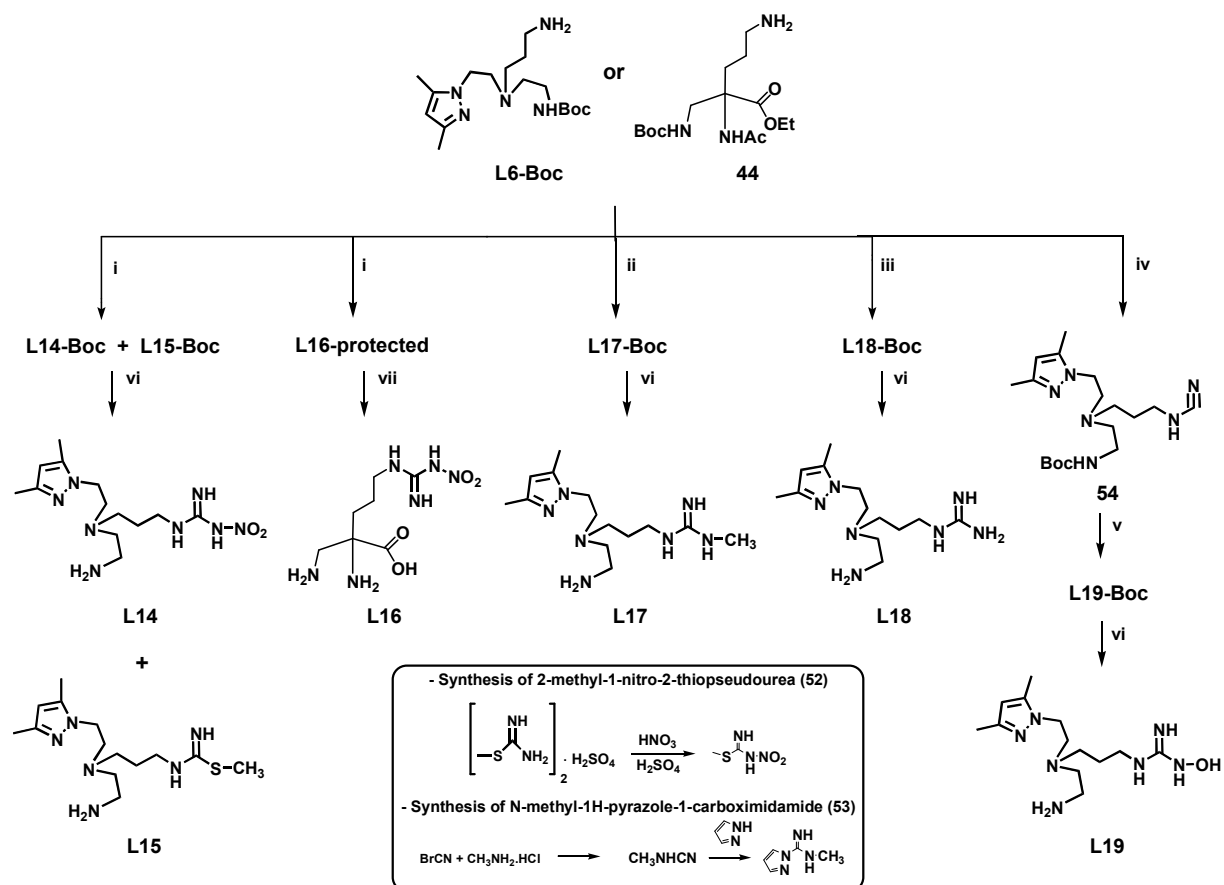
3. Synthesis of Conjugates with iNOS Recognizing Moieties and their Re(I) and ^{99m}Tc(I) Complexes

NO₂-L-Arg pendant amino acid (**L12** - δ 4.24, 1H; δ 3.13, 2H; δ 1.93 - 1.40, 4H; **L13** - δ 4.19, 1H; δ 3.10, 2H; δ 1.83 - 1.12, 4H) could also be found.

In the ¹³C-NMR spectra of **L11** – **L13** all the expected resonances could be observed, in particular the presence of resonances at δ 160.0, δ 156.3 and δ 158.8 corresponding to the carbon atom of the NO₂-guanidine which is indicative of the presence of the N⁰-NO₂-L-Arg moiety in all compounds. In all cases the ESI-MS data confirmed the proposed formulation.

3.1.2 - Conjugates Containing Alkyl-Amidine Moieties

As mentioned before, we have also proposed the synthesis of “lighter” compounds which contain a **pyrazolyl** or a **Dap** chelating backbone and different pendant amidine moieties for iNOS recognition (**Scheme 3.2**). The compounds **L6-Boc** and **44** were the precursors used for the preparation of **L14** – **L19**. These precursors contain a primary amine that was easily converted into different amidine groups by reaction with the appropriate amidinating agent, following described procedures.^{5b, 6c, 144}



Scheme 3.2: Synthesis of conjugates **L14** – **L19**: i) 2-methyl-1-nitro-2-thiopseudourea (**52**), EtOH, 40 °C, overnight, 54.9 % for **L14-Boc**, 22.7 % for **L15-Boc** and 86.3 % for **L16-protected**; ii) N-methyl-1H-

pyrazole-1-carboximidine hydrochloride (**53**), LiOH pH 10 – 11, water, 5d, 51.6 %; iii) 1H-pyrazole-1-carboximidamide, DIPEA, DMF, overnight, 25.8 %; iv) BrCN, Et₃N, CH₂Cl₂, 4 h, 61.9 %; v) H₂NOH.HCl, K₂CO₃, EtOH, 18 h, 46.0 %; vi) TFA, 2 h, 83.0 % for **L14**, 78.1 % for **L15**, 73.9 % for **L17**, 43.7 % for **L18** and 70.3 % for **L19**.

The synthesis of **L14** and **L16**, which bear a pendant *N*-nitroguanidine group, was accomplished by nitroguanylation of the precursors **L6-Boc** or **44** with 2-methyl-1-nitro-2-thiopseudourea, which was prepared by nitration of commercial available *S*-methylisothiurea hemisulfate salt (**Scheme 3.2**, inset).^{144c, 145} Subsequent deprotection of the corresponding intermediates **L14-Boc** and **L16-protected** gave the final compounds **L14** and **L16**. The *S*-methylisothiurea-containing conjugate **L15** was obtained as a side product in the preparation of **L14**. As isothiureas are a well-known class of inhibitors of NOS we decided to check whether **L15** has affinity for iNOS.¹⁴⁶ It is important to mention that in the case of **L16**, the side product **Dap-S**-methylisothiurea-containing conjugate was obtained in very small amounts which precluded its use in further studies.

The bioconjugate **L17** was prepared by reaction of **L6-Boc** with *N*-methyl-1*H*-pyrazole-1-carboximidamide (**53**), followed by Boc-deprotection of **L17-Boc** with TFA.^{144a} The *N*-methyl-1*H*-pyrazole-1-carboximidamide was synthesized by reaction of cyanogen bromide with methylamine to give the methylcyanamide, which was condensed with pyrazole as described in the literature (**Scheme 3.2**, inset).^{144a} This guanilating agent was purified by sublimation of the free pyrazole.

The bioconjugate **L18** was prepared using a procedure similar to the one applied to synthesize **L17** (reaction of **L6-Boc** with 1*H*-pyrazole-1-carboximidamide followed by Boc deprotection).

Reaction of **L6-Boc** with cyanogen bromide yielded the cyanamide **54**, which after reaction with hydroxylamine gave **L19-Boc**. Removal of the Boc-protecting group with TFA gave the final compound **L19**.^{144b}

Conjugates **L14** – **L19** were purified by semi-preparative RP-HPLC (> 95% purity) and thoroughly characterized by ESI-MS, multinuclear NMR (¹H, ¹³C, g-COSY, g-HSQC) and IR-spectroscopy.

The ESI-MS spectra of **L14** – **L19** present peaks at *m/z* values which are in agreement with the expected values for these compounds.

The IR spectrum of **L14** showed absorption bands at 2300 and 1550 cm⁻¹ attributed to the stretching bands of the NO₂ group (**Figure 3.1**).¹⁴⁷ These bands are absent in the IR spectrum of the precursor **L6** and **L15** (**Figure 3.1**). In the spectra of 2-methyl-1-nitro-2-thiopseudourea and **L15** a very

weak band at $\sim 2185\text{ cm}^{-1}$ was assigned to the asymmetric stretching vibration of the N-C-S group (Figure 3.1).¹⁴⁷

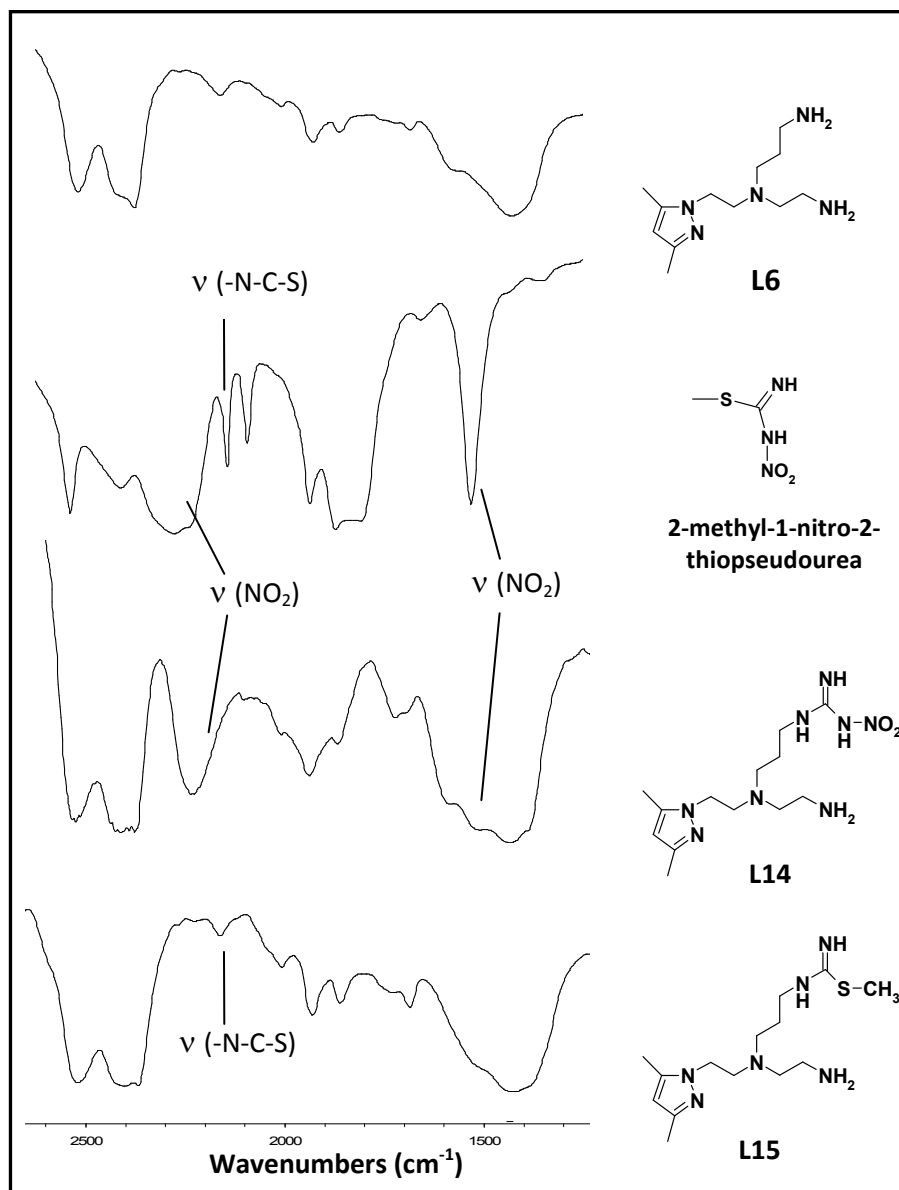


Figure 3.1: IR spectra (KBr pellets) of **L6**, 2-methyl-1-nitro-2-thiopseudourea, **L14** and **L15**.

In the ¹H-NMR spectra (D₂O) of the pyrazolyl-containing conjugates, besides the resonances due to the methylenic protons of the ligand backbone, we identified typical sharp singlets for the H(4) of the pyrazolyl ring (δ 6.03, **L14**; δ 5.85, **L15**; δ 6.01, **L17**; δ 6.13, **L18**; δ 5.98, **L19**) and the methyl groups of the same ring (δ 2.17/2.10, **L14**; δ 2.13/2.07, **L15**; δ 2.15/2.08, **L17**; δ 2.20/2.14, **L18**; δ 2.17/2.09, **L19**). Singlets for the S-methylisothioureia (**L15**) and N-methylguanidine (**L17**) groups were also found at δ 2.44 and δ 2.65, respectively. As a representative example of this family of compounds, the ¹H-NMR spectrum of **L15** is shown in **Figure 3.2**.

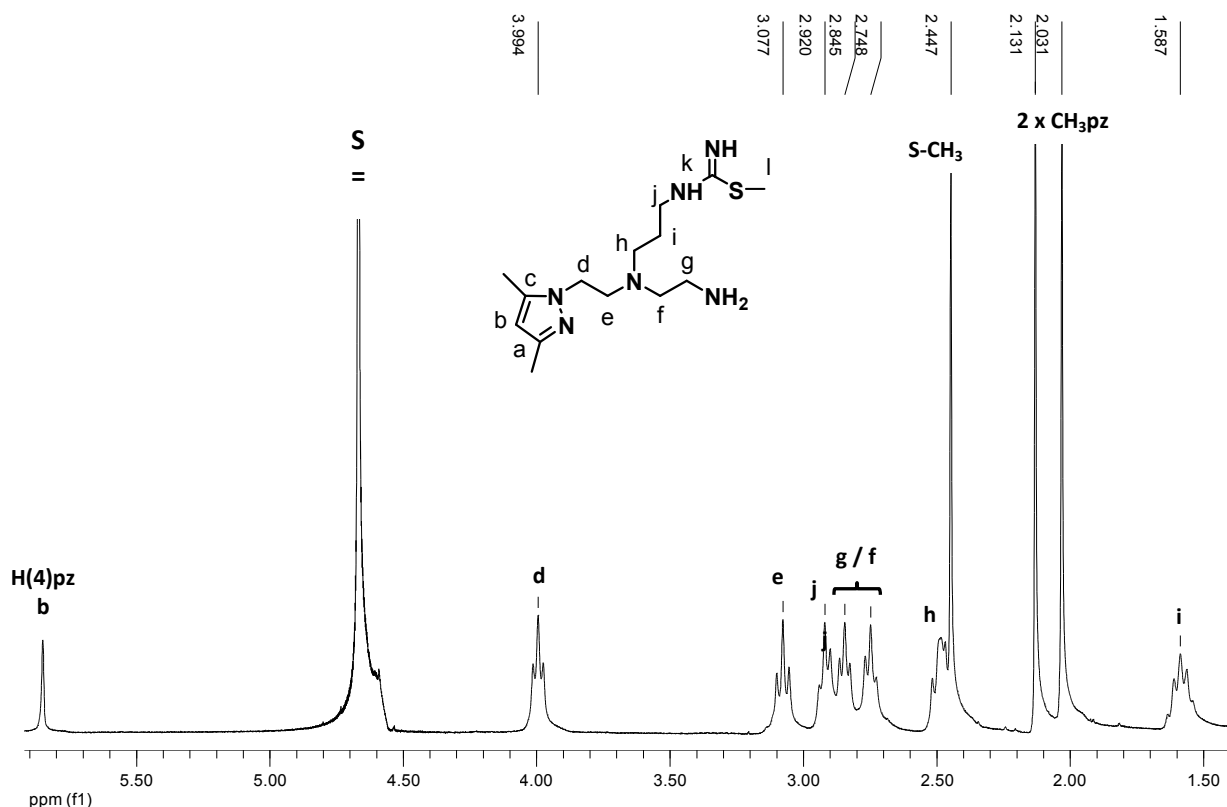


Figure 3.2: ^1H -NMR spectrum of **L15** in D_2O (S = residual solvent).

The chemical shifts as well as the pattern of the resonances in the ^1H -NMR spectrum of the **Dap**-containing conjugate **L16** are very similar with those found for the bifunctional chelator **L10**.

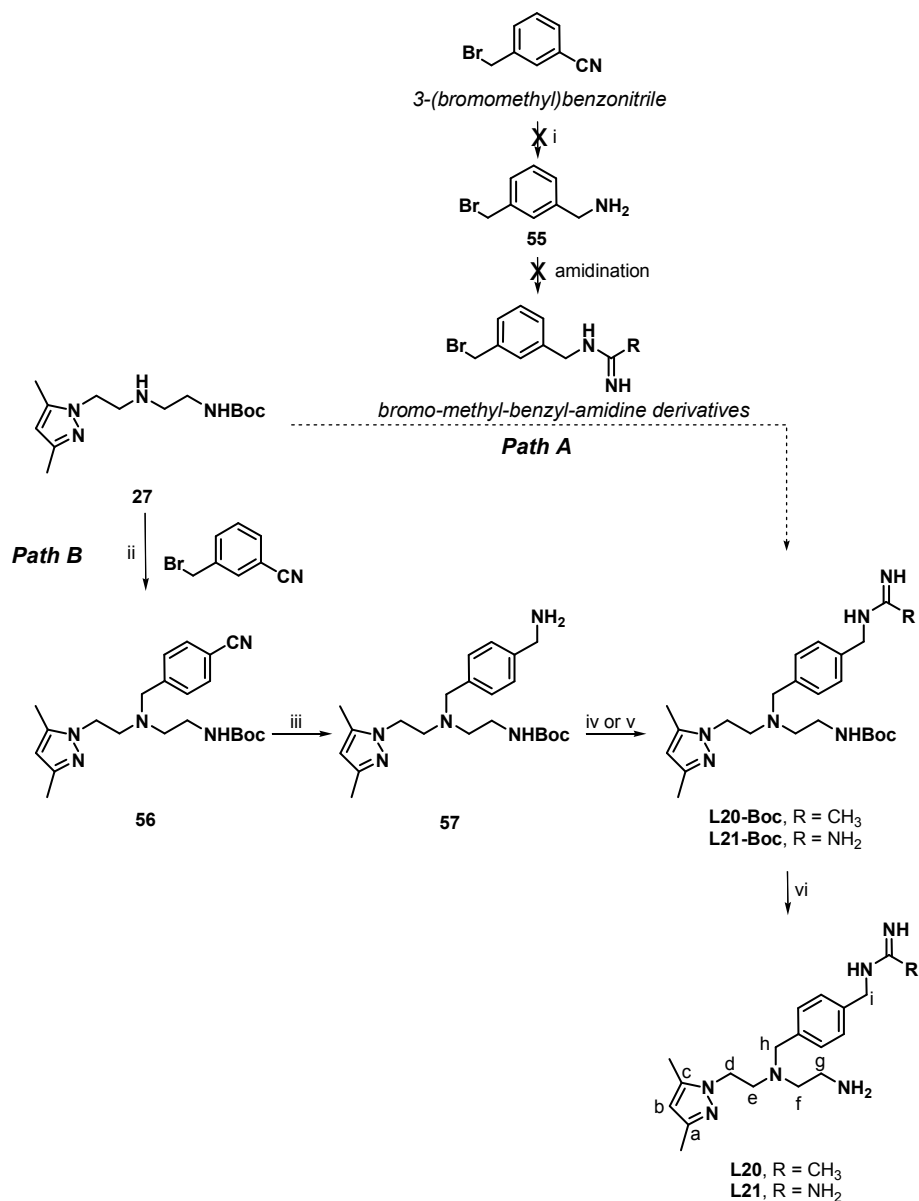
The ^{13}C spectra presented signals corresponding to all the expected carbon nuclei of **L14** – **L19**, including the amidine carbon signals at δ 158.3 (**L14**), 168.2 (**L15**), 157.3 (**L16**), 162.6 (**L17**), 156.1 (**L18**) and 156.1 (**L19**).

3.1.3 - Conjugates Containing Conformationally-Restricted Amidine Moieties

We designed two compounds containing a conformationally-restricted moiety with recognized affinity for iNOS, coupled to the **pyrazolyl-diamine** backbone (**L20** and **L21**). Compound **L20** bear an aromatic ring as a rigidifying backbone spacer and an acetamide pendant group, which is described to give compounds with high selectivity and potency for iNOS (**Scheme 3.3**).¹⁴⁸ Compound **L21** is a very close analog of **L20** but has a guanidine group, instead of an acetamide. **L21** was designed considering that guanidine-containing compounds are potential substrates of iNOS. The aromatic ring on **L20** and **L21** is expected to form π -stacking interactions with the heme group of the iNOS active site, yielding, most probably, compounds with improved affinity for iNOS.^{80b, 149}

3. Synthesis of Conjugates with iNOS Recognizing Moieties and their Re(I) and ^{99m}Tc(I) Complexes

Initially, we intended to synthesize a suitable precursor that could alkylate **27**, giving directly **L20-Boc** and **L21-Boc** (**Scheme 3.3, Path A**). In this context, the synthesis of the *bromo-methyl-benzyl-amidine derivatives* was tried as depicted in **Scheme 3.3, Path A**.



Scheme 3.3: Tentative synthesis of **55** and synthesis of conjugates **L20** and **L21**: i) NaBH₄, NiCl₂, Boc₂O, MeOH, r.t., 3 h 2) diethylenetriamine, r.t., 30 min, 11.0 %; ii) K₂CO₃, KI, ACN, reflux, 24 h, 55.6 %; iii) NaBH₄, NiCl₂, MeOH, r.t., overnight, 79.5 %; iv) methyl acetimidate, DIPEA, DMF, 48 h, 69.7 %; v) 1H-pyrazole-1-carboximidamide, DIPEA, DMF, overnight, 76.4 %; vi) TFA, CH₂Cl₂, r.t., 2 h, 50.0 % for **L20** and 38.8 % for **L21** (identification system for NMR spectra assignment is displayed for **L20** and **L21** as an example).

The reduction of the precursor compound 3-(bromomethyl)benzonitrile with NaBH₄/NiCl₂ was explored as an appropriate starting point (*i*, **Scheme 3.3, Path A**), however, under these

reduction conditions dehalogenation occurred as determined by mass spectrometry. After purification of the crude material a main crystalline product was obtained in very low yield (11 %). X-ray diffraction analysis of single crystals, obtained by recrystallization of the crystalline material from CH_2Cl_2 , revealed the formation of a side product, bis(3-methylbenzyl)amine, whose molecular structure is displayed in **Figure 3.3**. A thorough investigation of the literature revealed that the synthesis of symmetric secondary amines from nitriles is already described in literature using rhodium as catalyst. However, no reports were found when $\text{NaBH}_4/\text{NiCl}_2$ is used as reducing agent.¹⁵⁰ Other reducing agents were used to synthesize **55** (e.g. LiAlH_4 , low temperatures), however, dehalogenation was always observed.

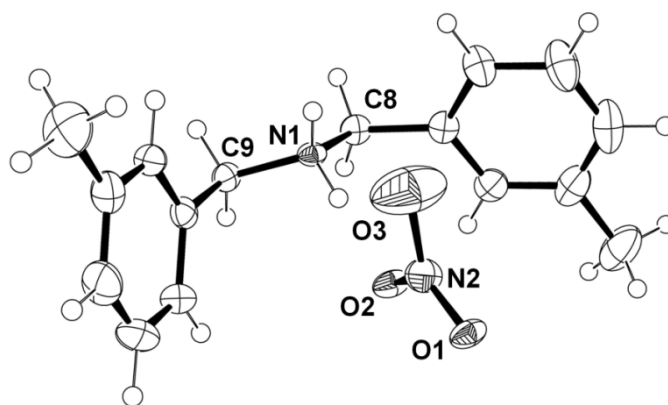


Figure 3.3: ORTEP view of the side product bis(3-methylbenzyl)amine obtained by reaction of 3-(bromomethyl)benzotrile with $\text{NaBH}_4/\text{NiCl}_2$. Vibrational ellipsoids are drawn at the 50% probability level. Selected bond distances (Å) and angles (°): C8 – N1, 1.497(4) Å; C9 – N1, 1.496(4) Å; O1 – N2, 1.258(4) Å; O2 – N2, 1.252(4) Å; O3 – N2, 1.522(5) Å; C9 – N1 – C8, 113.01(2)°; O1 – N2 – O2, 124.22(3)°; O1 – N2 – O3, 117.63(3)°; O2 – N2 – O3, 118.21(3)°.

To overcome such problem we decided to follow a different strategy, which is indicated in **Scheme 3.3 (Path B)**. We did a direct alkylation of **27** with 3-(bromomethyl)benzotrile. Then, **56** was reduced yielding **57**. Compound **57** allowed the preparation of **L20-Boc** and **L21-Boc** by reaction with methyl acetimidate hydrochloride or 1*H*-pyrazole-1-carboximidamide, respectively (**Scheme 3.3**). After deprotection, these intermediates afforded **L20** and **L21**. All intermediates and final compounds were fully characterized by the usual techniques. The reduction of the nitrile group in **56** was confirmed by $^1\text{H-NMR}$ and IR spectroscopy. The absence of the absorption band at 2229 cm^{-1} , attributed to the stretching bands of the $\text{C}\equiv\text{N}$ group, and the appearance of two resonances in the $^1\text{H-NMR}$ spectrum at δ 5.50 and 3.98, assigned to the additional amine and CH_2 groups, indicated the formation of **57**. $^1\text{H-NMR}$ of the final compounds **L20** and **L21** showed resonances for the pyrazole-diamine backbone (**L20** - δ 5.82, 1H^b ; δ 4.29, 2H^d ; δ 3.67 – 3.21, $6\text{H}^{e,f,g}$; δ 2.12, $3\text{H}^{\text{CH}_3\text{pz}}$; δ 2.08, $3\text{H}^{\text{CH}_3\text{pz}}$; **L21** - δ 5.86, 1H^b ; δ 4.08, 2H^d ; δ 3.04, 2H ; δ 2.88, 2H^e ; δ 2.80, 2H ; δ 2.20, $3\text{H}^{\text{CH}_3\text{pz}}$; δ 2.00, $3\text{H}^{\text{CH}_3\text{pz}}$) and

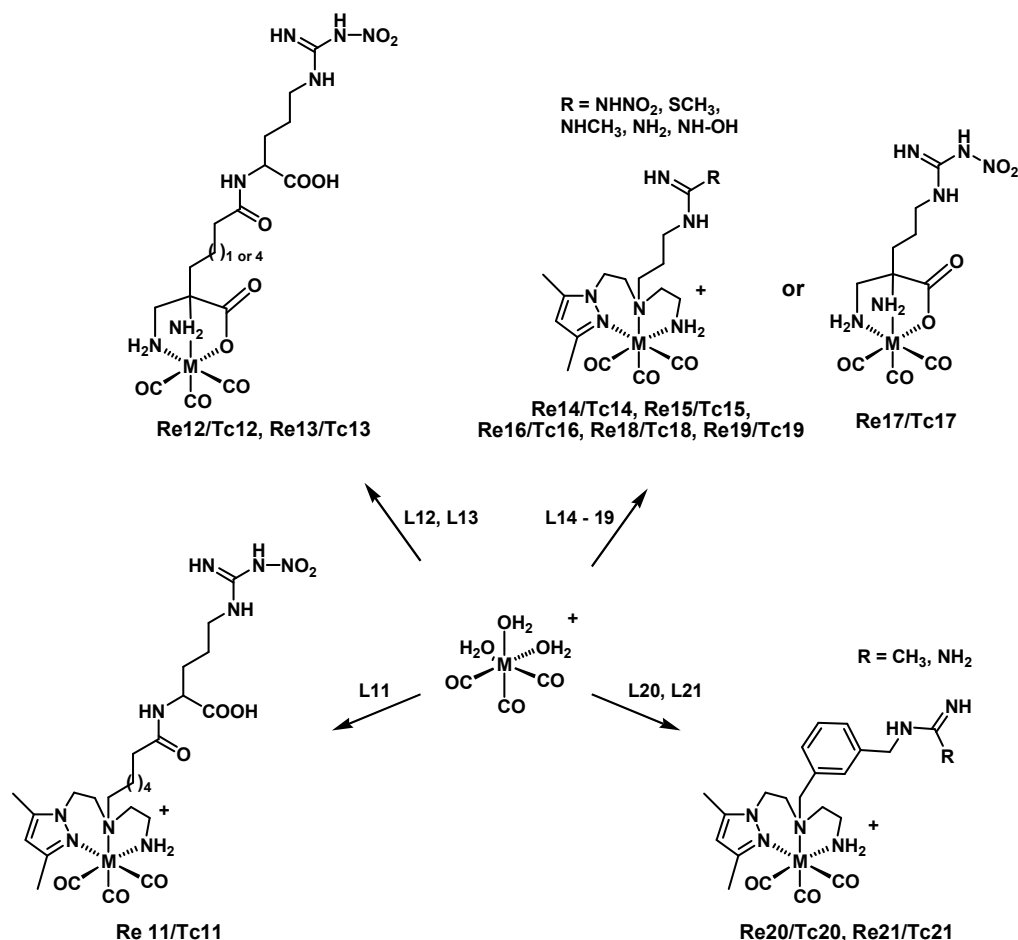
3. Synthesis of Conjugates with iNOS Recognizing Moieties and their Re(I) and ^{99m}Tc(I) Complexes

for the methyl-benzyl-amidine arms (**L20** - δ 7.40 – 7.22, 4H^{Ar}; δ 4.37, 2Hⁱ; δ 4.18, 2H^h; **L21** - δ 7.26 – 6.99, 4H^{Ar}; δ 4.30, 2Hⁱ; δ 3.71, 2H^h). The ¹H-NMR spectrum of **L20** presented one additional resonance at high field, compared to **L21**, attributed to the methyl protons of the amidine group (δ 2.15). In the ¹³C-NMR spectra of **L20** and **L21** all the expected resonances could be observed, in particular the presence of the central carbon atoms of the amidine moieties assigned at δ 165.2 and δ 157.5, respectively.

3.1.4 - Reactions of **L11** – **L21** with *fac*-[M(CO)₃]⁺ Precursors (M = Re or ^{99m}Tc)

3.1.4.1 - Synthesis and Characterization of the Re (I) Complexes

The reaction of **L11** – **L21** with equimolar amounts of the precursor *fac*-[Re(CO)₃(H₂O)₃]Br afforded **Re11** – **Re21** (Scheme 3.4).



Scheme 3.4: Synthesis of complexes of the type *fac*-[M(CO)₃(κ^3 -L)]^{0/+1} (M = Re/^{99m}Tc; **Re11/Tc11**, L = **L11**; **Re12/Tc12**, L = **L12**; **Re13/Tc13**, L = **L13**; **Re14/Tc14**, L = **L14**; **Re15/Tc15**, L = **L15**; **Re16/Tc16**, L = **L16**; **Re17/Tc17**, L = **L17**; **Re18/Tc18**, L = **L18**; **Re19/Tc19**, L = **L19**; **Re20/Tc20**, L = **L20**; **Re21/Tc21**, L = **L21**).

The rhenium complexes were obtained as air-stable colorless viscous oils in moderate/high yields (35 – 95 %), after purification by semi-preparative RP-HPLC. All complexes were thoroughly characterized by RP-HPLC, NMR and IR spectroscopy, ESI-MS and X-ray analysis in the case of **Re18**.

The ESI-MS spectra of **Re11** - **Re21** present prominent peaks at m/z values, which are in agreement with the expected values for those complexes. The isotopic pattern of the peaks were also in agreement with the presence of rhenium. As an example, in **Figure 3.4** is presented the mass spectrum of **Re13**, where a group of peaks centered at m/z 702.2 (most abundant m/z) is shown.

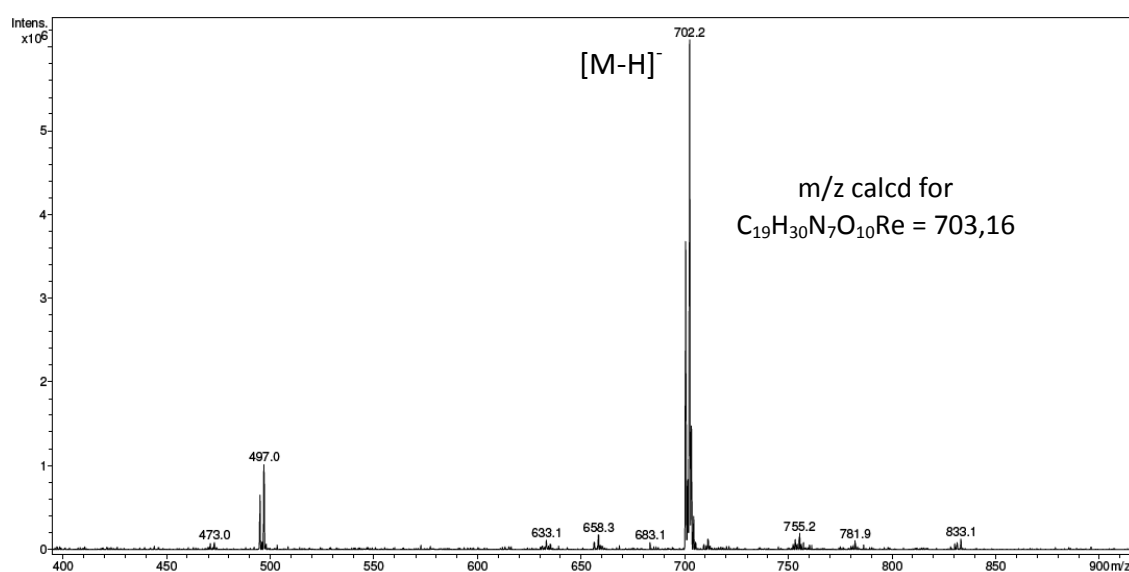


Figure 3.4: Mass spectrum of compound **Re13** in the negative mode obtained by ESI-MS.

The ¹H-NMR spectra of the complexes **Re11**, **Re14** – **Re15** and **Re17** – **Re21** present similar pattern, which compares with the pattern observed for **Re4** – **Re7** (**Section 2.1.2.1**). Indeed, the multiplicity and chemical shift of the diastereotopic protons CH₂ (d, e, f and g) and NH₂ (**Figure 3.5**) of the aliphatic chain, confirms the coordination of the ligand to the metal center in a tridentate fashion: through the nitrogen of the pyrazolyl ring and the two nitrogen atoms of the primary and secondary amines. To illustrate such behavior, the fully assigned ¹H-NMR spectrum of complex **Re17** is presented in **Figure 3.5** (¹³C-NMR spectrum is presented in **Figure 8.3**). The resonances corresponding to the N⁰-NO₂-L-Arg (**Re11**), alkyl-amidine (**Re14** – **Re19** not **Re16**), and benzyl-amidine (**Re20** and **Re21**) moieties appear with a pattern and chemical shifts similar to those observed for the free chelators, suggesting that no unspecific interactions between these moieties and the metal center are present.

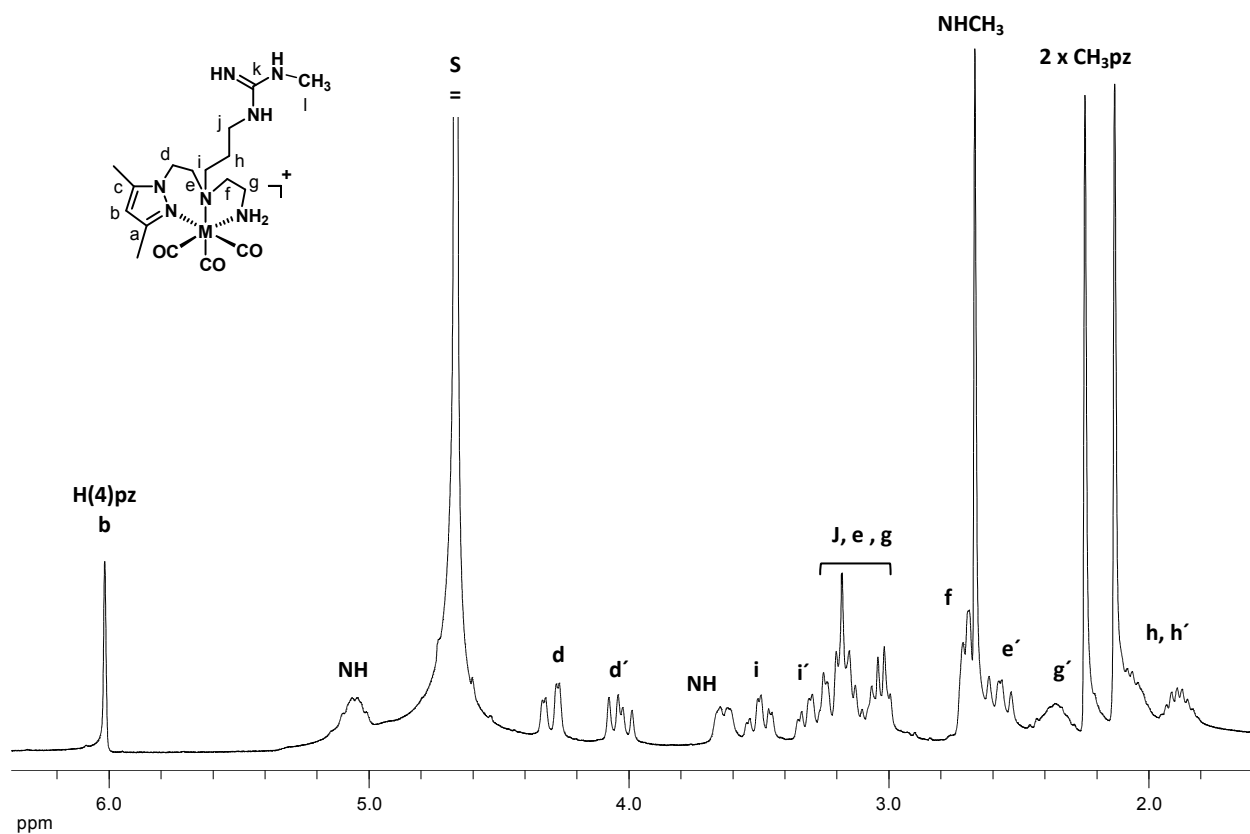


Figure 3.5: ¹H-NMR spectrum of **Re17** in D₂O (S = residual solvent).

High quality crystals of **Re18** were grown from a saturated methanolic solution of **Re18**. An ORTEP diagram of the cation of **Re18** is shown in **Figure 3.6**, together with a selection of bond lengths and angles. The coordination environment around the rhenium atom is defined by the three nitrogen atoms of the **pyrazolyl-diamine** backbone and the three carbonyl ligands, confirming the structure in solution assigned based on the NMR data. A summary of the crystallographic data of **Re18** is given in **Table 8.4** of Annexes.

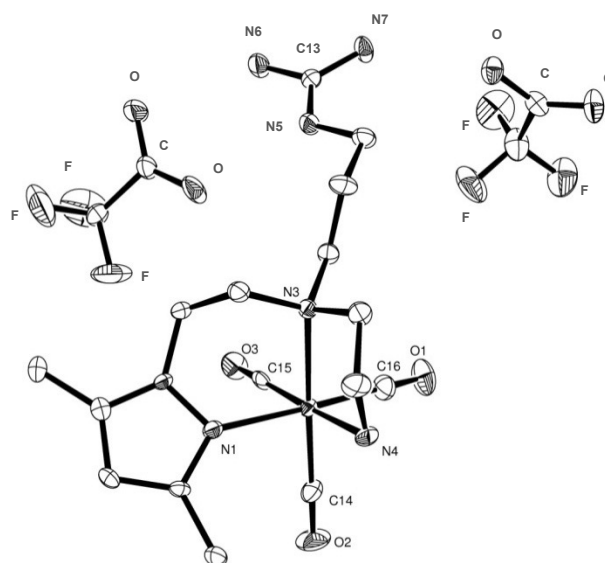


Figure 3.6: ORTEP view of **Re18**·[TFA]₂. The hydrogen atoms are omitted for clarity. Vibrational ellipsoids are drawn at the 50% probability level. Selected bond distances (Å) and angles (°): Re–C14, 1.907(5) Å; Re–C15, 1.909(5) Å; Re–C16, 1.925(5) Å; Re–N1, 2.210(4) Å; Re–N3, 2.286(4) Å; Re–N4, 2.220(4) Å; N6–C13, 1.335(6) Å; N7–C13, 1.319(6) Å; C14–Re–N1, 93.61(18)°; C15–Re–N1, 90.12(17)°; C14–Re–N3, 174.21(19)°; C16–Re–N3, 95.95(18)°; C16–Re–N4, 95.04(19)°; C14–Re–C15, 86.51(19)°; C14–Re–C16, 86.03(19)°; N1–Re–N3, 84.93(14)°; N1–Re–N4, 89.33(15)°.

The ¹H-NMR data of **Re12**, **Re13** and **Re16** indicated the expected tridentate coordination mode for the **Dap** chelating unit (*N,N,O* donor atom set) of **L12**, **L13** and **L16**. In fact, similar to what was described for **Re8** – **Re10** (Section 2.2.2.1), the ¹H-NMR spectra (CD₃OD) of **Re12**, **Re13** and **Re16** displayed four broad multiplets in the range δ 5.32 – 4.31, integrating for 1 H each, assigned to the diastereotopic protons of the NH₂ groups. The two CH₂^a protons become also diastereotopic. In the ¹H-NMR spectra, the pattern obtained for N^o-NO₂-L-Arg (**Re12** and **Re13**), and alkyl-amidine (**Re16**) moieties compares well with the pattern found for the free conjugates (**L12**, **L13** and **L16**). To illustrate such behavior, the fully assigned ¹H-NMR spectrum of complex **Re13** is presented in **Figure 3.7**. The corresponding ¹³C-NMR is presented in **Figure 8.4** (Annexes).

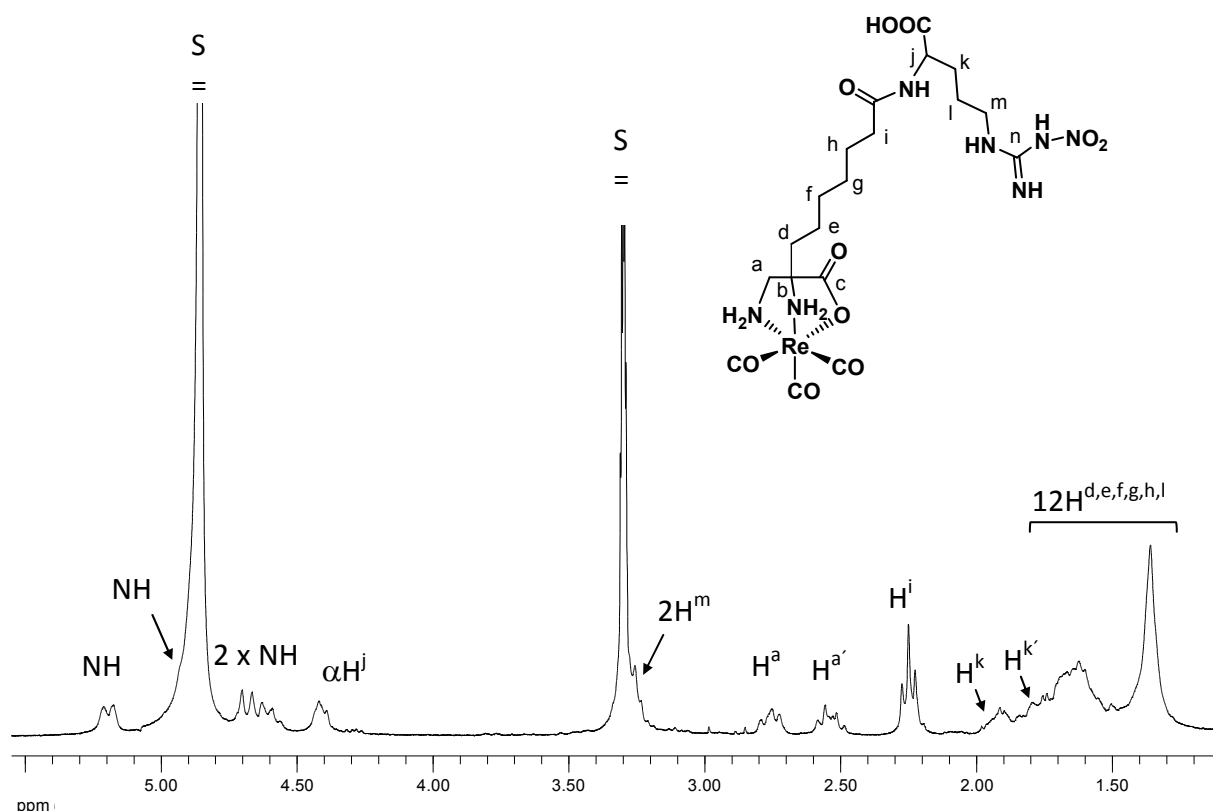


Figure 3.7: ¹H-NMR spectrum of **Re13** in CD₃OD (S = residual solvent).

The ¹³C-NMR spectra of **Re11** - **Re21** present the expected resonances, including the three resonances due to the carbon atoms of the C≡O ligands.

3.1.4.2 - Synthesis, Characterization and Biological Behavior of the ^{99m}Tc (I) Complexes

The complexes of the type *fac*-[^{99m}Tc(CO)₃(κ³-L)]⁺⁰ (**Tc11**, L = **L11**; **Tc12**, L = **L12**; **Tc13**, L = **L13**; **Tc14**, L = **L14**; **Tc15**, L = **L15**; **Tc16**, L = **L16**; **Tc17**, L = **L17**; **Tc18**, L = **L18**; **Tc19**, L = **L19**; **Tc20**, L = **L20**; **Tc21**, L = **L21**) were prepared by reacting the precursor *fac*-[^{99m}Tc(CO)₃(H₂O)₃]⁺ with an aqueous solution of **L11** – **L21** ([L] = 1 × 10⁻⁴ - 8 × 10⁻⁵ M), at 100 °C for ~45 min (**Scheme 3.4**). The radiocomplexes **Tc11** - **Tc21** were obtained in high yield (> 90 %) and were characterized by comparing their HPLC profiles with that of the corresponding Re(I) tricarbonyl complexes (**Re11** – **Re21**).

3.1.4.2.1 - In Vitro Studies of the ^{99m}Tc Tricarbonyl Complexes **Tc11** – **Tc21**

The stability of the ^{99m}Tc complexes was evaluated *in vitro* in the presence of excess of cysteine and histidine, as mentioned before. The complexes **Tc11**, **Tc14**, **Tc15**, **Tc17**, **Tc18**, **Tc19** and **Tc20** were stable and no decomposition was observed by RP-HPLC, even after 18h h at 37 °C. The only exception was **Tc15**. This complex, which contains the methyl thioguanidine moiety, decomposes in the presence of cysteine, most probably due to the oxidation of the sulfur atom (**Figure 3.8**).

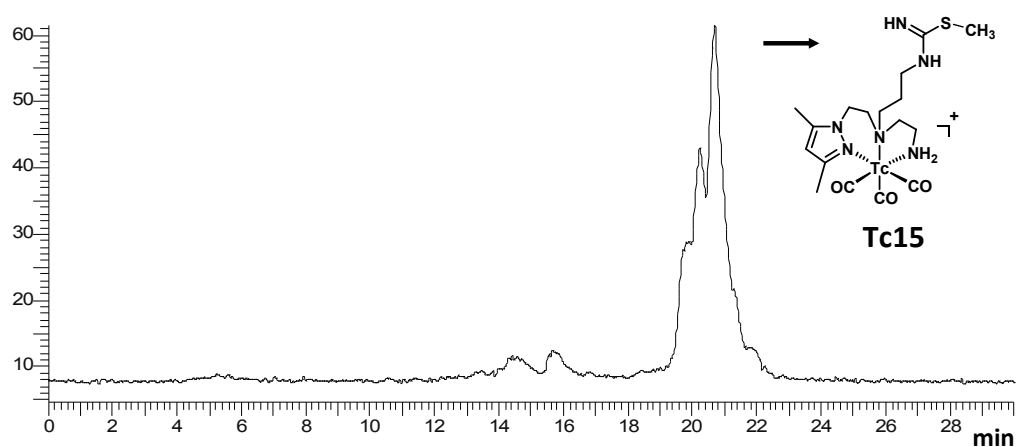


Figure 3.8: RP-HPLC chromatogram of **Tc15** after incubation with cysteine during 18h at 37 °C

The hydro(lipo)philic nature of the $^{99m}\text{Tc(I)}$ -complexes was evaluated by determining the partition coefficient ($\log P_{o/w}$) in physiological conditions following the procedure described in **Section 7.7**. The results found were: $\log P_{o/w} = -0.29 \pm 0.01$ (**Tc11**), -0.85 ± 0.22 (**Tc14**), -0.05 ± 0.12 (**Tc15**), -0.89 ± 0.20 (**Tc17**), -1.23 ± 0.15 (**Tc18**), -0.73 ± 0.10 (**Tc19**) and -0.763 ± 0.02 (**Tc20**).

3.2 – Conclusion

We have prepared novel **pyrazolyl-diamine** or **Dap** conjugates bearing moieties with recognized affinity for iNOS ($\text{N}^0\text{-NO}_2\text{-L-Arg}$, alkyl-amidine, and benzyl-amidine moieties). These conjugates reacted with the $\text{fac-}[\text{M}(\text{CO})_3(\text{H}_2\text{O})_3]^+$ precursor giving $\text{fac-}[\text{M}(\text{CO})_3(\kappa^3\text{-L})]^{+/0}$ complexes ($\text{M} = \text{Re}/^{99m}\text{Tc}$, $\text{L} = \text{L11} - \text{L21}$) in moderate yield and high radiochemical purity (^{99m}Tc). Based on NMR and IR spectroscopy, ESI-MS, and X-ray structural analysis, it is clear that **pyrazolyl-** or **Dap**-containing conjugates coordinate to the metal as neutral or anionic tridentate ligands, through the *N,N,N* or

3. Synthesis of Conjugates with iNOS Recognizing Moieties and their Re(I) and ^{99m}Tc(I) Complexes

N,N,O donor atom set, respectively. These results indicate that no unspecific interactions between the biological active part of the molecules and the metal center take place. Consequently, the iNOS recognizing moieties of the compounds are free to interact with the iNOS enzyme. Moreover, the resulting complexes showed a high stability and also good solubility in aqueous media, which was essential to perform the *in vitro/in vivo* experiments. In the following chapter the affinity towards iNOS of the conjugates **L11 – L21** and of the corresponding rhenium complexes (**Re11 – Re21**) will be determined *in vitro* and *in vivo*.

4 *in vitro* and *in vivo* Biological Evaluation

4. *in vitro* and *in vivo* Biological Evaluation

Aiming to evaluate the iNOS recognizing properties of the conjugates (**L11 – L21**) and Re(I) complexes (**Re11 – Re21**) prepared in **Chapter 3**, we studied the enzymatic activity of murine recombinant iNOS in the presence of those compounds.

In **Section 4.1** we will report the K_i and K_m values determined for **L11 – L21** and for **Re11 – Re21**. The enzymatic activity of iNOS was determined spectrophotometrically by monitoring the NO mediated conversion of oxyhemoglobin to methemoglobin at two wavelengths (401 and 421 nm). The kinetic parameters (K_m and K_i) for the compounds under study were determined using the direct linear plot of Eisenthal and Cornish-Bowden and the Hyper software (J.S. Easterby, University of Liverpool, UK).¹⁵¹

One of the prerequisites necessary to target a cytosolic enzyme with ^{99m}Tc complexes is their ability to cross the cell membranes. Since it is well known that levels of iNOS are increased in RAW 264.7 macrophages after treatment with endotoxins such as LPS and γ -interferon, we used this cell line model to evaluate the ability of the compounds to cross the cellular membrane and inhibit the NO production by interaction with iNOS. The efficacy of compounds to suppress the NO production in LPS-induced macrophages was determined using a colorimetric assay (Griess method) and the results will be reported in **Section 4.2**.

The biological evaluation of the rhenium complexes with the highest affinity for iNOS was also performed *in vivo* using the ^{99m}Tc surrogates and an animal model with localized iNOS overexpression. These results will be described in **Section 4.3**.

4.1 – Enzymatic Studies

Compounds that influence the rates of the reactions catalyzed by enzymes are termed inhibitors or substrates accordingly with their ability to reduce the rate (inhibition) or increase the substrate turnover (activation), respectively.

The relationship between a single substrate and enzyme concentration was interpreted in 1913 by Leonor Michaelis and Maud Menten with their classic Michaelis-Menten kinetics¹⁵² (**Equation 4.1**):

$$v = \frac{V_{\max}[S]}{K_m + [S]} \quad (4.1)$$

v - reaction rate

V_{\max} - maximum velocity

K_m - Michaelis-Menten constant (substrate concentration at half-maximal velocity)

$[S]$ - Substrate concentration

The prerequisite of this kinetic model is that the concentration of enzyme is much lower than the concentration of substrate $[S]$ (i.e. enzyme concentration is the limiting factor). The *Michaelis-Menten* equation (4.1) describes a rectangular hyperbolic dependence of v on $[S]$ (**Figure 4.1**). In such curves, as $[S]$ is increased, v approaches the limiting value, V_{\max} , in an asymptotic fashion. V_{\max} can be determined experimentally from a substrate saturation curve, and K_m can be derived from $\frac{V_{\max}}{2}$ (**Figure 4.1**).¹⁵³

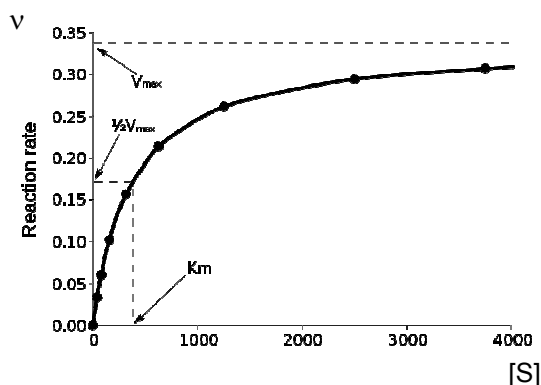


Figure 4.1: Saturation curve for an enzyme showing the relation between the concentration of substrate and rate. The units of K_m and $[S]$ are concentration, e.g. mM or μM , and the units of V_{\max} and v are amount of product over time, typically $\mu\text{mol}/\text{min}$ or similar.

The rearrangement of the *Michaelis-Menten* equation is the mathematical basis to transform it into a straight-line equation. *Lineweaver-Burk* analysis (or double reciprocal plot) is one of the best known methods of linearizing substrate velocity data so that the kinetic constants K_m and V_{\max} can be determined. Taking the reciprocal of both sides of the *Michaelis-Menten* equation (4.1), the equality **Equation 4.2** is obtained.¹⁵⁴

$$\frac{1}{v} = \left(\frac{K_m}{V_{\max}} \right) \left(\frac{1}{[S]} \right) + \frac{1}{V_{\max}} \quad (4.2)$$

The kinetic constants K_m and V_{\max} can be determined from the slope and intercept values of the linear fit of the data in a *Lineweaver-Burk* plot (**Figure 4.2**).

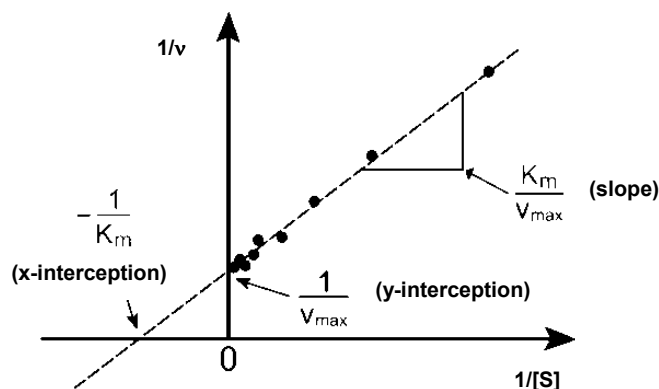


Figure 4.2: Lineweaver-Burk double-reciprocal plot, depicting extrapolations that allow the determination of K_m and V_{max} .

Other graphical methods for presenting enzyme kinetic data are *Eadie—Hofstee* (v as a function of $v/[S]$), *Hanes—Wolff* ($[S]/v$ as a function of $[S]$), and *Eisenthal—Cornish-Bowden* direct plots (v as function of $[S]$).

The method used in this thesis was the direct linear plot of *Eisenthal-Cornish Bowden* which has several advantages to the widely used methods of least squares: 1) It is very simple to construct; 2) requires no modification of the data; 3) it is a non-parametric method which avoids the undesired influence of errors caused by the use of reciprocals. For example, in the *Lineweaver-Burk* plot ($1/v$ Vs $1/[S]$) the lowest values of $[S]$ correspond to the highest values of $1/[S]$, and because of the details of linear regression, these data points are weighted more heavily in the analysis.^{154b, 155}

Like the above-mentioned methods, the direct linear plot is also a linearization (**Equation 4.3**) of the *Michaelis-Menten* equation:

$$V_{max} = v + \frac{v}{[S]} K_m \quad (4.3)$$

For fixed values of $[S]$ and v the **Equation 4.3** behaves as a straight line. Two pairs of ($[S]$, v) data values generate two straight lines which intersect as shown in **Figure 4.3 A**. The common intersection point between the lines is the best estimate of k_m and V_{max} . Considering more than two ($[S]$, v) pairs, and these are error free, these lines will also intersect in a point as shown in **Figure 4.3 B**. In a non-ideal experiment the best estimates of k_m and V_{max} are taken as the median value of a set of experiments (**Figure 4.3 C**).¹⁵⁶

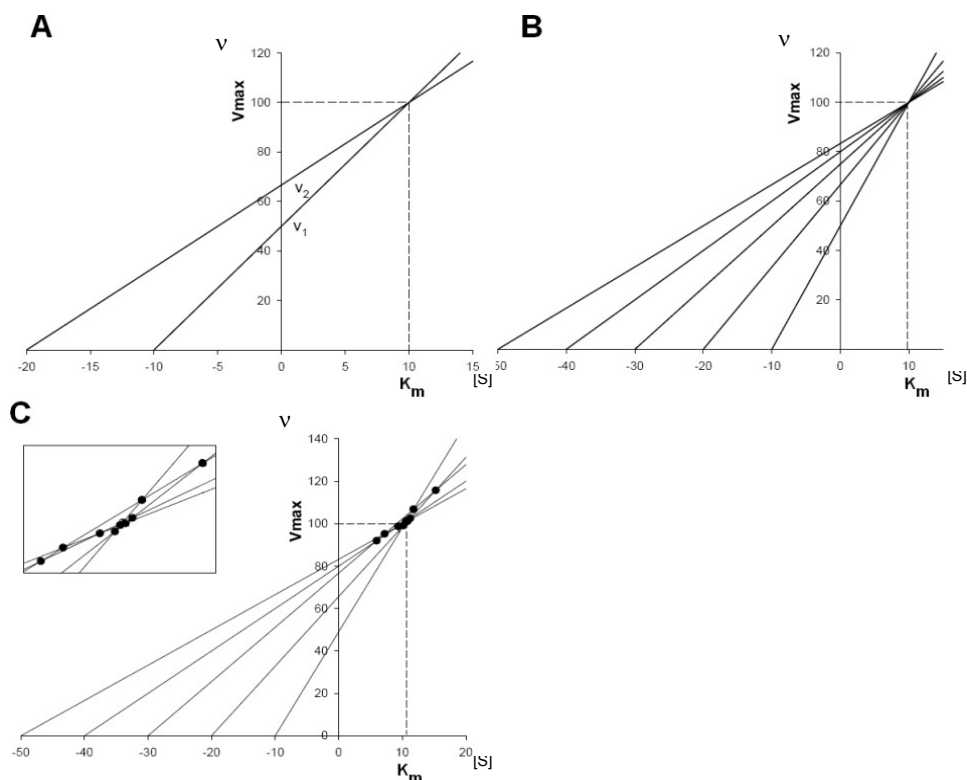


Figure 4.3: **A and B)** The direct linear plot is a graph of straight lines defined by $([S], v)$ data pairs on a K_m, V_{max} coordinate system. The intersection of the lines defines the K_m and V_{max} . **C)** The direct linear plot for $([S], v)$ data with experimental errors do not converge and the k_m and V_{max} are then taken as the median of the values.

The *Michaelis-Menten* equation for the rate (v) of an enzyme catalyzed reaction in the presence of an inhibitor is given by:

$$v = \frac{V_{max}^{app}[S]}{[S] + \underbrace{K_m^{app}}_{K_m \left(1 + \frac{[I]}{K_i}\right)}} \quad (4.4)$$

where K_m^{app} is the apparent k_m value of the substrate in the presence of an inhibitor. **Equation 4.4** shows that, the extent to which the reaction is slowed depends on the inhibitor concentration $[I]$ and the dissociation constant, K_i , for the enzyme inhibitor complex.^{154b} Using a fixed concentration of an inhibitor and different concentrations of the substrate, the K_m^{app} can be obtained from a direct linear plot similar to the one shown in **Figure 4.3**. Knowing the K_m^{app} , the k_m of the substrate and the concentration of the inhibitor, the K_i can be directly calculated from $K_m^{app} = K_m \left(1 + \frac{[I]}{K_i}\right)$.

4.1.1 – Enzymatic Activity of iNOS in the Presence of L11 – L21 and Re11 – Re21.

As mentioned before, the iNOS activity was determined spectrophotometrically by monitoring the NO-mediated conversion of oxyhemoglobin (6 μM) to methemoglobin at two wavelengths (401 and 421 nm), using a methemoglobin minus oxyhemoglobin extinction coefficient of $77.2 \text{ mM}^{-1}\text{cm}^{-1}$.¹⁵⁷ The oxyhemoglobin was prepared as described in **Section 7.9.1**. Briefly, bovine hemoglobin was reduced to oxyhemoglobin with excess of sodium dithionite. The sodium dithionite was later removed by dialysis. The concentration of oxyhemoglobin was determined spectrophotometrically using $\epsilon_{415 \text{ nm}} = 131 \text{ mM}^{-1}\text{cm}^{-1}$.¹⁵⁸

The kinetic parameters (K_m and K_i) for the compounds under study were determined using the conditions described in **Section 7.9.2**. The methodology applied is exemplified using the natural substrate L-Arg (**Section 7.9.2.1**). In **Figure 4.4** is shown the conversion of oxyhemoglobin (Fe^{2+}) to methemoglobin (Fe^{3+}) by NO, produced from the conversion of L-Arg to L-Cit, catalyzed by iNOS.

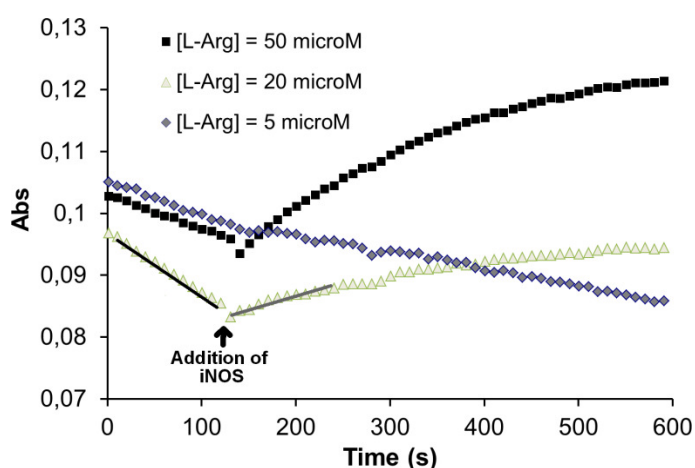


Figure 4.4: Kinetic curves of the conversion of L-Arg in L-Cit and NO catalyzed by iNOS. Standard incubations were constructed in a quartz cuvette (600 μM) containing 50 mM HEPES pH 7.4, 6 μM oxyhemoglobin, 200 μM NADPH, 10 μM H_4B , 100 μM DTT and different concentrations of L-Arg. Reactions were initiated by the addition of iNOS enzyme ($\sim 1 \text{ U}$) to the prewarmed cuvette ($\sim 2 \text{ min}$) and methemoglobin formation was followed by monitoring the increase in absorbance at dual wavelength (401 and 421 nm) for 10 min.

The difference of the slopes of the kinetic curves before and after addition of iNOS was used to determine the initial rate (v_0) for each L-Arg concentration (5, 20, 35, 50, 150 and 250 μM). These values were fitted to the *Michaelis-Menten* equation (**Figure 4.5 A**) and the k_m determined by the method of *Eisenthal* and *Cornish-Bowden* using the Hyper32 software (**Figure 4.5 B**).¹⁵⁹

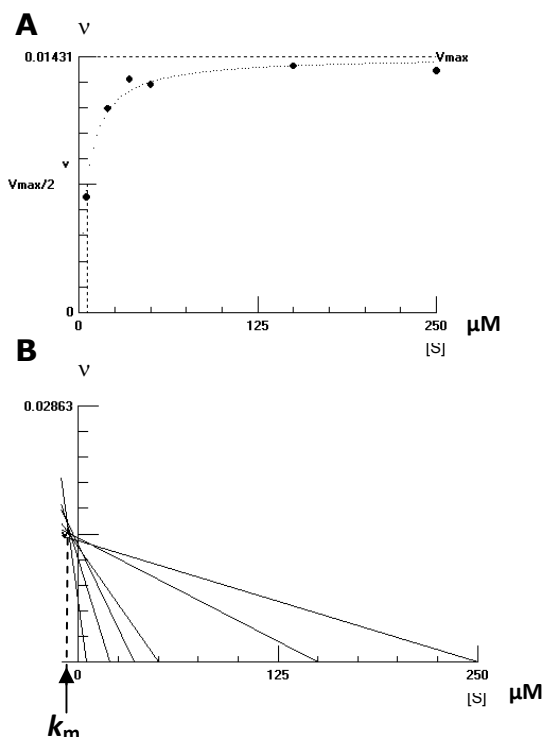


Figure 4.5: **A)** Initial rates of the iNOS catalyzed conversion of L-Arg into L-Cit and NO as a function of the concentration of L-Arg. The line is fitted to the *Michaelis–Menten* equation. **B)** *Eisenthal–Cornish-Bowden* direct plot was used to determine the k_m value of L-Arg.

The fit of the data indicate that the reaction can be described by the *Michaelis–Menten* equation. The k_m value obtained for the catalytic reaction of L-Arg by iNOS was 6 μM , which is in accordance with literature values.¹⁶⁰

The kinetic parameters of **L18/Re18**, **L19/Re19** and **L21/Re21**, potential NO-producing substrates, were determined as described above using three different concentrations of each compound (50 to 500 μM).

Inhibition constants of **L11 – L17**, **L20** and corresponding rhenium complexes **Re11 – Re17**, **Re20** were calculated by varying the concentration of the substrate L-Arg (20 – 150 μM) at a fixed concentration of the inhibitor (50 - 150 μM). The equation $K_i = [I]/((K_m^{\text{app}} / K_m) - 1)$ was used to determine the K_i values ($[I]$ is the inhibitor concentration, K_m is the *Michaelis-Menten* constant of L-Arg and K_m^{app} is the K_m apparent value of L-Arg obtained in the presence of each inhibitor). As an example, the K_m^{app} value obtained for L-Arg in the presence of inhibitor **Re11** was 72.5 μM that corresponds to a K_i of 8.69 μM (**Figure 4.6**).

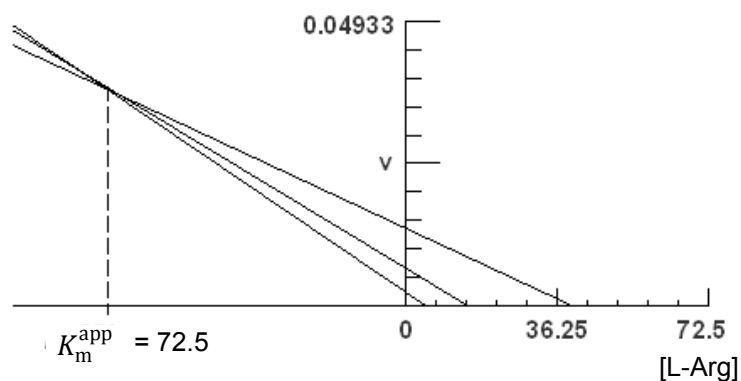
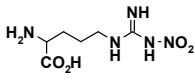
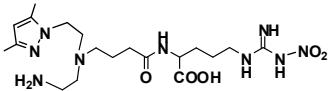
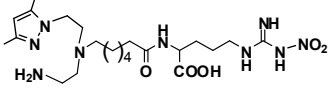
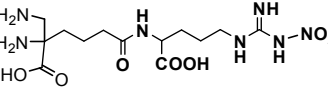
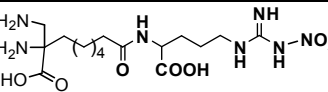
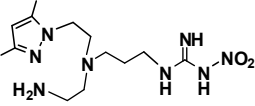
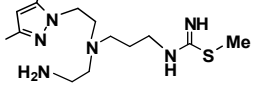
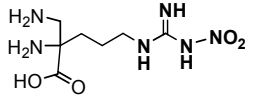
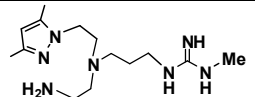
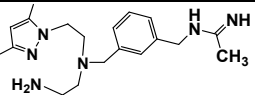
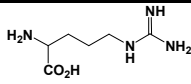
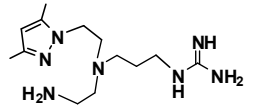
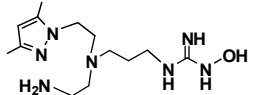
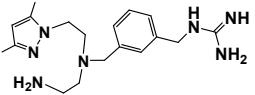


Figure 4.6: K_m^{app} value obtained for L-Arg (5, 15 and 40 μM) in the presence of **Re11** (100 μM) using the *Cornish-Bowden* direct plot.

Following a similar procedure, the kinetic parameters (K_i and K_m) of **L11** – **L21** and **Re11** – **Re21** were determined, and the results are summarized in **Table 4.1**.

Table 4.1: K_m and K_i values of conjugates and Re(I) complexes determined experimentally using the oxyhemoglobin NO capture assay.

| Inhibitor | k_i values (μM) ^a |
|---|---|
|  $\text{N}^{\omega}\text{-NO}_2\text{-L-Arg}$ | 3.00 ± 0.90 |
|  $\text{fac-}[\text{Re}(\text{CO})_3(\kappa^3\text{-L2})]$ | L2 178.11 ± 10.76 |
| $\text{fac-}[\text{Re}(\text{CO})_3(\kappa^3\text{-L2})]$ | Re2 84.15 ± 6.51 |
|  $\text{fac-}[\text{Re}(\text{CO})_3(\kappa^3\text{-L11})]$ | L11 36.05 ± 3.76 |
| $\text{fac-}[\text{Re}(\text{CO})_3(\kappa^3\text{-L11})]$ | Re11 6.15 ± 2.46 |
|  $\text{fac-}[\text{Re}(\text{CO})_3(\kappa^3\text{-L12})]$ | L12 6.19 ± 1.62 |
| $\text{fac-}[\text{Re}(\text{CO})_3(\kappa^3\text{-L12})]$ | Re12 57.19 ± 8.38 |
|  $\text{fac-}[\text{Re}(\text{CO})_3(\kappa^3\text{-L13})]$ | L13 759.62 ± 13.60 |
| $\text{fac-}[\text{Re}(\text{CO})_3(\kappa^3\text{-L13})]$ | Re13 258.68 ± 5.67 |

| | | |
|---|----------------------------|---|
|  | L14 | 1087.99 ± 183.03 |
| <i>fac</i> -[Re(CO) ₃ (κ ³ -L14)] | Re14 | 257.33 ± 52.99 |
|  | L15 | 1019.21 ± 73.59 |
| <i>fac</i> -[Re(CO) ₃ (κ ³ -L15)] | Re15 | 183.50 ± 30.88 |
|  | L16 | 29.43 ± 3.30 |
| <i>fac</i> -[Re(CO) ₃ (κ ³ -L16)] | R16 | 240.64 ± 4.63 |
|  | L17 | 413.82 ± 79.19 |
| <i>fac</i> -[Re(CO) ₃ (κ ³ -L17)] | Re17 | 454.94 ± 25.32 |
|  | L20 | 26.66 ± 2.75 |
| <i>fac</i> -[Re(CO) ₃ (κ ³ -L20)] | Re20 | 188.47 ± 7.52 |
| Substrate | | <i>k_m</i> values (μM)^a |
|  | N⁰-L-Arg | 6.00 ± 0.49 |
|  | L18 | 553.36 ± 132.65 |
| <i>fac</i> -[Re(CO) ₃ (κ ³ -L18)] | Re18 | 1035.35 ± 188.33 |
|  | L19 | 1675.20 ± 248.58 |
| <i>fac</i> -[Re(CO) ₃ (κ ³ -L19)] | Re19 | 1465.33 ± 172.15 |
|  | L21 | N.D. |
| <i>fac</i> -[Re(CO) ₃ (κ ³ -L21)] | Re21 | N.D. |

^a Results are given as a mean of three independent experiments.

N.D. - No iNOS activity was observed in the concentrations tested (100, 250 and 500 μM).

The enzymatic data demonstrate that derivatization of the NOS inhibitor N^{ω} -NO₂-L-Arg with the **pyrazolyl-diamine** and **Dap** chelating units affected negatively its binding to the active site of iNOS, as confirmed by the significantly higher K_i values found for **L2** (178 μ M), **L11** (36 μ M), **L12** (6 μ M) and **L13** (759 μ M) when compared with the K_i value determined for the corresponding free inhibitor (3 μ M). In the case of the conjugates containing the **pyrazolyl-diamine** chelating unit a longer spacer is responsible for a less negatively effect in the affinity for the enzyme (**L2**, C3-linker, K_i = 178 μ M Vs **L11**, C6-linker, K_i = 36 μ M). An opposite effect has been observed when the N^{ω} -NO₂-L-Arg is coupled to the **Dap** BFC. In this case the affinity of the inhibitors **L12** and **L13** decrease with increasing length of the spacer (**L12**, C3-linker, K_i = 6 μ M Vs **L13**, C6-linker, K_i = 759 μ M). Interestingly, the affinity of the N^{ω} -NO₂-L-Arg to the enzyme is almost unchanged upon conjugation to the **Dap** chelator with a 3 carbon linker (**L12**, K_i = 6 μ M). However, such affinity is lost upon metallation of **L12** to give **Re12** (K_i = 57 μ M). Unlike **L12**, reaction of the analog conjugates **L2** (K_i = 178 μ M), **L11** (K_i = 36 μ M), and **L13** (K_i = 759 μ M) with the organometallic moiety *fac*-[Re(CO)₃]⁺ gave complexes with increased inhibitory potencies (**Re2**, K_i = 84 μ M; **Re11**, K_i = 6 μ M; **Re13**, K_i = 258 μ M). It is worth to mention that **Re11** has an inhibitory potency comparable to that of the free inhibitor N^{ω} -NO₂-L-Arg (K_i = 3 μ M). The increased inhibitory potency after metallation occurs independently of the chelating unit involved in the stabilization of the organometallic core (e.g. **L11**, 36 μ M \rightarrow **Re11**, 6 μ M Vs **L13**, 759 μ M \rightarrow **Re13**, 258 μ M) and spacer length (e.g. **L2**, 178 μ M \rightarrow **Re2**, 84 μ M Vs **L11**, 36 μ M \rightarrow **Re11**, 6 μ M).

The affinity of the conjugates containing an integrated amidine moiety and a **pyrazolyl-diamine** backbone (**L14**, K_i = 1087 μ M; **L15**, K_i = 1675 μ M; **L17**, K_i = 413 μ M) is lower than that observed for conjugates **L2**, **L11**, and **L12**, which contain a pendant N^{ω} -NO₂-L-Arg moiety. These results indicate that the absence of an amino acid unit and the shortening of the spacer between the **pyrazolyl-diamine** chelating unit and the amidine moiety disturbs the interaction with the active site of iNOS. A less drastic effect was observed in the case of the conjugate containing the NO₂-guanidine moiety and the **Dap** chelating unit, which displayed good/moderate affinity for iNOS (**L16**, K_i = 29 μ M). The presence of a CO₂H group in the **Dap** chelating unit is most likely responsible for this increase in the affinity. This result underlines the importance of the interaction between a free carboxylic acid and the active site of NOS, through hydrogen bonding, for enzyme activity. Reaction of **L14**, **L15**, and **L17** with the *fac*-[Re(CO)₃]⁺ yielded complexes with similar (**Re17**, K_i = 454 μ M) or increased inhibitory potency (**Re14**, K_i = 257 μ M; **Re15**, K_i = 183 μ M) toward the enzyme. On the contrary, metallation of **L16** yielded a rhenium complex (**Re16**) with lower inhibitory potency (K_i = 240 μ M).

The ability of **L18** ($K_m = 553 \mu\text{M}$) and **L19** ($K_m = 1675 \mu\text{M}$), which contain a guanidine or N-hydroxyguanidine moiety, respectively, to interact with the active site of iNOS and produce NO, is negligible compared to the natural substrate of the enzyme (L-Arg, $K_m = 6 \mu\text{M}$). Metallation of **L18** and **L19** led to complexes with lower (**R18**, $K_m = 1035 \mu\text{M}$) or comparable (**Re19**, $K_m = 1465 \mu\text{M}$) NO producing properties, respectively. These results reinforce the difficulty in finding NOS substrates with good affinity for the enzyme, especially in the case of the rhenium complexes, as we have described previously.⁴

As mentioned before, compound 1400W is one of the most selective inhibitors of human iNOS reported to date, with nanomolar potency (K_d value $\sim 7 \text{ nM}$).⁷⁹ The conjugate **L20**, which contains the 1400W pharmacophore, was also tested as a competitive inhibitor of murine iNOS. The results indicated that, despite being an inhibitor with moderate potency for iNOS (**L20**, $K_i = 26 \mu\text{M}$), the original inhibitory potency of 1400W is seriously affected. This effect was even more pronounced when the bioconjugate **L20** was metallated with “ $\text{Re}(\text{CO})_3$ ” to give **Re20** ($K_i = 188 \mu\text{M}$).

Compounds **L21** and **Re21**, which have a conformationally-restricted benzyl-guanidine moiety, were expected to act as substrates of iNOS, however, under the concentrations tested no activity was observed.

4.2 – *in vivo* Biological Evaluation: NO Inhibition in LPS-Induced RAW 264.7 Macrophages

Since crossing the cell membrane and subsequent interaction with iNOS is mandatory for tracer uptake and retention *in vivo*, we have tested the conjugates **L2**, **L11** – **L17** and corresponding Re complexes (**Re2**, **Re11** – **Re17**) in LPS-induced RAW 264.7 macrophages. The substrate-containing compounds (**L18**, **L19**, **L21** and **Re18**, **Re19**, **Re21**) were not assayed in this cell model due to their low ability to recognize the iNOS active site, as demonstrated previously by the enzymatic studies. We chose this cell line because it is reported to have increased NO biosynthesis due to iNOS overexpression after treatment with endotoxins such as LPS. LPS-induced iNOS overexpression was confirmed by western blot analysis of protein extracts using an anti-iNOS antibody (**Figure 4.7**), following the procedure described in **Section 7.10.2**.

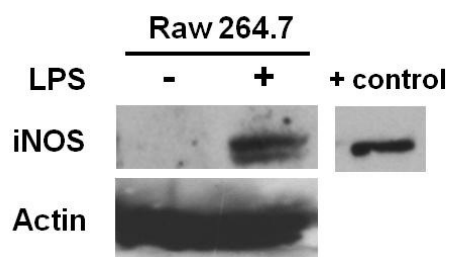


Figure 4.7: iNOS expression in RAW 264.7 macrophages after treatment with LPS for 24 h. Recombinant iNOS (6 μ g) was used as a positive control and actin as an internal loading control.

In the cell assay we have evaluated the *in vivo* ability of the compounds to suppress NO biosynthesis by measuring nitrite accumulation in the culture media using the Griess reagent method (Section 7.10.3).¹⁶¹ Figure 4.8 depicts the effect of tested compounds in nitrite production by LPS-induced macrophages. To assess the intrinsic cytotoxicity of the compounds at the concentration used in the NO assay (500 μ M) and, consequently, its influence in nitrite accumulation, we have also performed a cell viability assay (MTT assay, Section 7.10.4). The results obtained have shown that all compounds tested are nontoxic for the cells under the described experimental conditions as can be seen in Figure 4.8, and, therefore, no effect in NO production is expected.

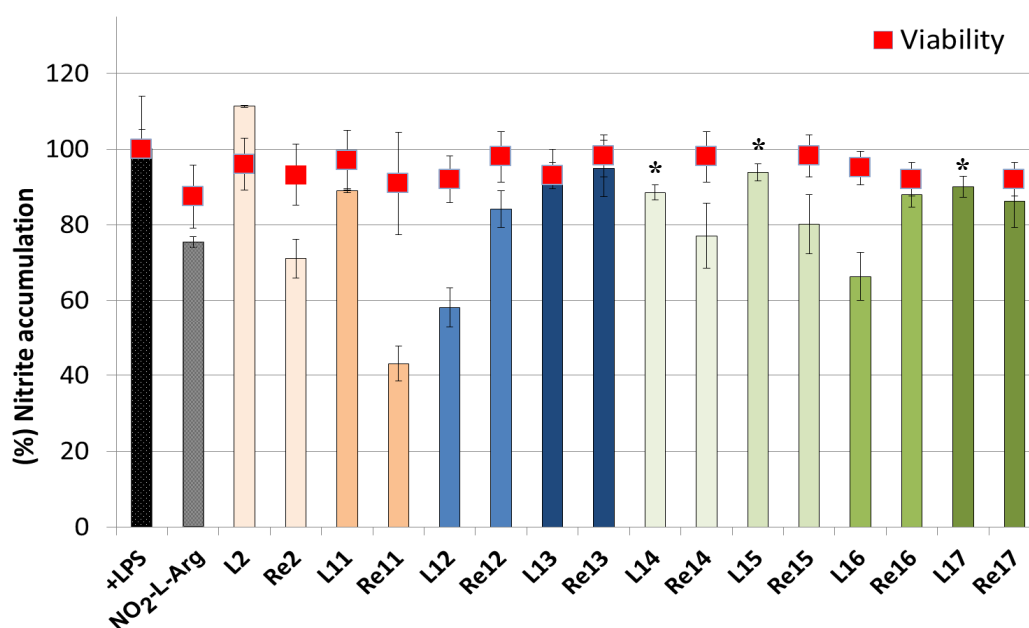


Figure 4.8: Effect of compounds L2, L11 – L17 and Re2, Re11 – Re17 in nitrite accumulation, and cell viability in LPS-induced RAW 264.7 macrophages (mean \pm S.D., n = 6). Final concentration of all compounds was 500 μ M. NO production and viability in LPS-induced cells in the absence of any compound (control) was considered 100%. This experiment was repeated three times with comparable results.* Cell viability was not evaluated.

The NO assay has demonstrated that **Re2** (ca. 30% inhibition) and **Re11** (ca. 50% inhibition), appeared as the most potent organometallic inhibitors of NO production by LPS-induced macrophages. Remarkably, **Re11** inhibited NO biosynthesis more effectively than the free inhibitor N^{ω} -NO₂-L-Arg (ca. 25%).

In the Dap-containing family the NO assay has demonstrated that **L12** (ca. 41 % inhibition), **L13** (ca. 5 % inhibition) and **L16** (ca. 33 % inhibition) displayed a significantly higher inhibitory potency than the corresponding rhenium complexes **Re12** (ca. 15 % inhibition), **Re13** (ca. 5 % inhibition) and **Re16** (ca. 12 % inhibition), respectively. Interestingly, **L16** presented an inhibitory potency comparable to that of the non-conjugated inhibitor N^{ω} -NO₂-L-Arg (ca. 25 % inhibition) and **L12** inhibited NO biosynthesis in a more effective way than N^{ω} -NO₂-L-Arg. This assay confirmed also that **L13** and **Re13** presented negligible inhibitory potency towards iNOS.

Analysis of the results obtained with the family of compounds containing the **pyrazolyl** chelator and the amidine moieties (**Re14**, **Re15** and **Re17**) has shown that all rhenium complexes were able to suppress NO production, however in a lower extent. The more pronounced effect was observed in the case of **Re14** and **Re15**, where ~ 20 % of NO suppression was observed. These results correlate well with the *in vitro* enzymatic assays obtained for this family of compounds, where complexes **Re14** and **Re15** exhibited also the highest inhibitory potency towards iNOS (**Re14**, $K_i = 257 \mu\text{M}$ and **Re15**, $K_i = 183 \mu\text{M}$ Vs **Re17**, $K_i = 454 \mu\text{M}$). The conjugates **L14**, **L15** and **L17** showed a minor capacity for inhibition of the NO biosynthesis (< 10 %).

Brought together, the results obtained in the cell assay with LPS-induced macrophages corroborate the main conclusions drawn from the *in vitro* enzymatic assays performed with purified iNOS. The rhenium complexes **Re2** and **Re11**, or more precisely the ^{99m}Tc analogs, appeared as the most promising compounds to target *in vivo* the iNOS enzyme.

Since the inhibition of NO biosynthesis is influenced not only by the intrinsic inhibitory capacity of the complexes, but also by their ability to cross cell membranes, we have also evaluated the internalization degree of the radioactive analogs (**Tc2** and **Tc11**) of the best performing rhenium complexes **Re2** and **Re11** in LPS-induced RAW 264.7 macrophages (**Figure 4.9**). These studies, performed as described in **Section 7.10.5**, allowed us to conclude that the affinity of **Re11** for the enzyme is strong enough to surpass its lower ability for crossing the cell membrane as demonstrated with its radioactive analog **Tc11** (**Figure 4.9**). In fact, when compared with **Tc2**, the radiocomplex **Tc11** has a lower internalization level ($0.43 \pm 0.06 \%$ for **Tc11** Vs $0.83 \pm 0.06 \%$ for **Tc2** internalization/mg protein).

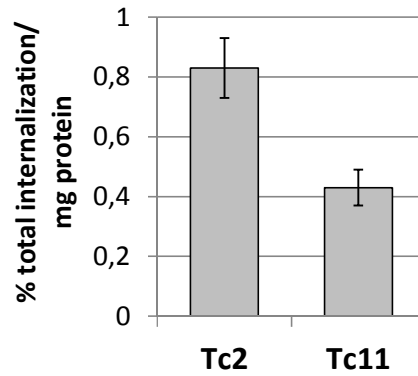


Figure 4.9: Internalization of the radioactive complexes **Tc2** and **Tc11** in LPS-induced RAW 264.7 macrophages (mean \pm S.D., $n = 4$; 37 °C, 4 h post-incubation). The internalization level is expressed as a percentage of applied radioactivity per milligram of total protein.

4.3 - *in vivo* Biodistribution Study in LPS-Treated Mice

In order to assess the potential of **Tc2** and **Tc11** for imaging *in vivo* of the expression of iNOS, we evaluate the biodistribution of these $^{99m}\text{Tc}(\text{I})$ complexes in an animal model with localized expression of the enzyme. The biodistribution studies were performed in mature male C57BL/6 mice: one group was treated with LPS (10 mg/kg, i.v.) to induce iNOS expression, and the control group was injected with PBS. LPS has been well documented to induce iNOS mRNA and protein expression in both rats and mice. Indeed, it has been demonstrated that iNOS expression after 6 – 7 h of LPS stimulation are increased in many organs, with the highest iNOS expression in the lungs.¹⁶² Following the procedure described in **Section 7.10.2** we have also confirmed increased levels of iNOS expression in lungs of LPS-treated mice by western blot analysis of total protein (**Figure 4.10**). Therefore, the LPS lung injury mouse model was used to assess the efficiency of **Tc2** and **Tc11** as an iNOS radiotracer.

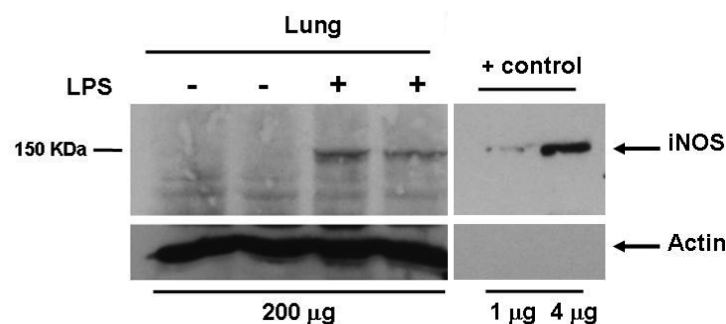


Figure 4.10: iNOS expression in the lungs of LPS-treated mice (10 mg/kg of LPS, 6 h). Recombinant iNOS (4 µg) was used as a positive control and actin as internal loading control.

The results of the biodistribution studies in normal, LPS-treated and LPS-treated mice blocked with a highly selective iNOS inhibitor (1400W) are shown in **Figure 4.11**. The biodistribution studies demonstrated that **Tc2** presented an overall higher uptake in most tissues of LPS-treated mice compared to the control group at 30 min postinjection (**Figure 4.11 A**). The highest uptake in both groups (PBS and LPS) was observed in the liver, intestine, and kidneys, which are likely to be the major metabolic and/or excretory sites for the tracer. In the organ expected to have the highest iNOS expression, the lungs, there was also an increase in the uptake (3.98 ± 0.76 % I.D./g) compared to the control group (0.99 ± 0.13 % I.D./g).

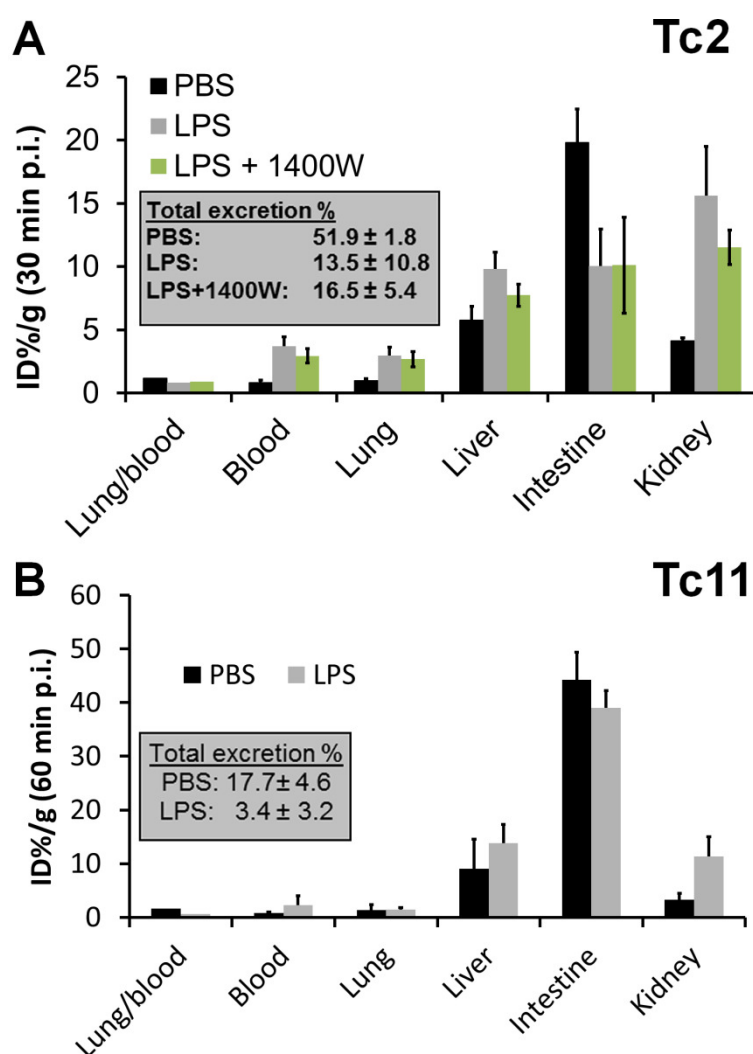


Figure 4.11: Biodistribution of **Tc2** (A, 30 min p.i.) and **Tc11** (B, 60 min p.i.) in control group (PBS), LPS-treated mice (LPS) and LPS-treated mice blocked with a highly selective iNOS inhibitor (LPS + 1400W) after intravenous injection (mean \pm S.D., n = 4 - 5).

Compound **Tc11** did not present any significant increase of radioactivity in the lungs of pretreated animals compared to the control group at 15 and 60 min postinjection (**Figure 4.11 B**).

Comparing **Tc2** and **Tc11** the highest lung uptake was observed for **Tc2** (3.98 ± 0.76 Vs 1.35 ± 0.99 % I.D./g; 30 min p.i. and 60 min p.i., respectively)(**Figure 4.11**).

To assess whether the increased uptake in the LPS-treated mice was due to specific binding of **Tc2** to iNOS, blocking studies with the highly selective iNOS inhibitor 1400W were carried out. For the group LPS + inhibitor, 5 mg/Kg of 1400W was co-injected with **Tc2** (**Figure 4.11 A**; LPS + 1400W). The inhibitor failed to block the increased uptake of **Tc2** in lungs of the LPS-treated group (2.67 ± 0.59 Vs 2.98 ± 0.63 % ID/g for LPS-treated mice with and without inhibitor, respectively), indicating that such increase may not be due to a specific binding of tracer **Tc2** to iNOS. Alternatively, we may hypothesize that the concentration of the inhibitor was not enough to block the iNOS, as described by Welch and co-workers.⁸⁵ The use of higher concentrations of 1400W is not possible since this inhibitor is highly toxic. In order to address this issue, further studies with less toxic and higher selective iNOS inhibitors should be used in new blocking studies.

HPLC analysis of serum and urine samples from both PBS, LPS and LPS + 1400W groups revealed that **Tc2** and **Tc11** are stable *in vivo* as more than 98 % of the radioactivity could be assigned to the original unchanged complexes.

4.4 - Conclusion

The biological affinity of the conjugates and corresponding rhenium complexes containing a **pyrazolyl-diamine** or a **Dap** chelating unit and iNOS recognizing moieties was tested *in vitro* with purified iNOS (oxyhemoglobin NO capture assay). The enzymatic assays confirmed again that the affinity of the conjugates with pendant inhibitors seemed to be less affected upon metallation with rhenium than the conjugates containing pendant substrates. Some of the inhibitor-containing rhenium complexes still present a considerable affinity for the enzyme. Indeed, the Re(I) complexes with a N^{ω} -NO₂-L-Arg moiety coupled to the **pyrazolyl-diamine** or **Dap** chelating unit through a spacer of 3- or 6-carbons presented remarkable affinity for iNOS (**Re2**, $K_i = 84 \mu\text{M}$; **Re11**, $K_i = 6 \mu\text{M}$; **Re12**, $K_i = 57 \mu\text{M}$). These unprecedented results motivated us to evaluate their ability to cross cellular membranes and to interact intracellularly with iNOS.

Both the conjugates and their Re(I) complexes were tested in RAW 264.7 macrophages, which present increased NO biosynthesis due to iNOS overexpression after treatment with LPS (confirmed by western blot). The results demonstrated that **Re2** (ca. 30% inhibition) and **Re11** (ca. 50% inhibition) inhibited NO biosynthesis in a more effective way.

The ability of **Re2** and **Re11** to interact with intracellular iNOS, and the moderate ability of the corresponding **Tc2** and **Tc11** analogs to cross cell membranes (accessed by internalization

studies), motivated us to evaluate the biodistribution of these ^{99m}Tc complexes in LPS-pretreated mature female C57BL/6 mice. Biodistribution studies in a mice model with localized iNOS expression have shown that **Tc2** has a higher uptake in the lungs of the LPS-treated mice than those in the control mice. The increased uptake in the lungs was not reduced by co-injection with the highly selective inhibitor 1400W, suggesting that the uptake in the lungs is not related with the specific binding of the **Tc2** to iNOS. However, further *in vivo* blocking studies with other iNOS inhibitors should be performed to confirm the iNOS-specific binding to the lungs.

6

Concluding Remarks and Perspectives

6. Concluding Remarks and Perspectives

The main goal of this thesis was the design and pre-clinical evaluation of $^{99m}\text{Tc}(\text{CO})_3$ -complexes containing iNOS-recognizing bioactive units for probing the overexpression of the enzyme *in vivo* associated to several diseases.

In this context, considering that tridentate chelators form stable complexes with the $\text{fac-}[^{99m}\text{Tc}(\text{CO})_3]^+$ core, we have synthesized and characterized new **pyrazolyl-diamine-** (**L4 – L7**) and diamino propionate- (**Dap**) containing chelators (**L8 – L10**), with different spacers (propyl or hexyl) and terminal functional groups (CO_2H and NH_2) for conjugation to L-Arg derivatives or transformation into bioactive units.

The chelators **L4 – L10** reacted with $(\text{NEt}_4)_2[\text{ReCO}_3\text{Br}_3]$ and/or $\text{fac-}[\text{M}(\text{CO})_3(\text{H}_2\text{O})_3]^+$ yielding model complexes of the type $\text{fac-}[\text{M}(\text{CO})_3(\kappa^3\text{-L})]^{+/0}$ ($\text{M} = \text{Re}/^{99m}\text{Tc}$; **Re4/Tc4**, **L = L4**; **Re5/Tc5**, **L = L5**; **Re6/Tc6**, **L = L6**; **Re7/Tc7**, **L = L7**; **Re8/Tc8**, **L = L8**; **Re9/Tc9**, **L = L9**; **Re10/Tc10**, **L = L10**) (Scheme 6.1).

1D- and 2D-NMR spectroscopic studies performed for the Re(I) complexes allowed a complete assignment of the resonances and elucidation of the coordination mode. In the case of **Re4 – Re7** the chemical shifts and splitting pattern of the diastereotopic protons of the pyrazolyl coordinating unit compare to those found for other complexes of the same type previously described by our group. The tridentate coordination mode of the **pyrazolyl-diamine** chelators through the *N,N,N* donor atom set was also confirmed by X-ray structural analysis of **Re4** and **Re5**.

The tridentate coordination mode of **L8 – L10** (*N,N,O* donor atom set of the **Dap** unit) to the metal center was also confirmed by NMR studies and X-Ray diffraction analysis of **Re8**.

The $^{99m}\text{Tc}(\text{I})$ tricarbonyl model complexes **Tc4 – Tc10** were prepared in high yield and high radiochemical purity. *In vitro* and *in vivo* studies demonstrated that the complexes are stable and present, in general, a good biological profile. The most favorable pharmacokinetic properties were found for **Tc4**, **Tc5**, **Tc8** and **Tc10**, which showed a good clearance from all organs and tissues. These results encouraged the use of **pyrazolyl-diamine-** and **Dap**-based compounds as bifunctional chelators for labeling iNOS-recognizing molecules with $\text{fac-}[^{99m}\text{Tc}(\text{CO})_3]^+$.

Following the promising results obtained with the model complexes, we developed synthetic strategies for the preparation of novel “bioactive” conjugates (**L11 – L21**) comprising the **pyrazolyl-diamine** and **Dap** chelating units linked to iNOS recognizing moieties (N^0 - NO_2 -L-Arg, alkyl-amidine, and conformationally-restricted benzyl-amidine moieties) through spacers of different lengths.

The conjugates reacted with the corresponding organometallic precursors, yielding compounds of the type $\text{fac-}[\text{M}(\text{CO})_3(\kappa^3\text{-L})]^{+/0}$ ($\text{M} = \text{Re}/^{99m}\text{Tc}$; **Re11/Tc11**, **L = L11**; **Re12/Tc12**, **L = L12**; **Re13/Tc13**, **L = L13**; **Re14/Tc14**, **L = L14**; **Re15/Tc15**, **L = L15**; **Re16/Tc16**, **L = L16**; **Re17/Tc17**, **L = L17**; **Re18/Tc18**, **L = L18**; **Re19/Tc19**, **L = L19**; **Re20/Tc20**, **L = L20**; **Re21/Tc21**, **L = L21**) which were

thoroughly characterized by the usual analytical techniques in chemistry and radiochemistry (Scheme 6.1).

The affinity of the conjugates **L2** ($K_i = 178 \mu\text{M}$), **L11** ($K_i = 36 \mu\text{M}$), **L12** ($K_i = 6 \mu\text{M}$), **L13** ($K_i = 759 \mu\text{M}$), **L14** ($K_i = 1087 \mu\text{M}$), **L15** ($K_i = 1019 \mu\text{M}$), **L16** ($K_i = 29 \mu\text{M}$), **L17** ($K_i = 413 \mu\text{M}$), **L18** ($K_m = 553 \mu\text{M}$), **L19** ($K_m = 1675 \mu\text{M}$), **L20** ($K_i = 26 \mu\text{M}$), **L21** ($K_m > 10000 \mu\text{M}$) and the respective complexes **Re2** ($K_i = 84 \mu\text{M}$), **Re11** ($K_i = 6 \mu\text{M}$), **Re12** ($K_i = 57 \mu\text{M}$), **Re13** ($K_i = 258 \mu\text{M}$), **Re14** ($K_i = 257 \mu\text{M}$), **Re15** ($K_i = 183 \mu\text{M}$), **Re16** ($K_i = 240 \mu\text{M}$), **Re17** ($K_i = 454 \mu\text{M}$), **Re18** ($K_m = 1035 \mu\text{M}$), **Re19** ($K_m = 1465 \mu\text{M}$), **Re20** ($K_i = 188 \mu\text{M}$), **Re21** ($K_m > 10000 \mu\text{M}$) have been tested *in vitro* as inhibitors or substrates of iNOS, using the oxyhemoglobin NO capture assay. The enzymatic studies demonstrated that the affinity for the enzyme of the conjugates with pendant enzyme inhibitors seemed to be less affected upon metallation with “Re(CO)₃” than the conjugates containing pendant substrates. In fact, the ability of **Re18**, **Re19**, and **Re21** to interact with the active site of iNOS and produce NO is negligible ($k_m > 1000 \mu\text{M}$) compared to the natural substrate L-Arg ($K_m = 6 \mu\text{M}$). Interestingly, metallation of the inhibitor-containing conjugates with the “Re(CO)₃” core led to complexes with improved affinity for iNOS (**L2/Re2**, **L11/Re11**, **L13/Re13**, **L14/Re14**, **L15/Re15**). Out of this trend are the matched pairs **L12/Re12**, **L16/Re16** and **L20/Re20**.

The Re(I)-complexes with a N^{ω} -NO₂-L-Arg moiety coupled to the **pyrazolyl-diamine** or **Dap** chelating unit through a spacer of 3- or 6-carbon atoms presented remarkable affinity for iNOS (**Re2**, $K_i = 84 \mu\text{M}$; **Re11**, $K_i = 6 \mu\text{M}$; **Re12**, $K_i = 57 \mu\text{M}$). It is worth mentioning that in the case of **Re11**, its inhibitory potency is comparable to that of the free inhibitor N^{ω} -NO₂-L-Arg ($K_i = 3 \mu\text{M}$).

The affinity of the conjugates and rhenium complexes containing an integrated alkyl-amidine moiety (**L14** $K_i = 1087 \mu\text{M}$, **Re14** $K_i = 257 \mu\text{M}$; **L15** $K_i = 1675 \mu\text{M}$, **Re15** $K_i = 183 \mu\text{M}$; **L16** $K_i = 29 \mu\text{M}$, **Re16** $K_i = 240 \mu\text{M}$; **L17** $K_i = 413 \mu\text{M}$, **Re17** $K_i = 454 \mu\text{M}$) for iNOS is in general smaller than that observed for the N^{ω} -NO₂-L-Arg-containing compounds (**L2/Re2**, **L11/Re11**, and **L12/Re12**). These results indicated that the absence of an amino acid unit and the shortening of the linker between the chelator and the amidine moiety disturbs the interaction with the active site of iNOS. Compounds **L20** and **Re20**, which have a conformationally-restricted benzyl-acetamidine moiety, derived from the potent inhibitor 1400W (K_d value $\sim 7 \text{ nM}$), were tested as competitive inhibitors of murine iNOS. The results indicated that, despite being an inhibitor with moderate potency for iNOS (**L20**, $K_i = 26 \mu\text{M}$), the remarkable potency of the parent compound 1400W is significantly affected. This effect was even more pronounced when the bioconjugate **L20** was metallated with “Re(CO)₃” to give **Re20** ($K_i = 188 \mu\text{M}$).

The conjugates (**L2**, **L11** – **L17**) and their respective Re(I) complexes (**Re2**, **Re11** – **Re17**) were tested in activated RAW 264.7 macrophages, which presented increased NO biosynthesis due to

iNOS overexpression after treatment with LPS (confirmed by western blot). The results have shown that, from all the studied compounds, **Re2** (ca. 30% inhibition) and **Re11** (ca. 50% inhibition) displayed the highest inhibitory potency towards NO-biosynthesis.

Based on the enzymatic assays with purified iNOS and on the cell studies with RAW 264.7 macrophages, **Re2** and **Re11**, which contain the N^{ω} -NO₂-L-Arg inhibitor and the **pyrazolyl-diamine-Re(CO)₃** unit separated by 3- or 6-carbon atoms, respectively, emerged as the most promising compounds for targeting iNOS *in vivo*. Therefore, the internalization of the ^{99m}Tc(I) surrogates in RAW 264.7 macrophages was evaluated. Both complexes could cross the cell membrane, presenting **Tc2** a higher cellular internalization than **Tc11**.

All together, the data obtained for **Re2/Tc2** and **Re11/Tc11** motivated the *in vivo* evaluation of the ^{99m}Tc (I) complexes in mature female C57BL/6 mice pretreated with LPS for localized overexpression of iNOS (confirmed by western blot). The results obtained showed that **Tc2** has a higher uptake in the lungs of the LPS-treated mice than in the lungs of the control mice, which correlates well with the higher cell internalization found for **Tc2**. The increased uptake in the lungs was not reduced by co-injection with the highly selective inhibitor 1400W, which may suggest that the uptake is not specific. However, we may hypothesize that the concentration of the inhibitor was not enough to block the iNOS, as previously described by Welch and co-workers.⁸⁵ Further *in vivo* blocking studies with other iNOS inhibitors should be performed to confirm the specificity of the binding to the lungs.

To get an insight into the structural parameters responsible for the affinity found for the conjugates and rhenium complexes, we have studied these compounds by molecular docking and molecular dynamics (MD) simulations, to establish structure-activity relationships. Compounds **L2**, **L11**, **L12**, **L13**, **L16**, **Re2**, **Re11**, **Re12**, **Re13**, and **Re16** were docked into the iNOS enzyme using a docking methodology, which was previously validated using a set of X-ray structures of iNOS complexed with known substrates/inhibitors. The best docking conformations obtained for our compounds were refined based on MD simulations, and we concluded that the decreased affinity of N^{ω} -NO₂-L-Arg towards iNOS, after conjugation to the **pyrazolyl-diamine** and **Dap**-based chelators (**L2**, **L11**, **L12** and **L13**), could be explained by the loss of strong H-bonding between its α -NH₃⁺ group and the CO₂⁻ groups of the heme propionate A and Glu371 residue.

Upon metallation, the increased potency found for **Re2** ($K_i = 84 \mu\text{M}$), **Re11** ($K_i = 6 \mu\text{M}$) and **Re13** ($K_i = 258 \mu\text{M}$), compared to **L2** ($K_i = 178 \mu\text{M}$), **L11** ($K_i = 36 \mu\text{M}$) and **L13** ($K_i = 759 \mu\text{M}$), can be explained by the additional contacts observed between iNOS and the organometallic tails of these complexes. Comparing the close analogs **Re2** (3-carbon atoms linker) and **Re11** (6-carbon atoms linker), the higher inhibitory potency found for **Re11** is certainly associated with the strong

electrostatic interactions found between the “Re(CO)₃” core and the Arg260 and Arg382 residues, due to the higher flexibility of the longer linker in **Re11**.

The striking difference in inhibitory potency observed for **Re11** and **Re13**, which share the common NOS recognizing unit (6-Carbon-N^o-NO₂-L-Arg moiety) but are stabilized by chelators of different nature (**Re11**: **pyrazolyl-diamine** based and **Re13**: **Dap**-based), can be rationalized in terms of the different position, and different contacts formed between the “Re(CO)₃” organometallic moiety and the enzyme. In fact, in the case of **Re13** the bulky organometallic moiety is not well accommodated inside the active pocket of iNOS and is oriented toward its “open entrance”. Such behavior is explained by the electrostatic destabilization (99.46 ± 11.80 kcal/mol) found in the interaction between the heme group and the C6-**Dap**-Re(CO)₃ organometallic tail, or more precisely, between the CO₂⁻ group of the heme propionate D and the CO₂⁻ group of the **Dap** unit.

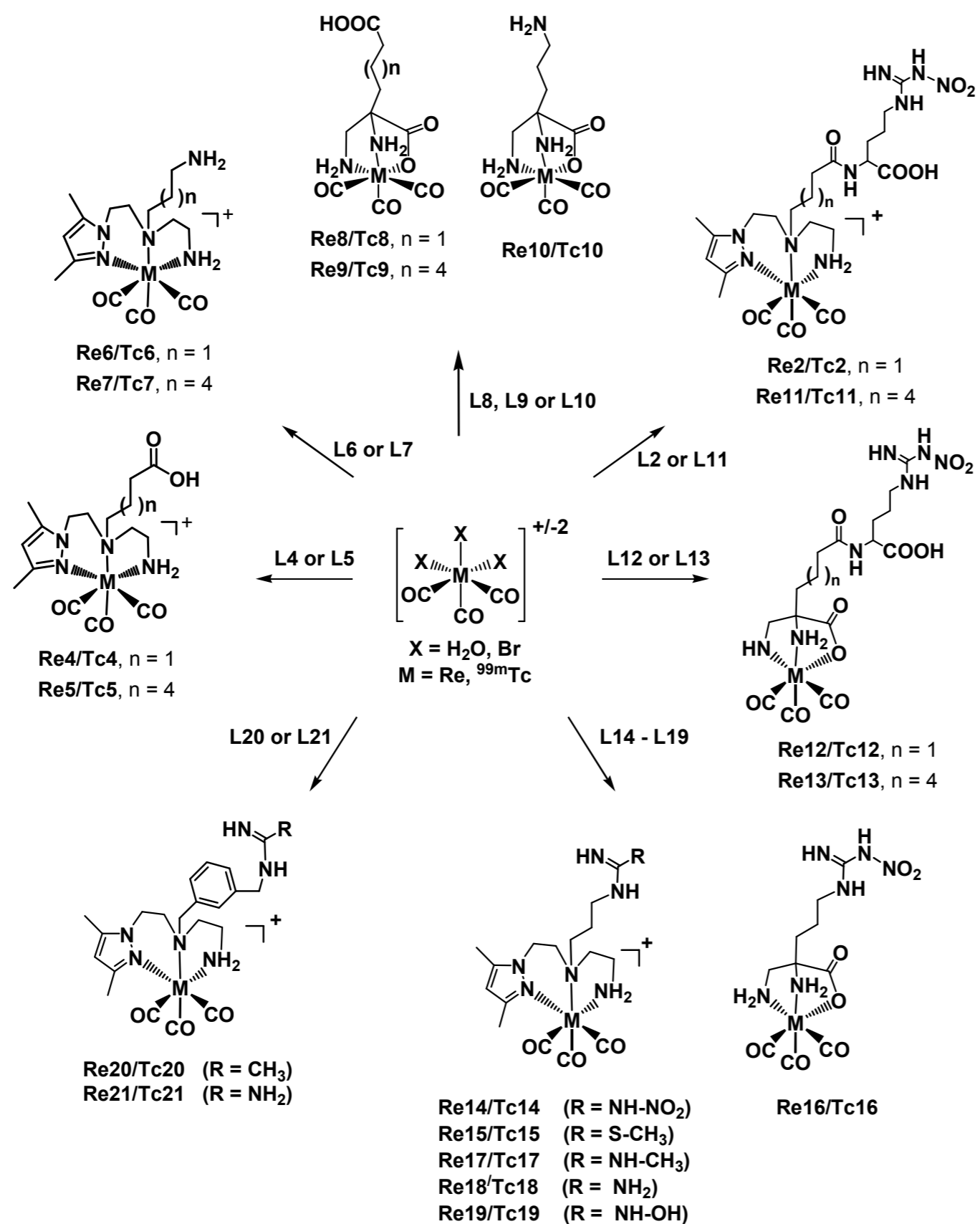
Metallation of **L12** and **L16** led to complexes with lower affinity (**Re12** and **Re16**), which could be most likely explained by the loss of the strong interactions present in the complexes **L12**:iNOS and **L16**:iNOS. In fact, inhibitors **L12** and **L16** show strong interactions between the -NH₃⁺ and CO₂⁻ groups of the **Dap** chelating unit and the polar residues of the iNOS binding cavity (Gln257, Arg260, Tyr341 and Asp376). After coordination to the “Re(CO)₃” core the NH₃⁺ and CO₂⁻ groups of the **Dap** chelator are no longer free to interact with the enzyme. The higher inhibitory potency found for **Re12** ($K_i = 57$ μM) when compared to **Re16** ($K_i = 240$ μM) can be explained by the absence of anchoring groups in **Re16** (e.g. CO₂⁻ group) and by the relatively less bulkiness of its organometallic tail, which provides a less extensive contact surface area.

Using the FEP methodology, we have also studied the effect on the binding affinity to iNOS of transforming **Re2** into **L2** and **Re11** into **L11**. We found that the free energy differences match the trend observed in the experimental data ($\Delta\Delta G_{\text{bind}}^{\text{calc}} \text{Re2} \rightarrow \text{L2} = 0.69 \pm 0.028$ kcal/mol, $\Delta\Delta G_{\text{bind}}^{\text{calc}} \text{Re11} \rightarrow \text{L11} = 6.80 \pm 1.10$ kcal/mol; $\Delta\Delta G_{\text{bind}}^{\text{exp}} \text{Re2} \rightarrow \text{L2} = 0.461 \pm 0.009$ kcal/mol, $\Delta\Delta G_{\text{bind}}^{\text{exp}} \text{Re11} \rightarrow \text{L11} = 1.129 \pm 0.210$ kcal/mol): 1) there is an energetic penalty for the transformation of the Re complexes into the ligands; 2) the higher energetic penalty found experimentally for the pair **Re11**/**L11** was confirmed by FEP. These data validate our docking and MD approach and support clearly our conclusions on the interactions occurring in the complexes.

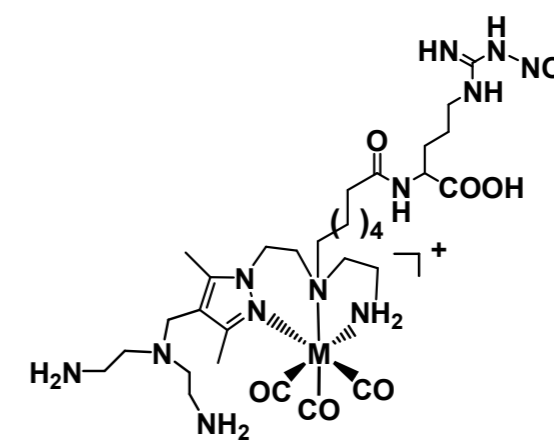
In conclusion, among all compounds studied, **Re2** and **Re11**, containing a **pyrazolyl-diamine** chelator, a 3- or 6-carbon atoms linker and a N^o-NO₂-L-Arg moiety, emerged as most interesting to target the iNOS enzyme. Combining enzymatic and computational studies it was possible to identify relevant structural features that seem to be crucial for ligand binding. Our computational methodology (Molecular docking combined with MD simulations and FEP calculations) showed a

good performance in terms of reproducing the experimental results, and can be applied with some confidence to predict the affinity of novel rhenium complexes prior to their synthesis. Based on our data, we envisaged that a rhenium complex similar to **Re11** but derivatized at the 4- position of the pyrazolyl ring with positively charged amines could be a promising complex to target iNOS (**Scheme 6.1**). We hypothesized that the free amines will interact with the heme propionates while the interaction between the “Re(CO)₃” core and the Arg260 and Arg382 residues will be conserved yielding complexes with improved affinity. Theoretical calculations (docking, MD simulations, FEP calculations) with such complexes is being considered as well as their synthesis and biological evaluation.

Main compounds described in this thesis.



Proposed compound for targeting iNOS



Scheme 6.1

7

Experimental part

7. Experimental Part

7.1 - Materials

All chemicals and solvents were of reagent grade and were used without purification, unless stated otherwise. The organometallic precursors $(\text{NEt}_4)_2[\text{Re}(\text{CO})_3(\text{Br})_3]$ and *fac*- $[\text{Re}(\text{CO})_3(\text{H}_2\text{O})_3]\text{Br}$ were prepared according to published methods.¹⁸⁵ Compounds **27**, **L4-Boc**, **L4** and **Re4** were synthesized as previously described.^{41a-d}

7.2 - Characterization and Purification Techniques

Elemental Analysis C, H, N, S

C, H, N and S analyses were performed using a EA110 CE Instruments automatic analyzer.

Infrared Spectroscopy (IR)

Infrared spectra were recorded as KBr pellets in a Bruker Tensor 27 spectrometer.

Nuclear Magnetic Resonance Spectrometry (NMR)

¹H- and ¹³C-NMR spectra were recorded in a Varian Unity 300 MHz spectrometer; ¹H and ¹³C chemical shifts were referenced to the residual solvent resonances relative to tetramethylsilane (SiMe_4). Multiplicities are reported using the following abbreviations: s (singlet), d (doublet), t (triplet), q (quartet), quint (quintuplet), m (multiplet), br (broad) or a suitable combination of them.

X-ray Crystallography

Crystallographic data of **Re8** were collected at 150 K on an Oxford Diffraction Xcalibur system with a Ruby detector. The program suite CrysAlis^{Pro} was used for data collection, semiempirical absorption correction, and data reduction.¹⁸⁶ Crystallographic data of **36-lactam**, **45**, **Re4**, **Re5**, bis(3-methylbenzyl)amine and **Re18** were collected at 150 K on a Bruker-AXS APEX-CCD area-detector diffractometer. Empirical absorption correction was carried out using SADABS.¹⁸⁷ Data collection and data reduction were done with the SMART and SAINT programs.¹⁸⁸ The structures were solved by direct methods with SIR97¹⁸⁹ and refined by full-matrix least-squares analysis with SHELXL97¹⁹⁰ using

the WINGX suite of programs. All non-hydrogen atoms were refined anisotropically. The hydrogen atoms were placed in calculated positions. Molecular graphics were prepared using ORTEP3.¹⁹¹ Significant crystal data collection and refinement parameters for **36-lactam**, **45**, **Re4**, **Re5**, **Re8**, bis(3-methylbenzyl)amine and **Re18** are listed in **Tables 8.1**, **8.2** and **8.4** (Annexes).

Column Chromatography

Some compounds were purified by column chromatography, using silica gel 60 with 70 - 230 mesh granulometry (ASTM Merck) and glass columns with dimensions appropriate to the amount of compound to purify.

Thin Layer Chromatography (TLC)

Some chemical reactions were monitored by TLC, using silica-gel plates MERCK 60-F₂₅₄ with 0.25 mm of thickness, in an aluminium support; the plates were analyzed with UV radiation or revealed with I₂.

High Performance Liquid Chromatography (HPLC)

Reversed phase HPLC (RP-HPLC) analyses were performed with a Perkin Elmer LC pump 200 coupled to an UV/VIS detector (Shimadzu SPD-10 AV or Perkin Helmer LC 290) or to a γ detector (Berthold-LB 507A or LB 509). The solvents were of HPLC grade and the water bidistilled from a quartz distillation unit. The solvents were filtered by Millipore 0.22 μ m filters and purged with helium.

Analytical Control

Column: Analytical, EC250/3 Nucleosil 100-5 C18, Macherey Nagel; **Pre-column:** EP 30/8 Nucleosil 100-7 C18, Macherey Nagel; **Flow:** 0.5 mL/min; **γ detection;** **UV detection:** λ = 254 or 220 nm; **Eluents:** **A** - TFA 0.1 % in H₂O; **B** - CH₃OH.

Semi-Preparative Purification of Compounds

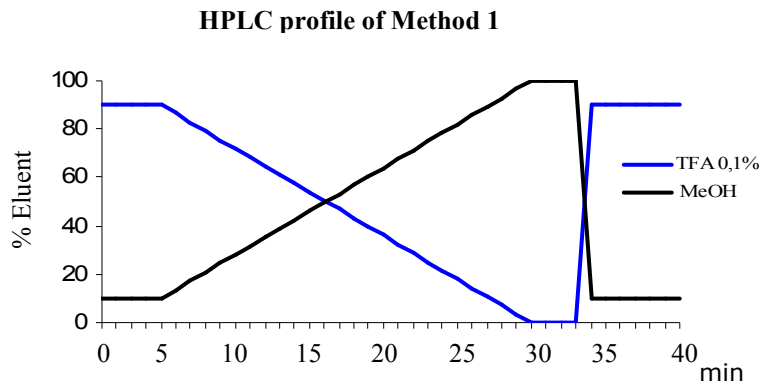
Column: Semi-Preparative, EP 250/8 Nucleosil 100-7 C18, Macherey Nagel; **Pre-column:** EP 30/8 Nucleosil 100-7 C18, Macherey Nagel; **Flow:** 2.0 mL/min; **UV detection:** λ = 254 or 220 nm; **Eluents:** **A** - TFA 0.1 % in H₂O; **B** - CH₃OH or **A** - Et₃N/CH₃COOH [2.1: 2.8 (v/v)]; **B** - MeOH.

Preparative Purification of Compounds

Column: Preparative, Waters μ Bondapak C18 (150/19 mm); **Pre-column:** Hypersil C18 (ODS), 4.6 \times 25 mm, 10 μ m; **Flow:** 5.0 mL/min; **UV detection:** λ = 254 or 220 nm; **Eluents:** **A** - TFA 0.1 % in H₂O; **B** - CH₃OH.

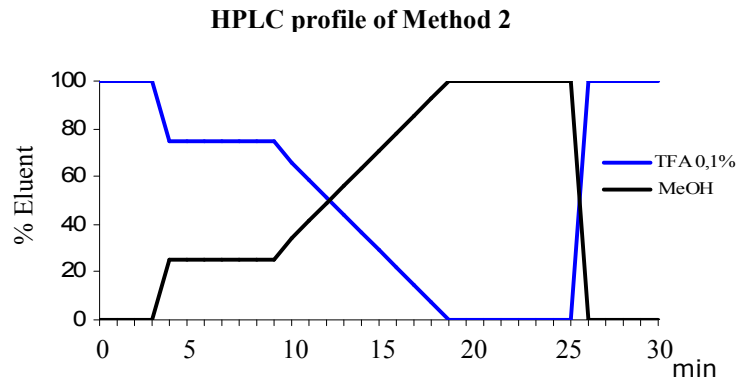
HPLC Method 1:

| Step | Time (min) | % A | % B |
|------|------------|--------------------|----------------------|
| 1 | 0 5 | 90 | 10 |
| 2 | 5 30 | 90 \rightarrow 0 | 10 \rightarrow 100 |
| 3 | 30 34 | 0 | 100 |
| 4 | 34 35 | 0 \rightarrow 90 | 100 \rightarrow 10 |
| 5 | 35 40 | 90 | 10 |



HPLC Method 2:

| Step | Time (min) | % A | % B |
|------|------------|----------------------|----------------------|
| 1 | 0 3 | 100 | 0 |
| 2 | 3 – 3.1 | 100 \rightarrow 75 | 0 \rightarrow 25 |
| 3 | 3.1 9 | 75 | 25 |
| 4 | 9 – 9.1 | 75 \rightarrow 66 | 25 \rightarrow 34 |
| 5 | 9.1 18 | 66 \rightarrow 0 | 34 \rightarrow 100 |
| 6 | 18 25 | 0 | 100 |
| 7 | 25 – 25.1 | 0 \rightarrow 100 | 100 \rightarrow 0 |
| 8 | 25.1 30 | 100 | 0 |



Mass Spectrometry

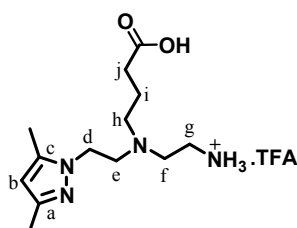
ESI/QITMS analyses of compounds were performed with a Bruker HCT instrument, which was acquired with the support of the Programa Nacional de Reequipamento Científico of FCT and is part of Rede Nacional de Espectrometria de Massa - RNEM).

Activity Measurements of Radioactive Solutions

The radioactivity of the ^{99m}Tc solutions was measured in an ionization chamber (Aloka, Curimeter IGC-3). The samples with activity less than 2 μCi were measured in a Gamma Counter (Berthold LB2111).

7.3 - Synthesis and Characterization of Compounds

7.3.1 - 4-((2-aminoethyl)(2-(3,5-dimethyl-1H-pyrazol-1-yl)ethyl)amino)butanoic acid (L4)

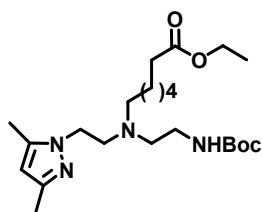


This compound was synthesized and characterized as previously reported by our group.^{41c}

$^1\text{H-NMR}$ (300 MHz, D_2O): δ_{H} (ppm) 6.11 (1H, s, CH_2^{b}), 4.50 (2H, t, CH_2^{d}), 3.53 (2H, t, CH_2^{e}), 3.44 (2H, m, $\text{CH}_2^{\text{g/f}}$), 3.35 (2H, m, $\text{CH}_2^{\text{g/f}}$), 3.15 (2H, m, CH_2^{j}), 2.29 (2H, t, CH_2^{h}), 2.16 (3H, s, CH_3Pz), 2.10 (3H, s, CH_3Pz), 3.15 (2H, m, CH_2^{i}).

$^{13}\text{C-NMR}$ (75.5 MHz, D_2O): δ_{C} (ppm) 183.0 (COOH), 165.3 (q, CF_3COO^-), 148.2 (C^{c}), 141.4 (C^{a}), 118.6 (q, CF_3COO^-), 106.0 (C^{b}), 54.2, 54.0, 52.0, 47.0, 38.4, 36.0, 24.7, 13.3 (CH_3Pz); 11.0 (CH_3Pz).

7.3.2 - Ethyl 7-((2-(*tert*-butoxycarbonylamino)ethyl)(2-(3,5-dimethyl-1*H*-pyrazol-1-yl)ethyl)amino)heptanoate (29)

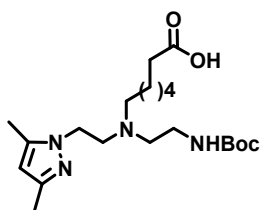


Ethyl-7-bromoheptanoate (0.670 g, 2.830 mmol), K_2CO_3 (0.390 g, 2.830 mmol), and a catalytic amount of KI were added to a solution of **27** (0.400 g, 1.40 mmol). After refluxing for 18h, the solution was filtered, vacuum dried, and the residue was purified by silica gel column chromatography using a gradient of EtOAc (50 \rightarrow 100 %) in hexane. **29** was obtained as a pale yellow oil upon removal of the solvents from the collected fractions. Yield: 80.7 % (0.500 g, 1.130 mmol).

1H -NMR (300 MHz, $CDCl_3$): δ_H (ppm) 5.72 (1H, s, CH^b), 5.05 (1H, br s, NHBoc), 4.08 (2H, q, OCH_2CH_3), 3.93 (2H, t, CH_2^d), 3.02 (2H, br m), 2.73 (2H, t), 2.46 (2H, t), 2.36 (2H, t), 2.23 (2H, t), 2.21 (3H, s, CH_3Pz), 2.17 (3H, s, CH_3Pz), 1.55 (2H, m), 1.32 (9H, s, CH_3), 1.27 (2H, m), 1.21 (5H, m, $OCH_2CH_3 + CH_2$), 1.16 (m, 2H).

HPLC (R_t): 21.0 min ($\lambda = 220$ nm, Method 1).

7.3.3 - 7-((2-(*tert*-butoxycarbonylamino)ethyl)(2-(3,5-dimethyl-1*H*-pyrazol-1-yl)ethyl)amino)heptanoic acid (L5-Boc)

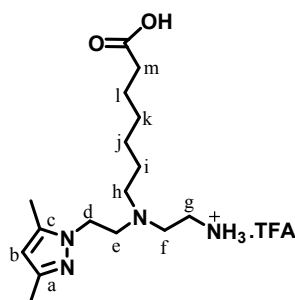


29 (0.500 g, 1.130 mmol) was dissolved in a H_2O/THF (1:10, 33 mL), and an excess of NaOH (0.450 g, 11.310 mmol) was added. The solution was refluxed overnight, carefully neutralized with 1 M HCl at 0 $^\circ C$ and extracted with CH_2Cl_2 . The organic phases were collected, dried over $MgSO_4$, filtered and the solvent evaporated. The crude product was purified by silica gel column chromatography using a gradient of MeOH (5 \rightarrow 100 %) in $CHCl_3$, giving a pale yellow oil corresponding to **L5-Boc** after evaporation of the solvent from the collected fractions. Yield: 85.8 % (0.400 g, 0.970 mmol).

1H -NMR (300 MHz, $CDCl_3$): δ_H (ppm) 5.70 (1H, s, CH^b), 5.16 (1H, br s, NHBoc), 3.91 (2H, t), 2.97 (2H, m), 2.72 (2H, t), 2.43 (2H, t), 2.35 (2H, t), 2.16 (3H, s, CH_3Pz), 2.12 (3H, s, CH_3Pz), 1.45 – 1.20 (10H, m), 1.37 (9H, s, CH_3).

HPLC (R_t): 20.0 min ($\lambda = 220$ nm, Method 1).

7.3.4 - 7-((2-aminoethyl)(2-(3,5-dimethyl-1H-pyrazol-1-yl)ethyl)amino)heptanoic acid (L5.TFA)



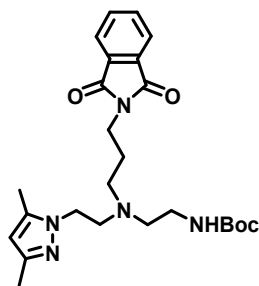
L5 was obtained directly by dissolving **L5-Boc** (0.170 g, 0.410 mmol) in a mixture of $\text{CH}_2\text{Cl}_2/\text{TFA}$ (1 mL/2 mL) and allowed to react for 3 h at room temperature with stirring. The residue obtained after evaporation of the solvent was dissolved in H_2O , filtered through a 0.45 μm Millipore® filter, and purified by preparative RP-HPLC (Method 1). The fractions containing **L5** were collected and the solvent removed to provide a clear viscous colorless oil. Yield: 92.7 % (0.160 g, 0.380 mmol, calcd. for $\text{C}_{16}\text{H}_{30}\text{N}_4\text{O}_2 \cdot \text{TFA}$).

$^1\text{H-NMR}$ (300 MHz, D_2O): δ_{H} (ppm) 5.94 (1H, s, CH^{b}), 4.35 (2H, t, CH_2^{d}), 3.59 (2H, t, CH_2^{e}), 3.44 (2H, m, CH_2^{f}), 3.33 (2H, m, CH_2^{g}), 3.09 (2H, m, CH_2^{m}), 2.23 (2H, m, CH_2^{h}), 2.20 (3H, s, CH_3Pz), 2.12 (3H, s, CH_3Pz), 1.52 (2H, m, CH_2^{l}), 1.45 (2H, m, CH_2^{l}), 1.18 (4H, m, CH_2^{j} , CH_2^{k}).

$^{13}\text{C-NMR}$ (75.5 MHz, D_2O): δ_{C} (ppm) 176.5 (CO), 165.3 (q, CF_3COO^-), 149.3 (Pz), 145.4 (Pz), 118.3 (q, CF_3COO^-), 106.4 (Pz), 54.3, 53.4, 49.8, 42.2, 33.8, 33.5, 27.7, 25.3, 24.4, 22.9, 12.5 (CH_3Pz), 9.8 (CH_3Pz).

ESI-MS (+) (m/z): 311.1 [$\text{M}+\text{H}$] $^+$, calcd. for $\text{C}_{16}\text{H}_{30}\text{N}_4\text{O}_2 = 310.2$.

HPLC (R_t): 18.6 min ($\lambda = 220$ nm, Method 1).

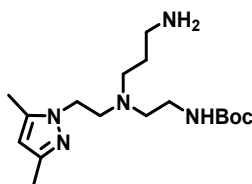
7.3.5 - tert-butyl 2-((2-(3,5-dimethyl-1H-pyrazol-1-yl)ethyl)(3-(1,3-dioxo-2,3-dihydro-1H-inden-2-yl)propyl)amino)ethylcarbamate (**30**)

A solution of **27** (1.110 g, 3.940 mmol), N-(3-bromopropyl)phthalimide (2.140 g, 8.050 mmol), and K_2CO_3 (1.10 g, 8.020 mmol) in dioxane (35 mL) was refluxed overnight. After reaction, the solution was filtered and the solvents evaporated to give an oily residue which was purified by silica gel column chromatography using a gradient of EtOAc (0 \rightarrow 100 %) in hexane. The fractions

containing **30** were collected, and the compound was obtained as a yellow oil after evaporation of the solvents. Yield: 77.9 % (1.450 g, 3.070 mmol).

¹H-NMR (300 MHz, CDCl₃): δ_H (ppm) 7.85 (2H, m, phthalimide), 7.72 (2H, m, phthalimide) 5.74 (1H, s, CH^b), 5.15 (1H, br s, NHBoc), 3.96 (2H, t, CH₂^d), 3.61 (2H, t, CH₂^e), 3.05 (2H, m, CH₂^f), 2.78 (2H, t, CH₂^h), 2.46 (4H, m, CH₂^g/CH₂^j), 2.20 (3H, s, CH₃Pz), 2.15 (3H, s, CH₃Pz), 1.76 1.66 (2H, m, CH₂ⁱ), 1.39 (9H, s, CH₃).

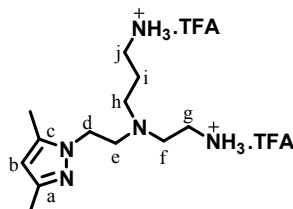
7.3.6 - *tert*-butyl 2-((3-aminopropyl)(2-(3,5-dimethyl-1H-pyrazol-1-yl)ethyl)amino)ethylcarbamate (L6-Boc)



To a solution of **30** (1.450 g, 3.070 mmol) in MeOH (10 mL) was added hydrazine hydrate (3.01 mL, 0.063 mol). After refluxing for 6 h, the solution was carefully acidified with 1 M HCl to pH 4 and a white precipitate was formed, which was removed by filtration. The obtained clear solution was neutralized with 1 M NaOH and extracted with CHCl₃. The organic layer was dried over MgSO₄. Removal of the solvent yielded an oily residue, which was purified by silica gel column chromatography using a gradient of MeOH (0 → 100 %) in CHCl₃. After evaporation of the solvents compound **L6-Boc** was obtained as a yellow oil. Yield: 86.3 % (0.090 g, 2.650 mmol).

¹H-NMR (300 MHz, CDCl₃): δ_H (ppm) 5.75 (1H, s, CH^b), 5.28 (2H, br s, NH₂), 5.10 (1H, br s, NHBoc), 3.96 (2H, t, CH₂^d), 3.07 (2H, m, CH₂^e), 2.76 (2H, t, CH₂^f), 2.60 (2H, t, CH₂^g), 2.48 (4H, m, CH₂^h/CH₂^j), 2.21 (3H, s, CH₃Pz), 2.19 (3H, s, CH₃Pz), 1.50 1.45 (2H, m, CH₂ⁱ), 1.42 (9H, s, CH₃).

7.3.7 - *N*-(2-aminoethyl)-*N*-(2-(3,5-dimethyl-1H-pyrazol-1-yl)ethyl)propane-1,3-diamine (L6.2TFA)



L6 was obtained directly by dissolving **L6-Boc** (0.060 g, 0.170 mmol) in a mixture of CH₂Cl₂/TFA (1 mL/ 2 mL) and allowed to react for 3 h at room temperature with stirring. The residue obtained after evaporation of the solvent was dissolved in H₂O, filtered through a 0.45 μm Millipore[®] filter, and purified by preparative RP-HPLC (Method 1). The fractions containing **L6** were collected

and the solvent removed to provide a clear viscous colorless oil. Yield: 54.1 % (0.040 g, 0.092 mmol, calcd. for $C_{12}H_{25}N_5 \cdot 2TFA$).

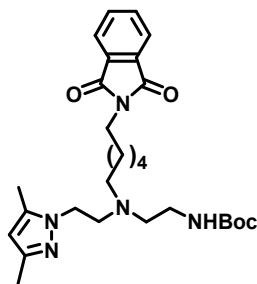
1H -NMR (300 MHz, D_2O): δ_H (ppm) 5.83 (1H, s, CH^b), 3.96 (2H, t, CH_2^d), 2.85 (2H, t, CH_2^e), 2.76 (4H, m, CH_2^f/CH_2^g), 2.66 (2H, m, CH_2^h), 2.51 (2H, t, CH_2^j), 2.11 (3H, s, CH_3Pz), 2.01 (3H, s, CH_3Pz), 1.61 (2H, m, CH_2^i).

^{13}C -NMR (75.5 MHz, D_2O): δ_C (ppm) 165.4 (q, CF_3COO^-), 151.2 (C^c), 144.1 (C^a), 118.7 (q, CF_3COO^-), 107.9 (C^b), 54.5 (C^e), 52.8 (C^f), 52.5 (C^d), 47.9 (C^h), 39.9 (C^j), 39.28 (C^g), 26.2 (C^i), 14.4 (CH_3Pz), 12.5 (CH_3Pz).

ESI-MS (+) (m/z): 240.2 $[M+H]^+$, calcd. for $C_{12}H_{25}N_5 = 239.2$.

HPLC (R_t): 16.8 min ($\lambda = 220$ nm, Method 1).

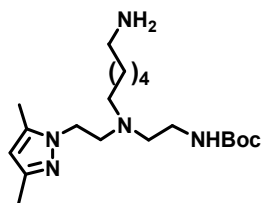
7.3.8 - *tert*-butyl 2-((2-(3,5-dimethyl-1H-pyrazol-1-yl)ethyl)(6-(1,3-dioxoisindolin-2-yl)hexyl)amino)ethylcarbamate (**31**)



31 was prepared as described for **30**. Starting with 0.490 g (1.740 mmol) of **27**, and 1.850 g (5.960 mmol) of N-(6-bromohexyl)phthalimide, a yellowish oil formulated as **31** was obtained after purification by silica gel column chromatography using a gradient of EtOAc (0 \rightarrow 100 %) in hexane. Yield: 50.0 % (0.450 g, 0.870 mmol).

1H -NMR (300 MHz, $CDCl_3$): δ_H (ppm) 7.81 (2H, m, phthalimide), 7.68 (2H, m, phthalimide), 5.73 (1H, s, CH^b), 5.04 (1H, br s, NHBoc), 3.93 (2H, t, CH_2^d), 3.64 (2H, t, CH_2^e), 3.03 (2H, m, CH_2^f), 2.75 (2H, t, CH_2^g), 2.46 (2H, t, CH_2^h), 2.38 (2H, t, CH_2^m), 2.20 (3H, s, CH_3Pz), 2.17 (3H, s, CH_3Pz), 1.67 1.57 (4H, m, CH_2^i , CH_2^l), 1.30 (9H, s, CH_3), 1.30 1.20 (4H, m, CH_2^j , CH_2^k).

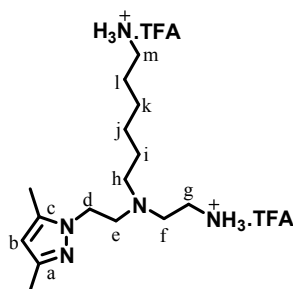
7.3.9 - *tert*-butyl 2-((6-aminohexyl)(2-(3,5-dimethyl-1*H*-pyrazol-1-yl)ethyl)amino)ethylcarbamate (L7-Boc)



L7-Boc was prepared as described for **L6-Boc**. Starting with 0.460 g (0.890 mmol) of **31** and 0.860 mL (0.017 mol) of hydrazine hydrate, a yellowish oil formulated as **L7-Boc** was obtained after purification by silica gel column chromatography using a gradient of MeOH (0 → 100%) in CHCl₃. Yield: 93.2 % (0.330 g, 0.830 mmol).

¹H-NMR (300 MHz, CDCl₃): δ_H (ppm) 5.70 (1H, s, CH^b), 5.02 (1H, br s, NHBoc), 3.91 (2H, t, CH₂^d), 3.00 (2H, m, CH₂^e), 2.72 (2H, t, CH₂^f), 2.62 (2H, t, CH₂^g), 2.44 (2H, t, CH₂^h), 2.35 (2H, t, CH₂^m), 2.17 (3H, s, CH₃Pz), 2.15 (3H, s, CH₃Pz), 1.55 (2H, m, CH₂ⁱ), 1.32 (9H, s, CH₃), 1.23 (6H, m, CH₂^j + CH₂^k + CH₂^l).

7.3.10 - *N*-(2-aminoethyl)-*N*-(2-(3,5-dimethyl-1*H*-pyrazol-1-yl)ethyl)hexane-1,6-diamine (L7.2TFA)



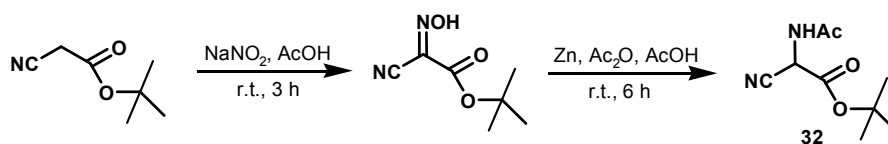
Deprotection of the Boc group in **L7-Boc** (0.080 g, 0.200 mmol) with CH₂Cl₂/TFA (1 mL/2 mL) gave, after purification by preparative RP-HPLC (Method 1), a colorless oil corresponding to **L7**. Yield: 49.0 % (0.050 g, 0.098 mmol, calcd. for C₁₅H₃₁N₅·2TFA).

¹H-NMR (300 MHz, D₂O): δ_H (ppm) 6.03 (1H, s, CH^b), 4.42 (2H, t, CH₂^d), 3.59 (2H, t, CH₂^e), 3.49 (2H, m, CH₂^f), 3.34 (2H, m, CH₂^g), 2.85 (2H, t, CH₂^m), 2.15 (2H, m, CH₂^h), 2.20 (3H, s, CH₃Pz), 2.12 (3H, s, CH₃Pz), 1.52 (4H, m, CH₂ⁱ, CH₂^l), 1.23 (4H, m, CH₂^j, CH₂^k).

¹³C-NMR (75.5 MHz, D₂O): δ_C (ppm) 165.4 (q, CF₃COO⁻), 150.3 (C^c), 144.2 (C^a), 118.6 (q, CF₃COO⁻), 107.1 (C^b), 54.0 (C^e), 51.9 (C^f), 49.8 (C^d), 42.2 (C^m), 39.3 (C^h), 33.8 (C^g), 26.7 (C^l), 25.4 (Cⁱ), 25.3 (C^k), 22.9 (C^l), 11.8 (CH₃Pz), 10.2 (CH₃Pz).

ESI-MS (+) (m/z): 282.2 [M+H]⁺, calcd. for C₁₅H₃₁N₅ = 281.2.

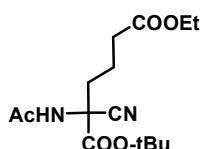
HPLC (R_t): 18.2 min (λ = 220 nm, Method 1).

7.3.11 - *Tert*-butyl 2-acetamido-2-cyanoacetate (**32**)

To a stirred solution of *tert*-butyl-cyanoacetate (5.600 g, 0.040 mol) and 45 % aq AcOH (50 mL) at 0 °C was added portion wise NaNO₂ (8.300 g, 0.120 mol) over 1.5 h. After the addition was completed, stirring was continued at room temperature for 3 h. The reaction mixture was extracted with Et₂O (3x). The collected ethereal solutions containing *tert*-butyl-isonitrosocanoacetate were immediately mixed with Ac₂O (10 mL, 0.105 mol) and AcOH (28 mL, 0.500 mol). With vigorous stirring, zinc powder (8.0 g, 0.125 mol) was added in small portions, and the stirring was continued for 6 h. After filtration, the solvent was evaporated at reduced pressure to give a pale yellow oil, which was purified by silica gel column chromatography using a gradient of EtOAc (25 → 100 %) in hexane. Compound **32** was recovered as yellowish oil. Yield: 9.6 % (0.761 g, 3.841 mmol). *R_f* (silica gel, hexane/ 50 % of EtOAc) = 0.30.

¹H-NMR (300 MHz, CDCl₃): δ_H (ppm) 6.39 (1H, s, AcNH), 5.40 (1H, d, CH), 2.11 (3H, s, COCH₃), 1.55 (9H, s).

¹³C-NMR (75.5 MHz, CDCl₃): δ_C (ppm) 169.5 (CO), 162.1 (CO), 114.3 (N≡C), 86.4 (C(CH₃)₃), 43.3 (CH), 27.3 (C(CH₃)₃), 22.6 (CH₃).

7.3.12 - 1-*tert*-butyl 6-ethyl 2-acetamido-2-cyanohexanedioate (**33**)

Metallic sodium (0.141 g, 5.880 mmol) was added to dry DMF under stirring. After complete dissolution of sodium, compound **32** (0.740 g, 3.730 mmol) was added and the solution warmed up to 60 °C for 30 min. After cooling down to room temperature, ethyl-4-bromobutyrate (0.539 mL, 3.730 mmol) was added to the solution in one portion. The reaction mixture was refluxed overnight and, after this time, turned deep brown from the initially orange color. Evaporation of the solvent gave a dark residue, which was treated with H₂O and extracted with EtOAc. The organic phases were collected, washed with brine, and dried over MgSO₄. After filtration, the organic phase was evaporated to give an orange oil, which was purified by silica gel column chromatography

using a gradient of EtOAc (25 → 100 %) in hexane. Yield: 54.3 % (0.630 g, 2.025 mmol). R_f (silica gel, hexane/ 50 % of EtOAc) = 0.40.

$^1\text{H-NMR}$ (300 MHz, CDCl_3): δ_H (ppm) 6.94 (1H, s, AcNH), 4.15 (2H, q, OCH_2CH_3), 2.37 (2H, m), 2.26 (1H, m), 2.08 (3H, s, COCH_3), 2.01 (1H, m), 1.82 (2H, m), 1.54 (9H, s), 1.27 (3H, t, OCH_2CH_3).

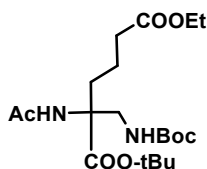
$^{13}\text{C-NMR}$ (75.5 MHz, CDCl_3): δ_C (ppm) 173.4 (CO), 169.7 (CO), 164.9 (CO), 116.6 (N≡C), 86.4 ($\text{C}(\text{CH}_3)_3$), 61.8, 57.1, 34.9, 32.9, 27.8 ($\text{C}(\text{CH}_3)_3$), 22.7, 18.9, 14.3.

ESI-MS (+) (m/z): 335.2 [$\text{M}+\text{Na}$] $^+$; calcd for $\text{C}_{15}\text{H}_{24}\text{N}_2\text{O}_5\text{Na}$ = 335.2.

Elemental analysis: Calcd. for $\text{C}_{15}\text{H}_{24}\text{N}_2\text{O}_5$: C, 57.68 %; H, 7.74 %; N, 8.97 %. Found: C, 57.50 %; H, 7.80 %; N, 8.81 %.

HPLC (R_t): 20.9 min (λ = 220 nm, Method 2).

7.3.13 - 1-*tert*-butyl 6-ethyl 2-acetamido-2-((*tert*-butoxycarbonylamino)methyl)hexanedioate (**34**)

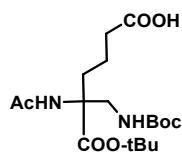


(Boc) $_2$ O (1.762 g, 8.080 mmol) and $\text{NiCl}_2 \cdot 6\text{H}_2\text{O}$ (0.040 g, 0.170 mmol) were added to a solution of **33** (0.630 g, 2.020 mmol) in MeOH (10 mL) cooled with an ice bath. To the green solution obtained was added NaBH_4 (1.216 g, 0.032 mol) in portions with stirring. The purple mixture was stirred overnight at 20 °C and diethylenetriamine (0.416 g, 4.040 mmol) was added. The reaction was stirred for 1 h before the volatile part of the mixture was removed by vacuum. The residue was partitioned between EtOAc and saturated NaHCO_3 solution. The organic phase was dried with MgSO_4 . Removal of the organic solvent gave a colorless residue. Compound **34** was purified by silica gel column chromatography using a gradient of EtOAc (25 → 100 %) in hexane and obtained as a pale yellow oil. Yield 96.5 % (0.817 g, 1.950 mmol). R_f (silica gel, hexane/ 50 % of EtOAc) = 0.45.

$^1\text{H-NMR}$ (300 MHz, CDCl_3): δ_H (ppm) 6.60 (1H, s, AcNH), 4.85 (1H, m, BocNH), 4.13 (2H, q, OCH_2CH_3), 3.85 (1H, br m, BocNHCH^a), 3.70 (1H, br m, BocNHCH^b), 2.29 (2H, m), 2.08 (3H, s, COCH_3), 1.74 (1H, m), 1.60 (1H, m), 1.49 (9H, s), 1.44 (2H, m), 1.41 (9H, s), 1.22 (3H, t, OCH_2CH_3).

$^{13}\text{C-NMR}$ (75.5 MHz, CDCl_3): δ_C (ppm) 173.1 (CO), 171.4 (CO), 169.7 (CO), 155.6 (CO), 85.3 ($\text{C}(\text{CH}_3)_3$), 83.2 ($\text{C}(\text{CH}_3)_3$), 65.0, 60.4, 44.7, 33.8, 31.8, 28.3 ($\text{C}(\text{CH}_3)_3$), 27.6 ($\text{C}(\text{CH}_3)_3$), 24.1, 19.1, 14.2.

Elemental analysis: Calcd. for $\text{C}_{20}\text{H}_{36}\text{N}_2\text{O}_7$: C, 57.67 %; H, 8.71 %; N, 6.73 %. Found: C, 57.50 %; H, 8.60 %; N, 7.00 %.

7.3.14 - 5-acetamido-6-*tert*-butoxy-5-((*tert*-butoxycarbonylamino)methyl)-6-oxohexanoic acid (**35**)

The intermediate **34** (0.600 g, 1.490 mmol) was dissolved in H₂O/MeOH, and an excess of NaOH (0.144 g, 3.600 mmol) was added. The solution was refluxed overnight, neutralized with 1 M HCl at 0 °C, and extracted with CH₂Cl₂. The organic phases were collected, dried over MgSO₄, filtered and the solvent evaporated. The crude product was purified by silica gel column chromatography using a gradient of EtOH (0 → 30 %) in CH₂Cl₂. Compound **35** was obtained as a colorless oil, which crystallizes upon standing. Yield: 65.6 % (0.380 g, 0.978 mmol). *R_f* (silica gel, CH₂Cl₂/ 10 % of EtOH) = 0.40.

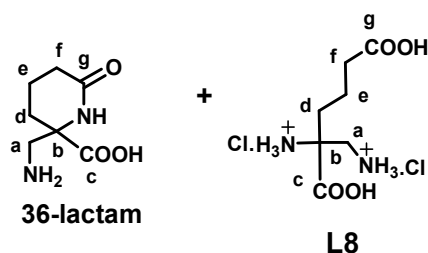
¹H-NMR (300 MHz, CDCl₃): δ_H (ppm) 6.79 (1H, s, AcNH), 4.94 (1H, m, BocNH), 3.83 – 3.65 (2H, m, BocNHCH^a and BocNHCH^{a'}), 2.33 (2H, m), 2.06 (3H, s, COCH₃), 1.74 (1H, m), 1.55 (3H, m), 1.48 (9H, s), 1.41 (9H, s).

¹³C-NMR (75.5 MHz, CDCl₃): δ_C (ppm) 177.9 (CO), 171.3 (CO), 170.6 (CO), 155.7 (CO), 85.7 (C(CH₃)₃), 79.4 (C(CH₃)₃), 65.1, 44.7, 33.8, 31.8, 28.3 (C(CH₃)₃), 27.7 (C(CH₃)₃), 23.9, 19.1.

ESI-MS (-) (*m/z*): 387.1 [M-H]⁻, 423.1 [M+Cl]⁻; calcd for C₁₈H₃₂N₂O₇ = 388.2.

Elemental analysis: Calcd. for C₁₈H₃₂N₂O₇: C, 55.66 %; H, 8.30 %; N, 7.21 %. Found: C, 55.03 %; H, 8.10 %; N, 6.96 %.

HPLC (*R_t*): 18.9 min (λ = 220 nm, Method 2).

7.3.15 – 2-amino-2-(aminomethyl)hexanedioic acid (**L8.2Cl**)

Compound **L8** was obtained directly by hydrolysis of the protecting groups of **35** (0.230 g, 0.610 mmol) with a 4 M HCl solution (5 mL). After refluxing for 18 h, the solvent was evaporated to dryness. The oily residue was thoroughly washed with CH₂Cl₂ and dried. The deprotection reaction afforded compound **L8** (60 % by ¹H-NMR) together with a side product, which was formulated as the lactam **36-lactam** (40 % by ¹H-NMR). After appropriate work up, 0.080 g of the mixture (**36-lactam** + **L8**) was obtained. Yield of **L8**: 30.0 % (0.048 g, 0.183 mmol, calcd. for C₇H₁₆N₂O₄·2Cl).

Characterization of the mixture **36-lactam** + **L8**:

IR (KBr, cm^{-1}): 1746vs, 1605vs, 1211m, 1179m and 1144m.

$^1\text{H-NMR}$ (300 MHz, D_2O): δ_{H} (ppm) 3.18 (2H, s, CH_2^{a} , **L8**), 3.03 (2H, q, CH_2^{a} , **36-lactam**), 2.09 (2H, t, CH_2^{f} , **L8**), 1.98 (2H, t, CH_2^{f} , **36-lactam**), 1.89 – 1.20 (8H, m, CH^{d} + CH^{e} , **L8** + **36-lactam**).

$^{13}\text{C-NMR}$ (75.5 MHz, D_2O): δ_{C} (ppm) 177.0 (CO), 176.6 (CO), 173.9 (CO), 169.9 (CO), 60.7 (C^{b} , **36-lactam**), 60.2 (C^{b} , **L8**), 44.2 (C^{a} , **36-lactam**), 42.0 (C^{a} , **L8**), 32.6 (C^{f} , **L8**), 32.3 (C^{d} , **L8**), 29.6 (C^{f} , **36-lactam**), 27.3 (C^{d} , **36-lactam**), 17.8 (C^{e} , **L8**), 16.4 (C^{e} , **36-lactam**).

ESI-MS (+) (m/z): 172.9 [$\text{M}+\text{H}$] $^+$ and 191.0 [$\text{M}+\text{H}$] $^+$; calcd for $\text{C}_7\text{H}_{12}\text{N}_2\text{O}_3 = 172.0$ (m/z for **36-lactam**) and for $\text{C}_7\text{H}_{14}\text{N}_2\text{O}_4 = 190.0$ (m/z for **L8**).

HPLC (R_{t}): 3.9 min ($\lambda = 220$ nm, Method 2).

Characterization of **36-lactam**: At pH > 4, **L8** converted almost quantitatively to **36-lactam**:

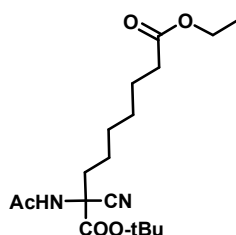
$^1\text{H-NMR}$ (300 MHz, D_2O): δ_{H} (ppm) 3.17 (2H, q, CH^{a}), 2.24 (2H, m, CH_2^{f}), 2.00 (1H, m, CH^{d}), 1.71 (2H, m, CH^{e}), 1.60 (1H, m, CH^{d}).

$^{13}\text{C-NMR}$ (75.5 MHz, D_2O): δ_{C} (ppm) 174.6 (C^{c}), 172.7 (C^{g}), 59.0 (CH^{b}), 42.5 (C^{a}), 27.9 (C^{f}), 25.6 (C^{d}), 14.7 (C^{e}).

ESI-MS (+) (m/z): 172.9 [$\text{M}+\text{H}$] $^+$; calcd for $\text{C}_7\text{H}_{12}\text{N}_2\text{O}_3 = 172.0$.

Elemental analysis: Calcd. for $\text{C}_7\text{H}_{13}\text{N}_2\text{O}_3 \cdot \text{HCl}$: C, 40.30 %; H, 6.28 %; N, 13.43 %. Found: C, 39.60 %; H, 6.68 %; N, 12.85 %. Single crystals suitable for X-Ray diffraction analysis were grown by slow evaporation of a solution of EtOH/ CH_2Cl_2 at room temperature.

7.3.16 - 1-tert-butyl 9-ethyl 2-acetamido-2-cyanononanedioate (**37**)



Sodium hydride (0.042 g, 1.800 mmol) was added to dry DMF under stirring at 80 °C. After complete dispersion, **32** (0.350 g, 1.800 mmol) was added and the solution warmed up to 100 °C. After 30 min under stirring, the mixture turned yellow and ethyl-7-bromoheptanoate (0.52 mL, 2.600 mmol) was added. The reaction mixture was kept under nitrogen at 100 °C overnight. Evaporation of the solvent gave a white residue, which was treated with H_2O and extracted with EtOAc. The organic phases were collected, washed with brine, and dried over MgSO_4 . After filtration, the organic phase

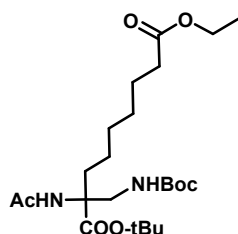
was evaporated to give an orange oil, which was purified by silica gel column chromatography using a gradient of EtOAc (0 → 100 %) in hexane. **37** was obtained as an orange oil after evaporation of the solvent. R_f (silica gel, hexane/ 70 % of EtOAc) = 0.38. Yield: 23.5 % (0.150 g, 0.423 mmol).

¹H-NMR (300 MHz, CDCl₃) δ_H (ppm) 6.19 (1H, s, NH), 4.11 (2H, q, OCH₂CH₃), 2.27 (2H, t, CH₂), 2.02 (2H, s, NHCOCH₃), 1.59 (2H, m, CH₂), 1.55 (9H, s, CH₃), 1.52 (9H, s, CH₃), 1.33 (5H, m, CH₂), 1.23 (3H, t, OCH₂CH₃).

¹³C-NMR (75 MHz, CDCl₃) δ_C (ppm) 173.7 (CO), 169.9 (CO), 165.1 (CO), 116.8 (C≡N), 84.9 (C(CH₃)), 60.2 (OCH₂CH₃), 57.5, 35.8, 33.9, 28.4, 28.3, 27.6 (C(CH₃)), 24.4, 23.4, 22.3, 14.1 (OCH₂CH₃).

ESI-MS (+) (m/z): 377.3 [M+Na]⁺, calcd. for C₁₈H₃₀N₂O₅ = 354.4.

7.3.17 - 1-*tert*-butyl 9-ethyl 2-acetamido-2-((*tert*-butoxycarbonylamino)methyl)nonanedioate (**38**)

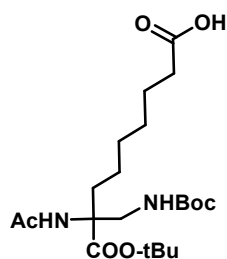


Compound **38** was prepared by using the same reduction conditions described for **34**. Briefly, (Boc)₂O (0.172 g, 0.800 mmol), NiCl₂·6H₂O (0.009 g, 0.040 mmol), NaBH₄ (1.216 g, 32.320 mmol) and diethylenetriamine (0.416 g, 4.040 mmol) were added to **11** (0.140 g, 0.400 mmol). Compound **38** was purified by silica gel column chromatography using a gradient of EtOAc (0 → 100 %) in hexane, and obtained as a white solid. R_f (silica gel, hexane/ 70 % of EtOAc) = 0.55. Yield: 54.5 % (0.100 g, 0.218 mmol).

¹H-NMR (300 MHz, CDCl₃): δ_H (ppm) 6.47 (1H, s, NH), 4.78 (1H, s, NH), 4.10 (2H, q, OCH₂CH₃), 3.79 (2H, dd, BocNHCH₂) 2.27 (3H, t, CH₂), 1.99 (3H, s, NHCOCH₃), 1.56 (10H, m, CH₂), 1.45 (9H, s, CH₃), 1.38 (9H, s, CH₃), 1.20 (7H, m, CH₂ + OCH₂CH₃), 1.02 (1H, t, CH₂).

¹³C-NMR (75 MHz, CDCl₃): δ_C (ppm) 173.6 (CO), 171.6 (CO), 169.5 (CO), 155.5 (CO), 82.9 (C(CH₃)), 79.1 (C(CH₃)), 65.2 (OCH₂CH₃), 60.1, 44.5, 34.1, 32.2, 28.9, 28.7, 28.1, 27.6 (C(CH₃)), 24.6, 23.9, 23.3, 14.1 (OCH₂CH₃).

ESI-MS (+) (m/z): 459.4 [M+H]⁺, calcd. for C₂₃H₄₂N₂O₇ = 458.3.

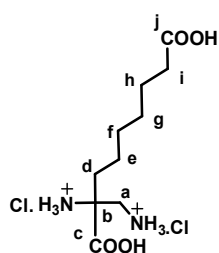
7.3.18 - 8-acetamido-9-*tert*-butoxy-8-((*tert*-butoxycarbonylamino)methyl)-9-oxononanoic acid (**39**)

The protected intermediate **38** (0.100 g, 0.210 mmol) was dissolved in H₂O/THF, and an excess of NaOH (0.043 g, 1.100 mmol) was added. The solution was allowed to react under stirring at 60 °C overnight. The reaction mixture was neutralized with 1 M HCl at 0 °C and extracted with CH₂Cl₂. The organic phases were collected, dried over MgSO₄, filtered and the solvent evaporated. The crude product was purified by silica gel column chromatography using a gradient of MeOH (0 → 10 %) in CH₂Cl₂, yielding **39** as colorless oil. R_f (silica gel, CH₂Cl₂/ 10 % of MeOH) = 0.29. Yield: 60.5 % (0.055 g, 0.127 mmol).

¹H-NMR (300 MHz, CDCl₃) δ_H (ppm) 6.61 (1H, s, NH), 4.92 (1H, s, NH), 3.81 (1H, m, BocNHCH₂), 3.79 (1H, m, BocNHCH₂), 2.29 (2H, m, CH₂), 2.01 (3H, s, NHCOCH₃), 1.57 (6H, m, CH₂), 1.45 (9H, s, CH₃), 1.38 (9H, s, CH₃), 1.27 (4H, s broad, CH₂).

¹³C-NMR (75.5 MHz, CDCl₃) δ_C (ppm) 171.7 (CO), 170.0 (CO), 155.6 (CO), 130.8, 128.7, 83.1 (C(CH₃)), 79.3 (C(CH₃)), 68.1, 65.3, 44.5, 38.6, 32.2, 30.3, 28.9, 28.8, 28.7, 28.3 (C(CH₃)), 27.7, 24.6, 23.9, 23.3.

ESI-MS (+) (m/z): 429.2 [M-H]⁻, calcd. for C₂₁H₃₈N₂O₇ = 430.3

7.3.19 - 2-amino-2-(aminomethyl)nonanedioic acid (**L9.2Cl**)

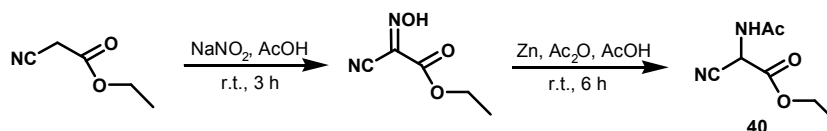
Compound **L9** was obtained directly by hydrolysis of the protecting groups of **39** (0.020 g, 0.046 mmol) with a 4 M HCl solution (5 mL). After refluxing for 22 h, the solvent was evaporated to dryness. The oily residue was thoroughly washed with CH₂Cl₂ and dried under reduced pressure to afford **L9** in pure form. Yield: 84.7 % (0.012 g, 0.039 mmol, calcd. for C₁₀H₂₂N₂O₄·Cl₂).

¹H-NMR (300 MHz, D₂O): δ_H (ppm) 3.24 (2H, s, CH₂^a), 2.21 (2H, t, CH₂ⁱ), 1.83 (1H, m, CH₂), 1.65 (1H, m, CH₂), 1.42 (2H, t, CH₂), 1.18 (6H, m, CH₂).

¹³C-NMR (75.5 MHz, D₂O): δ_C (ppm) 177.2 (CO), 176.8 (CO), 60.0 (C^b), 44.7 (C^a), 34.1 (Cⁱ), 33.4 (C^d), 28.3, 28.0, 24.3, 24.0.

HPLC (R_f): 5.9 min ($\lambda = 220$ nm, Method 2).

7.3.20 - Ethyl 2-acetamido-2-cyanoacetate (40)

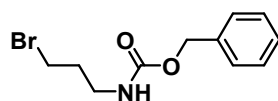


To a stirred solution of ethyl cyanoacetate (9.000 g, 0.079 mol) and 45 % aq AcOH (35 mL) at 0 °C was added portionwise NaNO_2 (16.300 g, 0.235 mol) over 1.5 h. After the addition was completed, the stirring was continued at room temperature overnight. The reaction mixture was extracted with Et_2O . The ethereal solution containing ethyl isonitrosocanoacetate was immediately mixed with Ac_2O (19 mL, 0.210 mol) and AcOH (56 mL, 1.000 mol). With vigorous stirring, zinc powder (16.000 g, 0.250 mol) was added in small portions and the stirring was continued for 6 h. After filtration, the solvent was evaporated at reduced pressure to give a pale yellow oil, which precipitated from MeOH. Compound **40** was recovered as a yellowish solid. Yield: 32.9 % (4.520 g, 0.026 mol).

$^1\text{H-NMR}$ (300 MHz, CDCl_3): δ_H (ppm) 6.41 (1H, s, AcNH), 5.51 (1H, d, CH), 4.36 (2H, q, OCH_2CH_3), 2.11 (3H, s, COCH_3), 1.36 (3H, t, OCH_2CH_3).

$^{13}\text{C-NMR}$ (75.5 MHz, CDCl_3): δ_C (ppm) 169.7 (CO), 163.4 (CO), 114.1 ($\text{N}\equiv\text{C}$), 64.2 (OCH_2CH_3), 42.8, 22.6, 13.9 (OCH_2CH_3).

7.3.21 –Benzyl *N*-(3-bromopropyl)carbamate (41)

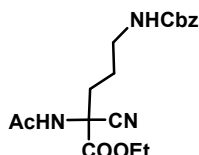


A solution of triphenylphosphine (9.400 g, 0.028 mol) and carbon tetrabromide (7.500 g, 0.028 mol) in dry THF was added dropwise (30 mL) to a solution of benzyl *N*-(3-hydroxypropyl)carbamate (3.000 g, 0.014 mol) in the same solvent (30 mL). After 48 h of stirring at room temperature, the solution was filtered to remove insoluble solids. After evaporation of filtrate, the residue was dissolved in CH_2Cl_2 and the solution washed with H_2O . The organic layer was dried over MgSO_4 , filtered and the solvent was evaporated to yield an oily residue, which was purified by silica gel column chromatography using a gradient of MeOH (0 → 100 %) in CH_2Cl_2 . After evaporation of the solvent, benzyl *N*-(3-bromopropyl)carbamate was obtained as an orange oil Yield: 78.5 % (3.200 g, 0.011 mol). R_f (silica gel, CHCl_3) = 0.5.

$^1\text{H-NMR}$ (300 MHz, CDCl_3): δ_{H} (ppm) 7.32 (5H, m, Cbz), 5.15 (1H, br s, CbzNH), 5.06 (2H, s, CH_2 of Cbz), 3.39 (2H, t, CH_2), 3.30 (2H, q, CH_2), 2.00 (2H, m, CH_2).

$^{13}\text{C-NMR}$ (75.5 MHz, CDCl_3 , ppm): δ_{C} 156.4, 136.3, 128.4, 128.0, 127.9, 66.6, 39.2, 32.3, 30.6.

7.3.22 - Ethyl 2-acetamido-5-(benzyloxycarbonylamino)-2-cyanopentanoate (**42**)



Compound **42** was obtained by reaction of **40** (1.000 g, 5.880 mmol) with metallic sodium (0.141 g, 5.880 mmol) in dry EtOH, followed by addition of **41** (1.60 g, 5.880 mmol), using a procedure similar to that described for **33**. Purification by column chromatography on silica gel, using a gradient of MeOH (0 \rightarrow 100 %) in EtOAc, gave **42** as a colorless oil. Yield: 39.4 % (0.841 g, 2.320 mmol). R_f (silica gel, Hexane/ 80 % of EtOAc) = 0.45.

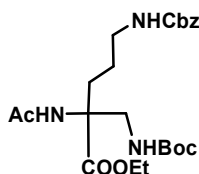
$^1\text{H-NMR}$ (300 MHz, CDCl_3): δ_{H} (ppm) 7.98 (1H, s, AcNH), 7.34 (5H, m, Cbz), 5.42 (1H, t, CbzNH), 5.09 (2H, s, Cbz), 4.28 (2H, q, OCH_2CH_3), 3.26 (2H, m, CH^{f}), 2.09 (2H, m, CH^{d}), 2.04 (3H, s, COCH_3), 1.81 (1H, m, CH^{e}), 1.68 (1H, m, CH^{e}), 1.28 (3H, t, OCH_2CH_3).

$^{13}\text{C-NMR}$ (75.5 MHz, CDCl_3): δ_{C} (ppm) 171.2 (CO), 166.8 (CO), 157.5 (CO), 136.5 (Cbz), 128.8 (Cbz), 128.5 (Cbz), 128.3 (Cbz), 116.9 ($\text{N}\equiv\text{C}$), 67.2 (Cbz), 64.1 (OCH_2CH_3), 57.5 (C^{b}), 40.0 (C^{f}), 32.8 (C^{d}), 25.6 (C^{e}), 22.3 (COCH_3), 14.2 (OCH_2CH_3).

Elemental analysis: Calcd. for $\text{C}_{18}\text{H}_{23}\text{N}_3\text{O}_5$: C, 59.82 %; H, 6.41 %; N, 11.63 %. Found: C, 59.60 %; H, 6.40 %; N, 11.63 %.

HPLC (R_t): 23.4 min ($\lambda = 220$ nm, Method 2).

7.3.23 - Ethyl 8-acetamido-13,13-dimethyl-3,11-dioxo-1-phenyl-2,12-dioxa-4,10-diazatetradecane-8-carboxylate (**43**)



Compound **43** was prepared using the same reduction conditions described for **34**. $(\text{Boc})_2\text{O}$ (1.015 g, 4.650 mmol), $\text{NiCl}_2\cdot 6\text{H}_2\text{O}$ (0.055 g, 0.230 mmol), NaBH_4 (0.700 g, 18.610 mmol) and diethylenetriamine (0.239 g, 2.320 mmol) was added to **42** (0.841 g, 2.320 mmol). After purification by silica gel column chromatography using a gradient of MeOH (0 \rightarrow 100 %) in EtOAc, compound **43**

was obtained as a pale yellow oil. Yield 40.4 % (0.437 g, 0.939 mmol). R_f (silica gel, hexane/ 80 % of EtOAc) = 0.50.

$^1\text{H-NMR}$ (300 MHz, CDCl_3): **Isomer a**: δ_H (ppm) 7.35 (5H, m, Cbz), 6.53 (1H, s, AcNH), 5.09 (2H, s, Cbz), 4.88 (2H, m, CbzNH + BocNH), 4.24 (2H, q, OCH_2CH_3), 3.85 (1H, m, BocNHCH^a), 3.61 (1H, m, BocNHCH^a), 3.17 (2H, m, CH^f), 2.23 (2H, m, CH^d), 2.01 (3H, s, COCH_3), 1.82 (1H, m, CH^e), 1.72 (1H, m, CH^e), 1.41 (9H, s), 1.27 (3H, t, OCH_2CH_3). **Isomer b**: δ_H (ppm) 7.58 (1H, s, AcNH), 7.37 (5H, m, Cbz), 5.12 (2H, s, Cbz), 4.88 (2H, m, CbzNH + BocNH), 4.36 (2H, q, OCH_2CH_3), 3.85 (1H, m, BocNHCH^a), 3.61 (1H, m, BocNHCH^a), 3.30 (2H, m, CH^f), 2.23 (2H, m, CH^d), 2.08 (3H, s, COCH_3), 1.82 (1H, m, CH^e), 1.72 (1H, m, CH^e), 1.41 (9H, s), 1.31 (3H, t, OCH_2CH_3).

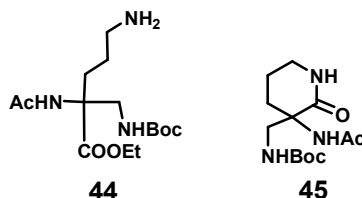
$^{13}\text{C-NMR}$ (75.5 MHz, CDCl_3): **Isomer a**: δ_c (ppm) 172.6 (CO), 170.1 (CO), 156.6 (CO), 156.2 (CO), 136.8 (Cbz), 128.8 (Cbz), 128.4 (Cbz), 128.3 (Cbz), 79.9 ($\text{C}(\text{CH}_3)_3$), 66.9, 64.7, 62.6 (OCH_2CH_3), 44.6, 41.0, 28.5 ($\text{C}(\text{CH}_3)_3$), 24.5, 24.1, 14.3 (OCH_2CH_3). **Isomer b**: δ_c (ppm) 172.8 (CO), 170.4 (CO), 156.9 (CO), 156.2 (CO), 136.4 (Cbz), 128.8 (Cbz), 128.4 (Cbz), 128.3 (Cbz), 79.9 ($\text{C}(\text{CH}_3)_3$), 67.4, 63.9, 62.6 (OCH_2CH_3), 40.0, 32.6, 29.8 ($\text{C}(\text{CH}_3)_3$), 25.9, 22.5, 14.3 (OCH_2CH_3).

ESI-MS (+) (m/z): 488.1 [$\text{M}+\text{Na}$] $^+$; calcd for $\text{C}_{23}\text{H}_{35}\text{N}_3\text{O}_7\text{Na}$ = 488.2.

Elemental analysis: Calcd. for $\text{C}_{23}\text{H}_{35}\text{N}_3\text{O}_7$: C, 59.34 %; H, 7.58 %; N, 9.03 %. Found: C, 59.00 %; H, 7.64 %; N, 8.99 %.

HPLC (R_t): 27.1 min (λ = 220 nm, Method 2).

7.3.24 - Ethyl 2-acetamido-5-amino-2-((*tert*-butoxycarbonylamino)methyl)pentanoate (**44**)



Compound **43** (0.437 g, 0.941 mmol) was dissolved in dry EtOH (15 mL) and Pd/C (Pd content 10 %, 0.215 g) was added. The solution was bubbled with H_2 at room temperature for 8 h and left overnight under H_2 atmosphere. The catalyst was filtered through celite, the filtrate was evaporated and the residue purified by silica gel column chromatography using a gradient of EtOH (0 \rightarrow 100 %) in CH_2Cl_2 . Compound **44** was obtained as a yellow viscous oil. Yield: 89.6 % (0.280 g, 0.844 mmol). R_f (silica gel, CH_2Cl_2 / 20 % of EtOH) = 0.20.

$^1\text{H-NMR}$ (300 MHz, CD_3OD): δ_H (ppm) 4.15 (2H, q, OCH_2CH_3), 3.57 (2H, s, BocNHCH_2^a), 2.87 (2H, t, CH^f), 1.94 (3H, s, COCH_3), 1.82 (2H, m, CH^d), 1.63 (2H, m, CH^e), 1.42 (9H, s), 1.24 (3H, t, OCH_2CH_3).

$^{13}\text{C-NMR}$ (75.5 MHz, CD_3OD): δ_c (ppm) 171.9 (CO), 171.8 (CO), 157.5 (CO), 79.1 ($\text{C}(\text{CH}_3)_3$), 62.5, 61.4, 42.0, 39.5, 29.3, 27.5 ($\text{C}(\text{CH}_3)_3$), 21.9, 21.5, 13.2 (OCH_2CH_3).

ESI-MS (+) (m/z): 331.4 $[M+H]^+$; calcd for $C_{15}H_{29}N_3O_5 = 331.2$.

HPLC (R_f): 15.2 min ($\lambda = 220$ nm, Method 2).

When the reaction was performed using a large excess of Pd/C catalyst (ratio of 1:1 of Pd/C to **17**), two compounds, formulated as **44** and **45**, were obtained in 51.4 and 18.7 % yield, respectively, after purification by silica gel column chromatography. Single crystals of **45** suitable for X-Ray diffraction analysis were grown by slow evaporation of a CH_2Cl_2 /EtOH solution at room temperature.

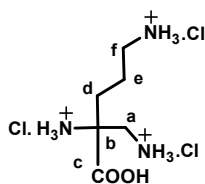
Characterization of 45: R_f (silica gel, CH_2Cl_2 / 20 % of EtOH) = 0.70.

1H -NMR (300 MHz, $CDCl_3$) δ_H (ppm) 7.16 (1H, s, AcNH), 6.32 (1H, br s, NH amide), 5.64 (1H, br m, BocNH), 3.64 (1H, m, BocNHCH^a), 3.50 (2H, m, CH₂^f), 3.31 (1H, m, BocNHCH^{a'}), 2.38 (1H, m, CH^d), 2.09 (1H, m, CH^{d'}), 2.01 (3H, s, COCH₃), 1.89 (2H, m, CH^e), 1.50 (9H, s).

^{13}C -NMR (75.5 MHz, $CDCl_3$) δ_c (ppm) 172.4 (CO), 170.5 (CO), 157.6 (CO), 80.4 ($C(CH_3)_3$), 59.1, 46.6, 42.5, 30.0, 28.5 ($C(CH_3)_3$), 23.6, 20.5.

ESI-MS (+) (m/z): 308.1 $[M+Na]^+$; calcd for $C_{13}H_{23}N_3O_4Na = 308.1$.

7.3.25 - 2,5-diamino-2-(aminomethyl)pentanoic acid (L10.3Cl)



Compound **L10** was obtained directly by hydrolysis of the protecting groups of **44** (0.047 g, 0.14 mmol) with a 4 M HCl solution (5 mL). The reaction mixture was refluxed overnight, cooled down to room temperature and washed with CH_2Cl_2 . Compound **L10** was recovered as a colorless oil, after drying the aqueous phase under vacuum. Yield 92.4 % (0.035 g, 0.129 mmol, calcd. for $C_6H_{15}N_3O_2Cl_3$).

IR (KBr, cm^{-1}): 1787m, 1619s and 1606s.

1H -NMR (300 MHz, D_2O): δ_H (ppm) 3.32 (2H, s, $NH_2CH_2^a$), 2.88 (2H, t, CH^f), 1.90 (1H, m, CH^d), 1.80 (1H, m, CH^{d'}), 1.74 (1H, m, CH^e), 1.62 (1H, m, CH^{e'}).

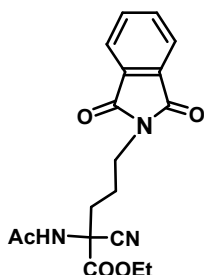
^{13}C -NMR (75.5 MHz, D_2O): δ_c (ppm) 171.2 (CO), 60.2, 42.5, 39.8, 30.5, 21.3.

ESI-MS (+) (m/z): 162.0 $[M+H]^+$; calcd for $C_6H_{15}N_3O_2 = 161.2$.

Elemental analysis: Calcd. for $C_6H_{15}N_3O_2 \cdot 3Cl$: C, 26.90 %; H, 5.65 %; N, 15.70 %. Found: C, 27.20 %; H, 6.00 %; N, 16.00 %.

ESI-MS (+) (m/z): 162.0 $[M+H]^+$; calcd for $C_6H_{15}N_3O_2 = 161.2$.

HPLC (R_f): 2.4 min ($\lambda = 220$ nm, Method 2).

7.3.26 - Ethyl 2-acetamido-2-cyano-5-(1,3-dioxoisindolin-2-yl)pentanoate (**46**)

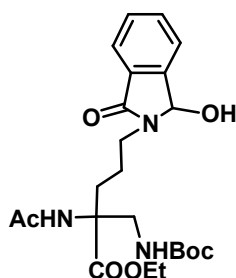
Compound **46** was obtained under the same reaction conditions described for **33** but reacting precursor **40** (0.680 g, 4.000 mmol) with 3-bromo-propylphthalimide (1.072 g, 4.000 mmol). **46** was isolated as a white solid, which precipitated from a solution of EtOH. Yield: 38.5 % (0.550 g, 1.540 mmol). R_f (silica gel, Hexane/ 25 % of EtOAc) = 0.45.

$^1\text{H-NMR}$ (300 MHz, CDCl_3): δ_H (ppm) 7.86 (2H, m, Phth), 7.77 (2H, m, Phth), 6.84 (1H, s, AcNH), 4.32 (2H, q, OCH_2CH_3), 3.79 (2H, m, CH_2Phth), 2.12 (2H, m, CH_2), 2.10 (3H, s, COCH_3), 1.96 (2H, m, CH_2), 1.35 (3H, t, OCH_2CH_3).

$^{13}\text{C-NMR}$ (75.5 MHz, CDCl_3): δ_C (ppm) 169.9 (CO), 168.6 (CO), 166.2 (CO), 134.5 (Phth), 131.9 (Phth), 123.6 (Phth), 116.1 ($\text{N}\equiv\text{C}$), 64.1 (OCH_2CH_3), 56.8, 37.0, 33.0, 23.8 (COCH_3), 22.7, 14.1 (OCH_2CH_3).

ESI-MS (+) (m/z): 380.1 [$\text{M}+\text{Na}$] $^+$; calcd for $\text{C}_{18}\text{H}_{19}\text{N}_3\text{NaO}_5 = 380.1$.

HPLC (R_t): 18.4 min ($\lambda = 220$ nm, Method 2).

7.3.27 - Ethyl 2-acetamido-2-((*tert*-butoxycarbonylamino)methyl)-5-(1-hydroxy-3-oxoisindolin-2-yl)pentanoate (**47**)

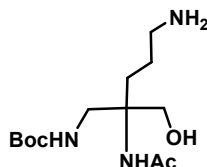
Compound **47** was prepared by using the same reduction conditions described for **34**. $(\text{Boc})_2\text{O}$ (0.671 g, 3.080 mmol), $\text{NiCl}_2\cdot 6\text{H}_2\text{O}$ (0.036 g, 0.150 mmol), NaBH_4 (0.466 g, 12.320 mmol) and diethylenetriamine (0.158 g, 1.540 mmol) were added to **46** (0.550 g, 1.540 mmol) and allowed to react. Compound **47** was purified by silica gel column chromatography using a gradient of EtOAc (0 \rightarrow 100 %) in hexane, and obtained as a pale yellow oil. Yield 29.4 % (0.210 g, 0.453 mmol). R_f (silica gel, EtOAc) = 0.30.

¹H-NMR (300 MHz, CDCl₃): δ_H (ppm) 7.8 – 7.4 (4H, m, Phth), 6.62 (1H, s, AcNH), 5.77 (1H, s, PhthOH) 4.88 (1H, m, BocNH), 4.22 (2H, q, OCH₂CH₃), 3.80 – 3.40 (2H, m, BocNHCH^a), 2.05 (3H, s, COCH₃), 2.00 - 1.80 (4H, m, CH₂), 1.63 (1H, m, CH₂), 1.37 (9H, s), 1.27 (3H, t, OCH₂CH₃).

ESI-MS (+) (*m/z*): 486.2 [M+Na]⁺; calcd for C₂₃H₃₃N₃NaO₇ = 486.2.

HPLC (R_t): 19.5 min (λ = 220 nm, Method 2).

7.3.28 - *tert*-butyl 2-acetamido-5-amino-2-(hydroxymethyl)pentylcarbamate (**48**)

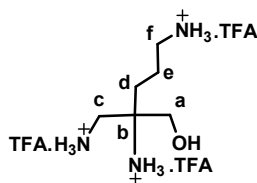


The precursor **47** (0.108 g, 0.234 mmol) was dissolved in a *i*-PrOH/H₂O (6:1, 10 mL) solution and NaBH₄ (0.070 g, 1.872 mmol) was added. The reaction mixture stirred at room temperature for 24 h. AcOH was added and the reaction heated at 80 °C for 24 h. The volatile solvent was evaporated from the reaction mixture and the resulting aqueous solution was neutralized with NaOH and extracted with EtOAc. The combined EtOAc extracts were washed with water, dried over MgSO₄ and filtered. After the evaporation of the solvent from the filtrate, the residue was purified by chromatography on silica gel using a gradient of EtOH (0 → 100 %) in CH₂Cl₂. Yield: 39.7 % (0.027 g, 0.093 mmol).

¹H-NMR (300 MHz, CD₃OD): δ_H (ppm) 3.59 (2H, dd, BocNHCH₂), 3.35 (2H, dd, HOCH₂), 2.90 (2H, t, CH₂NH₂), 1.96 (3H, s, COCH₃), 1.77 - 1.64 (4H, m, CH₂), 1.45 (9H, s).

¹³C-NMR (75.5 MHz, CDCl₃): δ_C (ppm) 173.9 (CO), 159.4 (CO), 80.4 (C(CH₃)₃), 63.4, 61.7, 43.4, 41.5, 28.92, 28.7 (C(CH₃)₃), 23.6, 22.4.

7.3.29 - 2,5-diamino-2-(aminomethyl)pentan-1-ol (L10-OH.3TFA)



Compound **L10-OH** was obtained directly by hydrolysis of the protecting groups of **48** (0.040 g, 0.140 mmol) with a 4 M HCl solution (5 mL). The reaction mixture was refluxed overnight, cooled down to room temperature and purified by semi-preparative RP-HPLC (Method 2). **L10-OH** was recovered as a colorless oil, after drying the collected fractions under vacuum. Yield 62.1 % (0.043 g, 0.087 mmol, calcd. for C₆H₁₇N₃O.3TFA).

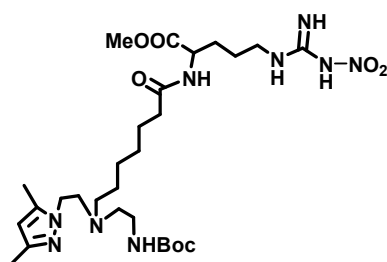
IR (KBr, cm^{-1}): 1642w, 1138vs, 663w.

$^1\text{H-NMR}$ (500 MHz, D_2O): δ_{H} (ppm) 3.75 (2H, dd, CH_2^{g}), 3.35 (2H, s, CH_2^{c}), 2.91 (2H, t, CH_2^{f}), 1.77-1.60 (4H, m, CH_2^{d} + CH_2^{e}).

$^{13}\text{C-NMR}$ (75.5 MHz, D_2O): δ_{C} (ppm) 64.4 (C^{a}), 59.4 (C^{b}), 44.2 (C^{c}), 40.9 (C^{f}), 30.5 (C^{d}), 23.6 (C^{e}).

ESI-MS (+) (m/z): 148.1 $[\text{M}+\text{H}]^+$; calcd for $\text{C}_6\text{H}_{17}\text{N}_3\text{O} = 147.1$

7.3.30 - Methyl 15-(2-(3,5-dimethyl-1H-pyrazol-1-yl)ethyl)-1-imino-21,21-dimethyl-1-(nitroamino)-8,19-dioxo-20-oxa-2,7,15,18-tetraazadocosane-6-carboxylate (49)

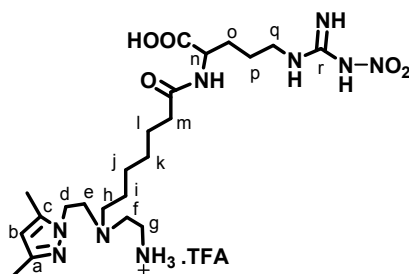


To a solution of **L5-Boc** (0.050 g, 0.120 mmol) in DMF were added triethylamine (0.036 g, 0.365 mmol) and *O*-benzotriazol-1-yl-*N,N,N',N'*-tetramethyluronium hexafluorophosphate (HBTU, 0.054 g, 0.145 mmol). After 10 minutes, *N*^ω-NO₂-L-Arg methyl ester (0.039 g, 0.145 mmol) was added, and the reaction mixture stirred at room temperature under a nitrogen atmosphere for 2 h. The solvent was then removed under vacuum, and the residue purified by silica gel column chromatography using a gradient of MeOH (0 → 100 %) in CHCl₃. The intermediate **49** was obtained as a yellowish oil. Yield: 66.6 % (0.050 g, 0.080 mmol).

$^1\text{H-NMR}$ (300 MHz, CDCl_3): δ_{H} (ppm) 7.69 (2H, br s, NH), 6.48 (1H, br s, NH), 5.70 (1H, s, CH^{b}), 5.10 (1H, br s, NH), 4.57 (1H, br s, NH), 3.91 (2H, t, CH_2), 3.69 (3H, s, OCH_3), 3.64 (1H, br m, CH^{n}), 2.98 (2H, m, CH_2), 2.72 (2H, t, CH_2), 2.44 (2H, t, CH_2), 2.36 (2H, t, CH_2), 2.22 (2H, m, CH_2), 2.19 (3H, s, CH_3Pz), 2.16 (3H, s, CH_3Pz), 1.89 (1H, m, CH_2), 1.70 – 1.52 (7H, m, CH_2), 1.40 (9H, s, CH_3), 1.39 – 1.15 (6H, m, CH_2).

$^{13}\text{C-NMR}$ (75.5 MHz, CDCl_3): δ_{C} (ppm) 174.3 (CO), 172.6 (CO), 159.4 (C^{f}), 159.4 (CO), 147.3 (Pz), 138.9 (Pz), 104.9 (Pz), 78.9 ($\text{C}(\text{CH}_3)_3$), 54.1, 53.7, 53.3, 52.7, 50.6, 47.0, 40.3, 38.4, 36.2, 30.8, 28.8, 28.4, 26.7, 25.4, 24.6, 13.4 (CH_3Pz), 11.0 (CH_3Pz).

7.3.31 - 2-(7-((2-aminoethyl)(2-(3,5-dimethyl-1H-pyrazol-1-yl)ethyl)amino)heptanamido)-5-(3-nitroguanidino)pentanoic acid (L11.TFA)



L11 was obtained directly by simultaneous hydrolysis of the methyl ester group and Boc-deprotection of **49** (0.090 g, 0.144 mmol) with a 3 N HCl solution (5 mL) at room temperature for 72 h. After neutralization of the reaction mixture with 1 M NaOH solution, the water was evaporated and the residue extracted with MeOH. The solvent was evaporated, the residue dissolved in water and purified by RP-HPLC (Method 1) to give a colorless oil. Yield: 33.3 % (0.030 g, 0.048 mmol, calcd. for C₂₂H₄₁N₉O₅·TFA).

IR (KBr, cm⁻¹): ~ 1650s, 1390m, 1265m (NO₂), 1200m and 1130m.

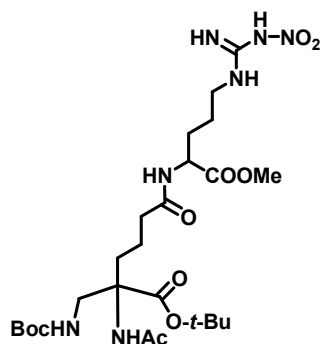
¹H-NMR (300 MHz, D₂O): δ_H (ppm) 5.76 (1H, s, CH^b), 4.34 (1H, br m, CHⁿ) 3.98 (2H, t, CH₂^d), 3.87 (2H, t, CH₂), 2.65 (4H, m, CH₂), 2.31 (2H, t, CH₂), 2.16 (3H, s, CH₃Pz), 2.14 (2H, m, CH₂), 2.06 (3H, s, CH₃Pz), 1.79 (1H, m, CH₂), 1.70 – 1.40 (7H, m, CH₂), 1.39 – 1.00 (6H, m, CH₂).

¹³C-NMR (75.5 MHz, D₂O): δ_C (ppm) 175.3 (CO), 172.7 (CO), 162.2 (q, CF₃COO⁻), 160.0 (C^r), 147.0 (Pz), 139.7 (Pz), 116.4 (q, CF₃COO⁻), 105.1 (Pz), 54.3, 53.1, 52.1, 51.1, 46.5, 40.5, 38.0, 35.4, 33.5, 28.9, 26.8, 26.6, 25.6, 24.7, 12.1 (CH₃Pz), 9.7 (CH₃Pz).

ESI-MS (+) (*m/z*): 550.2 [M+K]⁺; calcd for C₂₂H₄₁N₉O₅K = 550.2.

Elemental analysis: calcd. for C₂₂H₄₁N₉O₅·TFA: C, 46.06 %; H, 6.76 %; N, 20.15 %. Found: C, 45.40 %; H, 6.20 %; N, 19.60 %.

HPLC (R_t): 14.6 min (λ = 220 nm, Method 1).

7.3.32 - *tert*-butyl 2-acetamido-2-((*tert*-butoxycarbonylamino)methyl)-6-(1-methoxy-5-(3-nitroguanidino)-1-oxopentan-2-ylamino)-6-oxohexanoate (**50**)

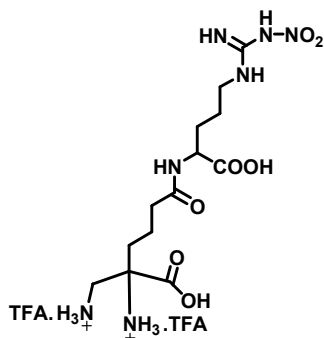
To a solution of **35** (0.087 g, 0.224 mmol) in DMF were added HBTU (0.101 g, 0.268 mmol). After 10 minutes at room temperature N^{ω} -NO₂-L-Arg methyl ester (0.072 g, 0.268 mmol) and triethylamine (0.070 g, 0.672 mmol) were added under stirring. The reaction mixture was stirred at room temperature under a nitrogen atmosphere for 2 h. The solvent was removed under vacuum, and the residue purified by silica gel column chromatography using a gradient of MeOH (0 → 100 %) in CHCl₃, yielding **50** as a colorless oil. R_f (silica-gel, CH₂Cl₂/ 15 % of MeOH) = 0.40. Yield: 55.3 % (0.075 g, 0.124 mmol).

¹H-NMR (300 MHz, CD₃OD): δ_H (ppm) 4.45 (1H, m, H_α), 3.90 (2H, s, BocNHCH₂), 3.72 (3H, s, COOCH₃), 3.27 (4H, m, CH₂), 2.29 (2H, m, CH₂), 1.99 (3H, s, NHCOCH₃), 1.94 (2H, s, CH₂), 1.69 (4H, m broad, CH₂), 1.41 (9H, s, CH₃), 1.35 (9H, s, CH₃).

¹³C-NMR (75.5 MHz, CD₃OD): δ_C (ppm) 172.9 (CO), 171.5 (CO), 170.9 (CO), 159.7 (CO), 156.4 (C, GuaNO₂), 156.1 (CO), 83.7 (C(CH₃)), 79.9 (C(CH₃)), 65.2, 52.9 (CH₃), 51.3, 44.8, 40.6, 35.9, 32.0, 30.2, 29.8, 28.5 (C(CH₃)), 28.0 (C(CH₃)), 25.0, 24.1, 19.7, 18.6.

HPLC (R_t): 20.0 min (λ = 220 nm, Method 2).

7.3.33 - 2-amino-2-(aminomethyl)-6-(1-carboxy-4-(2-nitroguanidino)butylamino)-6-oxohexanoic acid (L12.2TFA)



Compound **L12** was obtained directly by hydrolysis of the protecting groups of **50** (0.099 g, 0.163 mmol) with a 2 M HCl solution (3 mL). After refluxing for 18 h, the solvent was evaporated to dryness. The oily residue was thoroughly washed with CH₂Cl₂ and dried. After semi-preparative RP-HPLC purification (Method 2), **L12** was obtained as colorless oil. Yield: 81.4 % (0.078 g, 0.132 mmol, calcd. for C₁₃H₂₅N₇O₇·2TFA).

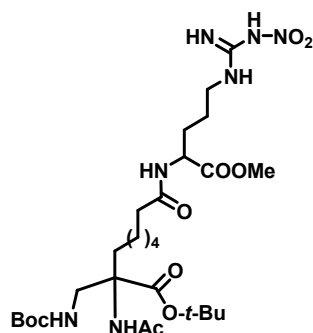
¹H-NMR (300 MHz, D₂O): δ_H (ppm) 4.24 (1H, m, H_α), 3.34 (2H, s, H₂NCH₂), 3.13 (4H, m, CH₂), 2.29 (2H, t, CH₂), 1.93 - 1.40 (6H, m, CH₂).

¹³C-NMR (75.5 MHz, D₂O): δ_C (ppm) 173.2 (CO), 169.2 (CO), 168.9 (CO), 160.3 (q, CF₃COO⁻), 156.3 (C, GuaNO₂), 113.5 (q, CF₃COO⁻), 57.6, 49.9, 37.9, 37.7, 31.9, 30.4, 25.1, 24.4, 20.7, 16.3.

ESI-MS (+) (*m/z*): 392.2 [M+H]⁺, calcd. for C₁₃H₂₅N₇O₇ = 391.2.

HPLC (R_t): 8.5 min (λ = 220 nm, Method 2).

7.3.34 - Tert-butyl 2-acetamido-2-((tert-butoxycarbonylamino)methyl)-9-(1-methoxy-5-(3-nitroguanidino)-1-oxopentan-2-ylamino)-9-oxononanoate (51)

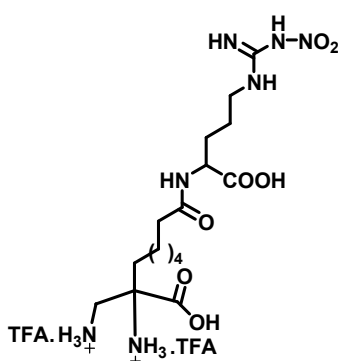


Compound **51** was prepared using the same conditions described for **50**. HBTU (0.058 g, 0.153 mmol), N^ω-NO₂-L-Arg methyl ester (0.041 g, 0.153 mmol) and triethylamine (0.039 g, 0.383 mmol) were added to **39** (0.055 g, 0.130 mmol). Compound **51** was purified by silica gel column chromatography using a gradient of MeOH (0 → 100 %) in CHCl₃, yielding a colorless oil. R_f (silica-gel, CH₂Cl₂/ 15 % of MeOH) = 0.44. Yield: 70.7 % (0.060 g, 0.092 mmol).

$^1\text{H-NMR}$ (300 MHz, CDCl_3): δ_H (ppm) 8.63 (1H, s, NH), 7.79 (2H, s, NH), 6.68 (2H, m, NH), 4.88 (1/2H, s, $\text{H}\alpha$), 4.56 (1/2H, s, $\text{H}\alpha$), 3.69 (3H, s, COOCH_3), 3.55 (2H, m, CH_2), 3.27 (2H, m, CH_2), 2.19 (3H, m, $\text{CH}_2 + \text{CH}$), 1.95 (3H, s, NHCOCH_3), 1.87 (1H, s, CH), 1.55 (6H, m broad, CH_2), 1.41 (9H, s, CH_3), 1.35 (9H, s, CH_3), 1.19 (6H, m broad, CH_2).

$^{13}\text{C-NMR}$ (75.5 MHz, CDCl_3): δ_C (ppm) 174.1 (CO), 172.7 (CO), 171.5 (CO), 170.1 (CO), 159.3 (CO), 155.7 (C, GuaNO_2), 82.9 (C(CH_3)), 79.3 (C(CH_3)), 65.1, 52.5 (CH_3), 50.7, 44.3, 40.3, 36.1, 32.1, 30.2, 29.6, 28.8, 28.2 (C(CH_3)), 27.6 (C(CH_3)), 25.2, 24.5, 23.9, 23.1.

7.3.35 - 2-amino-2-(aminomethyl)-9-(1-methoxy-5-(3-nitroguanidino)-1-oxopentan-2-ylamino)-9-oxononanoic acid (L13)



Compound **L13** was obtained directly by hydrolysis of the protecting groups of **51** (0.055 g, 0.128 mmol) with a 2 M HCl solution (3 mL) as previously described. After semi-preparative RP-HPLC purification (Method 2), **L13** was obtained as a white solid. Yield: 23.6 % (0.020 g, 0.030 mmol, calcd. for $\text{C}_{16}\text{H}_{31}\text{N}_7\text{O}_7 \cdot 2\text{TFA}$).

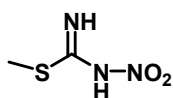
$^1\text{H-NMR}$ (300 MHz, D_2O): δ_H (ppm) 4.19 (1H, s, $\text{H}\alpha$), 3.27 (2H, m, H_2NCH_2), 3.10 (2H, t, $\text{CH}_2\text{NH}-\text{C}=\text{NH}_2$), 2.11 (2H, t, CH_2CONH), 1.83 - 1.40 (8H, m, CH_2), 1.36 - 1.12 (6H, s broad, CH_2).

$^{13}\text{C-NMR}$ (75.5 MHz, D_2O): δ_C (ppm) 177.4 (CO), 175.5 (CO), 171.7 (CO), 162.8 (q, CF_3COO^-), 158.8 (C, GuaNO_2), 118.3 (q, CF_3COO^-), 67.4, 60.6, 52.2, 42.4, 40.5, 35.3, 33.3, 28.1, 27.7, 25.1, 23.0, 22.3.

ESI-MS (+) (m/z): 434.1 $[\text{M}+\text{H}]^+$, calcd. for $\text{C}_{16}\text{H}_{31}\text{N}_7\text{O}_7 = 433.2$.

HPLC (R_t): 12.7 min ($\lambda = 220$ nm, Method 2).

7.3.36 - 2-methyl-1-nitro-2-thiopseudourea (52)



2-methyl-2-thiopseudouronium sulfate (2.00 g, 7.00 mol) was added portionwise over a period of 10 minutes to a nitrating mixture consisting of nitric acid (2 mL) and sulfuric acid (6 mL).

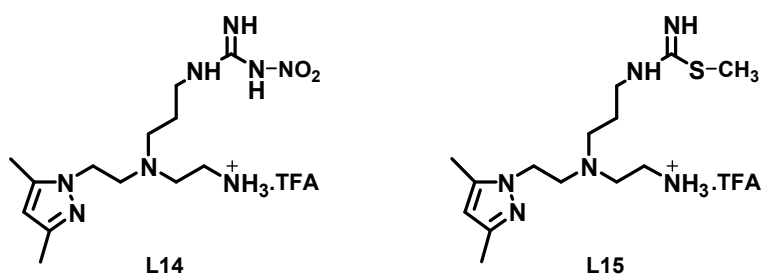
The nitration was carried out at $-10\text{ }^{\circ}\text{C}$ for half of the reacting substance, the remaining portion was added at $0 - 5\text{ }^{\circ}\text{C}$. The reaction mixture was poured in two portions into 15 g of ice. The precipitate obtained was filtered and thoroughly washed with water. Yield: 44.9 % (0.42 g, 3.14 mmol).

IR (KBr, cm^{-1}): 2299s, 2150w, 2100w, 1880s, 1539s.

$^1\text{H-NMR}$ (300 MHz, CDCl_3): δ_{H} (ppm) 2.51 (s, GuaSCH_3 , 3H).

Elemental analysis: calcd. for $\text{C}_2\text{H}_5\text{N}_3\text{O}_2\text{S}$: C, 17.77 %; H, 3.73 %; N, 31.09 %; S, 23.73 %. Found: C, 18.00 %; H, 3.95 %; N, 31.30 %; S, 24.00 %.

7.3.37 - **1-(3-((2-aminoethyl)(2-(3,5-dimethyl-1H-pyrazol-1-yl)ethyl)amino)propyl)-3-nitroguanidine (L14.TFA) and methyl 3-((2-aminoethyl)(2-(3,5-dimethyl-1H-pyrazol-1-yl)ethyl)amino)propylcarbamidimidothioate (L15.TFA)**



To a stirred solution of **L6-Boc** (0.080 g, 0.235 mmol) in anhydrous EtOH were added Et_3N (0.145 g, 1.410 mmol) and 2-methyl-1-nitro-2-thiopseudourea (**52**, 0.095 g, 0.706 mmol). The reaction temperature was then raised to $40\text{ }^{\circ}\text{C}$, and stirring continued overnight under nitrogen. The solvent was evaporated, and the crude residue was purified by silica gel column chromatography using a gradient of MeOH (0 \rightarrow 100 %) in CH_2Cl_2 , giving **L14-Boc** (0.055 g, 0.128 mmol, 54.4 %) and **L15-Boc** (0.022 g, 0.053 mmol, 22.5 %) as pure compounds. Boc-deprotection of **L14-Boc** (0.035 g, 0.082 mmol) and **L15-Boc** (0.020 g, 0.048 mmol) with TFA, followed by RP-HPLC purification (Method 2) gave **L14** (0.030 g, 0.068 mmol, 82.9 %, calcd. for $\text{C}_{13}\text{H}_{26}\text{N}_8\text{O}_2\cdot\text{TFA}$) and **L15** (0.016 g, 0.037 mmol, 77.1%, calcd. for $\text{C}_{14}\text{H}_{29}\text{N}_7\text{S}\cdot\text{TFA}$), respectively.

Characterization of L14

IR (KBr, cm^{-1}): 2242s (NO_2), 1950w, 1606m, 1537m (NO_2), 1442m.

$^1\text{H-NMR}$ (300 MHz, D_2O): δ_{H} (ppm) 6.03 (1H, s, CH^{b}), 4.42 (2H, t, CH_2), 3.56 (2H, t, CH_2), 3.46 (2H, m, CH_2), 3.32 (2H, m, CH_2), 3.18 (2H, t, CH_2), 3.09 (2H, m, CH_2), 2.17 (3H, s, CH_3Pz), 2.10 (3H, s, CH_3Pz), 1.84 (2H, m, CH_2).

$^{13}\text{C-NMR}$ (75.5 MHz, D_2O): δ_{C} (ppm) 162.9 (q, CF_3COO^-), 158.3 (C=N), 147.9 (Pz), 144.2 (Pz), 115.4 (q, CF_3COO^-), 106.7 (Pz), 50.6, 49.1, 41.6, 37.1, 33.0, 22.3, 22.0, 10.4 (CH_3Pz), 9.3 (CH_3Pz).

ESI-MS (+) (m/z): 327.0 [$\text{M}+\text{H}$] $^+$; calcd for $\text{C}_{13}\text{H}_{26}\text{N}_8\text{O}_2 = 326.2$.

HPLC (R_t): 16.2 min ($\lambda = 220$ nm, Method 2).

Characterization of L15

IR (KBr, cm^{-1}): 2530s, 2391s, 2181w, 1942w, 1591m, 1456s.

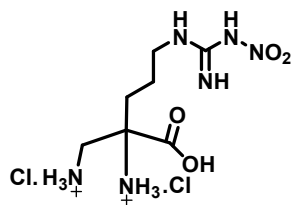
$^1\text{H-NMR}$ (300 MHz, D_2O): δ_H (ppm) 5.85 (1H, s, Pz), 3.99 (2H, t, CH_2), 3.07 (2H, t, CH_2), 2.92 (2H, m, CH_2), 2.86 (2H, m, CH_2), 2.76 (2H, m, CH_2), 2.48 (2H, m, CH_2), 2.44 (3H, s, SCH_3), 2.13 (3H, s, CH_3Pz), 2.07 (3H, s, CH_3Pz), 1.58 (2H, m, CH_2).

$^{13}\text{C-NMR}$ (75.5 MHz, D_2O): δ_c (ppm) 168.2 (C=N), 147.9 (Pz), 141.0 (Pz), 104.9 (Pz), 51.5, 49.8, 49.6, 44.9, 40.8, 36.0, 23.5, 12.5, 11.4 (CH_3Pz), 9.4 (CH_3Pz).

ESI-MS (+) (m/z): 313.2 [$\text{M}+\text{H}$] $^+$; calcd for $\text{C}_{14}\text{H}_{28}\text{N}_6\text{S}$ = 312.2.

HPLC (R_t): 11.4 min ($\lambda = 220$ nm, Method 2).

7.3.38 – 2-amino-2-(aminomethyl)-5-(3-nitroguanidino)pentanoic acid (L16.2Cl)



To a stirred solution of the precursor **44** (0.055 g, 0.166 mmol) in dried EtOH were added Et_3N (0.100 g, 0.996 mmol) and **52** (0.068 g, 0.498 mmol). The reaction temperature was raised to 40 °C, and stirring continued overnight under nitrogen. The solvent was evaporated, and the crude residue was purified by silica gel column chromatography using a gradient of MeOH (0 → 100 %) in CHCl_3 . After evaporation of the solvent from the collected fractions, **L16-protected** was obtained as a yellowish oil. Yield: 86.1 % (0.060 g, 0.143 mmol).

$^1\text{H-NMR}$ (300 MHz, D_2O): δ_H (ppm) 4.16 (2H, q, $-\text{OCH}_2\text{CH}_3$), 3.58 (2H, m, BocNHCH_2), 3.22 (2H, m, CH_2), 1.94 (3H, s, $-\text{COCH}_3$), 1.79 (2H, m, CH_2), 1.63 (2H, m, CH_2), 1.44 (9H, s), 1.24 (3H, t, $-\text{OCH}_2\text{CH}_3$).

Acidic hydrolysis of **L16-protected** (0.060 g, 0.143 mmol), followed by Sep-Pak purification gave **L16**. Yield: 88.9 % (0.041 g, 0.127 mmol, calcd. for $\text{C}_7\text{H}_{18}\text{N}_6\text{O}_4 \cdot 2\text{Cl}$).

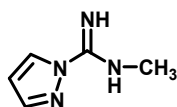
$^1\text{H-NMR}$ (300 MHz, D_2O): δ_H (ppm) 3.27 (2H, s, NH_2CH_2), 3.16 (2H, t, CH_2), 2.00 – 1.30 (4H, m, CH_2).

$^{13}\text{C-NMR}$ (75.5 MHz, D_2O): δ_c (ppm) 171.2 (CO), 157.3 (C, GuaNO_2), 61.2, 43.5, 36.8, 31.5, 22.3.

ESI-MS (+) (m/z): 251.0 [$\text{M}+1$] $^+$; calcd for $\text{C}_7\text{H}_{18}\text{N}_6\text{O}_4$ = 250.1

HPLC (R_t): 5.7 min ($\lambda = 220$ nm, Method 2).

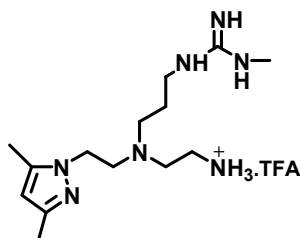
7.3.39 – N-methyl-1H-pyrazole-1-carboximidamide (53)



Cyanogen bromide (2.100 g, 0.019 mol) was dissolved in THF (30 mL) and sodium carbonate (4.200 g, 0.390 mol) was added. Methylamine (2 M solution in THF, 0.019 mol, 10 mL) was added dropwise over 10 minutes under stirring at 0 °C. The reaction mixture was then left to react for 2 h at room temperature before filtering off the white solid to give a clear solution of methylcyanamide. To this solution, pyrazole in solid (1.300 g, 0.019 mol) and a 4 M HCl solution in dioxane (0.019 mol, 4.75 mL) was added. After refluxing for 2 hours, the reaction mixture was allowed to cool down and diethyl ether was added to precipitate a cream waxy solid which was isolated. The solid was then further purified by sublimation in vacuum at 80 °C to remove unreacted pyrazole. Yield: 16.5 % (0.500 g, 3.13 mmol, calcd. for C₅H₈N₄·HCl).

¹H-NMR (300 MHz, DMSO-d₆): δ_H (ppm) 8.73 (1H, s, Pz), 8.07 (1H, s, Pz), 6.77 (1H, s, Pz), 2.50 (3H, s, CH₃).

7.3.40 – 1-(3-((2-aminoethyl)(2-(3,5-dimethyl-1H-pyrazol-1-yl) ethyl)amino)propyl)-3-methyl-guanidine (L17.TFA)



Method A: **53** (0.047 g, 0.294 mmol), and **L6-Boc** (0.050 g, 0.147 mmol) were mixed in water (pH 2 to 3). The pH of the solution was adjusted to 10 - 11 with lithium hydroxide monohydrate (0.018 g, 0.441 mmol). After stirring for 2 days at room temperature, 1 eq. of **53** was added and stirring continued for more 3 days. The solvent was removed, the residue dissolved in CH₂Cl₂, filtered, and purified by silica gel column chromatography using a gradient of MeOH (0 → 100 %) in CH₂Cl₂. Removal of the solvent from the collected fractions gave **L17-Boc**. Yield: 51.7 % (0.030 g, 0.076 mmol).

Method B: To a solution of **L6-Boc** (0.050 g, 0.147 mmol) in DMF was added **53** (0.047 g, 0.294 mmol), and DIPEA (0.037 g, 0.294 mmol) in the same solvent. After stirring at room temperature for 18 h the solvent was evaporated and the crude product purified by silica gel column chromatography using a gradient of MeOH (0 → 100 %) in CH₂Cl₂ to give **L17-Boc** as a pale yellow oil. Yield: 48.1% (0.028 g, 0.070 mmol).

L17-Boc (0.030 g, 0.076 mmol) was dissolved in a solution of CH₂Cl₂/TFA (1 mL/2 mL) and stirred at room temperature for 3 h. **L17** was obtained as colorless oil after purification by RP-HPLC (Method 2). Yield: 73.9 % (0.023 g, 0.056 mmol, calcd. for C₁₄H₂₉N₇ · TFA).

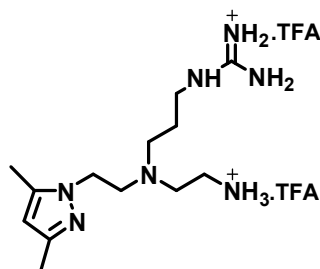
¹H-NMR (300 MHz, D₂O): δ_H (ppm) 6.01 (1H, s, CH^b), 4.38 (2H, t, CH₂), 3.53 (2H, t, CH₂), 3.51 (2H, m, CH₂), 3.38 (2H, m, CH₂), 3.27 (2H, m, CH₂), 3.03 (2H, m, CH₂), 2.65 (3H, s, C-NH-CH₃), 2.15 (3H, s, CH₃Pz), 2.08 (3H, s, CH₃pz), 1.79 (2H, m, CH₂).

¹³C-NMR (75.5 MHz, D₂O): δ_C (ppm) 165.3 (q, CF₃COO⁻), 162.6 (C=N), 155.7 (Pz), 148.4 (Pz), 115.6 (q, CF₃COO⁻), 106.1 (Pz), 51.4, 50.6, 49.2, 42.0, 37.3, 33.3, 26.6, 22.4, 11.0 (CH₃Pz), 9.3 (CH₃Pz).

ESI-MS (+) (*m/z*): 296.1 [M+H]⁺; calcd for C₁₄H₂₉N₇ = 295.2.

HPLC (R_t): 15.0 min (λ = 220 nm, Method 2).

7.3.41 – **1-(3-((2-aminoethyl)(2-(3,5-dimethyl-1H-pyrazol-1-yl)ethyl)amino)propyl)guanidine (L18.2TFA).**



L18-Boc was prepared using the same reaction conditions described for **L17-Boc** (Section 7.3.40, Method B). Starting from 0.190 g (0.559 mmol) of **L6-Boc**, 0.114 g of 1H-pyrazole-1-carboximidamide (0.783 mmol), and 0.101 g of DIPEA (0.783 mmol) in DMF, **L18-Boc** was obtained as a pale yellow oil after purification by silica gel column chromatography using a gradient of MeOH (0 → 100 %) in CH₂Cl₂. Yield: 25.8 % (0.055 g, 0.144 mmol).

L18 was obtained directly by treatment of **L18-Boc** (0.055 g, 0.144 mmol) with a TFA/CH₂Cl₂ solution (1 mL/2 mL) at room temperature for 3 h. The solvent was evaporated and the obtained residue dissolved in water and purified by RP-HPLC (Method 2) to give a colorless oil. Yield: 43.7 % (0.032 g, 0.063 mmol, calcd. for C₁₃H₂₇N₇ · 2TFA).

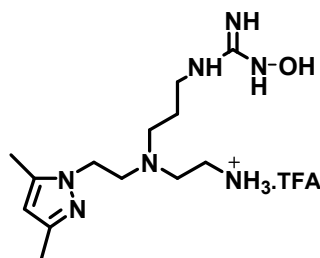
¹H-NMR (300 MHz, CD₃OD): δ_H (ppm) 6.13 (1H, s, CH^b), 4.50 (2H, t, CH₂), 3.53 (2H, t, CH₂), 3.43 (2H, m, CH₂), 3.29 (2H, m, CH₂), 3.11 (4H, m, CH₂), 2.20 (3H, s, CH₃pz), 2.14 (3H, s, CH₃pz), 1.83 (2H, m, CH₂).

¹³C-NMR (75.5 MHz, CD₃OD): δ_C (ppm) 162.3 (q, CF₃COO⁻), 156.1 (C=N), 147.3 (Pz), 145.6 (Pz), 115.5 (q, CF₃COO⁻), 107.4 (Pz), 50.5, 50.3, 49.0, 41.5, 37.2, 32.9, 22.0, 9.9 (CH₃Pz), 9.4 (CH₃Pz).

ESI-MS (+) (*m/z*): 282.1 [M+H]⁺; calcd for C₁₃H₂₇N₇ = 281.2.

HPLC (R_t): 13.8 min (λ = 220 nm, Method 2).

7.3.42 - 1-(3-((2-aminoethyl)(2-(3,5-dimethyl-1H-pyrazol-1-yl)ethyl)amino)propyl)-3-hydroxy-guanidine (L19.TFA).



To a solution of **L6-Boc** (0.090 g, 0.265 mmol) and Et₃N (0.040 g, 0.397 mmol) in dry CH₂Cl₂ at 0 °C was added BrCN (0.084 g, 0.795 mmol) dissolved in the same solvent. After overnight reaction at room temperature excess of BrCN (0.056 g, 0.530 mmol) was added at 0 °C to force reaction to completion. After 4 h of reaction, the solvent was evaporated and the crude cyanamide (**54**) purified by silica gel column chromatography using a gradient of MeOH (0 → 100 %) in EtOAc to give a pale yellow oil. Yield: 54.3 % (0.060 g, 0.144 mmol).

¹H-NMR (300 MHz, CD₃OD): δ_H (ppm) 5.77 (1H, s, CH^b), 5.65 (1H, br s, NH), 5.34 (1H, br s, NH), 4.08 (2H, t, CH₂), 3.52 (2H, m, CH₂), 3.11 (2H, m, CH₂), 2.89 (2H, m, CH₂), 2.58 (4H, m, CH₂), 2.21 (3H, s, CH₃Pz), 2.18 (3H, s, CH₃Pz), 1.87 (2H, m, CH₂), 1.40 (9H, s, CH₃).

¹³C-NMR (75.5 MHz, CDCl₃): δ_C (ppm) 158.9 (CO), 157.0 (cyanamide), 147.6 (Pz), 131.1 (Pz), 105.6 (Pz), 79.3 (C(CH₃)₃), 53.6, 52.9, 51.1, 45.8, 38.1, 37.5, 28.2 (C(CH₃)₃), 24.8, 13.1 (CH₃Pz), 10.8 (CH₃Pz).

A mixture of **54** (0.060 g, 0.144 mmol), K₂CO₃ (0.023 g, 0.330 mmol), and H₂NOH.HCl (0.046 g, 0.330 mmol) in anhydrous EtOH was stirred at room temperature for 18 h. The solution was then filtered to remove an insoluble white solid. After evaporation of the filtrate, the residue was purified by silica gel column chromatography using a gradient of MeOH (0 → 100 %) in CH₂Cl₂. Evaporation of the solvent from the collected fractions yielded **L19-Boc** as a colorless oil. Yield: 52.8 % (0.030 g, 0.076 mmol).

Compound **L19** was prepared using the standard TFA Boc-deprotection conditions described before. Starting from 0.030 g (0.076 mmol) of **L19**, a colorless oil formulated as **L19** was obtained after purification by RP-HPLC (Method 2). Yield: 69.7 % (0.022 g, 0.053 mmol, calcd. for C₁₃H₂₇N₇O · TFA).

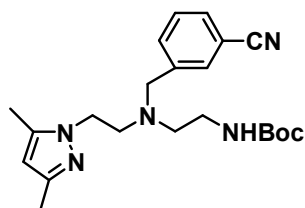
¹H-NMR (300 MHz, CD₃OD): δ_H (ppm) 5.98 (1H, s, CH^b), 4.33 (2H, t, CH₂), 3.48 (2H, t, CH₂), 3.37 (2H, m, CH₂), 3.28 (2H, m, CH₂), 3.15 (2H, m, CH₂), 3.03 (2H, m, CH₂), 2.17 (3H, s, CH₃Pz), 2.09 (3H, s, CH₃Pz), 1.79 (2H, m, CH₂).

$^{13}\text{C-NMR}$ (75.5 MHz, CD_3OD): δ_c (ppm) 165.4 (q, CF_3COO^-), 156.1 (C=N), 151.2 (Pz), 144.3 (Pz), 118.5 (q, CF_3COO^-), 108.2 (Pz), 54.6, 53.0, 52.6, 47.4, 41.1, 38.7, 27.0, 14.4 (CH_3Pz), 12.5 (CH_3Pz).

ESI-MS (+) (m/z): 298.1 [$\text{M}+\text{H}$] $^+$; calcd for $\text{C}_{13}\text{H}_{27}\text{N}_7\text{O}$ = 297.2.

HPLC (R_t): 14.2 min (λ = 220 nm, Method 2).

7.3.43 – *Tert*-butyl 2-((3-cyanobenzyl)(2-(3,5-dimethyl-1H-pyrazol-1-yl)ethyl)amino)ethylcarbamate (56)



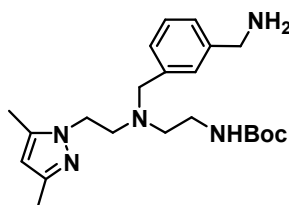
A solution of **27** (0.600 g, 2.125 mmol), 3-(bromomethyl)benzonitrile (0.833 g, 4.250 mmol), and K_2CO_3 (0.587 g, 4.250 mmol) in ACN (35 mL) was refluxed for 24 h. After reaction, the solution was filtered and the solvent evaporated to give an oily residue, which was purified by column chromatography purified by silica gel column chromatography using a gradient of EtOAc (0 \rightarrow 100 %) in hexane. The fractions containing **56** were collected and the compound was obtained as a colorless oil after evaporation of the solvent. Yield: 55.6 % (0.470 g, 1.183 mmol).

IR (KBr, cm^{-1}): 2229vw $\nu(\text{C}\equiv\text{N})$, 1711m, 1175m.

$^1\text{H-NMR}$ (300 MHz, CDCl_3): δ_H (ppm) 7.45 (1H, m, Ar) 7.29 (3H, m, Ar), 6.00 (1H, br m, *NH*Boc), 5.82 (1H, s, CH^b), 4.00 (2H, t, CH_2), 3.55 (2H, s, CH_2), 3.20 (2H, m, CH_2), 2.70 (2H, t, CH_2), 2.61 (2H, t, CH_2), 2.28 (3H, s, CH_3Pz), 1.98 (3H, s, CH_3Pz), 1.44 (9H, s, $\text{C}(\text{CH}_3)_3$).

$^{13}\text{C-NMR}$ (75.5 MHz, CDCl_3): δ_c (ppm) 156.6 (C=O, Boc), 147.5 (Pz), 141.2 (Pz), 138.7 (Ar), 133.0 (Ar), 132.0 (Ar), 130.8 (Ar), 129.1 (Ar), 119.1.2 (Ar), 112.6 (C \equiv N), 105.7 (Pz), 79.1 ($\text{C}(\text{CH}_3)_3$), 58.0, 53.4, 53.3, 46.7, 38.6, 28.7 ($\text{C}(\text{CH}_3)_3$), 13.6 (CH_3Pz), 10.9 (CH_3Pz).

7.3.44 – *Tert*-butyl 2-((3-(aminomethyl)benzyl)(2-(3,5-dimethyl-1H-pyrazol-1-yl)ethyl)amino)ethylcarbamate (57)



To a solution of **56** (0.382 g, 0.961 mmol) in MeOH (10 mL) cooled with an ice bath, was added $\text{NiCl}_2\cdot 6\text{H}_2\text{O}$ (0.023 g, 0.096 mmol) to give a green solution. NaBH_4 (0.290 g, 7.688 mmol) was added in portions with stirring and the resulting purple mixture was stirred overnight at 20 $^\circ\text{C}$. The

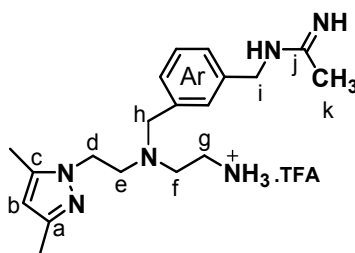
solvent was evaporated and the residue partitioned between EtOAc and a saturated NaHCO₃ solution. The organic phase was dried over MgSO₄. Removal of organic solvent gave a colorless residue. Compound **57** was used without any further purification. Yield 79.5 % (0.307 g, 0.764 mmol).

IR (KBr, cm⁻¹): 1713m, 1176m.

¹H-NMR (300 MHz, CDCl₃): δ_H (ppm) 7.17 – 6.98 (4H, m, Ar), 5.75 (1H, s, CH^b), 5.50 (2H, br m, NH₂), 3.98 (2H, s, CH₂), 3.78 (2H, m, CH₂), 3.56 (2H, s, CH₂), 3.14 (2H, m, CH₂), 2.76 (2H, t, CH₂), 2.56 (2H, t, CH₂), 2.23 (3H, s, CH₃Pz), 2.02 (3H, s, CH₃pz), 1.42 (9H, s, C(CH₃)).

¹³C-NMR (75.5 MHz, CDCl₃): δ_C (ppm) 156.5 (C=O, Boc), 147.5 (Pz), 139.5 (Pz), 139.2 (Ar), 128.8 (Ar), 128.7 (Ar), 127.3 (Ar), 127.4 (Ar), 125.9 (Ar), 105.2 (Pz), 79.1 (C(CH₃, overlapped with CDCl₃), 58.9, 53.4, 53.3, 47.0, 38.6, 28.7 (C(CH₃), 13.7 (CH₃Pz), 11.1 (CH₃Pz).

7.3.45 – N-(3-(((2-aminoethyl)(2-(3,5-dimethyl-1H-pyrazol-1-yl)ethyl)amino)methyl)benzyl)acetimidamide (L20.TFA)



A solution of **57** (0.116 g, 0.288 mmol), methyl acetimidate (0.063 g, 0.576 mmol), and DIPEA (0.074 g, 0.576 mmol) in DMF was refluxed for 48 h. After reaction, the DMF was evaporated to give an oily residue, which was purified by silica gel column chromatography using a gradient of MeOH (0 → 100 %) in CHCl₃. The fractions containing **L20-Boc** were collected and the compound was obtained as a colorless oil after evaporation of the elution solvents. Yield: 69.7 % (0.089 g, 0.200 mmol).

¹H-NMR (300 MHz, CDCl₃): δ_H (ppm) 7.40 – 7.19 (4H, m, Ar), 5.82 (1H, s, CH^b), 4.44 (2H, s, CH₂ⁱ), 4.22 (2H, t, CH₂^d), 3.64 (2H, s, CH₂^h), 3.17 (2H, m, CH₂), 2.82 (2H, t, CH₂), 2.60 (2H, t, CH₂), 2.29 (3H, s, NH-C-CH₃), 2.20 (3H, s, CH₃Pz), 2.15 (3H, CH₃Pz), 1.40 (9H, s, C(CH₃)).

¹³C-NMR (75.5 MHz, CDCl₃): δ_C (ppm) 164.1 (C^j), 156.3 (C=O, Boc), 147.2 (Pz), 139.3 (Pz), 139.0 (Ar), 128.6 (Ar), 128.4 (Ar), 127.1 (Ar), 127.0 (Ar), 125.7 (Ar), 105.1 (Pz), ~78.8 (C(CH₃), overlapped with CDCl₃), 58.7, 53.6, 53.1, 46.7, 38.3, 28.5 (C(CH₃), 28.1, 13.5 (C^k), 13.4 (CH₃Pz), 10.8 (CH₃Pz).

HPLC (R_t): 18.3 min (λ = 220 nm, Method 2).

Treatment of **L20-Boc** (0.068 g, 0.153 mmol) with $\text{CH}_2\text{Cl}_2/\text{TFA}$ (1 mL/2 mL), as previously described, gave a colorless oil corresponding to **L20** after purification by preparative RP-HPLC (Method 2). Yield: 50.0 % (0.035 g, 0.076 mmol, calcd. for $\text{C}_{19}\text{H}_{31}\text{N}_6 \cdot 1\text{TFA}$).

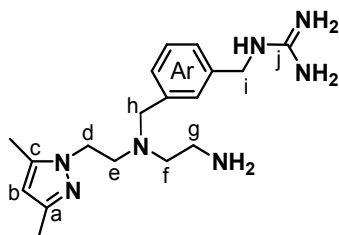
$^1\text{H-NMR}$ (300 MHz, CD_3OD): δ_{H} (ppm) 7.40 – 7.22 (4H, m, Ar), 6.05 (1H, s, CH_2^{b}), 4.37 (2H, s, CH_2^{i}) 4.29 (2H, t, CH_2^{d}), 4.18 (2H, s, CH_2^{h}), 3.67 – 3.21 (6H, m, CH_2), 2.15 (3H, s, H^{k}), 2.12 (3H, s, CH_3Pz), 2.08 (3H, s, CH_3Pz).

$^{13}\text{C-NMR}$ (75.5 MHz, CD_3OD): δ_{C} (ppm) 165.2 (C^{j}), 163.2 (q, CF_3COO^-), 147.9 (Pz), 145.1 (Pz), 131.7 (Ar), 130.4 (Ar), 130.2 (Ar), 129.6 (Ar), 129.2 (Ar), 116.0 (q, CF_3COO^-), 107.4 (Pz), 58.4 (C^{h}), 51.5 ($\text{C}^{\text{e/f/g}}$), 50.3 ($\text{C}^{\text{e/f/g}}$), 45.5 (C^{i}), 43.6 (C^{d}), 34.8 ($\text{C}^{\text{e/f/g}}$), 18.5 (C^{k}), 11.1 (CH_3Pz), 10.1 (CH_3Pz).

ESI-MS (+) (m/z): 343.1 $[\text{M}+\text{H}]^+$, calcd. for $\text{C}_{19}\text{H}_{30}\text{N}_6 = 342.2$.

HPLC (R_{t}): 15.1 min ($\lambda = 220$ nm, Method 2).

7.3.46 – 1-(3-(((2-aminoethyl)(2-(3,5-dimethyl-1H-pyrazol-1-yl)ethyl)amino)methyl)benzyl)guanidine (**L21.2TFA**)



L21-Boc was prepared using the same reaction conditions described for **L17-Boc** (Section 7.3.40, Method B). Starting from 0.065 g (0.162 mmol) of **57**, 0.036 g of 1H-pyrazole-1-carboximidamide (0.243 mmol), and 0.031 g of DIPEA (0.243 mmol) in DMF, **L21-Boc** was obtained as a pale yellow oil after purification by column chromatography ($\text{CH}_2\text{Cl}_2 \rightarrow \text{MeOH}$). Yield 76.4 % (0.055 g, 0.123 mmol). **L21-Boc** was isolated with a contamination of 10 % of free pyrazole based on the $^1\text{H-NMR}$, and used without any further purification.

IR (KBr, cm^{-1}): 1700s, 1169m.

$^1\text{H-NMR}$ (300 MHz, CD_3OD): δ_{H} (ppm) 7.29 – 7.10 (4H, m, Ar), 5.80 (1H, s, CH^{b}), 4.34 (2H, s, CH_2^{i}), 4.00 (2H, t, CH_2^{d}), 3.33 (2H, s, CH_2^{h}), 3.07 (2H, m, $\text{CH}_2^{\text{f/g}}$), 2.77 (2H, t, CH_2^{e}), 2.58 (2H, t, $\text{CH}_2^{\text{f/g}}$), 2.15 (3H, s, CH_3Pz), 2.13 (3H, s, CH_3Pz), 1.31 (9H, s, $\text{C}(\text{CH}_3)$).

$^{13}\text{C-NMR}$ (75.5 MHz, CD_3OD): δ_{C} (ppm) 157.5 (C^{j}), 157.1 ($\text{C}=\text{O}$, Boc), 154.0 (Pz), 144.0 (Pz), 140.1 (Ar), 129.3 (Ar), 128.7 (Ar), 128.3 (Ar), 127.6 (Ar), 125.9 (Ar), 104.8 (Pz), 78.8 ($\text{C}(\text{CH}_3)$), 58.5 ($\text{C}^{\text{h/i}}$), 53.6 ($\text{C}^{\text{f/g}}$), 53.3 (C^{e}), 46.6 (C^{d}), 44.9 ($\text{C}^{\text{h/i}}$), 38.2 ($\text{C}^{\text{f/g}}$), 27.6 ($\text{C}(\text{CH}_3)$), 11.7 (CH_3Pz), 9.9 (CH_3Pz).

HPLC (R_{t}): 18.2 min ($\lambda = 220$ nm, Method 2).

Treatment of **L21-Boc** (0.045 g, 0.101 mmol) with CH₂Cl₂/TFA (1 mL/2 mL) gave a colorless oil corresponding to **L21** after purification by preparative RP-HPLC (Method 2). Yield: 38.8 % (0.022 g, 0.040 mmol, calcd. for C₁₈H₂₉N₇·2TFA).

¹H-NMR (300 MHz, CD₃OD): δ_H (ppm) 7.24 (2H, m, Ar), 7.03 (2H, m, Ar), 5.86 (1H, s, CH^b), 4.30 (2H, s, CH₂ⁱ) 4.08 (2H, t, CH₂^d), 3.71 (2H, s, CH₂^h), 3.04 (2H, m, CH₂^{f/g}), 2.88 (2H, t, CH₂^e), 2.80 (2H, t, CH₂^{f/g}), 2.20 (3H, s, CH₃Pz), 2.00 (3H, s, CH₃Pz).

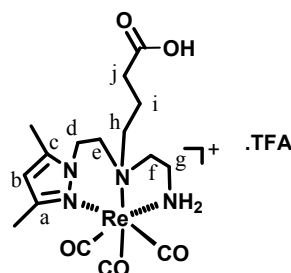
¹³C-NMR (75.5 MHz, CD₃OD): δ_C (ppm) 157.5 (C^j), 147.0 (Pz), 140.4 (Pz), 138.7 (Ar), 136.6 (Ar), 129.1 (Ar), 128.3 (Ar), 127.8 (Ar), 126.4 (Ar), 105.3 (pz), 58.6 (C^e), 52.6 (C^{f/g}), 50.8 (Cⁱ), 45.7 (C^d), 44.8 (C^h), 37.1 (C^{f/g}), 11.8 (CH₃Pz), 9.4 (CH₃Pz).

ESI-MS (+) (m/z): 344.1 [M+H]⁺, calcd. for C₁₈H₂₉N₇ = 343.2.

HPLC (R_t): 15.2 min (λ = 220 nm, Method 2).

7.4 – Synthesis and Characterization of Re Complexes of the Type *fac*-[Re(CO)₃(κ³-L)]

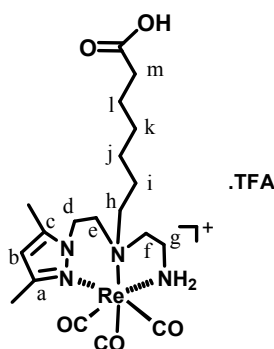
7.4.1 - *fac*-[Re(CO)₃(κ³-L4)]⁺ (Re4.TFA)



Re4 has been synthesized as previously described starting with (NEt₄)₂[ReBr₃(CO)₃].^{41c} The compound has been obtained as a viscous colorless oil after purification by preparative RP-HPLC (Method 1). Suitable crystals of *fac*-[Re(κ³-L4)(CO)₃]TFA·H₂O (**Re4**·TFA·H₂O) for X-ray diffraction analysis were grown by slow diffusion of CHCl₃ into a solution of the compound in MeOH.

¹H-NMR (300 MHz, D₂O): δ_H (ppm) 6.15 (1H, s, CH^b), 5.16 (1H, br s, NH), 4.40 (1H, dd, CH^d), 4.18 (1H, dd, CH^d), 3.73 (1H, m, NH), 3.59 (1H, m, CH^h), 3.43 (2H, m, CH^{e+h}), 3.14 (1H, m, CH^g), 2.81 (2H, m, CH₂^j), 2.63 (1H, m, CH₂^e), 2.52 (1H, m, CH^g), 2.40 (2H, m, CH^f), 2.34 (3H, s, CH₃Pz), 2.23 (3H, s, CH₃Pz), 2.13 (1H, m, CH₂ⁱ), 1.93 (1H, m, CH₂ⁱ).

¹³C-NMR (75.5 MHz, CD₃OD, ppm) δ_C 198.3 (C≡O), 194.5 (C≡O), 194.3 (C≡O), 176.0 (COOH), 146.6, 135.6, 108.7, 67.3, 62.5, 53.7, 43.6, 31.7, 30.7, 20.7, 16.0 (CH₃Pz) 11.5 (CH₃Pz).

7.4.2 - *fac*-[Re(CO)₃(κ³-L5)]⁺ (Re5.TFA)

L5 (0.050 g, 0.117 mmol) reacted with precursor *fac*-[Re(CO)₃(H₂O)₃]Br (0.043 g, 0.106 mmol) in refluxing water for 18 h (pH 7). After evaporation of the solvent the resulting residue was purified by preparative RP-HPLC (Method 1). Compound **Re5** was obtained as a colorless oil. Yield: 43 % (0.035 g, 0.050 mmol, calcd. for C₁₉H₃₀N₄O₅Re·TFA).

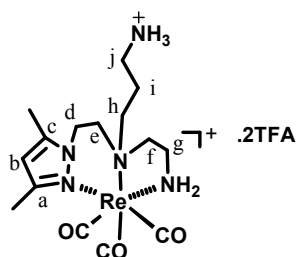
IR (KBr, cm⁻¹): 2030s and 1920s (C≡O) and 1668s (C=O).

¹H-NMR (300 MHz, CD₃OD): δ_H (ppm) 6.20 (1H, s, CH^b), 5.49 (1H, br s, NH), 4.50 (1H, dd, CH^d), 4.22 (1H, dd, CH^{d'}), 3.55 (1H, m, NH), 3.59 (1H, m, CH^m), 3.41 (2H, m, CH^e + CH^{m'}), 3.16 (1H, m, CH^g), 2.83 (2H, m, CH₂^f), 2.68 (1H, dd, CH^{e'}), 2.49 (1H, m, CH^{g'}), 2.43 (3H, s, CH₃Pz), 2.35 (3H, s, CH₃Pz), 2.32 (2H, t, CH₂^h), 1.80 (4H, m, CH₂ⁱ + CH₂^l), 1.45 (4H, m, CH₂^j + CH₂^k).

¹³C-NMR (75.5 MHz, CD₃OD): δ_C (ppm) 198.5 (C≡O), 198.1 (C≡O), 196.9 (C≡O), 180.7 (C=O), 158.3 (Pz), 148.5 (Pz), 112.4 (Pz), 71.9, 66.2, 57.6, 51.9 (overlapped with CD₃OD), 46.8, 37.9, 33.0, 30.9, 28.9, 28.7, 19.2 (CH₃Pz), 14.7 (CH₃Pz).

ESI-MS (+) (m/z): 581.1 [M]⁺, calcd. for C₁₈H₂₆N₄O₇Re = 581.2.

HPLC (R_t): 20.5 min (λ = 254 nm, Method 1).

7.4.3 - *fac*-[Re(CO)₃(κ³-L6)]⁺ (Re6.2TFA)

L6 (0.020 g, 0.043 mmol) reacted with precursor *fac*-[Re(CO)₃(H₂O)₃]Br (0.040 g, 0.051 mmol) in refluxing water for 18 h (pH 7). After evaporation of the solvent the resulting residue was purified by preparative RP-HPLC. Compound **Re6** was obtained as a colorless oil. Yield: 79 % (0.025 g, 0.034 mmol, calcd. for C₁₅H₂₆N₅O₃Re.2TFA).

IR (KBr, cm⁻¹): 3360m ν(NH₂), 2038s and 1954s (C≡O), 1680w δ(NH₂), 1190w and 1105w.

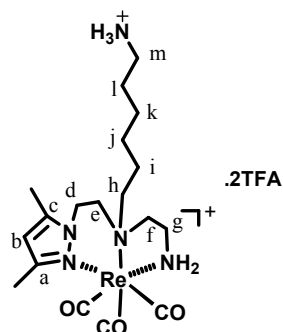
$^1\text{H-NMR}$ (300 MHz, D_2O) δ_{H} (ppm) 6.07 (1H, s, CH^{b}), 5.14 (1H, br s, NH), 4.35 (1H, dd, CH^{d}), 4.13 (1H dd, $\text{CH}^{\text{d'}}$), 3.65 (2H, m, NH/CH^{j}), 3.44 (1H, dd, $\text{CH}^{\text{j'}}$), 3.32 (1H, dd, CH^{e}), 3.11 (1H, m, CH^{e}), 2.98 (2H, t, CH_2^{h}), 2.77 (2H, m, CH_2^{f}), 2.63 (1H, dd, $\text{CH}^{\text{e'}}$), 2.47 (1H, m, $\text{CH}^{\text{e'}}$), 2.30 (3H, s, CH_3Pz), 2.19 (3H, s, CH_3Pz), 2.05 (2H, m, CH_2^{i}).

$^{13}\text{C-NMR}$ (75.5 MHz, D_2O , ppm) δ_{C} 197.3 ($\text{C}\equiv\text{O}$), 196.7 ($\text{C}\equiv\text{O}$), 195.5 ($\text{C}\equiv\text{O}$), 164.9 (q, CF_3COO^-), 156.5 (pz), 147.1 (pz), 118.0 (q, CF_3COO^-), 110.5 (pz), 65.7 (C^{j}), 63.9 (C^{f}), 55.4 (C^{e}), 49.7 (C^{d}), 44.9 (C^{e}), 39.9 (C^{b}), 25.2 (C^{i}), 18.0 (CH_3pz), 13.6 (CH_3pz).

ESI-MS (+) (m/z): 510.1 $[\text{M}]^+$, calcd. for $\text{C}_{15}\text{H}_{25}\text{N}_5\text{O}_3\text{Re}$ = 510.1.

HPLC (R_{t}): 18.2 min (λ = 254 nm, Method 1).

7.4.4 - *fac*- $[\text{Re}(\text{CO})_3(\kappa^3\text{-L7})]^+$ (Re7.2TFA)



L7 (0.060 g, 0.118 mmol) reacted with precursor *fac*- $[\text{Re}(\text{CO})_3(\text{H}_2\text{O})_3]\text{Br}$ (0.090 g, 0.118 mmol) in refluxing water for 18 h (pH 7). After evaporation of the solvent the resulting residue was purified by preparative RP-HPLC (Method 1). Compound **Re7** was obtained as a colorless oil. Yield: 54 % (0.05 g, 0.064 mmol, calcd. for $\text{C}_{18}\text{H}_{31}\text{N}_5\text{O}_3\text{Re}\cdot 2\text{TFA}$).

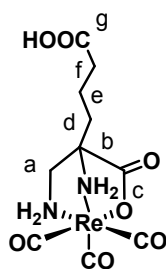
IR (KBr, cm^{-1}): 3394m $\nu(\text{NH}_2)$, 2106 and 1974s (CO), 1682w $\delta(\text{NH}_2)$, 1298m, 1105m, 896w and 778w.

$^1\text{H-NMR}$ (300 MHz, D_2O): δ_{H} (ppm) 6.07 (1H, s, CH^{b}), 5.09 (1H, br s, NH), 4.32 (1H, dd, CH^{d}), 4.13 (1H, dd, $\text{CH}^{\text{d'}}$), 3.64 (1H, m, NH), 3.52 (1H, m, CH^{m}), 3.32 (2H, m, CH^{e} + $\text{CH}^{\text{m'}}$), 3.18 (1H, m, CH^{e}), 2.90 (2H, t, CH_2^{h}), 2.75 (2H, m, CH_2^{f}), 2.58 (1H, dd, $\text{CH}^{\text{e'}}$), 2.43 (1H, m, $\text{CH}^{\text{e'}}$), 2.30 (3H, s, CH_3Pz), 2.19 (3H, s, CH_3Pz), 1.74 (4H, m, CH_2^{i} , CH_2^{j}), 1.34 (4H, m, CH_2^{j} + CH_2^{k}).

$^{13}\text{C-NMR}$ (300 MHz, D_2O , ppm) δ_{C} 198.8 ($\text{C}\equiv\text{O}$), 198.3 ($\text{C}\equiv\text{O}$), 197.2 ($\text{C}\equiv\text{O}$), 164.8 (q, CF_3COO^-), 157.8 (Pz), 148.3 (Pz), 118.0 (q, CF_3COO^-), 111.8 (Pz), 71.3 (C^{m}), 65.7 (C^{f}), 57.0 (C^{e}), 51.3 (C^{d}), 46.3 (C^{e}), 43.6 (C^{h}), 30.9 (C^{i}), 29.9 (C^{i}), 29.6 (C^{i}), 28.1 (C^{k}), 19.9 (CH_3Pz), 14.4 (CH_3Pz).

ESI-MS (+) (m/z): 276.0 $[\text{M} + 2\text{H}]^{2+}$, calcd. for $\text{C}_{18}\text{H}_{31}\text{N}_5\text{O}_3\text{Re}$ = 552.2.

HPLC (R_{t}): 18.9 min (λ = 254 nm, Method 1).

7.4.5 - *fac*-[Re(CO)₃(κ³-L8)] (Re8)

A mixture of **36-lactam** + **L8** (0.146 g, 0.194 mmol) reacted with precursor (Et₄N)₂[Re(CO)₃Br₃] (0.050 g, 0.194 mmol) in refluxing water for 18 h (pH 4). After cooling to room temperature and concentration of the solution, a white precipitate was obtained, which was isolated by centrifugation and washed several times with water and warm CH₂Cl₂ to remove excess [NEt₄]Br. The spectral data of this complex were in accordance with the formulation proposed for **Re8**. Analytical RP-HPLC analysis of the supernatant obtained after precipitation of **Re8** revealed still the presence of **36-lactam**, Re precursor and a small amount of **Re8**. By refluxing overnight at pH 8, the rhenium precursor was consumed and a mixture of **36-lactam** and a second new species, formulated as "*fac*-[Re(CO)₃(**36-lactam**)]", was obtained. Complexes **Re8** and as "*fac*-[Re(CO)₃(**36-lactam**)]" were isolated by RP-HPLC purification (Method 2). *fac*-[Re(CO)₃(κ³-L8)] (**Re8**): Yield: 54.9% (0.049 g, 0.106 mmol, calcd for C₁₀H₁₃N₂O₇Re). *fac*-[Re(CO)₃(**36-lactam**)]: Yield: 29.1% (0.025 g, 0.056 mmol, calcd for C₁₀H₁₁N₂O₆Re).

Characterization of *fac*-[Re(CO)₃(κ³-L8)] (**Re8**)

IR (KBr, cm⁻¹): 2021s, 1907s, 1884s, 1693m (C=O) and 1647m (C=O).

¹H-NMR (300 MHz, CD₃OD): δ_H (ppm) 5.32 (1H, m, NH₂C^b), 4.95 (1H, m, NH₂C^a), 4.75 (1H, m, NH₂CH₂^b), 4.64 (1H, m, NH₂CH₂^a), 2.76 (1H, m, CH₂^a), 2.59 (1H, m, CH₂^a), 2.33 (2H, m, CH₂^f), 1.78 (2H, m, CH₂^d), 1.67 (2H, m, CH₂^e).

¹³C-NMR (75.5 MHz, CD₃OD): δ_C (ppm) 198.3 (C≡O), 197.1 (C≡O), 181.2 (C^c), 177.2 (C^g), 67.0 (C^b), 46.6 (C^a), 35.0 (C^f), 34.8 (C^d), 19.9 (C^e).

ESI-MS (+) (*m/z*): 482.9 [M+Na]⁺; calcd for C₁₀H₁₃N₂O₇ReNa = 483.0.

Elemental analysis: Calcd. For C₁₀H₁₃N₂O₇Re: C, 26.14 %; H, 2.85 %; N, 6.10 %. Found: C, 26.07 %; H, 2.93 %; N, 6.25 %.

HPLC (R_i): 9.9 min (λ = 254 nm, Method 2). Single crystals of **Re8** suitable for X-ray diffraction analysis were grown by slow evaporation of a EtOH–CH₂Cl₂ solution at room temperature.

Characterization of *fac*-[Re(CO)₃(**36-lactam**)]

IR (KBr, cm⁻¹): 2022s, ~1918 s (C≡O), 1678 m, 1630m, 1585m, and 1416 m.

¹H-NMR (300 MHz, CD₃OD): δ_H (ppm) 4.78 (1H, m, NH₂CH₂^a, overlapped with H₂O peak; assigned from g-COSY spectrum), 4.63 (1H, m, NH₂CH₂^a), 2.86 (1H, m, CH₂^a), 2.55 (1H, m, CH₂^a), 2.45 (2H, m, CH₂^f), 2.20 (1H, m, CH₂^d), 1.76 (2H, m, CH₂^e) 1.58 (1H, m, CH₂^d).

¹H-NMR (300 MHz, DMSO-d⁶): δ_H (ppm) 4.93 (1H, m, NH₂CH₂^a), 4.80 (1H, m, NH₂CH₂^a), 2.87 (1H, br s, CH₂^a), 2.71 (1H, br s, CH₂^a), 2.36 (2H, br m, CH₂^f), 1.98 (1H, m, CH₂^d), 1.70 – 1.40 (3H, m, CH₂^e + CH₂^d).

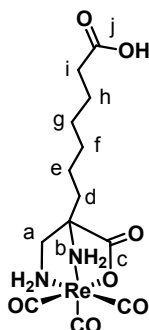
¹³C-NMR (75.5 MHz, CD₃OD, ppm) δ_C 199.2 (C≡O), 199.0 (C≡O), 197.8 (C≡O), 181.6 (C^c), 172.6 (C^g), 70.5 (C^b), 49.0 (C^a; overlapped with CD₃OD peak, assigned from HSQC spectrum), 28.9 (C^f), 26.7 (C^d), 18.3 (C^e).

¹³C-NMR (75.5 MHz, DMSO-d⁶): δ_C (ppm) 199.4 (C≡O), 198.9 (C≡O), 197.9 (C≡O), 177.1 (C^c), 170.2 (C^g), 68.5 (C^b), 47.4 (C^a), 27.6 (C^f), 25.1 (C^d), 16.8 (C^e).

ESI-MS (+) (*m/z*): 464.9 [M+Na]⁺; calcd for C₁₀H₁₁N₂O₆ReNa = 465.0.

ESI-MS (-) (*m/z*): 440.9 [M-H]⁻; calcd for C₁₀H₁₁N₂O₆Re = 442.0.

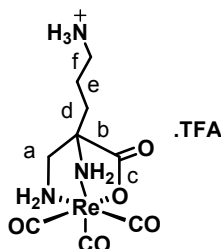
HPLC (R_t): 13.2 min (λ = 254 nm, Method 2).

7.4.6 - *fac*-[Re(CO)₃(κ³-L9)] (Re9)

L9 (0.012 g, 0.039 mmol) reacted with precursor *fac*-[Re(CO)₃(H₂O)₃]Br (0.013 g, 0.032 mmol) in refluxing water for 18 h (pH 7). After cooling to room temperature and concentration of the solution, a white precipitate was formed, which was discarded by centrifugation. The solvent was evaporated to dryness and the resulting oily residue was thoroughly washed with CH₂Cl₂ and dried. Yield: 89.0 % (0.018 g, 0.035 mmol, calcd for C₁₃H₁₉N₂O₇Re).

¹H-NMR (300 MHz, D₂O) δ_H (ppm) 4.80 (4H, NH₂C^a and NH₂C^b, overlapped with H₂O peak; assigned from g-COSY spectrum), 2.66 (1H, m, CH₂^a), 2.47 (1H, m, CH₂^{a'}), 1.97 (2H, m, CH₂ⁱ), 1.59 (2H, m, CH₂^d), 1.50 – 1.08 (8H, m, CH₂^{e,f,g,h}).

¹³C-NMR (75.5 MHz, D₂O): δ_C (ppm) 197.6 (C≡O), 196.1 (C≡O), 184.4, 181.0, 66.4, 44.9, 37.7, 33.2, 28.9, 28.4, 25.9, 22.6.

7.4.7 - *fac*-[Re(CO)₃(κ³-L10)] (Re10.TFA)

L10 (0.017 g, 0.065 mmol) reacted with precursor *fac*-[Re(CO)₃(H₂O)₃]Br (0.026 g, 0.065 mmol) in refluxing water for 18 h (pH 7). After evaporation of the solvent the resulting residue was purified by preparative RP-HPLC (Method 2). Compound **Re10** was obtained as a colorless oil. Yield: 79.2 % (0.028 g, 0.051 mmol, calcd for C₉H₁₄N₃O₅Re·TFA).

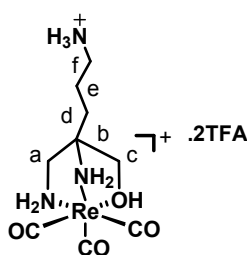
IR (KBr, cm⁻¹): 2028 s, ~1911 s (C≡O), ~1682 m, 1207 m and 1135 m.

¹H-NMR (300 MHz, D₂O): δ_H (ppm) 5.08 (1H, m, NH₂C^b), 4.74 (2H, m, NH₂C^b + NH₂C^a, overlapped with H₂O peak; assigned from g-COSY spectrum), 4.31 (1H, m, NH₂CH₂^a), 2.88 (2H, m, CH₂^f), 2.79 (1H, m, CH₂^a), 2.51 (1H, m, CH₂^a), 1.69 (2H, m, CH₂^d), 1.51 (2H, m, CH^e).

¹³C-NMR (75.5 MHz, CD₃OD): δ_C (ppm) 197.3 (C≡O), 195.9 (C≡O), 181.0 (C^c), 163.3 (q, CF₃COO⁻), 116.4 (q, CF₃COO⁻), 67.3 (C^b), 45.1 (C^a), 39.4 (C^f), 30.4 (C^d), 21.4 (C^e).

ESI-MS (+) (*m/z*): 431.8 [M+H]⁺; calcd for C₉H₁₅N₃O₅Re = 432.0.

HPLC (R_t): 5.5 min (λ = 254 nm, Method 2).

7.4.8 – Tentative synthesis of *fac*-[Re(CO)₃(κ³-L10-OH)] (Re10-OH.2TFA)

L10-OH (0.017 g, 0.034 mmol) reacted with precursor *fac*-[Re(CO)₃(H₂O)₃]Br (0.014 g, 0.034 mmol) in refluxing water for 18 h (pH 7). After evaporation of the solvent the resulting residue was purified by silica gel column chromatography using a gradient of EtOH (0 → 100 %) in CH₂Cl₂. Compound **Re10-OH** was obtained as a colorless oil. Yield: 64.7 % (0.014 g, 0.022 mmol, calcd for C₉H₁₇N₃O₄Re).

IR (KBr, cm⁻¹): 2028 s, ~1915 s (C≡O), ~1400s, 1206s and 1130s.

¹H-NMR (300 MHz, D₂O): δ_{H} (ppm) 4.74 (4H, m, NH₂C^b + NH₂C^a, overlapped with H₂O peak; assigned from g-COSY spectrum), 3.66 (1H, d, CH₂^c), 3.64 (1H, m, OH), 3.40 (1H, dd, CH₂^a), 2.97 (2H, m, CH₂^{a'} + CH₂^{c'}), 2.60 (2H, m, CH₂^f), 1.45 (4H, m, CH₂^d + CH₂^e).

¹H-NMR (300 MHz, DMSO-d⁶): δ_{H} (ppm) 4.64 (1H, m, NH₂C), 4.48 - 4.32 (3H, m, NH₂C), 3.71 (1H, m, CH₂), 3.45 (2H, m, OH + CH₂), 2.80 (1H, m, CH₂), 2.68 (3H, m, CH₂), 1.60 (4H, m, CH₂).

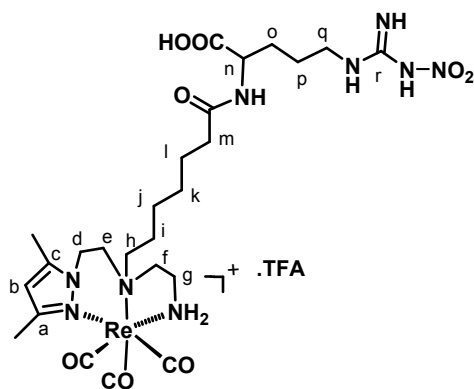
¹³C-NMR (75.5 MHz, D₂O): δ_{C} (ppm) 196.0 (C≡O), 195.4 (C≡O), 195.2 (C≡O), 70.3 (C^c), 61.9 (C^b), 47.9 (C^a), 39.5 (C^f), 29.6 (C^d), 21.6 (C^e).

ESI-MS (+) (*m/z*): 417.9 [M]⁺; calcd for C₉H₁₇N₃O₄Re = 418.0.

HPLC (R_t): 5.5 min (λ = 254 nm, Method 2; Eluents: **A** - TFA 0.1 % and **B** - MeOH).

HPLC (R_t): 4.3 min (λ = 254 nm, Method 2; Eluents: **A** - Et₃N-CH₃COOH [2.1: 2.8 (v/v)] and **B** - MeOH).

7.4.9 - *fac*-[Re(CO)₃(κ^3 -L11)] (Re11.TFA)



L11 (0.035 g, 0.055 mmol) reacted with precursor [Re(CO)₃(H₂O)₃]Br (0.022 g, 0.055 mmol) in refluxing H₂O for 18 h. After evaporation of the solvent the resulting residue was purified by preparative RP-HPLC (Method 1). Compound **Re11** was obtained as a colorless oil. Yield: 40.6 % (0.020 g, 0.022 mmol, calcd. for C₂₅H₄₁N₉O₈Re·TFA).

IR (KBr, cm⁻¹): 2024s and 1910s (C≡O), 1675s, 1290m, 1230m and 1135m.

¹H-NMR (300 MHz, CD₃OD): δ_{H} (ppm) 6.20 (1H, s, CH^b), 5.50 (1H, br s, NH), 4.55 - 4.49 (1H, dd, CH^d), 4.45 (1H, m, CHⁿ), 4.26 - 4.17 (1H, dd, CH^{d'}), 4.08 (1H, m, NH), 3.66 (1H, m, CH₂), 3.37 - 3.15 (7H, m, overlapped with CD₃OD), 2.82 (2H, m, CH₂), 2.71 - 2.62 (1H, m, CH₂), 2.57 - 2.43 (1H, m, CH₂), 2.44 (3H, s, CH₃Pz), 2.36 (3H, s, CH₃Pz), 2.29 (2H, t, CH₂), 1.93 (1H, m, CH₂), 1.80 - 1.60 (5H, m, CH₂), 1.42 (4H, m, CH₂).

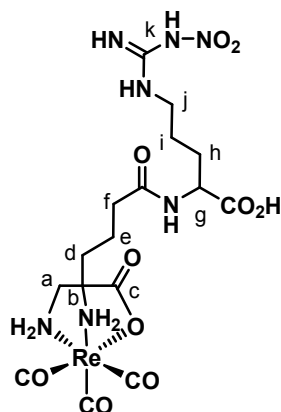
¹³C-NMR (300 MHz, CD₃OD): δ_{C} (ppm) 197.0 (C≡O), 176.2 (C=O), 175.0 (C=O), 166.6 (C^f), 155.9 (C^c), 145.6 (C^a), 109.2 (C^b), 68.7, 62.9, 53.4, 51.5, ~ 48.7 (2 signals overlapped with solvent CD₃OD), 43.7, 41.7, 37.8, 31.3, 31.0, 27.7, 26.5, 25.4, 16.0 (CH₃Pz), 11.4 (CH₃Pz).

ESI-MS (+) (*m/z*): 782.0 [M]⁺; calcd for C₂₅H₄₁N₉O₈Re = 782.2.

Elemental analysis: calcd. for $C_{25}H_{41}N_9O_8Re \cdot TFA$: C, 36.15 %; H, 4.72 %; N, 14.06 %. Found: C, 37.00 %; H, 4.90 %; N, 14.65 %.

HPLC (R_t): 24.0 min ($\lambda = 254$ nm, Method 1).

7.4.10 - *fac*-[Re(CO)₃(κ^3 -L12)] (Re12)



L12 (0.040 g, 0.064 mmol) reacted with precursor $[Re(CO)_3(H_2O)_3]Br$ (0.031 g, 0.077 mmol) in refluxing H_2O for 18 h. After evaporation of the solvent the resulting residue was purified by preparative RP-HPLC (Method 2). Compound **Re12** was obtained as a colorless oil. Yield: 75.7 % (0.032 g, 0.048 mmol, calcd. for $C_{16}H_{25}N_7O_{10}Re$).

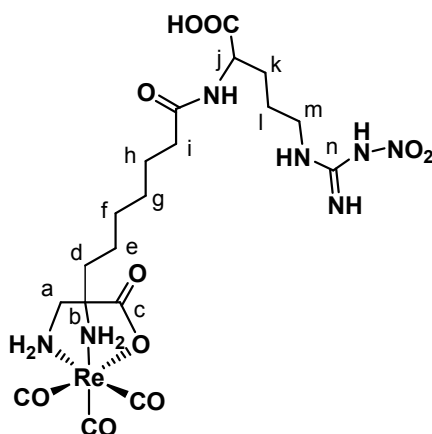
IR (KBr, cm^{-1}): 2010 and 1865 ($C\equiv O$), 1630 ($C=O$), 1590 (NO_2), 1270 (NO_2).

1H -NMR (300 MHz, CD_3OD): δ_H (ppm) 5.31 (1H, m, NH_2C), 4.92 (1H, NH_2C overlapped with H_2O peak; assigned from g-COSY spectrum), 4.80 (1H, m, NH_2CH_2), 4.63 (1H, m, NH_2CH_2), 4.44 (1H, m, H^b), 3.28 (2H, m, H^i), 2.79 (1H, m, H^a), 2.55 (1H, m, $H^{a'}$), 2.28 (2H, m, H^f), 1.90 - 1.59 (8H, m, CH_2).

^{13}C -NMR (75.5 MHz, CD_3OD): δ_C (ppm) 197.0 ($C\equiv O$), 195.7 ($C\equiv O$), 180.2 (CO), 174.6 (CO), 173.9 (CO), 159.8 (C, $GuaNO_2$), 65.8, 51.9, 45.3, 40.5, 35.4, 33.4, 28.6, 25.0, 19.5.

ESI-MS (-) (m/z): 660.1 [$M-H$]⁻; calcd for $C_{16}H_{25}N_7O_{10}Re = 561.6$.

HPLC (R_t): 16.8 min ($\lambda = 254$ nm, Method 2).

7.4.11 - *fac*-[Re(CO)₃(κ³-L13)] (Re13)

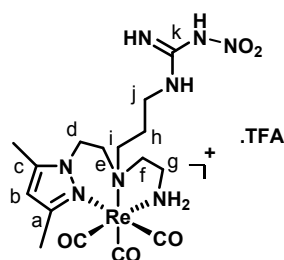
L13 (0.015 g, 0.023 mmol) reacted with precursor [Re(CO)₃(H₂O)₃]Br (0.010 g, 0.023 mmol) in refluxing H₂O for 18 h. After evaporation of the solvent, the resulting residue was purified by preparative RP-HPLC (Method 2). Compound **Re13** was obtained as a colorless oil. Yield: 74.1 % (12 mg, 0.017 mmol, calcd. for C₁₉H₃₁N₇O₁₀Re).

¹H-NMR (300 MHz, CD₃OD): δ_H (ppm) 5.21 (1H, m, NH₂C), 4.90 (1H, NH₂C overlapped with H₂O peak; assigned from g-COSY spectrum), 4.70 (1H, m, NH₂CH₂), 4.60 (1H, m, NH₂CH₂), 4.39 (H, m, Hⁱ), 3.20 (2H, m, H^m), 2.75 (1H, m, H^a), 2.55 (1H, m, H^{a'}), 2.25 (2H, m, Hⁱ), 1.91 - 1.3 (14H, m, CH₂).

¹³C-NMR (75 MHz, CD₃OD): δ_C (ppm) 196.9 (CO), 181.5 (CO), 176.4 (CO), 175.2 (C), 160.0 (C, GuaNO₂), 67.3, 53.1, 46.8, 41.7, 36.6, 35.2, 31.0, 30.6, 29.6, 26.7, 24.0, 19.5.

ESI-MS (-) (*m/z*): 702.2 [M-H]⁻; calcd for C₁₉H₃₁N₇O₁₀Re = 703.1.

HPLC (R_t): 18.5 min (λ = 254 nm, Method 2).

7.4.12 - *fac*-[Re(CO)₃(κ³-L14)] (Re14.TFA)

L14 (0.020 g, 0.045 mmol) reacted with precursor *fac*-[Re(CO)₃(H₂O)₃]Br (0.018 g, 0.045 mmol) in refluxing water for 18 h (pH 7). After evaporation of the solvent the resulting residue was purified by preparative RP-HPLC. Compound **Re14** was obtained as a colorless oil. Yield: 78.2 % (0.025 g, 0.035 mmol, calcd. for C₁₆H₂₆N₈O₅Re·TFA).

¹H-NMR (300 MHz, CD₃OD): δ_H (ppm) 5.99 (1H, s, CH^b), 5.35 (1H, br s, NH), 4.32 – 4.23 (1H, dd, CH^d), 4.07 – 4.00 (1H, m, CH^{d'}), 3.63 (1H, m, NH), 3.48 (1H, m, CHⁱ), 3.36 – 3.20 (2H, m, CH^{i'} + CH^e), 3.20 –

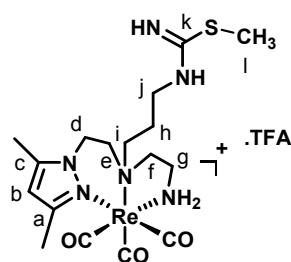
3.10 (2H, m, CHⁱ + CH^l), 3.00 (1H, m, CH^g), 2.67 (2H, m, CH^{g'} + CH^f), 2.54 (1H, m, CH₂^{e'}), 2.32 (1H, m, CH^{f'}), 2.22 (3H, s, CH₃Pz), 2.11 (3H, s, CH₃Pz), 2.10 (1H, m, CH₂^h), 1.90 (1H, m, CH₂^{h'}).

¹³C-NMR (75.5 MHz, CD₃OD): δ_c (ppm) 196.7 (C≡O), 196.2 (C≡O), 195.0 (C≡O), 161.4 (C=N), 155.9 (pz), 145.5 (pz), 110.1 (pz), 66.9, 64.0, 55.5, ~49.0 (overlapped with CD₃OD solvent peak), 44.4, 40.8, 26.0, 17.5, 13.1.

ESI-MS (+) (m/z): 597.0 [M]⁺, calcd. for C₁₆H₂₆N₈O₅Re = 597.1.

HPLC (R_t): 19.9 min (λ = 254 nm, Method 2).

7.4.13 - *fac*-[Re(CO)₃(κ³-L15)] (Re15.TFA)



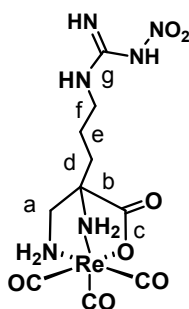
L15 (0.013 g, 0.030 mmol) reacted with precursor *fac*-[Re(CO)₃(H₂O)₃]Br (0.012 g, 0.030 mmol) in refluxing water for 18 h (pH 7). After evaporation of the solvent the resulting residue was purified by preparative RP-HPLC (Method 2). Compound **Re15** was obtained as a colorless oil. Yield: 95.7 % (0.020 g, 0.028 mmol, calcd. for C₁₇H₂₈N₆O₃ReS·TFA).

¹H-NMR (300 MHz, D₂O): δ_H (ppm) 6.04 (1H, s, CH^b), 5.03 (1H, br s, NH), 4.39 (1H, dd, CH^d), 4.07 (1H, m, CH^{d'}), 3.78 (1H, m, NH), 3.54 (1H, m, CH^l), 3.48 – 3.28 (2H, m, CHⁱ+CH^e), 3.28 – 3.19 (2H, m, CH^{i'}+CH^l), 3.03 (1H, m, CH^g), 2.74 (2H, m, CH^{g'} + CH^f), 2.59 (1H, m, CH₂^{e'}), 2.45 (3H, s, SCH₃), 2.37 (1H, m, CH^{f'}), 2.27 (3H, s, CH₃Pz), 2.15 (3H, s, CH₃Pz), 2.14 (1H, m, CH₂^h), 1.97 (1H, m, CH₂^{h'}).

¹³C-NMR (75.5 MHz, D₂O): δ_c (ppm) 191.7 (C≡O), 191.2 (C≡O), 189.9 (C≡O), 161.9 (C=N), 150.9 (pz), 141.4 (pz), 105.0 (pz), 61.4, 58.9, 50.3, 44.3, 39.4, 38.4, 21.4, 12.5, 10.4, 8.02.

ESI-MS (+) (m/z): 583.0 [M]⁺, calcd. for C₁₇H₂₈N₆O₃SRe = 583.1.

HPLC (R_t): 19.6 min (λ = 254 nm, Method 2).

7.4.14 - *fac*-[Re(CO)₃(κ³-L16)] (Re16)

L16 (0.028 g, 0.087 mmol) reacted with precursor [Re(CO)₃(H₂O)₃]Br (0.035 g, 0.088 mmol) in refluxing H₂O for 18 h. The solvent was removed under vacuum, and the resulting residue was dissolved in water and purified by preparative RP-HPLC (Method 2), giving a white solid formulated as **Re16**. Yield: 35.2 % (0.016 g, 0.030 mmol, calcd. for C₁₀H₁₈N₆O₇Re).

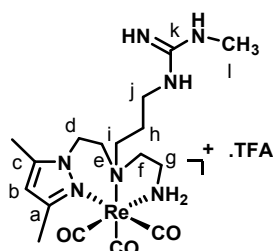
IR (KBr, cm⁻¹): 2020 and 1863 (C≡O), 1635 (C=O), 1596 (NO₂), 1279 (NO₂).

¹H-NMR (300 MHz, CD₃OD): δ_H (ppm) 5.32 (1H, m, NH₂C), 4.95 (1H, NH₂C overlapped with H₂O peak; assigned from g-COSY spectrum), 4.79 (1H, m, NH₂CH₂), 4.69 (1H, m, NH₂CH₂), 3.28 (2H, m, CH₂NH-C=N), 2.84 (1H, m, NH₂CH₂), 2.55 (1H, m, NH₂CH₂), 1.90 - 1.59 (4H, m, CH₂).

¹³C-NMR (75.5 MHz, CD₃OD): δ_C (ppm) 197.2 (C≡O), 196.2 (C≡O), 179.9 (CO), 160.0 (C, GuaNO₂), 65.8, 45.6, 41.5, 31.2, 23.3.

ESI-MS (+) (*m/z*): 543.0 [M+Na]⁺; calcd for C₁₀H₁₈N₆NaO₇Re = 544.0.

HPLC (R_t): 10.5 min (λ = 254 nm, Method 2).

7.4.15 - *fac*-[Re(CO)₃(κ³-L17)] (Re17.TFA)

L17 (0.030 g, 0.073 mmol) reacted with precursor *fac*-[Re(CO)₃(H₂O)₃]Br (0.029 g, 0.073 mmol) in refluxing water for 18 h (pH 7). After evaporation of the solvent the resulting residue was purified by preparative RP-HPLC (Method 2). Compound **Re17** was obtained as a colorless oil. Yield: 70.5 % (0.035 g, 0.051 mmol, calcd. for C₁₇H₂₉N₇O₃Re·TFA).

¹H-NMR (300 MHz, D₂O): δ_H (ppm) 6.01 (1H, s, CH^b), 5.06 (1H, br s, NH), 4.32 (1H, dd, CH^d), 4.02 (1H, m, CH^{d'}), 3.63 (1H, m, NH), 3.50 (1H, m, CHⁱ), 3.39 - 3.26 (2H, m, CH^{j'} + CH^e), 3.18 (2H, m, CHⁱ + CH^{i'}),

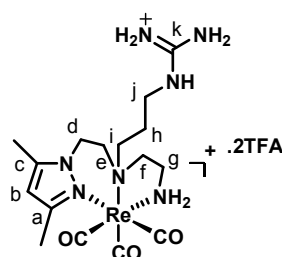
3.02 (1H, m, CH^g), 2.71 (2H, m, CH^g + CH^f), 2.66 (3H, s, C–NH–CH₃), 2.57 (1H, m, CH₂^e), 2.36 (1H, m, CH^f), 2.26 (3H, s, CH₃Pz), 2.16 (3H, s, CH₃Pz), 2.06 (1H, m, CH₂^h), 1.87 (1H, m, CH₂^h).

¹³C-NMR (75.5 MHz, D₂O): δ_c (ppm) 193.7 (C≡O), 193.3 (C≡O), 192.0 (C≡O), 162.4 (q, CF₃COO⁻), 161.9 (C=N), 155.7 (Pz), 152.9 (Pz), 115.3 (q, CF₃COO⁻), 107.0 (Pz), 63.7, 61.1, 52.5, 46.4, 41.4, 37.7, 26.7, 23.6, 14.5 (CH₃Pz), 10.1 (CH₃Pz).

ESI-MS (+) (*m/z*): 566.0 [M]⁺, calcd. for C₁₇H₂₉N₇O₃Re = 566.1.

HPLC (R_t): 19.2 min (λ = 254 nm, Method 2).

7.4.16 - *fac*-[Re(CO)₃(κ³-L18)] (Re18.TFA)



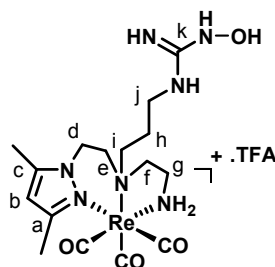
L18 (0.018 g, 0.035 mmol) reacted with precursor *fac*-[Re(CO)₃(H₂O)₃]Br (0.014 g, 0.035 mmol) in refluxing water for 18 h (pH 7). After evaporation of the solvent the resulting residue was purified by preparative RP-HPLC (Method 2). Compound **Re18** was obtained as a colorless oil. Yield: 80.6 % (0.022 g, 0.028 mmol, calcd. for C₁₆H₂₇N₇O₃Re·2TFA).

¹H-NMR (300 MHz, D₂O): δ_H (ppm) 6.21 (1H, s, CH^b), 5.57 (1H, br s, NH), 4.50 (1H, dd, CH^d), 4.22 (1H, m, CH^d), 4.10 (1H, m, NH), 3.71 (1H, m, CHⁱ), 3.47 (2H, m, CH^f + CH^e), 3.20 (2H, m, CH^f + CHⁱ), 3.14 (1H, m, CH^g), 2.84 (2H, m, CH^g + CH^f), 2.69 (1H, m, CH₂^f), 2.55 (1H, m, CH^f), 2.44 (3H, s, CH₃Pz), 2.36 (3H, s, CH₃Pz), 2.19 (1H, m, CH₂^h), 2.17 (1H, m, CH₂^h).

¹³C-NMR (75.5 MHz, D₂O): δ_c (ppm) 197.3 (C≡O), 196.7 (C≡O), 195.5 (C≡O), 164.9 (q, CF₃COO⁻), 158.5 (C=N), 156.5 (Pz), 147.1 (Pz), 118.0 (q, CF₃COO⁻), 110.5 (Pz), 65.7, 63.9, 55.4, 49.7, 44.9, 39.9, 25.2, 18.0 (CH₃pz), 13.6 (CH₃pz).

ESI-MS (+) (*m/z*): 552.2 [M]⁺, calcd. for C₁₆H₂₇N₇O₃Re = 552.1.

HPLC (R_t): 19.0 min (λ = 254 nm, Method 2).

7.4.17 - *fac*-[Re(CO)₃(κ³-L19)] (Re19.TFA)

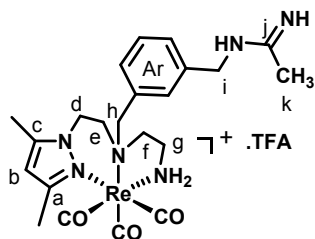
L19 (0.017 g, 0.041 mmol) reacted with precursor *fac*-[Re(CO)₃(H₂O)₃]Br (0.016 g, 0.041 mmol) in refluxing water for 18 h (pH 7). After evaporation of the solvent the resulting residue was purified by preparative RP-HPLC (Method 2). Compound **Re19** was obtained as a colorless oil. Yield: 53.7 % (0.015 g, 0.022 mmol, calcd. for C₁₆H₂₇N₇O₄Re·TFA).

¹H-NMR (300 MHz, D₂O): δ_H (ppm) 6.03 (1H, s, CH^b), 5.07 (1H, br s, NH), 4.28 (1H, dd, CH^d), 4.06 (1H, m, CH^{d'}), 3.64 (1H, m, NH), 3.49 (1H, m, CHⁱ), 3.35 – 3.23 (2H, m, CH^{i'} + CH^e), 3.20 (2H, m, CH^{i'} + CHⁱ), 3.07 (1H, m, CH^g), 2.73 (2H, m, CH^{g'} + CH^f), 2.60 (1H, m, CH₂^{e'}), 2.38 (1H, m, CH^{f'}), 2.27 (3H, s, CH₃Pz), 2.15 (3H, s, CH₃Pz), 2.10 (1H, m, CH₂^h), 1.91 (1H, m, CH₂^{h'}).

¹³C-NMR (75.5 MHz, D₂O): δ_C (ppm) 193.8 (C≡O), 193.2 (C≡O), 192.0 (C≡O), 162.0 (q, CF₃COO⁻), 158.0 (C=N), 152.9 (Pz), 143.5 (Pz), 115.0 (q, CF₃COO⁻), 107.0 (Pz), 63.6, 61.0, 52.4, 46.3, 41.4, 37.7, 23.4, 14.5 (CH₃Pz), 10.0 (CH₃Pz).

ESI-MS (+) (*m/z*): 567.9 [M]⁺, calcd. for C₁₆H₂₇N₇O₄Re = 368.1.

HPLC (R_t): 19.1 min (λ = 254 nm, Method 2).

7.4.18 - *fac*-[Re(CO)₃(κ³-L20)] (Re20.TFA)

L20 (0.035 g, 0.076 mmol) reacted with precursor *fac*-[Re(CO)₃(H₂O)₃]Br (0.031 g, 0.078 mmol) in refluxing water for 18 h (pH 7). After evaporation of the solvent the resulting residue was purified by preparative RP-HPLC (Method 2). Compound **Re20** was obtained as a colorless oil. Yield: 55.3 % (0.031 g, 0.042 mmol, calcd. for C₂₂H₃₀N₆O₃Re·1TFA).

¹H-NMR (300 MHz, CD₃OD): δ_H (ppm) 7.41 – 7.24 (4H, m, Ar), 6.02 (1H, s, CH^b), 5.24 (1H, m, NH), 4.54 (2H, dd, CH₂^h), 4.36 (2H, m, CH₂^d), 4.26 (2H, s, CH₂ⁱ), 4.26 (2H, m, CH₂^{d'}), 3.73 (1H, m, NH), 3.20 – 2.99

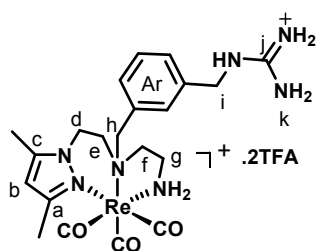
(1H, m, CH₂^{e,g}), 2.56 (2H, m, CH₂^{e'}), 2.52 – 2.37 (2H, m, CH₂^{c,c'}), 2.27 (3H, s, CH₃Pz), 2.14 (3H, s, CH₃Pz), 1.90 (3H, s, CH₃^k).

¹³C-NMR (75.5 MHz, CD₃OD): δ_c (ppm) 194.0 (C≡O), 193.9 (C≡O), 193.0 (C≡O), 163.0 (C^j), 154.1 (pz), 144.5 (pz), 138.6 (Ar), 132.1 (Ar), 131.6 (Ar), 131.2 (Ar), 129.1 (Ar), 128.1 (Ar), 107.5 (pz), 69.0, 60.9, 50.8, 46.0, 42.9, 41.8, 21.9 (C^k), 15.4 (CH₃Pz), 10.8 (CH₃Pz).

ESI-MS (+) (m/z): 613.1 [M]⁺, calcd. for C₂₂H₃₀N₆O₃Re = 613.2.

HPLC (R_t): 21.7 min (λ = 254 nm, Method 1).

7.4.19 - *fac*-[Re(CO)₃(κ³-L21)] (Re21.2TFA)



L21 (0.045 g, 0.078 mmol) reacted with precursor *fac*-[Re(CO)₃(H₂O)₃]Br (0.031 g, 0.078 mmol) in refluxing water for 18 h (pH 7). After evaporation of the solvent the resulting residue was purified by preparative RP-HPLC (Method 2). Compound **Re21** was obtained as a colorless oil. Yield: 79.8 % (0.050 g, 0.062 mmol, calcd. for C₂₁H₂₉N₇O₃Re·2TFA).

¹H-NMR (300 MHz, CD₃OD): δ_H (ppm) 7.42 – 7.27 (4H, m, Ar), 6.00 (1H, s, CH^b), 5.23 (1H, m, NH), 4.48 (2H, dd, CH₂^h), 4.33 (2H, s, CH₂ⁱ), 4.13 (2H, m, CH₂^d), 4.13 (2H, m, CH₂^{d'}), 3.74 (1H, m, NH), 3.20 (1H, m, CH₂^e), 3.00 (2H, m, CH₂^e), 2.56 (2H, m, CH₂^{e'}), 2.45 – 2.33 (2H, m, CH₂^{c,c'}), 2.25 (3H, s, CH₃Pz), 2.21 (3H, s, CH₃Pz).

¹³C-NMR (75.5 MHz, CD₃OD): δ_c (ppm) 194.6 (C≡O), 194.0 (C≡O), 193.0 (C≡O), 157.1 (C^j), 154.1 (pz), 144.4 (pz), 137.0 (Ar), 132.6 (Ar), 132.2 (Ar), 131.2 (Ar), 129.3 (Ar), 128.0 (Ar), 105.0 (pz), 69.2, 61.1, 51.3, 46.1, 44.4), 41.8, 14.4 (CH₃pz), 10.8 (CH₃pz).

HPLC (R_t): 22.4 min (λ = 254 nm, Method 1).

ESI-MS (+) (m/z): 614.2 [M]⁺, calcd. for C₂₁H₂₉N₇O₃Re = 614.2.

7.5 - Synthesis of ^{99m}Tc Complexes of the Type *fac*-[^{99m}Tc(CO)₃(κ³-L)]

7.5.1 - Preparation of the *fac*-[^{99m}Tc(CO)₃(H₂O)₃]⁺ Precursor

Na[^{99m}TcO₄] in NaCl 0.9% was eluted from a ⁹⁹Mo/^{99m}Tc generator. The radioactive synthon *fac*-[^{99m}Tc(CO)₃(H₂O)₃]⁺ was prepared by adding 1.5 - 2.0 mL of freshly eluted Na[^{99m}TcO₄] to a

Mallinckrodt IsoLink® kit, followed by heating for 30 min at 100 °C. The reaction vial was cooled and the solution neutralized with 1 M HCl (160 – 170 µL) to destroy the remaining boranocarbonate. The product was controlled by RP-HPLC.

7.5.2 - General Method for Preparing the ^{99m}Tc(I) Complexes

In a capped nitrogen purged glass vial, 100 µL of a 10⁻³ or 10⁻⁴ M solution of the ligands **L4** – **L21** were added to 900 µL of a solution of *fac*-[^{99m}Tc(CO)₃(H₂O)₃]⁺ (1 - 2 mCi) in PBS. The vial was incubated at 100 °C for 30 - 60 min and analyzed by RP-HPLC using the same method of the rhenium surrogates. Retention times: 21.1 min (**Tc2**), 20.0 min (**Tc4**), 21.3 min (**Tc5**), 18.8 min (**Tc6**), 19.4 min (**Tc7**), 10.0 min (**Tc8**), 13.4 min (**Tc9**), 4.3 min (**Tc10**), 24.4 min (**Tc11**), 16.9 min (**Tc12**), 18.6 min (**Tc13**), 20.2 min (**Tc14**), 20.7 min (**Tc15**), 10.7 min (**Tc16**), 20.3 min (**Tc17**), 19.9 min (**Tc18**), 20.1 min (**Tc19**), 23.0 min (**Tc20**) and 23.1 min (**Tc21**).

7.6 - *in vitro* Stability Studies: Stability in the Presence of Cysteine and Histidine

A solution (100 µL) of the ^{99m}Tc (I) complexes was incubated with a 1mM solution of cysteine or histidine (900 µL) in PBS, pH = 7.4 at 37 °C. During the incubation time (18 h) aliquots were analyzed by RP-HPLC.

7.7 – Partition Coefficient

The lipophilicity of the radioconjugates was evaluated by the “shakeflask” method which consists on determining the partition coefficient (P) in a biphasic system n-octanol/PBS 0.1 M, pH 7.4.¹⁹² Briefly, ^{99m}Tc(I) complex was added to a mixture of octanol (1 mL) and 0.1 M PBS pH 7.4 (1 mL), previously saturated in each other by stirring the mixture. This mixture was vortexed and centrifuged (3000 rpm, 10 min, room temperature) to allow phase separation. Aliquots of both octanol and PBS were counted in a gamma counter. The partition coefficient (P_{o/w}) was calculated by dividing the counts in the octanol phase by those in the buffer, and the results expressed as log P_{o/w}: log P_{o/w} = -0.795 ± 0.017 (**Tc4**), log P_{o/w} = -0.467 ± 0.071 (**Tc5**), log P_{o/w} = -0.366 ± 0.091 (**Tc6**), log P_{o/w} = 0.319 ± 0.010 (**Tc7**), log P_{o/w} = -2.006 ± 0.030 (**Tc8**), log P_{o/w} = -1.025 ± 0.022 (**Tc10**), log P_{o/w} = -0.290 ± 0.010 (**Tc11**), log P_{o/w} = -0.851 ± 0.22 (**Tc14**), log P_{o/w} = -0.050 ± 0.121 (**Tc15**), log P_{o/w} = -0.890 ± 0.201 (**Tc17**), log P_{o/w} = -1.231 ± 0.151 (**Tc18**), log P_{o/w} = -0.73 ± 0.100 (**Tc19**) and log P_{o/w} = -0.763 ± 0.021 (**Tc20**).

7.8 - *in vivo* Studies

All animal experiments were performed in compliance with the Portuguese Law and European Directives (Portaria 1131/97, Decretos-Lei nº 129/92 de 6 de Julho e 197/96 de 16 de Outubro and 86/609/CEE) regarding ethics, care and protection of animals used for experimental and other scientific proposes. The animals were housed in a temperature (22 - 23 °C) and humidity (45 - 65 %) controlled room with a 12 h light/12 h dark schedule.

7.8.1 - Biodistribution Studies in CD-1 Female Mice

The biodistribution of the ^{99m}Tc complexes **Tc4** – **Tc9** was evaluated in groups of 3 - 4 CD-1 female mice (Charles River outbred strain, from IFFA CREDO, Barcelona, Spain). Mice were intravenously injected with 100 μl of each complex (3 - 10 MBq) via the tail vein and the animals were kept in normal diet *ad libitum*. Animals were sacrificed by cervical dislocation at 1 and 4 h after injection. The administered dose and the radioactivity in the sacrificed animals were measured with a dose calibrator (Curiemeter IGC-3, Aloka, Tokyo, Japan or Carpintec CRC-15W, Ramsey, USA). The difference in radioactivity between the injected animal and the sacrificed animal was assumed to be due to excretion. Tissues and organs of interest were dissected, rinsed to remove excess blood, weighted, and their radioactivity was measured using the dose calibrator or a γ -counter. The uptake in the tissues or organs was calculated and expressed as percent injected dose per gram of tissue or organ (%ID/g). For blood, bone, muscle, and skin, total activity was estimated assuming that they represent 6, 10, 40, and 15 % of the total body weight, respectively.

7.8.2 - Biodistribution in C57BL/6 LPS-Treated Mice

These studies were performed in mature female C57BL/6 mice (10 – 14 weeks old) treated with LPS (10 mg/kg, iv), to induce iNOS expression, 6h before the radioactive compounds were injected. The control group was injected with PBS instead of LPS. Animals were then intravenously injected into the retro-orbital sinus with the radiocomplexes **Tc2** or **Tc11** (60 - 90 μCi) diluted in 100 μL of PBS pH 7.2. Mice were killed by cervical dislocation at 15 and 30 min (complex **Tc2**), and at 60 min (complex **Tc11**) after injection. The uptake in the tissues or organs was calculated as described above. Lungs from control and LPS-treated animals were harvested and analyzed latter by western Blot to demonstrate that 6h LPS-treatment was adequate to strongly increase iNOS expression in that organ.

7.8.3 - *in vivo* Stability/Metabolization

The *in vivo* stability of the $^{99m}\text{Tc}(\text{I})$ complexes was evaluated by RP-HPLC analysis of urine and blood.

Urine: The urine collected at the sacrifice time was centrifuged at 3000 rpm for 15 min and the supernatant was analyzed by RP-HPLC.

Blood: The blood was collected at the sacrifice time, centrifuged at 3000 rpm for 15 min at 4 °C, and the serum was separated. 100 μl aliquots of serum were sampled and treated with 200 μl of ethanol to precipitate the proteins. Samples were then centrifuged at 3000 rpm for 15 min at 4 °C. The supernatant was analyzed by RP-HPLC.

7.8.4 - Western Blot of Lungs of LPS-Treated Mice

Western blot experiments were also performed to demonstrate the overexpression of iNOS in the lungs of LPS-treated mice. Mice were induced with 5mg/kg of LPS (or PBS) for 6h. Lungs from non- treated and LPS-treated were harvested and homogenized on a pre-chilled manual Potter-Elvehjem homogenizer. Homogenates were centrifuged at 14000 g for 10 min at 4 °C and the supernatants removed for further use. The total protein content was determined by using the DC Protein Assay Kit (Biorad) according to the manufacturer's protocol. Briefly, this assay, similar to Lowry assay, is based on the reaction of protein with an alkaline copper tartrate solution, and the subsequent reduction of folin reagent by the copper-treated protein.¹⁹³ Reduced species of folin have a characteristic blue color with maximum absorbance at 750 nm. The protein content was determined by comparison with a BSA standard curve. Aliquots of protein (200 μg) from each sample were analyzed using standard western blot procedures. Briefly, protein extracts were subjected to electrophoresis on a 7% SDS-polyacrylamide gel and transferred electrophoretically onto nitrocellulose membranes. The blots were blocked with PBS-T containing 5% non-fat dry milk for 1 h. Then, the blotting membranes were incubated with primary antibodies against iNOS (1:1000, Sigma) and actin (1:8000, Sigma) separately overnight. Membranes were washed with PBS-T and incubated for 1 h with secondary antibody (goat anti-mouse IgG-HRP, Biorad) diluted 1:3000. Finally, membranes were developed using the SuperSignal WetsPico Substrate kit (Pierce, Rockford, IL) according to the manufacturer's instructions.

7.9 - Enzymatic Assays

7.9.1 - Preparation of Oxyhemoglobin

Oxyhemoglobin was prepared using a previously described protocol with some modifications.^{158a} Briefly, bovine hemoglobin in 50 mM HEPES pH 7.4 was reduced to oxyhemoglobin with 10-fold molar excess of sodium dithionite. Sodium dithionite was later removed by dialysis against 50 volumes of HEPES buffer for 18 hours at 4°C. The buffer was replaced 3 times. The concentration of oxyhemoglobin was determined spectrophotometrically using $\epsilon_{415\text{ nm}} = 131\text{ mM}^{-1}\text{cm}^{-1}$. Oxyhemoglobin was stored at -80°C before use.

7.9.2 - Determination of Kinetic Parameters

NOS assays were recorded on an Agilent Technologies 8453 UV-Vis diode array spectrophotometer with a thermostated multicuvette holder with stirring. The iNOS (mouse recombinant enzyme), bovine hemoglobin, NADPH, BH₄ (Tetrahydrobiopterin), HEPES and DTT were purchased from Sigma Chemical Co.

7.9.2.1 - Determination of K_m Values

All initial velocity measurements were recorded at 37 °C. Total reaction volumes were 600 μL and contained 50 mM HEPES pH 7.4, 6 μM oxyhemoglobin, 200 μM NADPH, 10 μM BH₄, 100 μM DTT and at least four concentrations of the L-Arg (5 – 250 μM). Reactions were initiated by the addition of iNOS enzyme (~ 1 U) to the prewarmed cuvette ($\sim 2 - 3$ min). The NO-mediated conversion of oxyhemoglobin to methemoglobin was followed by monitoring the increase in absorbance at dual wavelength (401 and 421 nm) for 10 min.¹⁵⁷ Controls were performed in the same conditions without enzyme. The kinetics parameters of **L18**, **L19** and **L21** were determined as described above using three concentrations of the substrates (50 – 500 μM).

7.9.2.2 - Determination of K_i Values

The K_i values were obtained by measuring inhibition with at least three concentrations of L-Arg (20 – 150 μM) in the presence of 50 - 150 μM of the inhibitor, in the conditions previously described. The formula used to calculate the K_i is: $K_i = [I] / ((K_m^{app} / K_m) - 1)$ where [I] is the inhibitor

concentration, K_m is the Michaelis-Menten constant of the substrate L-arginine and K_m^{app} is the apparent value of K_m for the substrate in the presence of the inhibitor. K_m value for L-arginine was determined as being 6 μM .

7.10 - Cell studies: RAW 264.7 Macrophages

7.10.1 - Cell Culture

RAW 264.7 macrophages were grown in Dulbecco's Modified Eagle Medium (DMEM) with GlutaMax I supplemented with 10 % heat-inactivated fetal bovine serum and 1 % penicillin/streptomycin antibiotic solution (all from Gibco, Alfacel, Lisbon). Cells were cultured in a humidified atmosphere of 95 % air and 5 % CO_2 at 37 °C, with the medium changed every other day. The cells were adherent in monolayers and, when confluent, were harvested from the cell culture flasks, using a scraper, and seeded further apart.

7.10.2 - Western Blot Analysis of LPS-Induced RAW 264.7 Macrophages

Western blot experiments were performed to demonstrate the overexpression of iNOS in LPS-induced RAW 264.7 macrophages. RAW 264.7 macrophages were treated with LPS (2 $\mu\text{g}/\text{mL}$) for 24 h and lysed in Cell Lytic-MT Extraction reagent (Sigma) supplemented with complete protease inhibitor cocktail tablets (Roche Applied Science). After 15 minutes on ice, lysates were centrifuged at 14000 g for 10 min at 4 °C to pellet the cellular debris and the supernatants removed for further use. The total protein content and the western blot analysis were performed as previously described in **Section 7.8.4**.

7.10.3 - Evaluation of the Inhibitory Effect of Compounds L11 – L20 and Re11 - Re20 in NO Biosynthesis in LPS-Induced RAW 264.7 Macrophages

Macrophages (in DMEM without phenol red and 10 % FBS) were plated at a density of 9×10^4 cells per well in 96-well plates. Cells were immediately induced with 10 μL of LPS (2 $\mu\text{g}/\text{mL}$ in PBS) for 4 h, and then incubated for 24 h in the presence of 500 μM of compounds. At the end of the incubation period, the culture medium was collected and assayed for nitrite production using the commercially available Griess reagent method (Sigma-Aldrich).^{161, 194} Each experiment was performed with six replicates and repeated three times.

Owing to solubility problems, compound **Re11** and **Re13** was dissolved in a 5 % MeOH/H₂O solution (10 mM solution) and further diluted with water, until a final concentration of 1 mM was reached. Final MeOH concentrations were ≤ 0.25 %, and were shown to not interfere neither with the nitrite assay nor with cell viability.

7.10.3.1 - Nitrite Assay

Nitrite concentrations were determined in the medium using Griess reagent (1 % sulfanilamide, 0.1 % *N*-1-naphthyl ethylenediamine, 2.5 % orthophosphoric acid; Sigma-Aldrich). 50 μ L of Griess reagent was mixed with an equal volume of medium at room temperature and absorbance was measured at 540 nm after 10 min. Fresh culture medium served as the blank in all experiments.

7.10.4 - Cell Viability Assay

Cell viability was evaluated by using a colorimetric method based on the tetrazolium salt MTT ([3-(4,5-dimethylthiazol-2-yl)-2,5-diphenyltetrazolium bromide]), which is reduced by viable cells to yield purple formazan crystals.¹⁹⁵ Cells were seeded in 96-well plates at a density of 9×10^4 cells per well, immediately induced with LPS (2 μ g/ml) for 4h, and then incubated for 24 h in the presence of the compounds (500 μ M). At the end of the incubation period the media was removed and the cells were incubated with MTT (0.5 mg/mL in culture medium; 200 μ l) for 3 - 4 h at 37 °C and 5 % CO₂. The purple formazan crystals formed inside the cells were then dissolved in 200 μ L of DMSO by thorough shaking, and the absorbance was read at 570 nm, using a plate spectrophotometer (Power Wave Xs; Bio-Tek). Each experiment was performed with six replicates and repeated two times. The results are expressed as percentage of the surviving cells in relation with the control.

7.10.5 - Cellular Internalization of the ^{99m}Tc (I) Complexes

Internalization assays of the radiocomplexes **Tc2** and **Tc11** were performed in RAW 264.7 macrophages seeded at a density of 0.3 million/well, in complete culture medium containing LPS 1 μ g/mL, in a 24-well tissue culture plates and allowed to attach and to induce the expression of iNOS for 24 h at 37 °C. Then, the culture medium was removed and the cells were incubated with about 200000 cpm of the radiocomplexes **Tc2** and **Tc11** in 0.5 mL of assay medium (Modified Eagle's Medium with 25 mM HEPES and 0.2% BSA) for a period of 5 min to 4 h at 37 °C. Incubation was terminated by washing the cells with ice-cold assay medium. Cell-surface bound radioligand was

removed by two steps of acid wash (50 mM glycine.HCl/100 mM NaCl, pH 2.8) at room temperature for 5 min. The pH was neutralized with cold PBS with 0.2% BSA, and subsequently the cells were lysed by 10 min incubation with 0.5 N NaOH at 37 °C to determine internalized radioligand. Total macrophage protein has been determined using a commercially available BioRad[®] DC Protein Kit assay.¹⁹³

7.11 – Computational Studies

7.11.1 – Docking Calculations

7.11.1.1 – Validation of Docking Conditions: Docking of L-Arg, N^ω-OH-L-Arg, **13**, **16**, **18**, **20**, **58** – **62** Inside iNOS

AutoDock4.2 was employed to perform protein-ligand docking calculations. The structure of iNOS used in the docking studies was taken from the Research Collaboratory for Structural Bioinformatics (RCSB) protein database (chain A of pdb 1QW4¹⁶⁴). The solvent molecules were removed, but the heme and H₄B were retained.

To validate the accuracy of our docking conditions, we have docked compounds with known affinity for iNOS (substrates and inhibitors) inside its active pocket (compounds **L-Arg**, **N^ω-OH-L-Arg**, **13**, **16**, **18**, **20**, **58** – **62**; **Figure 8.5**), and compared the obtained conformation with the conformation found in the X-ray structure. The 3D structures of the compounds were extracted from the pdb structures (L-Arg, pdb id 1NOD¹⁶³; N^ω-OH-L-Arg, pdb id 1DWV^{51a}; N^ω-propyl-L-Arg, **13**, pdb id 1QW4¹⁶⁴; L-thiocitrulline, **16**, pdb id 3NOD^{51a}; acetamidine, **18**, pdb id 1QW5¹⁶⁴; aminopyridine, **20**, pdb id 3EAI^{71a}; 4-fluoro-iminoethyl-L-lysine, **58**, pdb id 1R35¹⁶⁵; isothioureia, **59**, pdb id 1DF1¹⁶⁷; coumarin, **60**, pdb id 2BHJ¹⁶⁸; nitroindazole, **61**, pdb id 1M8E¹⁶⁹; quinazoline, **62**, pdb id 3E7T^{71a}). The rotatable bonds and atomic partial charges (Gasteiger) were assigned by using AutoDock tools. Torsions free to rotate during the docking process are depicted in **Figure 8.5** (Annexes). The LIGPLOT¹⁶⁶ program was used to generate schematic diagrams of the protein-ligand interactions for the above-mentioned X-ray structures to identify the main residues of the binding site of iNOS involved in ligand stabilization (**Figure 8.6** and **8.7**). According to these studies, the most important residues of the iNOS enzyme for catalytic activity were considered fully flexible during the docking process (Gln257, Tyr341, Trp366, Tyr367, Glu371).

The protein-ligand complexes were prepared with AutoDockTools: for each protein hydrogen atoms were added and Kollman united atom charges were assigned. Hydrogens were also added to the ligands, heme and H₄B, and charges were calculated by the Gasteiger-Marsili method. The Fe atom of heme was assigned a charge of +3. The ligands were docked inside a cubic grid box (48 Å ×

32 Å × 58 Å) centered on the Fe atom of the heme group with a grid spacing of 0.375 Å. In each docking simulation 100 independent Lamarckian genetic algorithm (LGA) runs were performed, with the population size set to 200, the number of energy evaluations set to 10 000 000 and the maximum number of generations set to 27 000. All other parameters were maintained at their default settings.^{101, 107} The resulting docked conformations within a RMSD of 2 Å were clustered together. RMSD between the experimental conformations and the conformations obtained by docking were computed to evaluate the accuracy of the calculated poses.

7.11.1.2 – Docking of L2, L11 – L13, L16, Re2, Re11 – Re13 and Re16 Inside iNOS

Docking of **L2**, **L11 – L13**, **L16**, **Re2**, **Re11 – Re13** and **Re16** was performed using the same conditions described above. The protonation state of the conjugates at physiologic pH was determined with Epik 1.6 (Schrödinger).¹⁹⁶ All rotatable bonds of **L16** were kept free to rotate. In the case of **L2**, **L11 – L13** all rotatable bonds were kept free with exception of the rotatable bonds of the pyrazolyl ring and N⁰-NO₂-L-Arg moiety, which was kept rigid in the same conformation found on the X-ray structure of this inhibitor complexed with nNOS (pdb id 1K2R) (**Figure 8.9**).¹⁹⁷ In the case of **Re2**, **Re11 – Re13** and **Re16** the 3D-structure information of the **pyrazolyl-diamine** and **Dap** chelating units were taken from the Cambridge Crystallographic Data Centre (reference numbers CCDC 789827 and 761462).^{26, 170} The docking experiments were carried out allowing **Re2**, **Re11 – Re13** and **Re16** to rotate freely with exception of the rotatable bonds of the chelators and N⁰-NO₂-L-Arg moieties (**Figure 8.9**), which were kept in the conformation found in the X-ray structures. A charge of +1 was assigned for the rhenium atom of **Re2** and **Re11**, while for **Re12**, **Re13** and **Re16** the charge was 0. The complexes **L2:iNOS**, **L11:iNOS**, **L12:iNOS**, **L13:iNOS**, **L16:iNOS**, **Re2:iNOS**, **Re11:iNOS**, **Re12:iNOS**, **Re13:iNOS** and **Re16:iNOS** chosen after analysis of the docking results were subjected to MD simulations.

7.11.1.3 – Docking of 20 – 21 inside iNOS, nNOS and eNOS Isoforms

Owing to the high conservation of the active site of the three isoforms, the residues identified in **Section 7.11.1.1** as being important for iNOS activity, were extrapolated for the others two isoforms. Accordingly, the following residues were considered fully flexible during the docking process: Gln257 (iNOS), Gln478 (nNOS) and Gln249 (eNOS); Tyr341 (iNOS), Tyr562 (nNOS) and Tyr333 (eNOS); Trp366 (iNOS), Trp587 (nNOS) and Trp358 (eNOS); Tyr367 (iNOS), Tyr588 (nNOS) and Tyr359 (eNOS); Glu371 (iNOS), Glu592 (nNOS) and Glu363 (eNOS). For complexes **20:iNOS**, **21:nNOS**, and **21:eNOS** for which X-ray structures do exist, the inhibitors were re-docked inside the active pocket of

the NOS isoforms using the same conditions described in **Section 7.11.1.1**. The RMSD between the experimental and computational structures of the inhibitors were computed to evaluate the accuracy of the calculated poses. In the case of the complexes **20:nNOS**, **20:eNOS**, and **21:iNOS** for which no X-ray structures were available, the same docking conditions were used to predict the binding mode of the inhibitors inside the NOS isoforms. The conformations from the lowest and more populated energy cluster returned by AutoDock that fulfilled some known structural criteria important for enzyme activity were subjected to MD simulations.

7.11.2 - Parameterization of the Compounds

7.11.2.1 – Parameterization of **20** and **21**

The protonation state of the inhibitors **20** and **21** at physiologic pH was determined with Epik 1.6 (Schrödinger).¹⁹⁶ To calculate the optimized geometries we used the Gaussian03 suite of programs and performed restricted Hartree–Fock (RHF) calculations, with the 6-31G(d) basis set. The atomic charges were further recalculated using RESP.¹²³ The topologies and parameters of the inhibitors compatible with the CHARMM all atoms force field were derived from the ParamChem server (<https://www.paramchem.org/>).¹⁹⁸

7.11.2.2 – Parameterization of **L2**, **L11 – L13**, **L16**, **Re2**, **Re11 – Re13** and **Re16**

DFT calculations give very accurate results for systems involving transition metals.¹⁹⁹ Among the plethora of existing density functional methods, we chose B3LYP which has been successfully used for transition-metal complexes namely for rhenium complexes.^{198, 200} The geometries of the inhibitors **L2**, **L11 – L13**, **L16**, **Re2**, **Re11 – Re13** and **Re16** were optimized using the B3LYP/6-31G* level of theory with the Gaussian 09 program (version A.02), while charge fitting was performed using the RESP program.^{123, 201} The Molecular Electrostatic Potential (MEP) computation was carried out using the same level of theory and the Connolly surface algorithm.²⁰² In the case of the Re complexes it was used the B3LYP level of theory with the 6-31G* basis set for all atoms and the SDD basis set for Re.²⁰³ A spin multiplicity of 1 and a radius of 1.47 Å for rhenium metal was considered in the DFT calculations. To evaluate the ability of the chosen functional to reproduce the X-ray structures of the rhenium complexes, the bond lengths and angles of the optimized structures were compared with the corresponding values found in the experimental crystal structures (**Table 8.8**). The results have shown that both HF/6-31G*/SDD and B3LYP/6-31G*/SDD calculated values reproduce satisfactorily the X-ray crystal structures. The charge derivation procedure was

automatically carried out using the R.E.D. (RESP ESP charge Derive) Server version 2.0.²⁰⁴ A detailed description of this procedure is reported in **Figure 8.27** (Annexes). RESP atomic charges calculated for **L2, L11 – L13, L16, Re2, Re11 – Re13** and **Re16** are presented in **Figures 8.32 – 8.41**.

The topologies and parameters of the organic molecules (**L2, L11 – L13, L16**) compatible with the CHARMM all atoms force field were derived from the ParamChem server (<https://www.paramchem.org/>).¹⁹⁸ Parameters for the metal fragment were taken from previous parameterization studies of technetium and rhenium complexes.^{40, 205} All the dihedral parameters involving the Re–ligand interactions were set to zero. This procedure has been used with success in the treatment of several different systems that have a metal atom covalently bonded.²⁰⁶ Lennard–Jones parameters are also not parameterized due to the fact that the Re metal is buried and that van der Waals interactions are not as important as the electrostatics.²⁰⁷ Lennard–Jones parameters for the Re metal were taken from the literature.^{205c}

7.11.3 – Molecular Dynamics Simulations

Based on the docking results, MD simulations for compounds **20, 21, L2, L11 – L13, L16, Re2, Re11 – Re13** and **Re16** were performed using NAMD^{116b} and CHARMM22 force field.¹²⁵ The NOS isoform exist as dimer with a structural Zn²⁺ ion coordinated by four cysteines (two cysteines from each monomer; Cys104 and Cys109 in iNOS; Cys326 and Cys331 in nNOS; Cys96 and Cys101 in eNOS). In order to avoid the challenging task of parameterization of the Zn²⁺ ion, which was shown to be 22 Å away from the bound site and have no effect on the ligand binding, this metal ion was excluded from the simulation. To increase length of the simulations without losing important structural information, only one oxygenase monomer was selected.

The oxo-ferryl form (compound I) of heme, which has an oxygen atom at the sixth coordination position of iron, was used. The force field parameters of the H₄B cofactor and compound I were kindly provided by Cho et al..^{60b} The propKa module of the PDB2PQR server (<http://kryptonite.nbcrc.net/pdb2pqr/>) was used to adjust the protonation states of ionizable residues at physiologic pH.²⁰⁸ Water molecules observed in the crystal structure were kept and additional TIP3P water molecules (box of dimension 10 Å x 10 Å x 10 Å) were modeled using the solvate package in VMD. Next, the systems were neutralized by adding counter ions with the autoionize package in VMD. The whole systems contained: *unbound iNOS* - 418 residues, 18319 water molecules and 9 Na⁺ (61723 atoms totally); *unbound nNOS* - 417 residues, 17049 water molecules and 3 Na⁺ (57798 atoms totally); *unbound eNOS* - 414 residues, 16850 water molecules and 2 Na⁺ (57176 atoms totally); **20:iNOS** - 418 residues, 18685 water molecules and 5 Na⁺ (62978 atoms totally); **20:nNOS** -

417 residues, 17939 water molecules and 1 Na⁺ (60514 atoms totally); **20:eNOS** - 414 residues, 18138 water molecules and 4 Na⁺ (60880 atoms totally); **21:iNOS** - 418 residues, 17039 water molecules and 2 Na⁺ (58020 atoms totally); **21:nNOS** - 417 residues, 17938 water molecules and 1 Cl⁻ (60524 atoms totally); **21:eNOS** - 414 residues, 18137 water molecules and 2 Na⁺ (60888 atoms totally); **L2:iNOS** - 418 residues, 17102 water molecules and 1 Na⁺ (58217 atoms in total); **L11:iNOS** - 418 residues, 17072 water molecules and 5 Na⁺ (58135 atoms in total); **L12:iNOS** - 418 residues, 17067 water molecules and 5 Na⁺ (58100 atoms in total); **L13:iNOS** - 418 residues, 17068 water molecules and 3 Na⁺ (58109 atoms in total); **L16:iNOS** - 418 residues, 17072 water molecules and 4 Na⁺ (58096 atoms in total); **Re2:iNOS** - 418 residues, 17070 water molecules and 3 Cl⁻ (58129 atoms in total); **Re11:iNOS** - 418 residues, 17064 water molecules and 3 Cl⁻ (58120 atoms in total); **Re12:iNOS** - 418 residues, 17073 water molecules and 1 Na⁺ (58119 atoms in total); **Re13:iNOS** - 418 residues, 17069 water molecules and 1 Na⁺ (58116 atoms in total); **Re16:iNOS** - 418 residues, 17072 water molecules and 1 Na⁺ (58097 atoms in total).

All models were subjected to 3000 energy minimization steps and then MD continued for another 8 ns in 2 fs time steps. Covalent bonds involving hydrogen atoms were constrained to their equilibrium length. The force field parameters were kept standard as specified by the charm force field. Short range nonbonded van der Waals interactions were computed every 2 fs, and the long-range electrostatic ones were computed every 4 fs. Starting from a switching distance of 1 nm, the Lennard-Jones potential was smoothly reduced to zero at a cutoff distance of 1.2 nm. The particle mesh Ewald (PME) algorithm with a grid spacing of 1 Å was used for electrostatics.²⁰⁹ The target temperature was 310 K in all simulations. This was controlled using Langevin dynamics with the friction coefficient set to 5 ps.²¹⁰ The pair list of the non-bonded interaction was recalculated for every ten time steps with a pair list distance of 16.0 Å. In NPT simulations (constant pressure, particle number, and temperature), pressure was controlled using the modified Langevin piston Nosé-Hoover method with a barostat oscillation coefficient of 200 fs and a damping coefficient of 50 fs.²¹¹ Target pressure was 1 atm. Harmonic constraints were used to restrain the H₄B cofactor to its crystallographic position with a harmonic force of 0.3 kcal/mol.

7.11.3.1 – Analysis of the Trajectories

VMD version 1.8.7 was used for trajectory analysis.¹⁸¹ Several detailed analyses were carried out for the last 3 ns of the equilibrated simulations. The average structures of the last 3 ns of the simulations were calculated using appropriate in-house scripts. The water molecules, which are within 3 Å from the inhibitors in each snapshot were identified by using appropriate Tcl script

executed within VMD, and the percentage of residence time calculated. The NAMDenenergy plugin of VMD was used to calculate the electrostatic and van der Waal interaction energies between protein and inhibitors for each frame of the MD trajectory. The hydrogen bond analysis was performed using the HBOND routine in VMD using a distance cut-off of 3.5 and an angle cut-off of 30. The volumes of the active site cavities of the unbound iNOS, nNOS and eNOS isoforms, as well as the volume of the complexes **L2**:iNOS, **L11**:iNOS, **Re2**:iNOS and **Re11**:NOS (calculated including the volume of the ligands) were calculated using the Volarea VMD Plug-in. The volumes were calculated for the last 3 ns of simulation using a box volume of 20.9, 18.7 and 25.5 Å³ centered on the Fe atom of the heme group and a probe radius of 1.0 Å.¹⁷⁵ The volumes of the inhibitors **L2**, **L11**, **Re2**, **Re11** and **Re13** were also calculated using the Volarea. All the pictures were made with the Pymol software.²¹²

7.11.4 – FEP Simulations

The alchemical FEP transformations were performed using the dual-topology paradigm, in which the initial and the final states are defined in terms of distinct, non-interacting topologies, and the interactions of the transformed atoms with their environment are scaled in terms of a linear parameter, λ , often called coupling parameter.^{116b, 213} In general, the atoms in the molecular topology are separated into three groups: (i) atoms which do not change during the simulation - *e.g.* the environment, (ii) the atoms describing the reference state, A, of the system, and (iii) the atoms that correspond to the target state, B, at the end of the alchemical transformation. The initial state was chosen to be the equilibrium state of the Re complexes **Re2** and **Re11**. The final state was set up such that the “Re(CO)₃” core in the complexes was vanished to give the ligands **L2** and **L11**. The energy and forces in the FEP simulations were defined such that the interaction of the “Re(CO)₃” core in the initial state with the rest of the system is effective at the beginning of the simulation ($\lambda = 0$), and nonexistent at the end of the simulation ($\lambda = 1$). In a typical FEP calculation for a transformation from state A to state B, many λ are needed in order to obtain a smooth transition from the initial state A to the final state B. A source of error in a FEP calculation involves the end points of the transformation. Due to the appearing and disappearing atoms, van der Waals' clashes occur and result in “end point catastrophes”, which prevent correct convergence of the calculation.²¹⁴ A number of schemes have been devised to circumvent this problem, among which the increasing of the number of intermediate λ states in the calculation to decrease the conformational difference between consecutive λ states.^{135, 183} To obtain an accurate estimate of the free energy, we increased the number of windows at the beginning and end of the FEP simulations, collecting data at several points with λ values close to zero or one. Another possible route for avoiding overlap of unbound

electrostatic potentials consists of allowing a bound (soft-core) vdW potential, to repel first all overlapping particles when λ tends towards either 0 or 1.^{183, 215}

The averaged structures of the complexes **Re2:iNOS** and **Re11:iNOS** calculated for the last 3 ns of simulation were used as starting points for FEP calculations. Several different simulation schemes were tried in order to find conditions that produced converging energy results with minimal dispersion. It was observed that the use of 24 intermediate states (0.0000001, 0.000001, 0.00001, 0.0001, 0.001, 0.01, 0.05, 0.1; between 0.1 and 0.9 the change in λ was linear with $\Delta\lambda$ of 0.1; at the final segments the progression of λ was 0.9, 0.95, 0.99, 0.999, 0.9999, 0.99999, 0.999999, 0.9999999) and total simulations times of 0.28 ns (2 ps equilibration + 10 ps accumulation per λ) were not enough to obtain convergence (**Figure 8.42**, Annexes). In order to achieve convergence each FEP calculation was split into more intermediate λ states (0.0000001, 0.000001, 0.00001, 0.0001, 0.001, 0.01, 0.05, 0.1; between 0.1 and 0.9 the change in λ was linear with $\Delta\lambda$ of 0.05; at the final segments the progression of λ was 0.9, 0.95, 0.99, 0.999, 0.9999, 0.99999, 0.999999, 0.9999999) and the simulation time was increased. At each intermediate λ state, equilibration was run for 16 ps, followed by 120 ps of FEP data collection. The extra intermediate states and the use of more steps for equilibration and acquisition at each λ increased the total length of the FEP simulation to 4.32 ns (**Figure 5.23**). To check the dependency of the results on the direction of the transformation, the free energy profiles of the backward transformation were also calculated. Considering the simulations in both free and bound states, as well as in the forward and backward directions, the total time of simulation was ~ 17 ns. A number of different schemes were explored to optimize the number of λ and the simulation time per λ . These results are summarized in **Table 8.9** and **8.10** (Annexes).

References

1. McCready, V. R., Milestones in nuclear medicine. *European Journal of Nuclear Medicine and Molecular Imaging* **2000**, *27* (0), s049-s079.
2. Saha, G. B., Production of Radionuclides. In *Fundamentals of Nuclear Pharmacy*, Springer New York: 2010; pp 49-66.
3. Jaffer, F. A.; Weissleder, R., Molecular Imaging in the Clinical Arena. *JAMA: The Journal of the American Medical Association* **2005**, *293* (7), 855-862.
4. Oliveira, B. L.; Correia, J. D. G.; Raposinho, P. D.; Santos, I.; Ferreira, A.; Cordeiro, C.; Freire, A. P., Re and ^{99m}Tc organometallic complexes containing pendant L-arginine derivatives as potential probes of inducible nitric oxide synthase. *Dalton Transactions* **2009**, (1), 152-162.
5. (a) Salermo, L., Sorrenti, V., Giacomo, C., Romeo, G., Siracusa, M. A., Progress in the Development of Selective Nitric Oxide Synthase (NOS) Inhibitors. *Curr. Pharm. Des.* **2002**, *8*, 177 - 200; (b) Xian, M.; Fujiwara, N.; Wen, Z.; Cai, T.; Kazuma, S.; Janczuk, A. J.; Tang, X.; Telyatnikov, V. V.; Zhang, Y.; Chen, X.; Miyamoto, Y.; Taniguchi, N.; Wang, P. G., Novel substrates for nitric oxide synthases. *Bioorganic and Medicinal Chemistry* **2002**, *10* (9), 3049-3055.
6. (a) Mansuy, D.; Boucher, J.-L., Alternative nitric oxide-producing substrates for no synthases. *Free Radical Biology and Medicine* **2004**, *37* (8), 1105-1121; (b) Lefèvre-Groboillot, D.; Boucher, J.-L.; Stuehr, D. J.; Mansuy, D., Relationship between the structure of guanidines and N-hydroxyguanidines, their binding to inducible nitric oxide synthase (iNOS) and their iNOS-catalysed oxidation to NO. *FEBS Journal* **2005**, *272* (12), 3172-3183; (c) T. B. Cai, D. L., Peng G. Wang N-hydroxyguanidines as substrates of nitric oxide synthases. *Curr Top Med Chem* **2005**, *5* (7), 721-736.
7. (a) Blow, N., In vivo molecular imaging: the inside job. *Nat Meth* **2009**, *6* (6), 465-469; (b) Meikle, S. R.; Beekman, F. J.; Rose, S. E., Complementary molecular imaging technologies: High resolution SPECT, PET and MRI. *Drug Discovery Today: Technologies* **2006**, *3* (2), 187-194; (c) Pysz, M. A.; Gambhir, S. S.; Willmann, J. K., Molecular imaging: current status and emerging strategies. *Clinical Radiology* **2010**, *65* (7), 500-516.
8. Massoud, T. F.; Gambhir, S. S., Molecular imaging in living subjects: seeing fundamental biological processes in a new light. *Genes & Development* **2003**, *17* (5), 545-580.
9. Kowalsky, R. J.; Falen, S., *Radiopharmaceuticals in Nuclear Pharmacy and Nuclear Medicine*. APhA publications: Washington D. C., USA, 2004.
10. (a) Saha, G. B., *Fundamentals of nuclear pharmacy*. 5th ed.; Springer-Verlag: NY, 2004; (b) Liu, S., The role of coordination chemistry in the development of target-specific radiopharmaceuticals. *Chemical Society Reviews* **2004**, *33* (7), 445-461.

References

11. Wester, H.-J., Nuclear Imaging Probes: from Bench to Bedside. *Clinical Cancer Research* **2007**, *13* (12), 3470-3481.
12. (a) Mariani, G.; Bruselli, L.; Kuwert, T.; Kim, E.; Flotats, A.; Israel, O.; Dondi, M.; Watanabe, N., A review on the clinical uses of SPECT/CT. *European Journal of Nuclear Medicine and Molecular Imaging* **2010**, *37* (10), 1959-1985; (b) Buck, A. K.; Nekolla, S.; Ziegler, S.; Beer, A.; Krause, B. J.; Herrmann, K.; Scheidhauer, K.; Wester, H.-J.; Rummeny, E. J.; Schwaiger, M.; Drzezga, A., SPECT/CT. *Journal of Nuclear Medicine* **2008**, *49* (8), 1305-1319; (c) Simon R, C., Multimodality Imaging: Beyond PET/CT and SPECT/CT. *Seminars in Nuclear Medicine* **2009**, *39* (5), 348-353.
13. Wadas, T. J.; Wong, E. H.; Weisman, G. R.; Anderson, C. J., Coordinating Radiometals of Copper, Gallium, Indium, Yttrium, and Zirconium for PET and SPECT Imaging of Disease. *Chemical Reviews* **2010**, *110* (5), 2858-2902.
14. Gambhir, S. S., Molecular imaging of cancer with positron emission tomography. *Nat Rev Cancer* **2002**, *2* (9), 683-693.
15. Bartholomä, M. D.; Louie, A. S.; Valliant, J. F.; Zubieta, J., Technetium and Gallium Derived Radiopharmaceuticals: Comparing and Contrasting the Chemistry of Two Important Radiometals for the Molecular Imaging Era. *Chemical Reviews* **2010**, *110* (5), 2903-2920.
16. Blower, P., Towards molecular imaging and treatment of disease with radionuclides: the role of inorganic chemistry. *Dalton Transactions* **2006**, (14), 1705-1711.
17. (a) Ametamey, S. M.; Honer, M.; Schubiger, P. A., Molecular Imaging with PET. *Chemical Reviews* **2008**, *108* (5), 1501-1516; (b) Ido, T.; Wan, C. N.; Casella, V.; Fowler, J. S.; Wolf, A. P.; Reivich, M.; Kuhl, D. E., Labeled 2-deoxy-D-glucose analogs. 18F-labeled 2-deoxy-2-fluoro-D-glucose, 2-deoxy-2-fluoro-D-mannose and 14C-2-deoxy-2-fluoro-D-glucose. *Journal of Labelled Compounds and Radiopharmaceuticals* **1978**, *14* (2), 175-183.
18. (a) Kassis, A. I.; Adelstein, S. J., Radiobiologic Principles in Radionuclide Therapy. *Journal of Nuclear Medicine* **2005**, *46* (1 suppl), 4S-12S; (b) Volkert, W. A.; Hoffman, T. J., Therapeutic Radiopharmaceuticals. *Chemical Reviews* **1999**, *99* (9), 2269-2292.
19. (a) Nilsson, S.; Larsen, R. H.; Fossa, S. D.; Balteskard, L.; Borch, K. W.; Westlin, J. E.; Salberg, G.; Bruland, O. S., First clinical experience with alpha-emitting radium-223 in the treatment of skeletal metastases. *Clin Cancer Res* **2005**, *11* (12), 4451-9; (b) Nilsson, S.; Franzen, L.; Parker, C.; Tyrrell, C.; Blom, R.; Tennvall, J.; Lennernas, B.; Petersson, U.; Johannessen, D. C.; Sokal, M.; Pigott, K.; Yachnin, J.; Garkavij, M.; Strang, P.; Harmenberg, J.; Bolstad, B.; Bruland, O. S., Bone-targeted radium-223 in symptomatic, hormone-refractory prostate cancer: a randomised, multicentre, placebo-controlled phase II study. *Lancet Oncol* **2007**, *8* (7), 587-94.

20. A Phase III Study of Alpharadin (Radium-223) in Patients With Symptomatic Hormone Refractory Prostate Cancer With Skeletal Metastases (ALSYMPCA). <http://clinicaltrials.gov/cta/show/NCT00699751?sect=abcdefghi> (accessed 20-02-2012).
21. (a) Stepanek, J.; Ilvonen, S. A.; Lampinen, J. S.; Savolainen, S. E.; Välimäki, P. J.; Kuronen, A. A., Radiation Spectra of ^{111}In , ^{113}mIn and ^{114}mIn . *Acta Oncologica* **2000**, *39* (6), 667-671; (b) Kassis, A. I.; Walicka, M. A., Double-Strand Break Yield Following ^{125}I Decay Effects of DNA Conformation. *Acta Oncologica* **2000**, *39* (6), 721-726; (c) Tavares, A. A. S.; Tavares, J. M. R. S., $^{99\text{mTc}}$ Auger electrons – Analysis on the effects of low absorbed doses by computational methods. *Applied Radiation and Isotopes* **2011**, *69* (3), 607-608; (d) Buchegger, F.; Perillo-Adamer, F.; Dupertuis, Y.; Bischof Delaloye, A., Auger radiation targeted into DNA: a therapy perspective. *European Journal of Nuclear Medicine and Molecular Imaging* **2006**, *33* (11), 1352-1363.
22. (a) Alberto, R., The Chemistry of Technetium–Water Complexes within the Manganese Triad: Challenges and Perspectives. *European Journal of Inorganic Chemistry* **2009**, *2009* (1), 21-31; (b) Abram, U.; Alberto, R., Technetium and rhenium: coordination chemistry and nuclear medical applications. *Journal of the Brazilian Chemical Society* **2006**, *17*, 1486-1500.
23. DRYTEC Technetium-99m generator, http://www.gedrytec.com/design/technical_features_without_annotations.html. (accessed December 2011).
24. (a) Lee, J. S.; Lee, J.-S.; Park, U.-J.; Son, K.-J.; Han, H.-S., Development of a high performance $^{188}\text{W}/^{188}\text{Re}$ generator by using a synthetic alumina. *Applied Radiation and Isotopes* *67* (7-8), 1162-1166; (b) Dias, C. R.; Jeger, S.; Osso Jr, J. A.; Müller, C.; De Pasquale, C.; Hohn, A.; Waibel, R.; Schibli, R., Radiolabeling of rituximab with ^{188}Re and $^{99\text{mTc}}$ using the tricarbonyl technology. *Nuclear Medicine and Biology* **2011**, *38* (1), 19-28.
25. R. Dilworth, J.; J. Parrott, S., The biomedical chemistry of technetium and rhenium. *Chemical Society Reviews* **1998**, *27* (1), 43-55.
26. Palma, E.; Correia, J. D. G.; Oliveira, B. L.; Gano, L.; Santos, I. C.; Santos, I., $^{99\text{mTc}}(\text{CO})_3$ -labeled pamidronate and alendronate for bone imaging. *Dalton Transactions* **2011**, *40* (12), 2787-2796.
27. Palma, E.; Correia, J. D. G.; Campello, M. P. C.; Santos, I., Bisphosphonates as radionuclide carriers for imaging or systemic therapy. *Molecular BioSystems* **2011**, *7* (11), 2950-2966.
28. Fritzberg, A. R.; Kasina, S.; Eshima, D.; Johnson, D. L., Synthesis and biological evaluation of technetium-99m MAG3 as a hippuran replacement. *J. Nucl. Med.* **1986**, *27* (1), 111.
29. Leonard, J.-P.; Nowotnik, D. P.; Neirinckx, R. D., Technetium-99m-d,1-HM-PAO: A New Radiopharmaceutical for Imaging Regional Brain Perfusion Using SPECT—A Comparison with Iodine-123 HIPDM. *Journal of Nuclear Medicine* **1986**, *27* (12), 1819-1823.

References

30. (a) Mendes, F.; Gano, L.; Fernandes, C.; Paulo, A.; Santos, I., Studies of the myocardial uptake and excretion mechanisms of a novel ^{99m}Tc heart perfusion agent. *Nuclear Medicine and Biology* (0); (b) Mendes, F.; Paulo, A.; Santos, I., Metalloprobes for functional monitoring of tumour multidrug resistance by nuclear imaging. *Dalton Transactions* **2011**, 40 (20), 5377-5393.
31. Bååth, M.; Kölbeck, K. G.; Danielsson, R., Somatostatin receptor scintigraphy with ^{99m}Tc -depreotide (neospect) in discriminating between malignant and benign lesions in the diagnosis of lung cancer: a pilot study. *Acta Radiologica* **2004**, 45 (8), 833-839.
32. Francesconi, L. C.; Zheng, Y.; Bartis, J.; Blumenstein, M.; Costello, C.; De Rosch, M. A., Preparation and Characterization of [^{99}TcO] Apcitide: A Technetium Labeled Peptide. *Inorganic Chemistry* **2004**, 43 (9), 2867-2875.
33. Kung, M.-P.; Stevenson, D. A.; Plössl, K.; Meegalla, S. K.; Beckwith, A.; Essman, W. D.; Mu, M.; Lucki, I.; Kung, H. F., [^{99m}Tc]TRODAT-1: a novel technetium-99m complex as a dopamine transporter imaging agent. *European Journal of Nuclear Medicine and Molecular Imaging* **1997**, 24 (4), 372-380.
34. Schibli, R.; Schubiger, A., Current use and future potential of organometallic radiopharmaceuticals. *European Journal of Nuclear Medicine and Molecular Imaging* **2002**, 29 (11), 1529-1542.
35. Alberto, R.; Ortner, K.; Wheatley, N.; Schibli, R.; Schubiger, A. P., Synthesis and Properties of Boranocarbonate: A Convenient in Situ CO Source for the Aqueous Preparation of [$^{99m}\text{Tc}(\text{OH})_2\text{CO}_3$] $^+$. *Journal of the American Chemical Society* **2001**, 123 (13), 3135-3136.
36. Bruno L. Oliveira, M. M., Flávio Figueira, Elisa Palma, Lurdes Gano, Isabel C. Santos, Isabel Santos, João D. G. Correia, Pharmacokinetic modulation of fac- $^{99m}\text{Tc}(\text{CO})_3$ $^+$ with bifunctional pyrazolyl-containing chelators.
37. (a) Mundwiler, S.; Kundig, M.; Ortner, K.; Alberto, R., A new [2 + 1] mixed ligand concept based on [$^{99m}\text{Tc}(\text{OH})_2\text{CO}_3$] $^+$: a basic study. *Dalton Transactions* **2004**, (9), 1320-1328; (b) Santos, I.; Paulo, A.; Correia, J. D. G., Rhenium and Technetium Complexes Anchored by Phosphines and Scorpionates for Radiopharmaceutical Applications Contrast Agents III. Krause, W., Ed. Springer Berlin / Heidelberg: 2005; Vol. 252, pp 45-84; (c) Correia, J. D. G.; Domingos, Â.; Santos, I.; Alberto, R.; Ortner, K., Re Tricarbonyl Complexes with Ligands Containing P,N,N and P,N,O Donor Atom Sets: Synthesis and Structural Characterization. *Inorganic Chemistry* **2001**, 40 (20), 5147-5151; (d) Schibli, R.; La Bella, R.; Alberto, R.; Garcia-Garayoa, E.; Ortner, K.; Abram, U.; Schubiger, P. A., Influence of the Denticity of Ligand Systems on the in Vitro and in Vivo Behavior of $^{99m}\text{Tc}(\text{I})$ -Tricarbonyl Complexes: A Hint for the Future Functionalization of Biomolecules. *Bioconjugate Chemistry* **2000**, 11 (3), 345-351.

38. van Staveren, D. R.; Benny, P. D.; Waibel, R.; Kurz, P.; Pak, J.-K.; Alberto, R., S-Functionalized Cysteine: Powerful Ligands for the Labelling of Bioactive Molecules with Triaquatricarbonyltechnetium-99m(1+) ($[^{99m}\text{Tc}(\text{OH}_2)_3(\text{CO})_3]^+$). *Helvetica Chimica Acta* **2005**, *88* (3), 447-460.
39. van Staveren, D. R.; Mundwiler, S.; Hoffmanns, U.; Pak, J. K.; Spingler, B.; Metzler-Nolte, N.; Alberto, R., Conjugation of a novel histidine derivative to biomolecules and labelling with $[^{99m}\text{Tc}(\text{OH}_2)_3(\text{CO})_3]^+$. *Organic and Biomolecular Chemistry* **2004**, *2* (18), 2593-2603.
40. James, S.; Maresca, K. P.; Allis, D. G.; Valliant, J. F.; Eckelman, W.; Babich, J. W.; Zubieta, J., Extension of the Single Amino Acid Chelate Concept (SAAC) to Bifunctional Biotin Analogues for Complexation of the $\text{M}(\text{CO})_3+1$ Core (M = Tc and Re): Syntheses, Characterization, Biotinidase Stability, and Avidin Binding. *Bioconjugate Chemistry* **2006**, *17* (3), 579-589.
41. (a) Alves, S.; Paulo, A.; Correia, J. D. G.; Domingos, A.; Santos, I., Coordination capabilities of pyrazolyl containing ligands towards the $\text{fac-}[\text{Re}(\text{CO})_3]^+$ moiety. *Journal of the Chemical Society, Dalton Transactions* **2002**, (24), 4714-4719; (b) Vitor, R. F.; Alves, S.; Correia, J. D. G.; Paulo, A.; Santos, I., Rhenium(I)- and technetium(I) tricarbonyl complexes anchored by bifunctional pyrazole-diamine and pyrazole-dithioether chelators. *Journal of Organometallic Chemistry* **2004**, *689* (25), 4764-4774; (c) Alves, S.; Paulo, A.; Correia, J. D. G.; Gano, L.; Smith, C. J.; Hoffman, T. J.; Santos, I., Pyrazolyl Derivatives as Bifunctional Chelators for Labeling Tumor-Seeking Peptides with the $\text{fac-}[\text{M}(\text{CO})_3]^+$ Moiety (M = ^{99m}Tc , Re): Synthesis, Characterization, and Biological Behavior. *Bioconjugate Chemistry* **2005**, *16* (2), 438-449; (d) Alves, S.; Correia, J. D. G.; Santos, I.; Veerendra, B.; Sieckman, G. L.; Hoffman, T. J.; Rold, T. L.; Figueroa, S. D.; Retzliff, L.; McCrate, J.; Prasanphanich, A.; Smith, C. J., Pyrazolyl conjugates of bombesin: a new tridentate ligand framework for the stabilization of $\text{fac-}[\text{M}(\text{CO})_3]^+$ moiety. *Nuclear Medicine and Biology* **2006**, *33* (5), 625-634; (e) João D. G. Correia, A. P., Isabel Santos, Re and Tc Complexes with Pyrazolyl-Containing Chelators: from Coordination Chemistry to Target-Specific Delivery of Radioactivity *Curr. Radiopharm.* **2009**, *2* (4), 277-294.
42. Garcia, R.; Paulo, A.; Domingos, Â.; Santos, I.; Ortner, K.; Alberto, R., Re and Tc Complexes Containing B-H...M Agostic Interactions as Building Blocks for the Design of Radiopharmaceuticals. *Journal of the American Chemical Society* **2000**, *122* (45), 11240-11241.
43. Zobi, F.; Spingler, B.; Alberto, R., Syntheses, Structures and Reactivities of $[\text{CpTc}(\text{CO})_3\text{X}]^+$ and $[\text{CpRe}(\text{CO})_3\text{X}]^+$. *European Journal of Inorganic Chemistry* **2008**, *2008* (27), 4205-4214.
44. Suzuki, K.; Shimmura, N.; Thipyapong, K.; Uehara, T.; Akizawa, H.; Arano, Y., Assessment of Macrocyclic Triamine Ligands As Synthons for Organometallic ^{99m}Tc Radiopharmaceuticals. *Inorganic Chemistry* **2008**, *47* (7), 2593-2600.

References

45. (a) Correia, J. D. G.; Paulo, A.; Raposinho, P. D.; Santos, I., Radiometallated peptides for molecular imaging and targeted therapy. *Dalton Transactions* **2011**, 40 (23), 6144-6167; (b) Raposinho, P. D.; Correia, J. D. G.; Oliveira, M. C.; Santos, I., Melanocortin-1 receptor-targeting with radiolabeled cyclic α -melanocyte-stimulating hormone analogs for melanoma imaging. *Peptide Science* **2010**, 94 (6), 820-829.
46. (a) Alberto, R., New Organometallic Technetium Complexes for Radiopharmaceutical Imaging Contrast Agents III. Krause, W., Ed. Springer Berlin / Heidelberg: 2005; Vol. 252, pp 1-44; (b) Banerjee, S. R.; Maresca, K. P.; Francesconi, L.; Valliant, J.; Babich, J. W.; Zubieta, J., New directions in the coordination chemistry of ^{99m}Tc : a reflection on technetium core structures and a strategy for new chelate design. *Nuclear Medicine and Biology* **2005**, 32 (1), 1-20.
47. Marletta, M. A., Nitric oxide synthase structure and mechanism. *Journal of Biological Chemistry* **1993**, 268 (17), 12231-4.
48. (a) W. K. Alderton, C. E. C., and R. G. Knowles, Nitric oxide synthases: structure, function and inhibition. *Biochemistry Journal* **2001**, 357, 593-615; (b) Moncada, S.; Palmer, R. M.; Higgs, E. A., Nitric oxide: physiology, pathophysiology, and pharmacology. *Pharmacological Reviews* **1991**, 43 (2), 109-142.
49. Shaul, P. W.; Smart, E. J.; Robinson, L. J.; German, Z.; Yuhanna, I. S.; Ying, Y.; Anderson, R. G. W.; Michel, T., Acylation Targets Endothelial Nitric-oxide Synthase to Plasmalemmal Caveolae. *Journal of Biological Chemistry* **1996**, 271 (11), 6518-6522.
50. (a) Li, H.; Poulos, T. L., Structure-function studies on nitric oxide synthases. *Journal of Inorganic Biochemistry* **2005**, 99 (1), 293-305; (b) Kerwin, J. F.; Lancaster, J. R.; Feldman, P. L., Nitric oxide: a new paradigm for second messengers. *Journal of Medicinal Chemistry* **1995**, 38 (22), 4343-62; (c) Marletta, M. A., Nitric oxide synthase structure and mechanism. *Journal of Biological Chemistry* **1993** 268, 12231-12234.
51. (a) Crane, B. R.; Arvai, A. S.; Ghosh, D. K.; Wu, C.; Getzoff, E. D.; Stuehr, D. J.; Tainer, J. A., Structure of Nitric Oxide Synthase Oxygenase Dimer with Pterin and Substrate. *Science* **1998**, 279 (5359), 2121-2126; (b) Fischmann, T. O.; Hruza, A.; Niu, X. D.; Fossetta, J. D.; Lunn, C. A.; Dolphin, E.; Prongay, A. J.; Reichert, P.; Lundell, D. J.; Narula, S. K.; Weber, P. C., Structural characterization of nitric oxide synthase isoforms reveals striking active-site conservation. *Nat Struct Mol Biol* **1999**, 6 (3), 233-242.
52. (a) Rusche, K. M.; Spiering, M. M.; Marletta, M. A., Reactions Catalyzed by Tetrahydrobiopterin-Free Nitric Oxide Synthase†. *Biochemistry* **1998**, 37 (44), 15503-15512; (b) Wei, C.-C.; Wang, Z.-Q.; Durra, D.; Hemann, C.; Hille, R.; Garcin, E. D.; Getzoff, E. D.; Stuehr, D. J., The Three

- Nitric-oxide Synthases Differ in Their Kinetics of Tetrahydrobiopterin Radical Formation, Heme-Dioxy Reduction, and Arginine Hydroxylation. *Journal of Biological Chemistry* **2005**, *280* (10), 8929-8935.
53. Abu-Soud, H. M.; Feldman, P. L.; Clark, P.; Stuehr, D. J., Electron transfer in the nitric-oxide synthases. Characterization of L-arginine analogs that block heme iron reduction. *Journal of Biological Chemistry* **1994**, *269* (51), 32318-26.
54. Stevens-Truss, R.; Marletta, M. A., Interaction of Calmodulin with the Inducible Murine Macrophage Nitric Oxide Synthase. *Biochemistry* **1995**, *34* (48), 15638-15645.
55. Chen, P.-F.; Tsai, A.-L.; Berka, V.; Wu, K. K., Mutation of Glu-361 in Human Endothelial Nitric-oxide Synthase Selectively Abolishes L-Arginine Binding without Perturbing the Behavior of Heme and Other Redox Centers. *Journal of Biological Chemistry* **1997**, *272* (10), 6114-6118.
56. Crane, B. R.; Sudhamsu, J.; Patel, B. A., Bacterial Nitric Oxide Synthases. *Annual Review of Biochemistry* **2010**, *79* (1), 445-470.
57. Davydov, R.; Ledbetter-Rogers, A.; Martásek, P.; Larukhin, M.; Sono, M.; Dawson, J. H.; Masters, B. S. S.; Hoffman, B. M., EPR and ENDOR Characterization of Intermediates in the Cryoreduced Oxy-Nitric Oxide Synthase Heme Domain with Bound L-Arginine or NG-Hydroxyarginine. *Biochemistry* **2002**, *41* (33), 10375-10381.
58. Couture, M.; Stuehr, D. J.; Rousseau, D. L., The Ferrous Dioxygen Complex of the Oxygenase Domain of Neuronal Nitric-oxide Synthase. *Journal of Biological Chemistry* **2000**, *275* (5), 3201-3205.
59. Zhu, Y.; Silverman, R. B., Revisiting Heme Mechanisms. A Perspective on the Mechanisms of Nitric Oxide Synthase (NOS), Heme Oxygenase (HO), and Cytochrome P450s (CYP450s). *Biochemistry* **2008**, *47* (8), 2231-2243.
60. (a) Cho, K.-B.; Carvajal, M. A.; Shaik, S., First Half-Reaction Mechanism of Nitric Oxide Synthase: The Role of Proton and Oxygen Coupled Electron Transfer in the Reaction by Quantum Mechanics/Molecular Mechanics. *The Journal of Physical Chemistry B* **2008**, *113* (1), 336-346; (b) Cho, K.-B.; Derat, E.; Shaik, S., Compound I of Nitric Oxide Synthase: The Active Site Protonation State. *Journal of the American Chemical Society* **2007**, *129* (11), 3182-3188.
61. Werner, E. R.; Gorren, A. C. F.; Heller, R.; Werner-Felmayer, G.; Mayer, B., Tetrahydrobiopterin and Nitric Oxide: Mechanistic and Pharmacological Aspects. *Experimental Biology and Medicine* **2003**, *228* (11), 1291-1302.
62. Wink, D. A.; Mitchell, J. B., Chemical biology of nitric oxide: insights into regulatory, cytotoxic, and cytoprotective mechanisms of nitric oxide. *Free Radical Biology and Medicine* **1998**, *25* (4-5), 434-456.
63. (a) John, G., Glutamate, nitric oxide and cell-cell signalling in the nervous system. *Trends in Neurosciences* **1991**, *14* (2), 60-67; (b) Dawson, M. D., Ph.D, Ted M.; Dawson, P. D., Valina L., NITRIC OXIDE SYNTHASE: Role as a Transmitter/Mediator in the Brain and Endocrine System. *Annual Review*

References

- of Medicine* **1996**, *47* (1), 219-227; (c) Duncan, A. J.; Heales, S. J. R., Nitric oxide and neurological disorders. *Molecular Aspects of Medicine* **26** (1-2), 67-96.
64. Korhonen, R.; Lahti, A.; Kankaanranta, H.; Moilanen, E., Nitric Oxide Production and Signaling in Inflammation. *Current Drug Targets - Inflammation and Allergy* **2005**, *4* (4), 471-479.
65. Bogdan, C., Nitric oxide and the immune response. *Nat Immunol* **2001**, *2* (10), 907-916.
66. Wink, D. A.; Mitchell, J. B., Nitric oxide and cancer: an introduction. *Free Radical Biology and Medicine* **2003**, *34* (8), 951-954.
67. (a) Ji, H.; Erdal, E. P.; Litzinger, E. A.; Seo, J.; Zhu, Y.; Xue, F.; Fang, J.; Huang, J.; Silverman, R. B., Selective Neuronal Nitric Oxide Synthase Inhibitors. *Frontiers in Medicinal Chemistry* **2009**, *4*, 842-882; (b) Fukumura, D.; Kashiwagi, S.; Jain, R. K., The role of nitric oxide in tumour progression. *Nat Rev Cancer* **2006**, *6* (7), 521-534; (c) Fukumura, D.; Jain, R. K., Role of nitric oxide in angiogenesis and microcirculation in tumors. *Cancer metastasis reviews* **1998**, *17* (1), 77-89.
68. (a) Huang, P. L.; Huang, Z.; Mashimo, H.; Bloch, K. D.; Moskowitz, M. A.; Bevan, J. A.; Fishman, M. C., Hypertension in mice lacking the gene for endothelial nitric oxide synthase. *Nature* **1995**, *377* (6546), 239-242; (b) Vallance, P.; Leiper, J., Blocking NO synthesis: how, where and why? *Nat Rev Drug Discov* **2002**, *1* (12), 939-950; (c) Di Giacomo, C.; Sorrenti, V.; Salerno, L.; Cardile, V.; Guerrera, F.; Siracusa, M. A.; Avitabile, M.; Vanella, A., Novel Inhibitors of Neuronal Nitric Oxide Synthase. *Exp. Biol. Med.* **2003**, *228* (5), 486-490; (d) Zicha, J.; Pechánová, O.; Dobesová, Z.; Kunes, J., Hypertensive response to chronic NG-nitro-L-arginine methyl ester (L-NAME) treatment is similar in immature and adult Wistar rats. *Clin. Sci.* **2003**, *105* (4), 483-489.
69. Jia, Q.; Cai, T.; Huang, M.; Li, H.; Xian, M.; Poulos, T. L.; Wang, P. G., Isoform-Selective Substrates of Nitric Oxide Synthase. *Journal of Medicinal Chemistry* **2003**, *46* (12), 2271-2274.
70. Leiper, J.; Nandi, M., The therapeutic potential of targeting endogenous inhibitors of nitric oxide synthesis. *Nat Rev Drug Discov* **2011**, *10* (4), 277-291.
71. (a) Garcin, E. D.; Arvai, A. S.; Rosenfeld, R. J.; Kroeger, M. D.; Crane, B. R.; Andersson, G.; Andrews, G.; Hamley, P. J.; Mallinder, P. R.; Nicholls, D. J.; St-Gallay, S. A.; Tinker, A. C.; Gensmantel, N. P.; Mete, A.; Cheshire, D. R.; Connolly, S.; Stuehr, D. J.; Aberg, A.; Wallace, A. V.; Tainer, J. A.; Getzoff, E. D., Anchored plasticity opens doors for selective inhibitor design in nitric oxide synthase. *Nat Chem Biol* **2008**, *4* (11), 700-707; (b) Ji, H.; Stanton, B. Z.; Igarashi, J.; Li, H.; Martásek, P.; Roman, L. J.; Poulos, T. L.; Silverman, R. B., Minimal Pharmacophoric Elements and Fragment Hopping, an Approach Directed at Molecular Diversity and Isozyme Selectivity. Design of Selective Neuronal Nitric Oxide Synthase Inhibitors. *Journal of the American Chemical Society* **2008**, *130* (12), 3900-3914.
72. Proskuryakov, S. Y.; Konoplyannikov, A. G.; Skvortsov, V. G.; Mandrugina, A. A.; Fedoseev, V. M., Structure and activity of NO synthase inhibitors specific to the L-arginine binding site. *Biochemistry* **2005**, *70* (1), 8-23.

73. Fukuto, J. M.; Wood, K. S.; Byrns, R. E.; Ignarro, L. J., NG-Amino-L-arginine: A new potent antagonist of L-arginine-mediated endothelium-dependent relaxation. *Biochemical and Biophysical Research Communications* **1990**, *168* (2), 458-465.
74. Wolff, D. J.; Lubeskie, A., Inactivation of Nitric Oxide Synthase Isoforms by Diaminoguanidine and NG-Amino-L-arginine. *Archives of Biochemistry and Biophysics* **1996**, *325* (2), 227-234.
75. Zhang, H. Q.; Fast, W.; Marletta, M. A.; Martasek, P.; Silverman, R. B., Potent and Selective Inhibition of Neuronal Nitric Oxide Synthase by N^ω-Propyl-L-arginine. *Journal of Medicinal Chemistry* **1997**, *40* (24), 3869-3870.
76. Moore, W. M.; Webber, R. K.; Jerome, G. M.; Tjoeng, F. S.; Misko, T. P.; Currie, M. G., L-N⁶-(1-Iminoethyl)lysine: A Selective Inhibitor of Inducible Nitric Oxide Synthase. *Journal of Medicinal Chemistry* **1994**, *37* (23), 3886-3888.
77. Frey, C.; Narayanan, K.; McMillan, K.; Spack, L.; Gross, S. S.; Masters, B. S.; Griffith, O. W., L-thiocitrulline. A stereospecific, heme-binding inhibitor of nitric-oxide synthases. *Journal of Biological Chemistry* **1994**, *269* (42), 26083-26091.
78. Collins, J. L.; Shearer, B. G.; Oplinger, J. A.; Lee, S.; Garvey, E. P.; Salter, M.; Duffy, C.; Burnette, T. C.; Furfine, E. S., N-Phenylamidines as Selective Inhibitors of Human Neuronal Nitric Oxide Synthase: Structure-Activity Studies and Demonstration of in Vivo Activity. *Journal of Medicinal Chemistry* **1998**, *41* (15), 2858-2871.
79. Garvey, E. P.; Oplinger, J. A.; Furfine, E. S.; Kiff, R. J.; Laszlo, F.; Whittle, B. J. R.; Knowles, R. G., 1400W Is a Slow, Tight Binding, and Highly Selective Inhibitor of Inducible Nitric-oxide Synthase in Vitro and in Vivo. *Journal of Biological Chemistry* **1997**, *272* (8), 4959-4963.
80. (a) Ji, H.; Li, H.; Flinspach, M.; Poulos, T. L.; Silverman, R. B., Computer Modeling of Selective Regions in the Active Site of Nitric Oxide Synthases: Implication for the Design of Isoform-Selective Inhibitors. *Journal of Medicinal Chemistry* **2003**, *46* (26), 5700-5711; (b) Tafi, A.; Angeli, L.; Venturini, G.; Travagli, M.; Corelli, F.; Botta, M., Computational Studies of Competitive Inhibitors of Nitric Oxide Synthase (NOS) Enzymes: Towards the Development of Powerful and Isoform-Selective Inhibitors *Curr Med Chem* **2006**, *13* (16), 1929-1946.
81. (a) Huang, H.; Martásek, P.; Roman, L. J.; Silverman, R. B., Synthesis and Evaluation of Peptidomimetics as Selective Inhibitors and Active Site Probes of Nitric Oxide Synthases. *Journal of Medicinal Chemistry* **2000**, *43* (15), 2938-2945; (b) Silverman, R. B., Design of Selective Neuronal Nitric Oxide Synthase Inhibitors for the Prevention and Treatment of Neurodegenerative Diseases. *Accounts of Chemical Research* **2009**, *42* (3), 439-451.

References

82. (a) Nagano, T.; Yoshimura, T., Bioimaging of Nitric Oxide. *Chemical Reviews* **2002**, *102* (4), 1235-1270; (b) Hong, H.; Sun, J.; Cai, W., Multimodality imaging of nitric oxide and nitric oxide synthases. *Free Radical Biology and Medicine* **2009**, *47* (6), 684-698.
83. Pomper, M. G.; Musachio, J. L.; Scheffel, U.; Macdonald, J. E.; McCarthy, D. J.; Reif, D. W.; Villemagne, V. L.; Yokoi, F.; Dannals, R. F.; Wong, D. F., Radiolabeled Neuronal Nitric Oxide Synthase Inhibitors: Synthesis, In Vivo Evaluation, and Primate PET Studies. *Journal of Nuclear Medicine* **2000**, *41* (8), 1417-1425.
84. Roeda, D.; Crouzel, C.; Brouillet, E.; Valette, H., Synthesis and in vivo distribution of no-carrier-added N(ω)-nitro-L-arginine [11C]methyl ester, a nitric oxide synthase inhibitor. *Nuclear Medicine and Biology* **1996**, *23* (4), 509-512.
85. Zhang, J.; McCarthy, T. J.; Moore, W. M.; Currie, M. G.; Welch, M. J., Synthesis and Evaluation of Two Positron-Labeled Nitric Oxide Synthase Inhibitors, S-[11C]Methylisothiurea and S-(2-[18F]Fluoroethyl)isothiurea, as Potential Positron Emission Tomography Tracers1. *Journal of Medicinal Chemistry* **1996**, *39* (26), 5110-5118.
86. Zhou, D.; Lee, H.; Rothfuss, J. M.; Chen, D. L.; Ponde, D. E.; Welch, M. J.; Mach, R. H., Design and Synthesis of 2-Amino-4-methylpyridine Analogues as Inhibitors for Inducible Nitric Oxide Synthase and in Vivo Evaluation of [18F]6-(2-Fluoropropyl)-4-methyl-pyridin-2-amine as a Potential PET Tracer for Inducible Nitric Oxide Synthase. *Journal of Medicinal Chemistry* **2009**, *52* (8), 2443-2453.
87. Jensen, F., *Introduction to Computational Chemistry*. Wiley: 2006.
88. Kitchen, D. B.; Decornez, H.; Furr, J. R.; Bajorath, J., Docking and scoring in virtual screening for drug discovery: methods and applications. *Nat Rev Drug Discov* **2004**, *3* (11), 935-949.
89. I.M, K., Computer-aided drug discovery and development (CADD): In silico-chemico-biological approach. *Chemico-Biological Interactions* **2008**, *171* (2), 165-176.
90. Kuntz, I. D.; Blaney, J. M.; Oatley, S. J.; Langridge, R.; Ferrin, T. E., A geometric approach to macromolecule-ligand interactions. *Journal of Molecular Biology* **1982**, *161* (2), 269-288.
91. (a) Apostolakis, J.; Plückthun, A.; Caflisch, A., Docking small ligands in flexible binding sites. *Journal of Computational Chemistry* **1998**, *19* (1), 21-37; (b) Claußen, H.; Buning, C.; Rarey, M.; Lengauer, T., FlexE: efficient molecular docking considering protein structure variations. *Journal of Molecular Biology* **2001**, *308* (2), 377-395.
92. Sousa, S. F.; Fernandes, P. A.; Ramos, M. J., Protein–ligand docking: Current status and future challenges. *Proteins: Structure, Function, and Bioinformatics* **2006**, *65* (1), 15-26.
93. Böhm, H.-J., The computer program LUDI: A new method for the de novo design of enzyme inhibitors. *Journal of Computer-Aided Molecular Design* **1992**, *6* (1), 61-78.

94. Rarey, M.; Kramer, B.; Lengauer, T.; Klebe, G., A Fast Flexible Docking Method using an Incremental Construction Algorithm. *Journal of Molecular Biology* **1996**, *261* (3), 470-489.
95. Ewing, T. J. A.; Kuntz, I. D., Critical evaluation of search algorithms for automated molecular docking and database screening. *Journal of Computational Chemistry* **1997**, *18* (9), 1175-1189.
96. Miller, M. D.; Kearsley, S. K.; Underwood, D. J.; Sheridan, R. P., FLOG: A system to select 'quasi-flexible' ligands complementary to a receptor of known three-dimensional structure. *Journal of Computer-Aided Molecular Design* **1994**, *8* (2), 153-174.
97. Metropolis, N.; Rosenbluth, A. W.; Rosenbluth, M. N.; Teller, A. H.; Teller, E., *Equation of State Calculations by Fast Computing Machines*. AIP: 1953; Vol. 21, p 1087-1092.
98. Goodsell, D. S.; Olson, A. J., Automated docking of substrates to proteins by simulated annealing. *Proteins: Structure, Function, and Bioinformatics* **1990**, *8* (3), 195-202.
99. Taylor, R. D.; Jewsbury, P. J.; Essex, J. W., A review of protein-small molecule docking methods. *Journal of Computer-Aided Molecular Design* **2002**, *16* (3), 151-166.
100. Jones, G.; Willett, P.; Glen, R. C.; Leach, A. R.; Taylor, R., Development and validation of a genetic algorithm for flexible docking. *Journal of Molecular Biology* **1997**, *267* (3), 727-748.
101. Morris, G. M.; Goodsell, D. S.; Halliday, R. S.; Huey, R.; Hart, W. E.; Belew, R. K.; Olson, A. J., Automated docking using a Lamarckian genetic algorithm and an empirical binding free energy function. *Journal of Computational Chemistry* **1998**, *19* (14), 1639-1662.
102. Mangoni, M.; Roccatano, D.; Di Nola, A., Docking of flexible ligands to flexible receptors in solution by molecular dynamics simulation. *Proteins: Structure, Function, and Bioinformatics* **1999**, *35* (2), 153-162.
103. Eldridge, M. D.; Murray, C. W.; Auton, T. R.; Paolini, G. V.; Mee, R. P., Empirical scoring functions: I. The development of a fast empirical scoring function to estimate the binding affinity of ligands in receptor complexes. *Journal of Computer-Aided Molecular Design* **1997**, *11* (5), 425-445.
104. Rognan, D.; Lauemøller, S. L.; Holm, A.; Buus, S.; Tschinke, V., Predicting Binding Affinities of Protein Ligands from Three-Dimensional Models: Application to Peptide Binding to Class I Major Histocompatibility Proteins. *Journal of Medicinal Chemistry* **1999**, *42* (22), 4650-4658.
105. Muegge, I.; Martin, Y. C., A General and Fast Scoring Function for Protein-Ligand Interactions: A Simplified Potential Approach. *Journal of Medicinal Chemistry* **1999**, *42* (5), 791-804.
106. Gohlke, H.; Hendlich, M.; Klebe, G., Knowledge-based scoring function to predict protein-ligand interactions. *Journal of Molecular Biology* **2000**, *295* (2), 337-356.
107. Morris, G. M.; Huey, R.; Lindstrom, W.; Sanner, M. F.; Belew, R. K.; Goodsell, D. S.; Olson, A. J., AutoDock4 and AutoDockTools4: Automated docking with selective receptor flexibility. *Journal of Computational Chemistry* **2009**, *30* (16), 2785-2791.

References

108. AutoDock 4.2 User Guide. Available at: <http://autodock.scripps.edu/faqs-help/manual/autodock-4-2-user-guide>. (accessed December 2011).
109. Huey, R.; Morris, G. M.; Olson, A. J.; Goodsell, D. S., A semiempirical free energy force field with charge-based desolvation. *Journal of Computational Chemistry* **2007**, *28* (6), 1145-1152.
110. Ball, P., Water as an active constituent in cell biology. *Chemical Reviews* **2008**, *108* (1), 74-108.
111. John E, L., Just add water! The effect of water on the specificity of protein-ligand binding sites and its potential application to drug design. *Chemistry and Biology* **1996**, *3* (12), 973-980.
112. Alonso, H.; Bliznyuk, A. A.; Gready, J. E., Combining docking and molecular dynamic simulations in drug design. *Medicinal Research Reviews* **2006**, *26* (5), 531-568.
113. Davis, A. M.; St-Gallay, S. A.; Kleywegt, G. J., Limitations and lessons in the use of X-ray structural information in drug design. *Drug Discovery Today* **2008**, *13* (19-20), 831-841.
114. Schotte, F.; Lim, M.; Jackson, T. A.; Smirnov, A. V.; Soman, J.; Olson, J. S.; Phillips, G. N.; Wulff, M.; Anfinrud, P. A., Watching a Protein as it Functions with 150-ps Time-Resolved X-ray Crystallography. *Science* **2003**, *300* (5627), 1944-1947.
115. (a) Kempf, J.; Loria, J., Protein dynamics from solution NMR. *Cell Biochemistry and Biophysics* **2002**, *37* (3), 187-211; (b) Mittermaier, A.; Kay, L. E., New Tools Provide New Insights in NMR Studies of Protein Dynamics. *Science* **2006**, *312* (5771), 224-228.
116. (a) Allen, M. P., Introduction to molecular dynamics simulation. . In *Computational soft matter: from synthetic polymers to proteins* [Online] In N. Attig, K. B., H. Grubmüller, and K. Kremer, Ed. John von Neumann Institute for Computing, NIC-Directors: 2004; (b) Phillips, J. C.; Braun, R.; Wang, W.; Gumbart, J.; Tajkhorshid, E.; Villa, E.; Chipot, C.; Skeel, R. D.; Kalé, L.; Schulten, K., Scalable molecular dynamics with NAMD. *Journal of Computational Chemistry* **2005**, *26* (16), 1781-1802; (c) Martin Karplus, J. A. M., Molecular dynamics simulations of biomolecules. *Nature Structural Biology* **2002**, *9*, , 646 - 652; (d) Warshel, A., Molecular Dynamics Simulations of Biological Reactions. *Accounts of Chemical Research* **2002**, *35* (6), 385-395.
117. (a) Weiner, S. J.; Kollman, P. A.; Case, D. A.; Singh, U. C.; Ghio, C.; Alagona, G.; Profeta, S.; Weiner, P., A new force field for molecular mechanical simulation of nucleic acids and proteins. *Journal of the American Chemical Society* **1984**, *106* (3), 765-784; (b) Cornell, W. D.; Cieplak, P.; Bayly, C. I.; Gould, I. R.; Merz, K. M.; Ferguson, D. M.; Spellmeyer, D. C.; Fox, T.; Caldwell, J. W.; Kollman, P. A., A Second Generation Force Field for the Simulation of Proteins, Nucleic Acids, and Organic Molecules. *Journal of the American Chemical Society* **1995**, *117* (19), 5179-5197; (c) Weiner, S. J.; Kollman, P. A.; Nguyen, D. T.; Case, D. A., An all atom force field for simulations of proteins and nucleic acids. *Journal of Computational Chemistry* **1986**, *7* (2), 230-252; (d) Duan, Y.; Wu, C.; Chowdhury, S.; Lee, M. C.; Xiong, G.; Zhang, W.; Yang, R.; Cieplak, P.; Luo, R.; Lee, T.; Caldwell, J.;

- Wang, J.; Kollman, P., A point-charge force field for molecular mechanics simulations of proteins based on condensed-phase quantum mechanical calculations. *Journal of Computational Chemistry* **2003**, *24* (16), 1999-2012; (e) Wang, J.; Wolf, R. M.; Caldwell, J. W.; Kollman, P. A.; Case, D. A., Development and testing of a general amber force field. *Journal of Computational Chemistry* **2004**, *25* (9), 1157-1174; (f) Case, D. A.; Cheatham, T. E.; Darden, T.; Gohlke, H.; Luo, R.; Merz, K. M.; Onufriev, A.; Simmerling, C.; Wang, B.; Woods, R. J., The Amber biomolecular simulation programs. *Journal of Computational Chemistry* **2005**, *26* (16), 1668-1688.
118. (a) Brooks, B. R.; Bruccoleri, R. E.; Olafson, B. D.; States, D. J.; Swaminathan, S.; Karplus, M., CHARMM: A program for macromolecular energy, minimization, and dynamics calculations. *Journal of Computational Chemistry* **1983**, *4* (2), 187-217; (b) Brooks, B. R.; Brooks, C. L.; Mackerell, A. D.; Nilsson, L.; Petrella, R. J.; Roux, B.; Won, Y.; Archontis, G.; Bartels, C.; Boresch, S.; Caflisch, A.; Caves, L.; Cui, Q.; Dinner, A. R.; Feig, M.; Fischer, S.; Gao, J.; Hodoscek, M.; Im, W.; Kuczera, K.; Lazaridis, T.; Ma, J.; Ovchinnikov, V.; Paci, E.; Pastor, R. W.; Post, C. B.; Pu, J. Z.; Schaefer, M.; Tidor, B.; Venable, R. M.; Woodcock, H. L.; Wu, X.; Yang, W.; York, D. M.; Karplus, M., CHARMM: The biomolecular simulation program. *Journal of Computational Chemistry* **2009**, *30* (10), 1545-1614.
119. (a) Jorgensen, W. L.; Maxwell, D. S.; Tirado-Rives, J., Development and Testing of the OPLS All-Atom Force Field on Conformational Energetics and Properties of Organic Liquids. *Journal of the American Chemical Society* **1996**, *118* (45), 11225-11236; (b) Pranata, J.; Wierschke, S. G.; Jorgensen, W. L., OPLS potential functions for nucleotide bases. Relative association constants of hydrogen-bonded base pairs in chloroform. *Journal of the American Chemical Society* **1991**, *113* (8), 2810-2819.
120. (a) Christen, M.; Hünenberger, P. H.; Bakowies, D.; Baron, R.; Bürgi, R.; Geerke, D. P.; Heinz, T. N.; Kastenholz, M. A.; Kräutler, V.; Oostenbrink, C.; Peter, C.; Trzesniak, D.; van Gunsteren, W. F., The GROMOS software for biomolecular simulation: GROMOS05. *Journal of Computational Chemistry* **2005**, *26* (16), 1719-1751; (b) Scott, W. R. P.; Hünenberger, P. H.; Tironi, I. G.; Mark, A. E.; Billeter, S. R.; Fennen, J.; Torda, A. E.; Huber, T.; Krüger, P.; van Gunsteren, W. F., The GROMOS Biomolecular Simulation Program Package. *The Journal of Physical Chemistry A* **1999**, *103* (19), 3596-3607.
121. Mulliken, R. S., *Criteria for the Construction of Good Self-Consistent-Field Molecular Orbital Wave Functions, and the Significance of LCAO-MO Population Analysis*. AIP: 1962; Vol. 36, p 3428-3439.
122. Besler, B. H.; Merz, K. M.; Kollman, P. A., Atomic charges derived from semiempirical methods. *Journal of Computational Chemistry* **1990**, *11* (4), 431-439.
123. Bayly, C. I.; Cieplak, P.; Cornell, W.; Kollman, P. A., A well-behaved electrostatic potential based method using charge restraints for deriving atomic charges: the RESP model. *The Journal of Physical Chemistry* **1993**, *97* (40), 10269-10280.

References

124. Gasteiger, J.; Marsili, M., Iterative partial equalization of orbital electronegativity—a rapid access to atomic charges. *Tetrahedron* **1980**, *36* (22), 3219-3228.
125. Mackerell, A. D.; Bashford, D.; Bellott; Dunbrack, R. L.; Evanseck, J. D.; Field, M. J.; Fischer, S.; Gao, J.; Guo, H.; Ha, S.; Joseph-McCarthy, D.; Kuchnir, L.; Kuczera, K.; Lau, F. T. K.; Mattos, C.; Michnick, S.; Ngo, T.; Nguyen, D. T.; Prodhom, B.; Reiher, W. E.; Roux, B.; Schlenkrich, M.; Smith, J. C.; Stote, R.; Straub, J.; Watanabe, M.; Wiorkiewicz-Kuczera, J.; Yin, D.; Karplus, M., All-Atom Empirical Potential for Molecular Modeling and Dynamics Studies of Proteins. *The Journal of Physical Chemistry B* **1998**, *102* (18), 3586-3616.
126. Mackerell, A. D.; Feig, M.; Brooks, C. L., Extending the treatment of backbone energetics in protein force fields: Limitations of gas-phase quantum mechanics in reproducing protein conformational distributions in molecular dynamics simulations. *Journal of Computational Chemistry* **2004**, *25* (11), 1400-1415.
127. (a) Mackerell, A. D.; Banavali, N.; Foloppe, N., Development and current status of the CHARMM force field for nucleic acids. *Biopolymers* **2000**, *56* (4), 257-265; (b) Ponder, J.; Case, D., Force fields for protein simulations. *Advances in protein chemistry* **2003**, *66*, 27-85.
128. Swope, W. C.; Andersen, H. C.; Berens, P. H.; Wilson, K. R., *A computer simulation method for the calculation of equilibrium constants for the formation of physical clusters of molecules: Application to small water clusters*. AIP: 1982; Vol. 76, p 637-649.
129. Ryckaert, J.-P.; Ciccotti, G.; Berendsen, H. J. C., Numerical integration of the cartesian equations of motion of a system with constraints: molecular dynamics of n-alkanes. *Journal of Computational Physics* **1977**, *23* (3), 327-341.
130. (a) Bergdorf, M.; Peter, C.; Hünenberger, P., Influence of cut-off truncation and artificial periodicity of electrostatic interactions in molecular simulations of solvated ions: A continuum electrostatics study. *The Journal of Chemical Physics* **2003**, *119* (17), 9129-9144; (b) Weber, W.; Hünenberger, P. H.; McCammon, J. A., Molecular Dynamics Simulations of a Polyalanine Octapeptide under Ewald Boundary Conditions: Influence of Artificial Periodicity on Peptide Conformation. *The Journal of Physical Chemistry B* **2000**, *104* (15), 3668-3675.
131. (a) Ewald, P. P., Die Berechnung optischer und elektrostatischer Gitterpotentiale. *Annalen der Physik* **1921**, *369* (3), 253-287; (b) Darden, T., Particle mesh Ewald: An N-log(N) method for Ewald sums in large systems. *J. Chem. Phys.* **1993**, *98* (12), 10089.
132. Berendsen, H., Molecular dynamics with coupling to an external bath. *J. Chem. Phys.* **1984**, *81* (8), 3684.
133. Nosé, S., A unified formulation of the constant temperature molecular dynamics methods. *J. Chem. Phys.* **1984**, *81* (1), 511.

134. Huang, S.-Y.; Grinter, S. Z.; Zou, X., Scoring functions and their evaluation methods for protein-ligand docking: recent advances and future directions. *Physical Chemistry Chemical Physics* **2010**, *12* (40), 12899-12908.
135. Chipot, C.; Pearlman, D. A., Free Energy Calculations. The Long and Winding Gilded Road. *Molecular Simulation* **2002**, *28* (1-2), 1-12.
136. Brandsdal, B. O.; Österberg, F.; Almlöf, M.; Feierberg, I.; Luzhkov, V. B.; Åqvist, J., Free Energy Calculations and Ligand Binding. In *Advances in protein chemistry*, Valerie, D., Ed. Academic Press: 2003; Vol. Volume 66, pp 123-158.
137. Oliveira, B. L.; Raposinho, P. D.; Mendes, F.; Figueira, F. v.; Santos, I.; Ferreira, A. n.; Cordeiro, C.; Freire, A. P.; Correia, J. D. G., Re and Tc Tricarbonyl Complexes: From the Suppression of NO Biosynthesis in Macrophages to in Vivo Targeting of Inducible Nitric Oxide Synthase. *Bioconjugate Chemistry* **2010**, *21* (12), 2168-2172.
138. Raposinho, P.; Xavier, C.; Correia, J.; Falcão, S.; Gomes, P.; Santos, I., Melanoma targeting with α -melanocyte stimulating hormone analogs labeled with $^{99m}\text{Tc}(\text{CO})_3$: effect of cyclization on tumor-seeking properties. *Journal of Biological Inorganic Chemistry* **2008**, *13* (3), 449-459.
139. Liu, Y.; Pak, J. K.; Schmutz, P.; Bauwens, M.; Mertens, J.; Knight, H.; Alberto, R., Amino Acids Labeled with $^{99m}\text{Tc}(\text{CO})_3$ and Recognized by the I-type Amino Acid Transporter LAT1. *Journal of the American Chemical Society* **2006**, *128* (50), 15996-15997.
140. Caddick, S.; Judd, D. B.; Lewis, A. K. D.; Reich, M. T.; Williams, M. R. V., A generic approach for the catalytic reduction of nitriles. *Tetrahedron* **2003**, *59* (29), 5417-5423.
141. Yu, G.; Wang, S.; Wang, K.; Hu, Y.; Hu, H., A Novel Approach to 1,2-Dihydro-2-oxo-3-pyridinecarboxylic Ester via Aromatization Induced by Deamidation. *ChemInform* **2004**, *35* (37).
142. (a) Horii, Z.-I.; Iwata, C.; Tamura, Y., Reduction of Phthalimides with Sodium Borohydride. *The Journal of Organic Chemistry* **1961**, *26* (7), 2273-2276; (b) Osby, J. O.; Martin, M. G.; Ganem, B., An exceptionally mild deprotection of phthalimides. *Tetrahedron Letters* **1984**, *25* (20), 2093-2096.
143. Lim, N. C.; Ewart, C. B.; Bowen, M. L.; Ferreira, C. L.; Barta, C. A.; Adam, M. J.; Orvig, C., Pyridine-tert-Nitrogen-Phenol Ligands: N,N,O-Type Tripodal Chelates for the $[\text{M}(\text{CO})_3]^+$ Core (M = Re, Tc). *Inorganic Chemistry* **2008**, *47* (4), 1337-1345.
144. (a) Gillies, I. Process for the preparation of NG-monomethyl-L-arginine hydrochloride. 1997; (b) Renodon-Cornière, A.; Dijols, S.; Perollier, C.; Lefevre-Groboillot, D.; Boucher, J.-L.; Attias, R.; Sari, M.-A.; Stuehr, D.; Mansuy, D., N-Aryl N'-Hydroxyguanidines, A New Class of NO-Donors after Selective Oxidation by Nitric Oxide Synthases: Structure-Activity Relationship. *Journal of Medicinal Chemistry* **2001**, *45* (4), 944-954; (c) Fishbein, L.; Gallagher, J. A., The Preparation and Reactions of 2-

References

- Alkyl-1-(or 3)-nitro-2-thiopseudourea. Part I. Reaction with Amines1. *Journal of the American Chemical Society* **1954**, *76* (7), 1877-1879; (d) Philip, S. K.; Rajasekharan, K. N., Ecofriendly Synthesis of Novel Benzo-1,2,3-triazol-1-yl-(N-aryl)amidines and Their Conversion to Guanidines. *Synthetic Communications* **2011**, *41* (11), 1593-1602; (e) Katritzky, A. R. R., B. V., Recent developments in guanylating agents *Arkivoc* **2005**, *4*, 49 – 87.
145. Seo, J.; Martásek, P.; Roman, L. J.; Silverman, R. B., Selective l-nitroargininylaminopyrrolidine and l-nitroargininylaminopiperidine neuronal nitric oxide synthase inhibitors. *Bioorganic and Medicinal Chemistry* **2007**, *15* (5), 1928-1938.
146. Litzinger, E. A.; Martásek, P.; Roman, L. J.; Silverman, R. B., Design, synthesis, and biological testing of potential heme-coordinating nitric oxide synthase inhibitors. *Bioorganic and Medicinal Chemistry* **2006**, *14* (9), 3185-3198.
147. Long, D. A., Infrared and Raman characteristic group frequencies. Tables and charts George Socrates John Wiley and Sons, Ltd, Chichester, Third Edition, 2001. Price £135. *Journal of Raman Spectroscopy* **2004**, *35* (10), 905-905.
148. (a) Shearer, B. G.; Lee, S.; Franzmann, K. W.; White, H. A. R.; Sanders, D. C. J.; Kiff, R. J.; Garvey, E. P.; Furfine, E. S., Conformationally restricted arginine analogues as inhibitors of human nitric oxide synthase. *Bioorganic and Medicinal Chemistry Letters* **1997**, *7* (13), 1763-1768; (b) Maccallini, C.; Patruno, A.; Bešker, N.; Ali, J. I.; Ammazalorso, A.; De Filippis, B.; Franceschelli, S.; Giampietro, L.; Pesce, M.; Reale, M.; Tricca, M. L.; Re, N.; Felaco, M.; Amoroso, R., Synthesis, Biological Evaluation, and Docking Studies of N-Substituted Acetamidines as Selective Inhibitors of Inducible Nitric Oxide Synthase. *Journal of Medicinal Chemistry* **2009**, *52* (5), 1481-1485.
149. Grädler, U.; Fuchß, T.; Ulrich, W.-R.; Boer, R.; Strub, A.; Hesslinger, C.; Anézo, C.; Diederichs, K.; Zaliani, A., Novel nanomolar imidazo[4,5-b]pyridines as selective nitric oxide synthase (iNOS) inhibitors: SAR and structural insights. *Bioorganic and Medicinal Chemistry Letters* **2011**, *21* (14), 4228-4232.
150. (a) Galan, A.; De Mendoza, J.; Prados, P.; Rojo, J.; Echavarren, A. M., Synthesis of secondary amines by rhodium catalyzed hydrogenation of nitriles. *The Journal of Organic Chemistry* **1991**, *56* (1), 452-454; (b) Salvatore, R. N.; Yoon, C. H.; Jung, K. W., Synthesis of secondary amines. *Tetrahedron* **2001**, *57* (37), 7785-7811.
151. (a) Robert E. Eisenthal; Cornish-Bowden, A., The direct linear plot. A new graphical procedure for estimating enzyme kinetic parameters. *Biochem J.* **1974**, *139* (3), 715 – 720. ; (b) Cornish-Bowden, A., *Fundamentals of Enzyme Kinetics*. 2 ed.; Portland Press: London, 1995.
152. Michael A, S., Michaelis-Menten mechanism reconsidered: implications of fractal kinetics. *Journal of Theoretical Biology* **1995**, *176* (1), 115-124.
153. Garrett, R.; Grisham, C., *Biochemistry, third edition*. Brooks Cole: 2004.

154. (a) Lineweaver, H.; Burk, D., The Determination of Enzyme Dissociation Constants. *Journal of the American Chemical Society* **1934**, *56* (3), 658-666; (b) Copeland, R., *Enzymes: A Practical Introduction to Structure, Mechanism, and Data Analysis*. Wiley-VCH: 2000.
155. Atkins, G. L.; Nimmo, I. A., A comparison of seven methods for fitting the Michaelis-Menten equation. *Biochem. J.* **1975**, *149* (3), 775-777.
156. Cornish-Bowden, A., *Fundamentals of Enzyme Kinetics*. Portland Press: 2004.
157. Knowles, R. G.; Moncada, S., Nitric oxide synthases in mammals. *Biochem. J.* **1994**, *298* (2), 249-258.
158. (a) Wolff, D. J.; Gauld, D. S.; Neulander, M. J.; Southan, G., Inactivation of Nitric Oxide Synthase by Substituted Aminoguanidines and Aminoisothioureas. *Journal of Pharmacology and Experimental Therapeutics* **1997**, *283* (1), 265-273; (b) Noack, E.; Kubitzek, D.; Kojda, G., Spectrophotometric determination of nitric oxide using hemoglobin. *Neuroprotocols* **1992**, *1* (2), 133-139.
159. *Hyper32*, Copyright J S Easterby:
<http://homepage.ntlworld.com/john.easterby/software.html>.
160. Hevel JM, M. M., Nitric-oxide synthase assays. *Methods Enzymol.* **1994**, *233*, 250 - 8.
161. Sun, J.; Zhang, X.; Broderick, M.; Fein, H., Measurement of Nitric Oxide Production in Biological Systems by Using Griess Reaction Assay. *Sensors* **2003**, *3* (8), 276-284.
162. (a) Speyer, C. L.; Neff, T. A.; Warner, R. L.; Guo, R.-F.; Sarma, J. V.; Riedemann, N. C.; Murphy, M. E.; Murphy, H. S.; Ward, P. A., Regulatory Effects of iNOS on Acute Lung Inflammatory Responses in Mice. *The American Journal of Pathology* **2003**, *163* (6), 2319-2328; (b) Kan, W.; Zhao, K.-s.; Jiang, Y.; Yan, W.; Huang, Q.; Wang, J.; Qin, Q.; Huang, X.; Wang, S., Lung, Spleen, and Kidney Are the Major Places for Inducible Nitric Oxide Synthase Expression in Endotoxic Shock: Role of P38 Mitogen-Activated Protein Kinase in Signal Transduction of Inducible Nitric Oxide Synthase Expression. *Shock* **2004**, *21* (3), 281-287.
163. Crane, B. R.; Arvai, A. S.; Ghosh, S.; Getzoff, E. D.; Stuehr, D. J.; Tainer, J. A., Structures of the N ω -Hydroxy-L-Arginine Complex of Inducible Nitric Oxide Synthase Oxygenase Dimer with Active and Inactive Pterins. *Biochemistry* **2000**, *39* (16), 4608-4621.
164. Fedorov, R.; Hartmann, E.; Ghosh, D. K.; Schlichting, I., Structural Basis for the Specificity of the Nitric-oxide Synthase Inhibitors W1400 and N ω -Propyl-L-Arg for the Inducible and Neuronal Isoforms. *Journal of Biological Chemistry* **2003**, *278* (46), 45818-45825.
165. Ann Hallinan, E.; Kramer, S. W.; Houdek, S. C.; Moore, W. M.; Jerome, G. M.; Spangler, D. P.; Stevens, A. M.; Shieh, H. S.; Manning, P. T.; Pitzele, B. S., 4-Fluorinated L-lysine analogs as selective i-NOS inhibitors: methodology for introducing fluorine into the lysine side chain. *Organic and Biomolecular Chemistry* **2003**, *1* (20), 3527-3534.

References

166. Wallace, A. C.; Laskowski, R. A.; Thornton, J. M., LIGPLOT: a program to generate schematic diagrams of protein-ligand interactions. *Protein Engineering* **1995**, *8* (2), 127-134.
167. Crane, B. R.; Rosenfeld, R. J.; Arvai, A. S.; Ghosh, D. K.; Ghosh, S.; Tainer, J. A.; Stuehr, D. J.; Getzoff, E. D., N-terminal domain swapping and metal ion binding in nitric oxide synthase dimerization. *EMBO J* **1999**, *18* (22), 6271-6281.
168. Jackson, S. A.; Sahni, S.; Lee, L.; Luo, Y.; Nieduzak, T. R.; Liang, G.; Chiang, Y.; Collar, N.; Fink, D.; He, W.; Laoui, A.; Merrill, J.; Boffey, R.; Crackett, P.; Rees, B.; Wong, M.; Guilloteau, J.-P.; Mathieu, M.; Rebello, S. S., Design, synthesis and characterization of a novel class of coumarin-based inhibitors of inducible nitric oxide synthase. *Bioorganic and Medicinal Chemistry* **2005**, *13* (8), 2723-2739.
169. Rosenfeld, R. J.; Garcin, E. D.; Panda, K.; Andersson, G.; Åberg, A.; Wallace, A. V.; Morris, G. M.; Olson, A. J.; Stuehr, D. J.; Tainer, J. A.; Getzoff, E. D., Conformational Changes in Nitric Oxide Synthases Induced by Chlorzoxazone and Nitroindazoles: Crystallographic and Computational Analyses of Inhibitor Potency. *Biochemistry* **2002**, *41* (47), 13915-13925.
170. Liu, Y.; Oliveira, B. L.; Correia, J. D. G.; Santos, I. C.; Santos, I.; Spingler, B.; Alberto, R., Syntheses of bifunctional 2,3-diamino propionic acid-based chelators as small and strong tripod ligands for the labelling of biomolecules with ^{99m}Tc. *Organic and Biomolecular Chemistry* **2010**, *8* (12), 2829-2839.
171. Gunsteren, W. F. v.; Mark, A. E., Validation of molecular dynamics simulation. *The Journal of Chemical Physics* **1998**, *108* (15), 6109-6116.
172. Delker, S. L.; Ji, H.; Li, H.; Jamal, J.; Fang, J.; Xue, F.; Silverman, R. B.; Poulos, T. L., Unexpected Binding Modes of Nitric Oxide Synthase Inhibitors Effective in the Prevention of a Cerebral Palsy Phenotype in an Animal Model. *Journal of the American Chemical Society* **2010**, *132* (15), 5437-5442.
173. Oliveira, B. L., Moreira, I.S., Santos, I., Fernandes, P.A., Ramos, M.J., Correia, J.D.G., Insights into the structural determinants for selective inhibition of Nitric Oxide Synthase isoforms. *in preparation*.
174. Aparna, V.; Desiraju, G. R.; Gopalakrishnan, B., Insights into ligand selectivity in nitric oxide synthase isoforms: A molecular dynamics study. *Journal of Molecular Graphics and Modelling* **2007**, *26* (2), 457-470.
175. *Volarea*, João Ribeiro, Group of Computational BioChemistry, Faculty of Sciences of the University of Porto, Porto, Portugal: <http://www.compbiochem.org/Software/molSPACE/Home.html>.
176. Morais, M.; Raposinho, P.; Oliveira, M.; Correia, J.; Santos, I., Evaluation of novel ^{99m}Tc(I)-labeled homobivalent α -melanocyte-stimulating hormone analogs for melanocortin-1 receptor targeting. *Journal of Biological Inorganic Chemistry*, 1-15.

177. (a) Meggers, E., From Conventional to Unusual Enzyme Inhibitor Scaffolds: The Quest for Target Specificity. *Angewandte Chemie International Edition* **2011**, *50* (11), 2442-2448; (b) Feng, L.; Geisselbrecht, Y.; Blanck, S.; Wilbuer, A.; Atilla-Gokcumen, G. E.; Filippakopoulos, P.; Kräling, K.; Celik, M. A.; Harms, K.; Maksimoska, J.; Marmorstein, R.; Frenking, G.; Knapp, S.; Essen, L.-O.; Meggers, E., Structurally Sophisticated Octahedral Metal Complexes as Highly Selective Protein Kinase Inhibitors. *Journal of the American Chemical Society* **2011**, *133* (15), 5976-5986.
178. Jacobson, O.; Weiss, I. D.; Szajek, L.; Farber, J. M.; Kiesewetter, D. O., 64Cu-AMD3100—A novel imaging agent for targeting chemokine receptor CXCR4. *Bioorganic and Medicinal Chemistry* **2009**, *17* (4), 1486-1493.
179. (a) Chang, C.-e. A.; Chen, W.; Gilson, M. K., Ligand configurational entropy and protein binding. *Proceedings of the National Academy of Sciences* **2007**, *104* (5), 1534-1539; (b) Mobley, D. L.; Dill, K. A., Binding of Small-Molecule Ligands to Proteins: “What You See” Is Not Always “What You Get”. *Structure* **2009**, *17* (4), 489-498; (c) Gao, C.; Park, M.-S.; Stern, H. A., Accounting for Ligand Conformational Restriction in Calculations of Protein-Ligand Binding Affinities. *Biophysical Journal* **2010**, *98* (5), 901-910; (d) Perola, E.; Charifson, P. S., Conformational Analysis of Drug-Like Molecules Bound to Proteins: An Extensive Study of Ligand Reorganization upon Binding. *Journal of Medicinal Chemistry* **2004**, *47* (10), 2499-2510; (e) Diehl, C.; Engström, O.; Delaine, T.; Håkansson, M.; Genheden, S.; Modig, K.; Leffler, H.; Ryde, U.; Nilsson, U. J.; Akke, M., Protein Flexibility and Conformational Entropy in Ligand Design Targeting the Carbohydrate Recognition Domain of Galectin-3. *Journal of the American Chemical Society* **2010**, *132* (41), 14577-14589.
180. Steinkellner, G.; Rader, R.; Thallinger, G.; Kratky, C.; Gruber, K., VASCo: computation and visualization of annotated protein surface contacts. *BMC Bioinformatics* **2009**, *10* (1), 32.
181. Humphrey, W.; Dalke, A.; Schulten, K., VMD: Visual molecular dynamics. *Journal of Molecular Graphics* **1996**, *14* (1), 33-38.
182. (a) Perez, M. A. S.; Fernandes, P. A.; Ramos, M. J., Substrate Recognition in HIV-1 Protease: A Computational Study. *The Journal of Physical Chemistry B* **2010**, *114* (7), 2525-2532; (b) Pearlman, D. A., A Comparison of Alternative Approaches to Free Energy Calculations. *The Journal of Physical Chemistry* **1994**, *98* (5), 1487-1493; (c) Jérôme Hénin; Chris Harrison; Chipot, C. A tutorial for alchemical FEP in NAMD. <http://www.ks.uiuc.edu/~char/tutorials/FEP/> (accessed 19-10-2011).
183. Pohorille, A.; Jarzynski, C.; Chipot, C., Good Practices in Free-Energy Calculations. *The Journal of Physical Chemistry B* **2010**, *114* (32), 10235-10253.
184. Shirts, M. R.; Pitera, J. W.; Swope, W. C.; Pande, V. S., *Extremely precise free energy calculations of amino acid side chain analogs: Comparison of common molecular mechanics force fields for proteins*. AIP: 2003; Vol. 119, p 5740-5761.

References

185. (a) Lazarova, N.; James, S.; Babich, J.; Zubietta, J., A convenient synthesis, chemical characterization and reactivity of $[\text{Re}(\text{CO})_3(\text{H}_2\text{O})_3]\text{Br}$: the crystal and molecular structure of $[\text{Re}(\text{CO})_3(\text{CH}_3\text{CN})_2\text{Br}]$. *Inorganic Chemistry Communications* **2004**, *7* (9), 1023-1026; (b) Alberto, R.; Schibli, R.; Egli, A.; August Schubiger, P.; Herrmann, W. A.; Artus, G.; Abram, U.; Kaden, T. A., Metal carbonyl syntheses XXII. Low pressure carbonylation of $[\text{MOCl}_4]^-$ and $[\text{MO}_4]^-$: the technetium(I) and rhenium(I) complexes $[\text{NEt}_4]_2[\text{MCl}_3(\text{CO})_3]$. *Journal of Organometallic Chemistry* **1995**, *493* (1-2), 119-127.
186. Oxford Diffraction Ltd. *CrysAlis^{Pro} Software system*, 171.32; Oxford, UK, 2007.
187. *SADABS, Area-Detector Absorption Correction*, Bruker AXS Inc.: Madison, WI, 2004.
188. *SAINT, Area-Detector Integration Software*, 7.23; Bruker AXS Inc.: Madison, WI, 2004.
189. Altomare, A.; Burla, M. C.; Camalli, M.; Cascarano, G. L.; Giacovazzo, C.; Guagliardi, A.; Moliterni, A. G. G.; Polidori, G.; Spagna, R., SIR97: A New Tool for Crystal Structure Determination and Refinement. *J. Appl. Crystallogr.* **1999**, *32* (1), 115-119.
190. Sheldrick, G. M., A short history of SHELX. *Acta Cryst.* **2008**, *A64* (1), 112-122.
191. Farrugia, L. J., ORTEP-3 for Windows - a version of ORTEP-III with a Graphical User Interface (GUI). *J. Appl. Cryst.* **1997**, *30* (1), 565-565.
192. Troutner, D. E.; Volkert, W. A.; Hoffman, T. J.; Holmes, R. A., A neutral lipophilic complex of $^{99\text{m}}\text{Tc}$ with a multidentate amine oxime. *The International Journal of Applied Radiation and Isotopes* **1984**, *35* (6), 467-470.
193. Lowry, O. H.; Rosebrough, N. J.; Farr, A. L.; Randall, R. J., Protein measurement with the folin phenol reagent. *Journal of Biological Chemistry* **1951**, *193* (1), 265-275.
194. Green, L. C.; Wagner, D. A.; Glogowski, J.; Skipper, P. L.; Wishnok, J. S.; Tannenbaum, S. R., Analysis of nitrate, nitrite, and ^{15}N nitrate in biological fluids. *Analytical Biochemistry* **1982**, *126* (1), 131-138.
195. Tim, M., Rapid colorimetric assay for cellular growth and survival: Application to proliferation and cytotoxicity assays. *Journal of Immunological Methods* **1983**, *65* (1-2), 55-63.
196. Shelley, J.; Cholleti, A.; Frye, L.; Greenwood, J.; Timlin, M.; Uchimaya, M., Epik: a software program for pKa prediction and protonation state generation for drug-like molecules. *Journal of Computer-Aided Molecular Design* **2007**, *21* (12), 681-691.
197. Raman, C. S.; Li, H.; Martasek, P.; Southan, G.; Masters, B. S. S.; Poulos, T. L., Crystal Structure of Nitric Oxide Synthase Bound to Nitro Indazole Reveals a Novel Inactivation Mechanism. *Biochemistry* **2001**, *40* (45), 13448-13455.
198. Vanommeslaeghe, K.; Hatcher, E.; Acharya, C.; Kundu, S.; Zhong, S.; Shim, J.; Darian, E.; Guvench, O.; Lopes, P.; Vorobyov, I.; Mackerell, A. D., CHARMM general force field: A force field for

drug-like molecules compatible with the CHARMM all-atom additive biological force fields. *Journal of Computational Chemistry* **2010**, *31* (4), 671-690.

199. Ziegler, T., Approximate density functional theory as a practical tool in molecular energetics and dynamics. *Chemical Reviews* **1991**, *91* (5), 651-667.

200. (a) Becke, A. D., Density-functional thermochemistry. III. The role of exact exchange. *The Journal of Chemical Physics* **1993**, *98* (7), 5648-5652; (b) Sousa, S. F.; Fernandes, P. A.; Ramos, M. J., General Performance of Density Functionals. *The Journal of Physical Chemistry A* **2007**, *111* (42), 10439-10452; (c) Lee, C.; Yang, W.; Parr, R. G., Development of the Colle-Salvetti correlation-energy formula into a functional of the electron density. *Physical Review B* **1988**, *37* (2), 785; (d) Li, X.; Liu, X.; Wu, Z.; Zhang, H., DFT/TDDFT Studies on the Electronic Structures and Spectral Properties of Rhenium(I) Pyridinylbenzimidazole Complexes. *The Journal of Physical Chemistry A* **2008**, *112* (44), 11190-11197.

201. Cornell, W. D.; Cieplak, P.; Bayly, C. I.; Kollmann, P. A., Application of RESP charges to calculate conformational energies, hydrogen bond energies, and free energies of solvation. *Journal of the American Chemical Society* **1993**, *115* (21), 9620-9631.

202. Connolly, M., Analytical molecular surface calculation. *Journal of Applied Crystallography* **1983**, *16* (5), 548-558.

203. (a) Andrae, D.; Häußermann, U.; Dolg, M.; Stoll, H.; Preuß, H., Energy-adjusted ab initio pseudopotentials for the second and third row transition elements. *Theoretical Chemistry Accounts: Theory, Computation, and Modeling (Theoretica Chimica Acta)* **1990**, *77* (2), 123-141; (b) T. H. Dunning Jr.; Hay, P. J., in *Modern Theoretical Chemistry*. H. F. Schaefer III ed.; Plenum: New York, 1976; Vol. 3, p 1-28; (c) M. Dolg, U. W., H. Stoll, and H. Preuss, Energy-adjusted ab initio pseudopotentials for the first row transition elements *J. Chem. Phys.* **1987**, *86* (2), 866 - 873.

204. (a) Dupradeau, F.-Y.; Pigache, A.; Zaffran, T.; Savineau, C.; Lelong, R.; Grivel, N.; Lelong, D.; Rosanski, W.; Cieplak, P., The R.E.D. tools: advances in RESP and ESP charge derivation and force field library building. *Physical Chemistry Chemical Physics* **2010**, *12* (28), 7821-7839; (b) Dupradeau, F.-Y.; Cézard, C.; Lelong, R.; Stanislawiak, É.; Pêcher, J.; Delepine, J. C.; Cieplak, P., R.E.D.D.B.: A database for RESP and ESP atomic charges, and force field libraries. *Nucleic Acids Research* **2008**, *36* (suppl 1), D360-D367; (c) Vanquelef, E.; Simon, S.; Marquant, G.; Garcia, E.; Klimerak, G.; Delepine, J. C.; Cieplak, P.; Dupradeau, F.-Y., R.E.D. Server: a web service for deriving RESP and ESP charges and building force field libraries for new molecules and molecular fragments. *Nucleic Acids Research* **2011**, *39* (suppl 2), W511-W517.

205. (a) Cundari, T. R.; Fu, W., Genetic algorithm optimization of a molecular mechanics force field for technetium. *Inorganica Chimica Acta* **2000**, *300-302*, 113-124; (b) Reichert, D. E.; Welch, M. J., Applications of molecular mechanics to metal-based imaging agents. *Coordination Chemistry*

References

- Reviews* **2001**, *212* (1), 111-131; (c) Wolohan, P.; Reichert, D. E., CoMSIA and docking study of rhenium based estrogen receptor ligand analogs. *Steroids* **2007**, *72* (3), 247-260; (d) Desbouis, D.; Struthers, H.; Spiwok, V.; Küster, T.; Schibli, R., Synthesis, In Vitro, and In Silico Evaluation of Organometallic Technetium and Rhenium Thymidine Complexes with Retained Substrate Activity toward Human Thymidine Kinase Type 1. *Journal of Medicinal Chemistry* **2008**, *51* (21), 6689-6698; (e) Stichelberger, M.; Desbouis, D.; Spiwok, V.; Scapozza, L.; Schubiger, P. A.; Schibli, R., Synthesis, in vitro and in silico assessment of organometallic Rhenium(I) and Technetium(I) thymidine complexes. *Journal of Organometallic Chemistry* **2007**, *692* (6), 1255-1264.
206. (a) Hoops, S. C.; Anderson, K. W.; Merz, K. M., Force field design for metalloproteins. *Journal of the American Chemical Society* **1991**, *113* (22), 8262-8270; (b) Peters, M. B.; Yang, Y.; Wang, B.; Füsti-Molnár, L. s.; Weaver, M. N.; Merz, K. M., Structural Survey of Zinc-Containing Proteins and Development of the Zinc AMBER Force Field (ZAFF). *Journal of Chemical Theory and Computation* **2010**, *6* (9), 2935-2947; (c) Sousa, S.; Fernandes, P.; Ramos, M., Effective tailor-made force field parameterization of the several Zn coordination environments in the puzzling FTase enzyme: opening the door to the full understanding of its elusive catalytic mechanism. *Theoretical Chemistry Accounts: Theory, Computation, and Modeling (Theoretica Chimica Acta)* **2007**, *117* (1), 171-181.
207. Norrby, P.-O.; Brandt, P., Deriving force field parameters for coordination complexes. *Coordination Chemistry Reviews* **2001**, *212* (1), 79-109.
208. (a) Dolinsky, T. J.; Nielsen, J. E.; McCammon, J. A.; Baker, N. A., PDB2PQR: an automated pipeline for the setup of Poisson–Boltzmann electrostatics calculations. *Nucleic Acids Research* **2004**, *32* (suppl 2), W665-W667; (b) Li, H.; Robertson, A. D.; Jensen, J. H., Very fast empirical prediction and rationalization of protein pKa values. *Proteins: Structure, Function, and Bioinformatics* **2005**, *61* (4), 704-721; (c) Dolinsky, T. J.; Czodrowski, P.; Li, H.; Nielsen, J. E.; Jensen, J. H.; Klebe, G.; Baker, N. A., PDB2PQR: expanding and upgrading automated preparation of biomolecular structures for molecular simulations. *Nucleic Acids Research* **2007**, *35* (suppl 2), W522-W525.
209. Essmann, U.; Perera, L.; Berkowitz, M. L.; Darden, T.; Lee, H.; Pedersen, L. G., A smooth particle mesh Ewald method. *The Journal of Chemical Physics* **1995**, *103* (19), 8577-8593.
210. Grest, G. S.; Kremer, K., Molecular dynamics simulation for polymers in the presence of a heat bath. *Physical Review A* **1986**, *33* (5), 3628.
211. (a) Hoover, W. G., Canonical dynamics: Equilibrium phase-space distributions. *Physical Review A* **1985**, *31* (3), 1695; (b) Feller, S. E.; Zhang, Y.; Pastor, R. W.; Brooks, B. R., Constant pressure molecular dynamics simulation: The Langevin piston method. *The Journal of Chemical Physics* **1995**, *103* (11), 4613-4621; (c) NOSÉ, S., A molecular dynamics method for simulations in the canonical

- ensemble. *Molecular Physics: An International Journal at the Interface Between Chemistry and Physics* **2002**, *100* (1), 191 - 198.
212. DeLano, W. L., The PyMOL Molecular Graphics System. DeLano Scientific: San Carlos, CA, USA., 2002
213. Bhandarkar, M.; R. Brunner; C. Chipot; A. Dalke; S. Dixit, NAMD user's guide, version 2.6b1. Theoretical Biophysics Group, University of Illinois and Beckman Institute, Urbana, IL., 2005.
214. Pitera, J. W.; van Gunsteren, W. F., A Comparison of Non-Bonded Scaling Approaches for Free Energy Calculations. *Molecular Simulation* **2002**, *28* (1-2), 45-65.
215. (a) Zacharias, M.; Straatsma, T. P.; McCammon, J. A., *Separation shifted scaling, a new scaling method for Lennard-Jones interactions in thermodynamic integration*. AIP: 1994; Vol. 100, p 9025-9031; (b) Beutler, T. C.; Mark, A. E.; van Schaik, R. C.; Gerber, P. R.; van Gunsteren, W. F., Avoiding singularities and numerical instabilities in free energy calculations based on molecular simulations. *Chemical Physics Letters* **1994**, *222* (6), 529-539.
216. Coleman, R. G.; Sharp, K. A., Travel Depth, a New Shape Descriptor for Macromolecules: Application to Ligand Binding. *Journal of Molecular Biology* **2006**, *362* (3), 441-458.